Lithosphere – Mantle Interactions

A thesis presented by

Thorsten Wolfgang Becker

to The Department of Earth and Planetary Sciences

in partial fulfillment of the requirements for the degree of Doctor of Philosophy
in the subject of Geophysics

Harvard University
Cambridge, Massachusetts

April 2002

Advisor: Prof. Richard O'Connell Thorsten Wolfgang Becker

Lithosphere–Mantle Interactions

Abstract

We study the interaction between lithospheric dynamics and mantle convection to establish a comprehensive model of large-scale deformation that can be tested using a variety of surface observables. In chapter 1 we explore subduction and upper-mantle convection using fluid-dynamic models. Comparing results from analog and numerical experiments, we show that key observations in subduction zones can be explained using fluid flow. We analyze contrasting styles of back-arc deformation based on the balance between viscous dissipation and gravitational energy release in the subducting plate. By combining a wide range of geological and geophysical data in chapter 2 we are able to reconstruct the subduction history of the Central Mediterranean. Subduction initiated slowly and lead to episodic back-arc spreading, as predicted from our models for predominantly slab-pull driven subduction. Based on these regional studies, we estimate global deformation in the lithosphere from spherical-circulation calculations. Chapter 3 describes a comprehensive and quantitative comparison between mantle models from tomography and geodynamics. Establishing such a benchmark for three-dimensional structure is important if we want to move from the mapping phase of tomography to hypothesis testing. To examine the dynamic self-consistency of our flow models, we study the torques on the plates in chapter 4 and reevaluate arguments of the plate-driving force discussion. We substantiate the finding that slab pull contributes most to the driving forces but find that a range of models can explain plate motions. Velocity inversions are shown to have limited sensitivity to parameterized plate-boundary forces, here included in a velocity model for the first time. Chapter 5 deals with a first application of our deformation model: the prediction of finite-strain development in the uppermost mantle and its comparison with seismic anisotropy. We can fit a range of anisotropy data for oceanic and young continental plate-regions and compare our global models with surface-wave derived azimuthal anisotropy. Alignment of fast propagation axes with finite strain leads to low misfits and better results than the absolute plate motion hypothesis. Three-dimensional flow modeling with realistic plate geometries may provide the needed tool to interpret seismic anisotropy quantitatively as an indicator of mantle flow.

Our battered suitcases were piled on the sidewalk again;
we had longer ways to go.
But no matter, the road is life.
Jack Kerouac

Contents

List of Figures

List of Tables

Acknowledgments

I thank my advisor Richard O'Connell for the continuing encouragement for all my research, be it in geodynamics or seismology. His physical intuition and insight have been an invaluable guide to my work, and his support throughout the last five years have been the foundation of the research that is presented here. Of the other Harvard faculty, especially James Rice, Göran Ekström, Adam Dziewonski, and John Shaw are thanked for their help, advice, and collaboration. Claudio Faccenna, who was visiting from Universitá Roma III, got me started on thinking about subduction; he has also substantially contributed to the experiments in chapter 1 and the synthesis of geological data in chapter 2. Working with Claudio in Cambridge and in Rome was fun and furthered my understanding of geological problems. Other people that provided helpful suggestions and reviews of related manuscripts include Hans-Peter Bunge, Brad Hager, Rob van der Hilst, Carolina Lithgow-Bertelloni, Bernhard Steinberger, Stephen Zatman, and Shijie Zhong. Bernhard is also thanked for providing his flow code.

My fellow students Lapo Boschi, Mathieu Dumberry, Pippa Halverson, Jamie Kellogg, Bogdan Kustowski, Yu Gu, Chris Guzofski, Meredith Nettles, and Sabine Stanley made working at Harvard fun and were of help with minor and major problems. Jamie contributed a lot with his suggestions on various aspects of the work that is presented here; our formal collaborations were great, be it on blobs or strain. Without Jamie, I would also know so much less about US pop culture. Without Pippa as a squash partner, I would have been less zen-like in my approach to life as a graduate student. Cintia Santana, Mathieu, and especially Meredith supplied very careful and constructive comments on this thesis which were very useful. Bogdan and Miaki Ishii are thanked for their assistance with `MINEOS`.

Discussions with Karen Fischer at Brown University and especially with Paul Silver were what started me on the study of strain and anisotropy in the mantle (chapter 5), particularly the main focus of sec. 5.7.3 was worked out during a visit to DTM. Scott King kindly provided the finite element program `CONMAN` that was used for the numerical experiments in chapter 1. The willingness of several researchers to make tomographic and shear wave splitting data easily available was crucial for chapters 3 and 5. Partial funding for my Ph.D. program was provided by a *Doktorandenstipendium* of the *Deutscher Akademischer Austauschdienst* and by NSF under grants EAR-9814666 and EAR-0001046. Most figures were prepared with GMT by Wessel and Smith (1991).

Most importantly, I would like to thank all my friends and family back home and in the US for keeping me sane and on track.

Introduction

Our efforts to understand the dynamical processes in the Earth's interior and how they shape surface geology are closely linked to some of the most fundamental questions in solid earth sciences that concern the driving forces of plate tectonics and the mechanics of plate boundaries. Therefore, sections of this thesis discuss the effective stiffness of slabs and the manner in which torques act on plates, both of which are persistently reappearing problems. While we can, definitely, not finally answer all issues that are brought up along the way, we make good progress toward a comprehensive global model of the effects of mantle flow on surface deformation.

Besides the general attempt to quantify the effect of convection on the lithosphere, another aim of this thesis is the inclusion of a wide range of datasets as constraints for mantle flow. There has been considerable progress over the last twenty years in our theoretical understanding of convection in the Earth's mantle based on numerical models. During the last ten years or so, geophysicists have also begun to develop principal insights into what rheological effects might cause plates and plate tectonics to operate in general. However, we are still in the early stages of quantitatively constraining our convection models with surface observables. This is due in part to the fact that high-quality datasets and modeling methods are only now beginning to be readily available. The recent years have, for example, brought better observations of seismic wave propagation which can be brought to bear on high-resolution seismic tomography. Shear-wave splitting measurements are now being made routinely. While still sparse, anisotropy data and phase-velocity inversions from surface waves have the potential to give us a strong quantitative constraint on flow at depth. Another example is the wide range of geodesy-based velocity and strain-rate measurements that are accumulating. Our long-term goal is to develop a general convection model, both in a theoretical and in a technical sense, that can account for as many of those observations as possible and so guide us in focusing our research efforts to the more interesting regions where such a general model fails.

We use numerical calculations to make predictions about the Earth and to generate synthetic datasets that can then be compared to a range of observations. Our goal –to understand present-day global to regional-scale lithospheric deformation– implies that our modeling philosophy has to be guided by the simplifications that are needed to distill the underlying physics of the problem. We will not try to include all potential mechanisms to simulate the mantle but rather ask how complex we have to make models such that first-order effects are accounted for. In chapters 1 and 2, we study subduction and upper mantle flow. Combining numerical and analog modeling gives us the unique opportunity to jointly evaluate the validity of the model assumptions inherent within each method. We find that the viscous bending of the oceanic plate can be used to explain contrasting styles of overriding-plate deformation and compare our model predictions to nature. We use our models to explain a wide range of geological and geophysical data from the Mediterranean and find that slab interaction with the phase transition at 660-km was important for the episodic opening of back-arc basins. This interaction between temporarily confined convection and the lithosphere is an example of how seemingly remote processes like transient slab-flattening can leave evidence on the surface which we can use to constrain the time-dependence of flow in the mantle.

Seismic tomography has been used to argue for a general propensity of slabs to penetrate through 660-km and to image the global structure of mantle convection. We therefore review the current state of seismological mapping efforts in chapter 3 when we begin to construct a global model. We substantiate earlier results and conclude that there is, indeed, strong evidence for whole-mantle style convection and long-term mass flux between the upper and lower mantle. However, the dynamics are not simple, and transient slab-holdup at 660-km is an attractive explanation for both the complexity found in heterogeneity spectra and our finding that geodynamic models of mantle structure do not agree well with tomography except at the longest wavelengths. We also discuss some of the problems that are related to the resolution of different types of tomographic models and inversion methods. These seemingly technical issues become important when we interpret wavespeed anomalies as density for our global flow models. Yet, they are often overlooked, and it is worth noting that some of the inferences on petrological and geodynamical parameters that are in the literature are likely to be affected by these differences between tomographic models.

The next step toward our global lithospheric deformation model is the evaluation of dynamical consistency. We approach this issue in the framework of a plate-velocity inversion in chapter 4. Since we cannot yet treat plates and mantle flow in a single convection model, such an evaluation of the driving forces derived from density in the mantle is needed. We find that a range of models is suited to explain the observed plate motions and confirm the importance of slab-pull. Remarkably, a two-sided viscous drag, as expected for a weak slab, leads to better results than a one-sided slab-pull that is transmitted through a strong stress-guide. The addition of parameterized edge forces, which we include in a velocity inversion for the first time, does not consistently improve the fit above models that have only mantle-based driving forces and lithospheric thickening. Consistent with our finding from chapter 3 that some of the tomographic models are not imaging large-scale, slab-related density structure in the upper mantle, those models lead to inferior plate velocity predictions.

Based on this improved understanding of global mantle circulation, we address the first application of such models to lithospheric and upper-mantle deformation in chapter 5. We develop a tool to predict finite-strain in mantle flow to be compared with observations from seismic anisotropy. We can explain most of the signal that is observed in oceanic plates and find a good model-fit for azimuthal anisotropy as derived from surface waves. Our results indicate that we can use quantitative estimates of misfit to distinguish between different density structures in the mantle. Shear-wave splitting data has different spatial resolution and coverage than surface waves and is used to complement these global models. We explore the role of mantle flow in applications of our method to several plate boundary regions, and find that anisotropy in young continental and oceanic plates is well explained by the orientation of fast propagation directions with the largest axis of the finite-strain ellipsoid.

Chapter 1

Subduction: a numerical and laboratory modeling approach

1.1 Abstract

We discuss numerical and laboratory experiments modeling subduction of oceanic lithosphere in the upper mantle from its beginnings as a gravitational instability to the fully developed slab. A two-dimensional finite element code is applied to model Newtonian creep of mantle and lithospheric material in the numerical experiments. Analog media are used in the scaled laboratory experiments: a sand mixture models the brittle crust, silicone putty simulates creep in the lower crust and mantle lithosphere, and glucose syrup serves as the asthenosphere analog. Both model approaches are based on density and viscosity heterogeneities in a Stokes flow model; they show similar results and reproduce first-order observations of the subduction process in nature. Subduction nucleates slowly and a pronounced slab forms only when the viscosity contrast between oceanic plate and mantle is smaller than a threshold value. We find that the subduction velocity and angle are time-dependent and increase roughly exponentially over tens of millions of years before the slab reaches the 660-km discontinuity. The style of subduction is controlled by the prescribed velocity of convergence, the density contrast between the plates, and the viscosity contrast between the oceanic plate and the mantle. These factors can be combined in the buoyancy number F, which expresses the ratio between the driving slab pull and the resisting viscous dissipation in the oceanic plate. Variations in F control the stress in the plates, the speed and dip of subduction, and the rate of trench retreat, reproducing the contrasting styles of subduction observed in nature. The subduction rate is strongly influenced by the work required to bend the lithosphere as it subducts.

1.2 Introduction

Wadati-Benioff and high seismic-velocity zones indicate that oceanic lithosphere sinks back into the mantle, attaining various shapes and suffering contrasting modes of deformation (Isacks and Molnar, 1971; Isacks and Barazangi, 1977). These subduction zones have been studied extensively for a number of reasons: first, the corresponding trench thrust-interfaces are responsible for some of the largest earthquakes ever recorded. Second, the subduction process is thought to be intimately related to tectonic processes in the overriding plates, such as the formation of orogens in compressive regimes, volcanism, and back-arc spreading in extensional regimes. Thirdly, slab pull is a large (*e.g.* Forsyth and Uyeda, 1975) or the largest (*e.g.* Lithgow-Bertelloni and Richards, 1995) contribution to the forces that drive the tectonic plates (see chapter 4). A number of studies of the physical processes that govern the style of subduction have compared individual subduction zones to identify the key parameters (*e.g.* Jarrard, 1986). Unfortunately, as in the case of factors that might determine the dip of the subduction zone, this procedure does not always provide satisfactory results and correlations are found to be weak (Jarrard, 1986). This might be due to the assumption that the observed present-day geometry of the slabs is the result of a steady-

The work presented in this chapter was done in collaboration with Claudio Faccenna (University of Rome, III) and results were published in modified form in the *Journal of Geophysical Research* (Becker, Faccenna, O'Connell, and Giardini, 1999a). All laboratory experiments were performed by C. Faccenna.

state process. Some studies indicate substantial time-dependent behavior of the evolution of subducted slabs (*e.g.* Tao and O'Connell, 1993; Zhong and Gurnis, 1995), and suggest that the present configuration represents only a snapshot of the mantle flow.

A second possible procedure to address the physics of subduction is the construction of a model in which the influence of different parameters can be tested and compared with observations. This can be achieved with either laboratory (*e.g.* Kincaid and Olson, 1987; Shemenda, 1993; Gouillou-Frottier *et al.*, 1995; Griffiths *et al.*, 1995; Faccenna *et al.*, 1996) or numerical (*e.g.* Christensen and Yuen, 1984; Zhong and Gurnis, 1995; Christensen, 1996; Tetzlaff and Schmeling, 2000) experiments; these two approaches are complementary. While laboratory models give a direct representation of the physical processes and allow the simulation of complex rheologies in three dimensions, numerical experiments are easier to study and replicate quantitatively. In this chapter we discuss the results of both approaches to modeling the formation and evolution of slabs in the upper mantle. By comparing the two models we are able to identify and characterize simple yet important physical effects that govern the style of subduction. We test the following parameters: 1) the velocity of convergence (*e.g.* Luyendyk, 1970; Tovish and Schubert, 1978; Cross and Pilger, 1982; Furlong *et al.*, 1982), 2) the age of the oceanic lithosphere at the subduction zone (*e.g.* Stevenson and Turner, 1972; Molnar and Atwater, 1978; Uyeda and Kanamori, 1979; Cross and Pilger, 1982; Sacks, 1983), here expressed as the density contrast between oceanic plate and upper mantle (compare the age-density diagrams of *e.g.* Oxburgh and Turcotte (1976), and Cloos (1993)), and 3) the viscosity contrast between the oceanic plate and the upper mantle. As a function of these parameters, we are able to model slab trajectories in a fluid upper mantle and to observe trench migration at the surface. We analyze the state of stress in the slab and overriding plate, the velocity and dip of the slab, and the mode of trench migration that result from the force equilibrium.

The subduction process is found to be similar in the two model approaches: it initiates slowly as a gravitational instability and proceeds more rapidly as dense material sinks into the mantle. The speed of the downwelling increases roughly exponentially once the slab pull has overcome the resisting forces. This behavior continues until the slab reaches the 660-km discontinuity, typically after a few tens of millions of years. While the convergence velocity and the negative buoyancy of the oceanic plate represent the main driving forces in the system, the viscous drag in the oceanic plate as it bends provides the major resisting force. This dynamical competition controls the style of subduction in the upper mantle and can be characterized by the buoyancy number F. We first present the model assumptions, techniques, and results of our numerical and laboratory experiments, and subsequently discuss the relevance of our findings for subduction in nature.

1.3 Model definition: assumptions and boundary conditions

Our experiments are set up in the following framework:

1. Following a design adopted by previous authors (*e.g.* Jacoby and Schmeling, 1981; Kincaid and Olson, 1987; Gurnis and Hager, 1988; Tao and O'Connell, 1992a; Zhong and Gurnis, 1995; Gouillou-Frottier *et al.*, 1995; Griffiths *et al.*, 1995; Faccenna *et al.*, 1996), the experimental setting and the materials have been chosen to model a viscous slab. This rheology is an appropriate description since it has been supposed that lithosphere subjected to stress over geological timescales acts as a fluid of some sort. In fact, with an elastic lithosphere it is not possible to predict the shape of most of the Wadati-Benioff zones (Bevis, 1986), their strain rate (Bevis, 1988), and the highly curved subduction zones observed in some island arcs like the Marianas (Hsui, 1988). Furthermore, slabs exhibit significant deep, in-plane lateral deformation at depth (Giardini and Woodhouse, 1984) and appear to be folded at the transition zone (*e.g.* van der Hilst *et al.*, 1991), suggesting that the sinking lithosphere behaves similarly to a viscous fluid (Tao and O'Connell, 1992a). Some of the arguments in favor of slabs that are not only mainly viscously deforming, but are also of comparable viscosity to the surrounding mantle, are taken up again in sec. 2.3.
   In addition, the plates have been modeled using a viscosity that is constant both laterally within the plate and with depth. The plate viscosity, therefore, represents an average, effective value for the different parts of the lithosphere that are usually analyzed in terms of "Christmas tree" strength diagrams for the various crust and mantle materials (*e.g.* Ranalli, 1995). Analytic results demonstrate that the formation of an instability is not significantly modified by the approximation of depth independence (Martinod and Davy, 1992). Since the viscosity is homogeneous laterally, however, our subsequent statements about the importance of plate viscosities refer mainly to the regions involved in the subduction process, that is, the plate margin (*e.g.*

Jacoby and Schmeling, 1981). We furthermore use a Newtonian rheology, whereas laboratory data indicate that the upper mantle deforms obeying a power law with a stress exponent of $\sim$3 (*e.g.* Brace and Kohlstedt, 1980; Ranalli, 1995).

2. Horizontal tectonic stresses from lithospheric thickening, basal drag under the oceanic plate, resistance to motion of the continental roots, and plate reorganization (chapter 4) have been modeled by an oceanic plate that advances at a constant rate toward a fixed overriding plate. Such prescribed velocities are a common simplification in models of subduction since the initiation process is complicated to treat: some trick (*e.g.* pre-existing fault or weak zone) is usually applied to get the subduction process started. We will address these problems in sec. 1.6.1.
   The upper plate in our model is lighter than the subducting one, similar to the continent/ocean density differences in nature. However, our overriding plate is also more resistant than the subducting one. This difference is needed to obtain realistic subduction in the model, though continental areas are thought to be weaker than oceanic ones in general (*e.g.* Ranalli, 1995). Therefore, if the overriding plates in our models are to be compared directly with nature, then strong, old continental regions would be the most suitable analog (Figure 1.1).

3. Previous experiments indicated that the presence of a pre-existing fault or weak zone fixed in space exerts a strong control on the shape of the slab (Zhong and Gurnis, 1995; King and Ita, 1995; Hassani *et al.*, 1997) and on its velocity (King and Hager, 1990). In our model, deformation is initiated at a passive margin without the presence of a weak zone to avoid the a priori definition of the slab trajectory. Once subduction starts, the shape and the position of the converging margin evolve dynamically self-consistent under the prescribed boundary conditions.

4. We do not consider the effect of temperature variations or phase changes with depth. As in previous models, this approximation has been adopted since our analysis is restricted to slab formation and evolution in the upper mantle where the subduction zone preserves its thermal field to first-order (Wortel, 1982). Further, the numerical experiments have been constructed to be directly comparable to the laboratory ones, and it is one of our main points that first-order observations of subduction in nature can be explained by a simple Stokes flow model without any additional complications from thermal or phase change effects.

5. We assume a mantle with no trench-relative motion; flow is then only produced by the relative plate motion, and we do not consider the effect of global (*e.g.* Ricard *et al.*, 1991) or local background mantle flow (*e.g.* Tao and O'Connell, 1992a; Russo and Silver, 1994; Olbertz *et al.*, 1997) that is not directly related to subduction.

On the basis of these assumptions our experiments are scaled to the Earth using the Navier-Stokes equation for an incompressible fluid in the infinite Prandtl number and Boussinesq approximations. The resulting formula is Stokes' equation with a driving term due to density perturbations $\Delta\rho$ (sec. 2.3.1):

$$\mu\nabla^2\mathbf{u} - \nabla p_d - g\Delta\rho\mathbf{e}_z = \mathbf{0}. \tag{1.1}$$

Here the gravitational acceleration g is taken in z direction with unit vector $\mathbf{e}_z$, p_d is the dynamic pressure, $\mathbf{u}$ is the velocity, and μ is the dynamic viscosity. If we define a characteristic length L, velocity U, and density difference $\Delta\rho_0$, the characteristic pressure can be expressed as $p_c = \mu U/L$, the timescale is $t_c = L/U$, and the non-dimensionalized version of (1.1) follows as

$$\widehat{\nabla^2\mathbf{u}} - \widehat{\nabla p_d} - F\widehat{\Delta\rho}\mathbf{e}_z = \mathbf{0}. \tag{1.2}$$

We introduce the buoyancy number F (*e.g.* Houseman and Gubbins, 1997)

$$F = \frac{L^2 g\Delta\rho_0}{\mu U}, \tag{1.3}$$

which represents the ratio of the driving buoyancy to the resisting viscous forces. (F can be transformed into the Rayleigh number with $\Delta\rho = \rho_0\alpha\Delta T$ and $U = \varkappa/L$. Here, ΔT is a temperature difference; α and $\varkappa$ are the thermal expansion and diffusion coefficients, respectively.) For the Stokes flow problem, the appropriate scaling for U is $U \propto \Delta\rho R^2 g/\mu$, and the buoyancy number reduces to the length scale ratio L^2/R^2. As demonstrated in sec. 1.5.2,

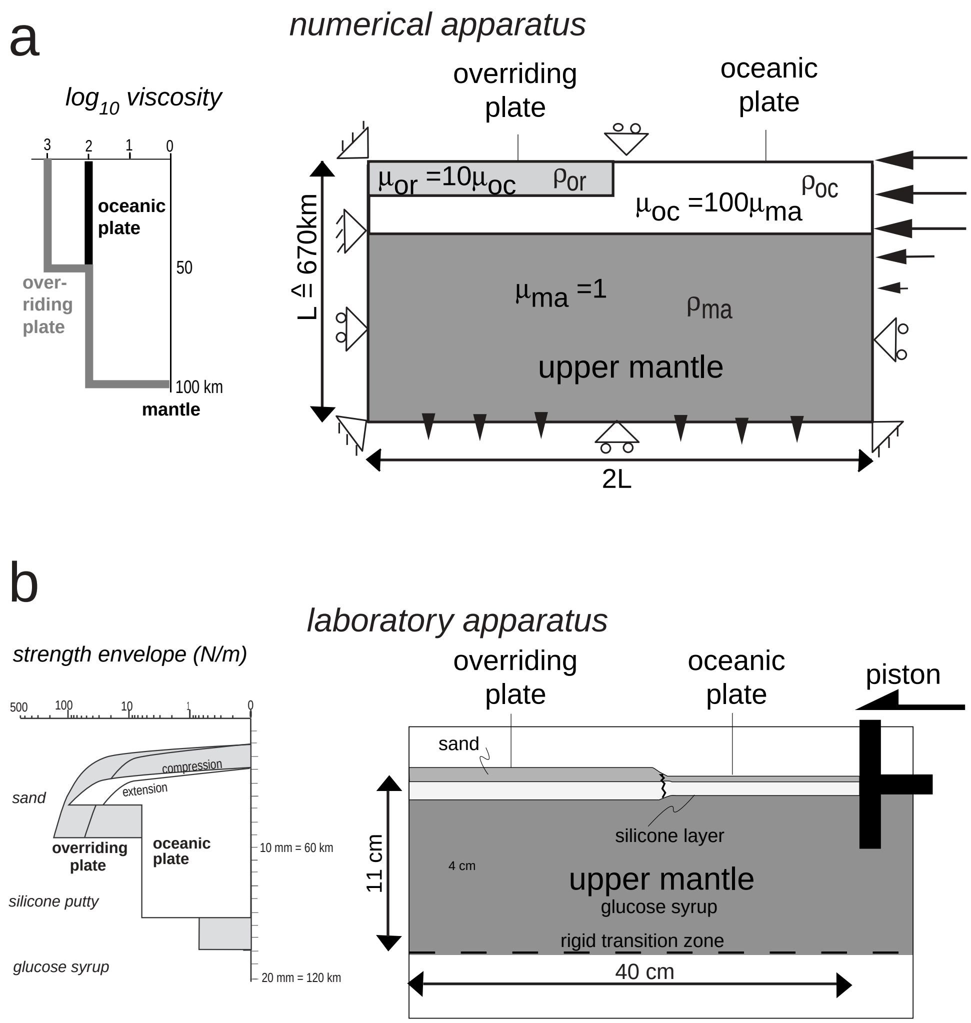

Figure 1.1: (a) Numerical and (b) experimental setups, boundary conditions, and corresponding viscosity and yield-strength envelopes of the lithospheric material used in the experiments. The laboratory strength envelopes have been calculated using a Mohr-Coulomb criterion for the sand layer and a creep law for the silicone layer (see Davy and Cobbold, 1991; Faccenna *et al.*, 1999). In particular, the latter has been estimated by multiplying the measured silicone putty viscosity with the velocity of convergence and dividing it by the thickness of the silicone layer. Arrows indicate prescribed velocities, open triangles with dashes and circles no and free-slip boundary conditions, respectively. (See Table 1.2 for definition of variables.)

the characteristic U for our models is the velocity of convergence, u_r, while the governing viscosity μ is that of the oceanic lithosphere and L is the domain height corresponding to the upper mantle. Taking characteristic numbers for Earth as those given in Table 1.1, $F \sim 14$.

1.4 Methods

1.4.1 Numerical experiments

We use the two-dimensional, Cartesian, finite element code for incompressible convection `CONMAN` by King *et al.* (1990). A material field that corresponds to the density anomalies is advected with a zero diffusivity, while only two material isolines (indicated in Figures 1.2, 1.4, and 1.6) are used to track the boundary between plates; we assign a constant Newtonian viscosity within each different material. As discussed by Lenardic and Kaula (1993),

Table 1.1: Material constants and buoyancy number for Earth, numerical and laboratory reference model. Parameters are μ: dynamic viscosity; L: domain height; g: gravitational acceleration; ρ: density; u_r: velocity of convergence; p: pressure; σ: stress; Φ: viscous dissipation; t: time; and F: buoyancy number. Abbreviations are c, characteristic; oc, oceanic plate; ma, mantle; or, overriding plate; sl, silica layer; and eff, effective.

nature	*num. ref. model (non-dim. units)*	*lab. ref. model (7)*
$\mu_{\mathrm{ma}} = 2.5\times10^{20}$ Pa s	$\mu_{\mathrm{ma}} = 0.1$	$\mu_{\mathrm{ma}} \approx 50$ Pa s
$\mu_{\mathrm{oc}} = 2.5\times10^{22}$ Pa s	$\mu_{\mathrm{oc}} = 10$	$\overline{\mu}_{\mathrm{oc}}^{\mathrm{eff}} \approx 7\times10^{5}$ Pa s
		$\mu_{\mathrm{oc}}^{\mathrm{sl}} \approx 7\times10^{4}$ Pa s
$\mu_{\mathrm{or}} = 2.5\times10^{23}$ Pa s	$\mu_{\mathrm{or}} = 10\mu_{\mathrm{oc}}$	$\mu_{\mathrm{or}} \approx 10^{4}$ Pa s
$L = L_c = 6.7\times10^{5}$ m	$L = 1$	$L = 1.1\times10^{-1}$ m
$g = 9.81$ m/s^2		$g = 9.81$ m/s^2
$\rho_{\mathrm{oc}} = 3300$ kg/m^3	$\rho_0 = 1$	$\rho_{\mathrm{oc}} = 1474$ kg/m^3
$\rho_{\mathrm{or}}^{\mathrm{upper}} = 2800$ kg/m^3		$\rho_{\mathrm{or}} = 1282$ kg/m^3
$\rho_{\mathrm{or}}^{\mathrm{lower}} = 3300$ kg/m^3	$g\Delta\rho_{\mathrm{ma}}^{\mathrm{oc}} = 70$	
$\rho_{\mathrm{ma}} = 3220$ kg/m^3		$\rho_{\mathrm{ma}} = 1410$ kg/m^3
$\Delta\rho_{\mathrm{ma}}^{\mathrm{oc}} = 80$ kg/m^3		$\Delta\rho_{\mathrm{ma}}^{\mathrm{oc}} = 64$ kg/m^3
$u_r = 10^{-9}$ m/s ≈ 3.2 cm/yr	$u_r = 0.5$	$u_r = 6.9\times10^{-7}$ m/s
$p_{\mathrm{c}} = \sigma_{\mathrm{c}} = \mu_{\mathrm{oc}}u_r/L \approx 37.3$ MPa	$\sigma_{\mathrm{c}} = 50$	$\sigma_{\mathrm{c}} \approx 4.2$ Pa
$\Phi_{\mathrm{c}} = \sigma_{\mathrm{c}}^2/\mu_{\mathrm{oc}} \approx 56$ nW/m^3	$\Phi_{\mathrm{c}} = 250$	
$t_{\mathrm{c}} = L/u_r \approx 21$ Myr	$t_{\mathrm{c}} = 2$	$t_{\mathrm{c}} = 46$ hours
	$1 \equiv 10.5$ Myr	$1h \equiv 0.5$ Myr
$F = \frac{L^2 g\Delta\rho_{\mathrm{ma}}^{\mathrm{oc}}}{\mu_{\mathrm{oc}}u_r} \approx 14.1$	$F = 14$	$F \approx 15.7$

the numerical method we use has shortcomings for strong viscosity contrasts and an unavoidable numerical diffusion is introduced. However, since we are only interested in simple convection processes without multiple overturns, these inaccuracies have a limited effect in our models, and in general, the viscosity and material fields match well. The geometry of our computational domain is rectangular with 1:2 aspect ratio to simulate an upper mantle region of dimensions 670 km $\times$ 1340 km. The experimental design and model parameters are summarized in Figure 1.1a and Table 1.1. A regularly spaced finite element mesh of 128$\times$128 second-order elements is applied for all models shown here. We estimate that our results are accurate to within a total relative error of $< 5\%$ with respect to mesh refinement from 64$\times$64 to 256$\times$256 elements and other inaccuracies such as those mentioned above. The oceanic lithosphere is driven from the right side of the box at a prescribed horizontal convergence velocity u_r toward a fixed overriding plate characterized by a more viscous (10 times) and less dense upper crustal layer. The boundary conditions on the upper boundary and the lower parts of the side boundaries are free slip, while the lower boundary has a prescribed vertical outflow to enforce mass conservation (too small to show up in the flow field plots) and no constraint on the horizontal velocity. We examined the influence of different boundary conditions, such as no slip instead of free slip along the lower sides of the box and found no substantial differences in model behavior (sec. 1.5.4). The ratio between oceanic and mantle viscosity ($\mu_{\mathrm{oc}}/\mu_{\mathrm{ma}}$) and the density contrasts between the plates are varied for different experiments to explore how F controls the style of subduction.

1.4.2 Laboratory experiments

Laboratory models have a layered setup (Davy and Cobbold, 1991; Martinod and Davy, 1994; Faccenna *et al.*, 1999, and references therein) to simulate the stratified lithospheric rheological profile (*e.g.* Ranalli and Murphy, 1986), while similarity criteria with respect to the Earth are fulfilled (Davy and Cobbold, 1991) (Figure 1.1b). The model lithosphere consists of sand mixed with ethyl cellulose to represent the brittle behavior of the upper crust, overlying silicone putty, which represents the viscous rheology of the lower crust and mantle lithosphere; the brittle-ductile layers rest on glucose syrup mimicking the asthenosphere.

The mixture of sand and ethyl cellulose is a cohesionless Mohr-Coulomb material with a mean frictional angle of 30°. For the strain rates that are characteristic of our experiments, the silicone putty is a Newtonian fluid with a viscosity of 10^4 to 10^5 Pa s at room temperature (Weijermars, 1992; Davy and Cobbold, 1991). We can vary its density by changing the fraction of inert fillers (galena powder). The glucose syrup is a Newtonian low-viscosity

Table 1.2: Experimental parameters used for the laboratory models. The underlying, glucose mantle layer has a density of 1410 kg/m^3 and viscosity of $\sim$50 Pa s, h is the thickness of the layer. Notes: [1]: $\Delta\rho^{oc}_{ma} = 45$ kg/m^3 for experiment 9, 64 kg/m^3 for experiment 7, and 75 kg/m^3 for experiment 15. [2]: Values are averaged for upper and lower silicone layer; viscosity is measured at room temperature. [3]: During the first 20 hours after which $u_r = 0$.

	h, [mm]	ρ, [kg/m^3]	ρ_{avg},[1] [kg/m^3]	μ, [10^4 Pa s]
		experiment 9		
oceanic plate			1455	
silicone layer[2]	9	1440		7
sand layer	3	1500		
overriding plate			1282	
silicone layer[2]	10	1270		3
sand layer	7	1300		
velocity u_r	6.9	10^{-7} m/s		
buoyancy no. F	11			
		experiment 7		
oceanic plate			1474	
silicone layer[2]	9	1465		7
sand layer	3	1500		
overriding plate			1282	
silicone layer[2]	10	1270		3
sand layer	7	1300		
velocity u_r	6.9	10^{-7} m/s		
buoyancy no. F	15.7			
		experiment 15		
oceanic plate			1485	
silicone layer[2]	9	1480		7
sand layer	3	1500		
overriding plate			1282	
silicone layer[2]	10	1270		3
sand layer	7	1300		
velocity u_r	6.9[3]	10^{-7} m/s		
buoyancy no. F	18.4[3]			

($\sim$10 to 100 Pa s) and high-density fluid. As in other models (*e.g.* Kincaid and Olson, 1987), the plate/slab viscosity is chosen to be $\sim$1000 times the mantle viscosity to obtain a "plate-like" behavior. Our experiments are conducted at constant room temperature.

At an analogue depth of the 660-km phase transition, we imposed a rigid surface to simulate a deep transition zone where the slab can be anchored and flatten out. This flattening is observed in many subduction zones on Earth (chapter 3). In reality, the 660-km phase transition's strongest effect on subduction is probably due to the viscosity increase (*e.g.* Hager, 1984; Mitrovica and Forte, 1997) between upper and lower mantle. The buoyancy effect of the phase transition due to the negative Clapeyron slope of the olivine γ-spinel to perovskite/magnesiowüstite transition (*e.g.* Christensen and Yuen, 1984) is still being debated. However, slab flattening results naturally in layered viscous media and the effect of the phase transitions may be smaller than initially thought (*e.g.* Tetzlaff and Schmeling, 2000; King, 2001).

Two different plates are prepared (Figure 1.1b). One has a lower mean bulk density than the glucose syrup, simulating an upper overriding ("continental") plate; the second, subducting "oceanic" plate is denser than the glucose syrup (Table 1.2), with varying densities in different models to simulate its age-dependence (*e.g.* Turcotte and Schubert, 1982). Details on the similarity criteria, material rheology, and experimental technique can be found in Davy and Cobbold (1991) and Faccenna *et al.* (1996, 1999). Models are constructed and deformed inside a rectangular plexiglas tank (dimensions are 47 cm long, 25 cm high and 35 cm wide; Figure 1.1b). A compressional stress regime is achieved by displacing a rigid piston at constant velocity perpendicular to the plate margin. The piston is confined to the upper middle part of the tank, and the glucose syrup is free to move underneath. For each model we estimate the buoyancy number F. However, the comparison between the laboratory experiments which have a layered, complicated rheology (Figure 1.1b) and the purely viscous numerical models (Figure 1.1a) is not straightforward and is based on a scaling argument described in sec. 1.5.3.

1.5 Results

1.5.1 Effect of the buoyancy number F

We present three numerical and two laboratory experiments to illustrate how the style of subduction depends upon F. The first, numerical "reference" model with $F = 14$ is illustrated in Figure 1.2 at 0, 21, 42, and 63 Myr. During the first stage of deformation the oceanic plate thickens, and a large instability forms at the boundary with the stiff overriding plate, progressively growing in depth while reducing its lateral extent (Figures 1.2a and 1.2b). The formation of downwelling instabilities in nature is governed by the competition between advection and diffusion of the cold thermal anomaly that leads to the negative buoyancy of oceanic material, as discussed in sec. 2.1.7.

Both the stiff overriding and the oceanic plate are initially (at the undeformed, $t = 0$, state) subjected to mainly horizontal compression. After the formation stage, the instability develops the shape of a slab, sinking into the mantle at a shallow angle. The stress state in the subducting oceanic plate is basically downdip extension from 26 Myr on and at a maximum at the trench, while the deformation within the overriding plate changes from in-plane compression to extension (Figure 1.2c). The downward velocity of the oceanic plate increases until 40 Myr and leads to a rapid growth in the depth of the subduction zone with time. The maximum downward velocity of the slab tip is 72% of the convergence velocity u_r and reached shortly before the slab is slowed down by the effect of the lower boundary (Figure 1.3). Afterward, the slab reaches the lower part of the box (47 Myr), its speed decreases as the tip thickens, and experiences deep compression since it cannot flow at the same rate through the lower boundary (Figures 1.2d and 1.3). As a consequence, the stress changes from in-plane extension to in-plane compression at about half depth. The closed bottom boundary can be considered as an end-member case of maximum slab impediment. Contrasting models with a free bottom boundary (not presented here) show a similar style of subduction, but the slab undergoes only downdip tension, and the initial subduction velocity is higher by $\sim 15\%$.

The second numerical experiment (Figure 1.4) has a buoyancy number that is a factor of 2 larger than the reference model ($F = 28$). The first stage of deformation is similar to the $F = 14$ model, but now the velocity of subduction is greater, while the maximum downward slab tip velocity ($\sim 1.9 u_r$) is again reached shortly before the slab is slowed down by the lower boundary (Figure 1.3). In this experiment the trench migrates toward the ocean at half the velocity of subduction (Figure 1.5), and the upper plate is in extension during the entire experiment. Moreover, a larger amount of upper plate material, as compared to the reference model, is dragged down and ablated into the subduction zone. The slab reaches the bottom after 34 Myr (Figure 1.4c) causing a decrease in the rate of subduction and of trench migration (Figures 1.3 and 1.5).

Figure 1.6 shows the evolution of the third numerical experiment where the buoyancy forces are decreased twofold compared to the reference model ($F = 7$). The velocity of subduction is slower for this model, reaching a value of $<$63% of u_r (Figure 1.3). The slab is also thicker and sinks at an initially lower-dipping angle into the mantle. This causes a migration of the trench at constant rate toward the overriding plate (Figure 1.5), which is subjected to compression, particularly during the first stages of the experiment (Figure 1.6). Further, a smaller amount of upper plate material than in the reference model is ablated and subducted. The slab reaches the bottom of the box after 60 Myr. When we decreased F further, subduction was slowed down and ceased ultimately when the tectonic style was transformed into an underthrusting regime at $F \approx 2.5$.

To compare these findings with laboratory models, we choose two out of a total of 30 performed by Faccenna and coworkers. In the laboratory reference experiment 7 shown in Figure 1.7 the density contrast between the oceanic plate and the mantle is 64 kg/m^3, and $F = 15.7$ with $\overline{\mu}_{\rm oc}^{\rm eff} \approx 7 \times 10^5$ Pa s. Subduction develops slowly from an instability at the plate boundary, and it takes 20 hours (10 Myr) until a 4 cm long slab sinks into the mantle (see also Faccenna *et al.*, 1996, 1999). The subduction speed then increases to roughly the convergence velocity after 30 hours; at this stage (Figures 1.7 and 1.8) the slab has also attained a steeper dip (Figure 1.8 inset). The thinning observed in its middle portion suggests that strong tensional forces are pulling the slab down (Figure 1.7a). During the whole experiment the overriding plate is not subjected to substantial compression or extension, and the trench is essentially stationary. The apparent trench migration toward the continent is due to an erosion of both upper plate layers into the subduction zone, while the amount of eroded material is approximately constant and $\sim$30% of the total amount of subducted material. Hence the shortening produced by the advancing piston is entirely transmitted to the subduction zone (Figure 1.10). After $\sim$45 hours (Figure 1.7b) the slab reaches and anchors at the rigid transition zone, causing compression and folding at its tip. The description of the deformation at depth is beyond the scope of this paper, and experiments with a more realistic viscosity increase are discussed elsewhere

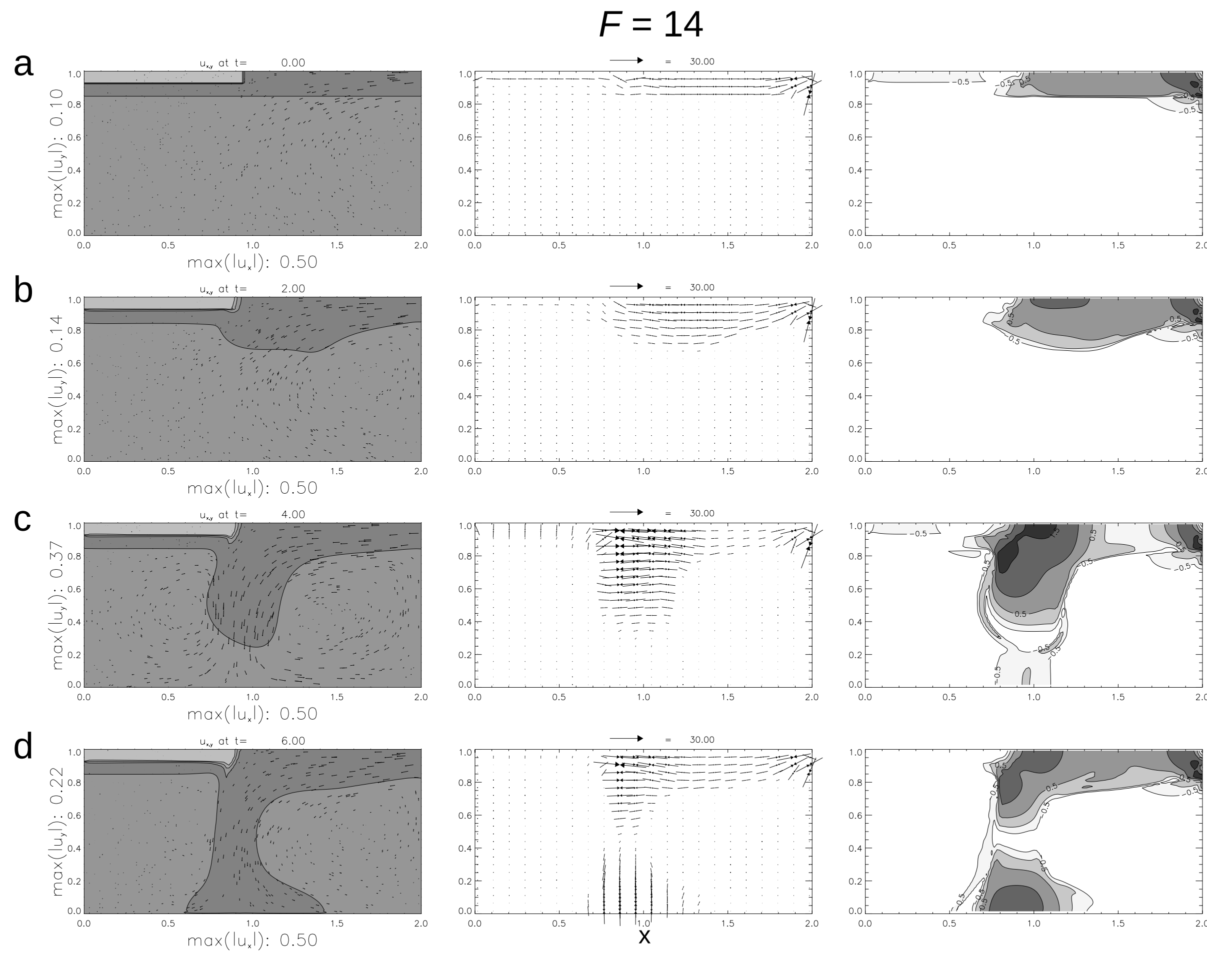

Figure 1.2: Material contour lines and flow field (left), orientation and magnitude of the principal compressional stress axis (middle), and decadic logarithm of the viscous dissipation $\log(\Phi)$ (right) for the numerical reference experiment with $F = 14$. All quantities are given in non-dimensional units. The time steps are 0 (a), 21 (b), 42 (c), and 63 Myr (d). Vectors scale with the magnitude of the local field, and the velocity of convergence that we prescribe on the right-hand side is 0.5, corresponding to 3.2 cm/yr in nature. Stresses of magnitude 30 as indicated by the reference vector above the center plots correspond to 22.5 MPa. Φ for incompressible 2-D flow is calculated by $(\sigma_{xx}^2 + \sigma_{xz}^2)/\mu$, and $\log(\Phi)$ isolines are plotted from -0.5 to 2.0 in 0.5–intervals (Table 1.1).

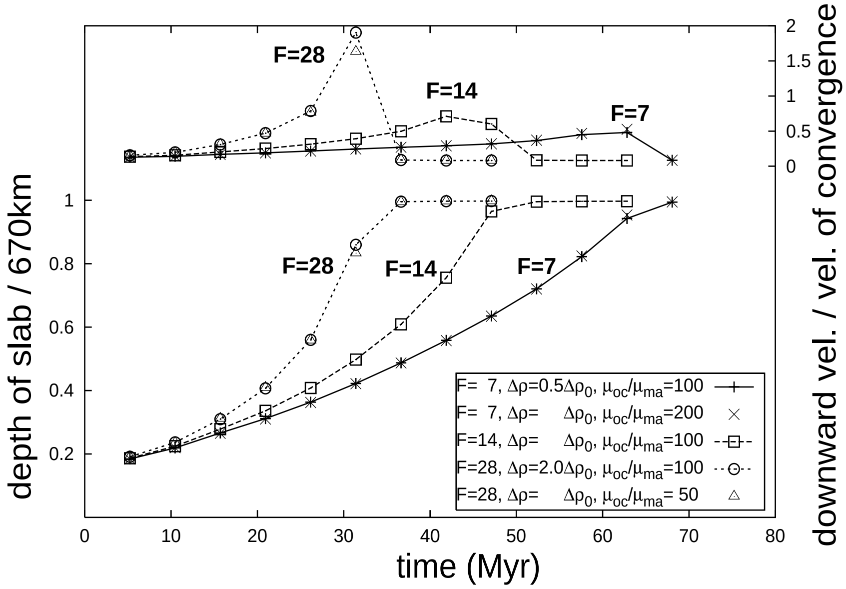

Figure 1.3: Depth of the slab (bottom, depth defined by the lowest point of the isomaterial line used to mark the boundary between oceanic and mantle material in Figure 1.2) and downward velocity of the slab tip (top) versus time. We show data from numerical models: reference with $\Delta\rho = \Delta\rho_0$ and $\mu_{oc}/\mu_{ma} = 100$ ($F = 14$), two models with $\Delta\rho = 2\Delta\rho_0$ and $\mu_{oc}/\mu_{ma} = 100$, and $\Delta\rho = \Delta\rho_0$ and $\mu_{oc}/\mu_{ma} = 50$, respectively (both equating to $F = 28$); and finally two models with $\Delta\rho = 0.5\Delta\rho_0$ and $\mu_{oc}/\mu_{ma} = 100$, and $\Delta\rho = \Delta\rho_0$ and $\mu_{oc}/\mu_{ma} = 200$, respectively ($F = 7$).

(Faccenna *et al.*, 2001b). For our experiments it is sufficient that the slab tip is anchored at depth. We then stop the piston and observe that the hinge of the slab starts to roll back with respect to its anchored tip; the slab progressively rotates and decreases its dip to 60°, producing extension of the overriding plate (Figure 1.7c, 1.8 inset, and 1.10). We note that the numerical and laboratory reference models are alike in terms of the deformation state, the time dependence of subduction speed, and the absence of trench migration (compare Figures 1.3 and 1.5 with Figures 1.8 and 1.10).

A decrease in F as in the numerical $F = 7$ model of Figure 1.6 can be illustrated by laboratory experiment 9 (Figure 1.11) where the density contrast between ocean and mantle is 45 kg/m^3 and $F = 11$. Initial deformation is followed by underthrusting of the oceanic under the overriding plate after 13 hours (6 Myr) and a 1 cm long slab sinks at a low angle ($< 20°$) into the mantle (Figures 1.8 inset and 1.11b). After 10 cm of compression (Figure 1.11d) the slab has grown to 3 – 4 cm length, and its dip is $\sim 30°$. Since the velocity of subduction is lower than the velocity of convergence, the excess compression causes internal bulk shortening and thickening of the slab (Figure 1.10). As in the numerical experiment with low F, we now observe trench migration toward the upper plate which is subjected to compression. The rate of subduction is constant and mainly controlled by the advance of the piston (Figure 1.8). At the same time, the slab dip progressively increases under the weight of the subducted material (Figures 1.11d and 1.9). The experiment is halted after 54 hours when a 4 – 5 cm long, 60° dipping slab sinks into the mantle. The fraction of material from the upper plate that gets dragged down into the subduction zone is $\sim$ 15% of the total amount of subducted material.

In summary, laboratory and numerical experiments indicate that the buoyancy number F controls the speed and the deformational style of subduction as well as the shape of the slab and the mode of trench migration. Different system behavior can be realized by varying the density contrasts of the plates.

1.5.2 Role of viscosity, u_r, and relative density contrasts between plates

In the numerical models described in sec. 1.5.1, the value of F is changed by varying the absolute density contrast, $g\Delta\rho_0$, between subducting plate and the mantle. However, experiments with the same corresponding values for F (7, 14, 28), which were done by changing the viscosity of the oceanic plate or the velocity of convergence but leaving $g\Delta\rho_0$ constant, give very similar results to those illustrated above (Figure 1.3). This demonstrates that the parameters adopted in (1.3) for F represent the relevant controls on the style of model subduction.

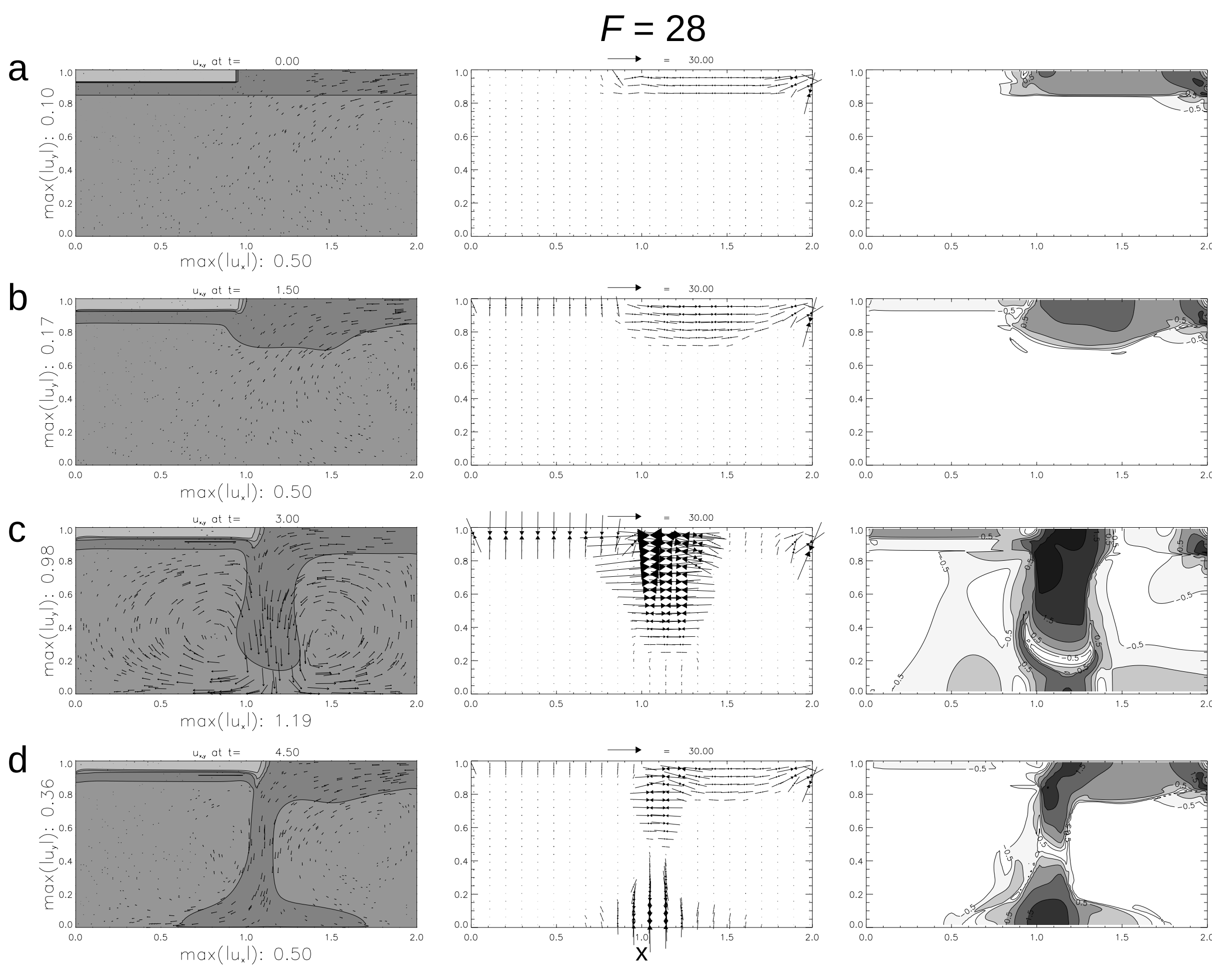

Figure 1.4: Evolution of numerical model $F = 28$; see Figure 1.2 explanation. Time steps are different since $F > 14$ implies a faster subduction and correspond to 0, 15.8, 31.5, and 47.3 Myr. The characteristic velocity and stress are the same as in Figure 1.2.

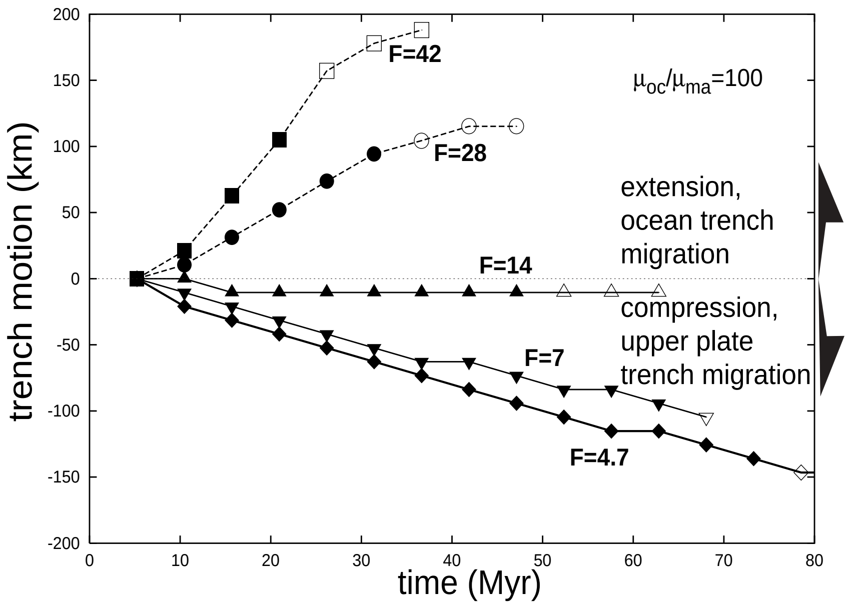

Figure 1.5: Motion of the trench for $\mu_{oc}/\mu_{ma} = 100$ (defined by the boundary between upper and oceanic plate material) versus time for numerical models with buoyancy numbers of $F = 4.7$, 7, 14, 28, and 42. (End-member models with $F = 4.7$ and 42 are not discussed in the text.) Solid symbols change to open ones for close to bottom ($z > 0.97$) depths.

Further numerical experiments were conducted to investigate the roles of the absolute and relative density contrasts between the plates by varying the density of the overriding and the oceanic plate separately with respect to a fixed mantle density. We find that the density contrast between the oceanic plate and mantle (the slab pull) is the major control on the speed of subduction. The density difference between overriding and oceanic plate (leading to a spreading tendency of the overriding plate) on the other hand plays a subordinate role, and its effect on the depth versus time curves as in Figure 1.3 is smaller by a factor of ~ 5.5. The density difference between these plates, however, has about the same effect on the rate of trench migration and the deformation state in the lithosphere as the mantle-ocean buoyancy contrast.

1.5.3 Free subduction and viscous dissipation

As shown by the plots of the decadic logarithm of the viscous dissipation Φ on the right-hand side of Figures 1.2, 1.4, and 1.6, dissipation in the numerical models is most pronounced in the trench area, within the high-viscosity slab, and on the right boundary. The latter is an artifact of our prescribed convergence velocity. Since the rheology is Newtonian, the deformation is broadly distributed with a significant concentration in the trench area. The maximum values of Φ are 20%, 50%, and 126% of the characteristic Φ_c of 56 nW/m^3 for $F = 7$, 14, and 28, respectively (Table 1.1). Since Φ_c is of the order of typical radiogenic heat production rates of basalts (*e.g.* Stacey, 1992, p. 300), our Newtonian models do not predict excessive heat production due to shear heating. A viscous heating feedback mechanism between the rheology and the strain field can be expected to be important for a power law rheology (*e.g.* van den Berg and Yuen, 1997) and we cannot rule out that possibility here. We will nonetheless interpret our subduction models as controlled by viscous dissipation in the oceanic plate, and more specifically by viscous bending of the slab.

To investigate further the driving and resisting forces contributing to the balance expressed by F, the role of the slab pull and the viscous dissipation within the oceanic plate were studied with four numerical experiments in which no convergence velocity was prescribed. The piston push is used to initiate the subduction, but u_r is set to zero afterward, and the system is left free to evolve. As in previous models, the length of the slab increases rapidly with time before it is slowed down by the lower boundary (Figure 1.12). Furthermore, the trench rolls back toward the oceanic plate after the piston is halted. We tested three models with the geometry shown in Figure 1.1a (density contrasts yielding $F = 7$, 14, and 28) and one model with a thicker oceanic plate and $F = 14$ (if F were to be calculated for the usual $u_r \neq 0$).

Following Turcotte and Schubert (1982) and Conrad and Hager (1997), the experimental data in Figure 1.12 were fit by calculating the viscous dissipation per unit length due to the bending of oceanic lithosphere which scales as $u^2 \mu_{oc} R^3 / r^3$. Here, u is the local subduction velocity at time t, R is the half width of the bending plate,

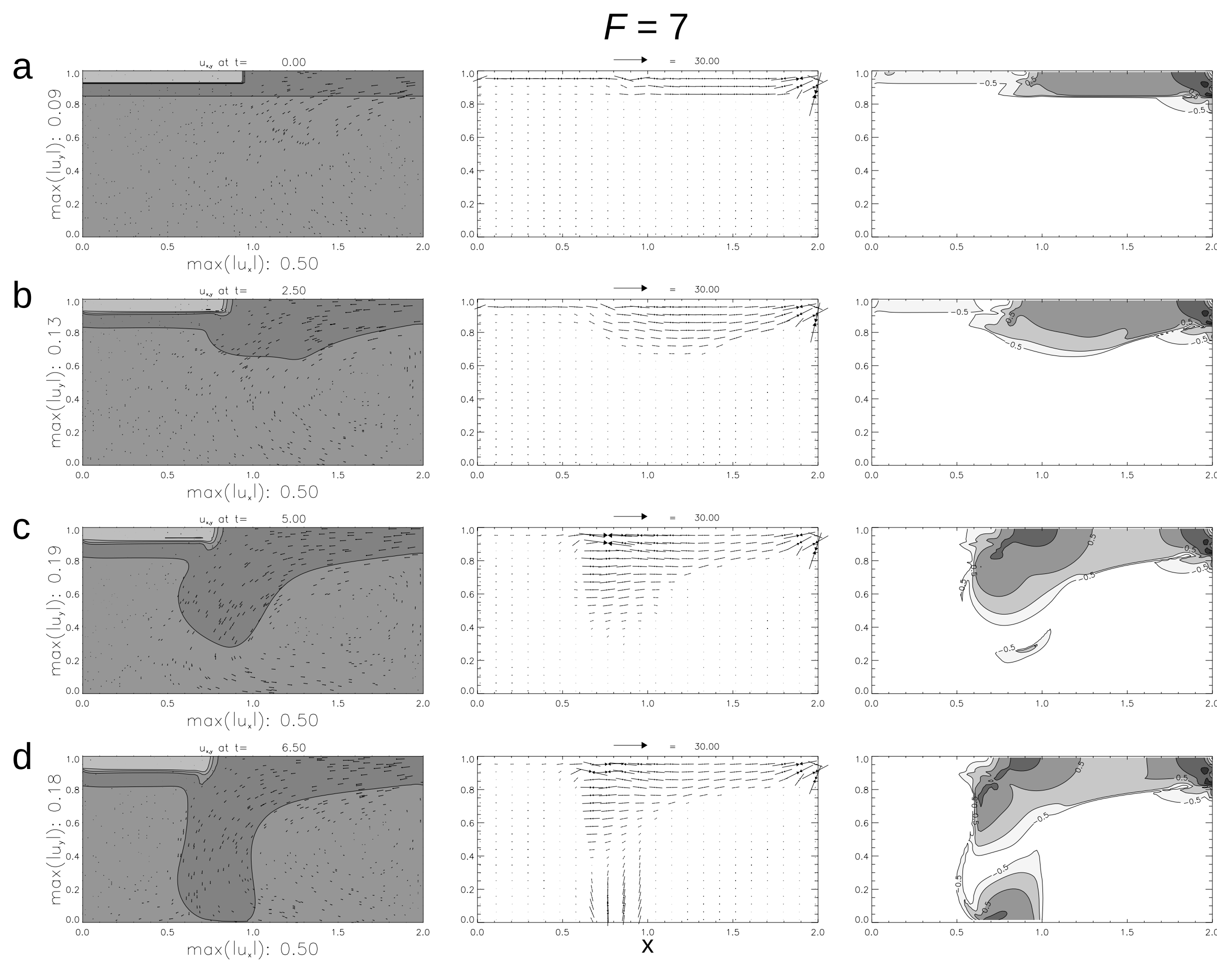

Figure 1.6: Evolution of numerical model $F = 7$; see Figure 1.2 explanation. Time steps are different since $F < 14$ implies a slower subduction and correspond to 0, 26.3, 52.2, and 68.3 Myr. The characteristic velocity and stress are the same as in Figure 1.2.

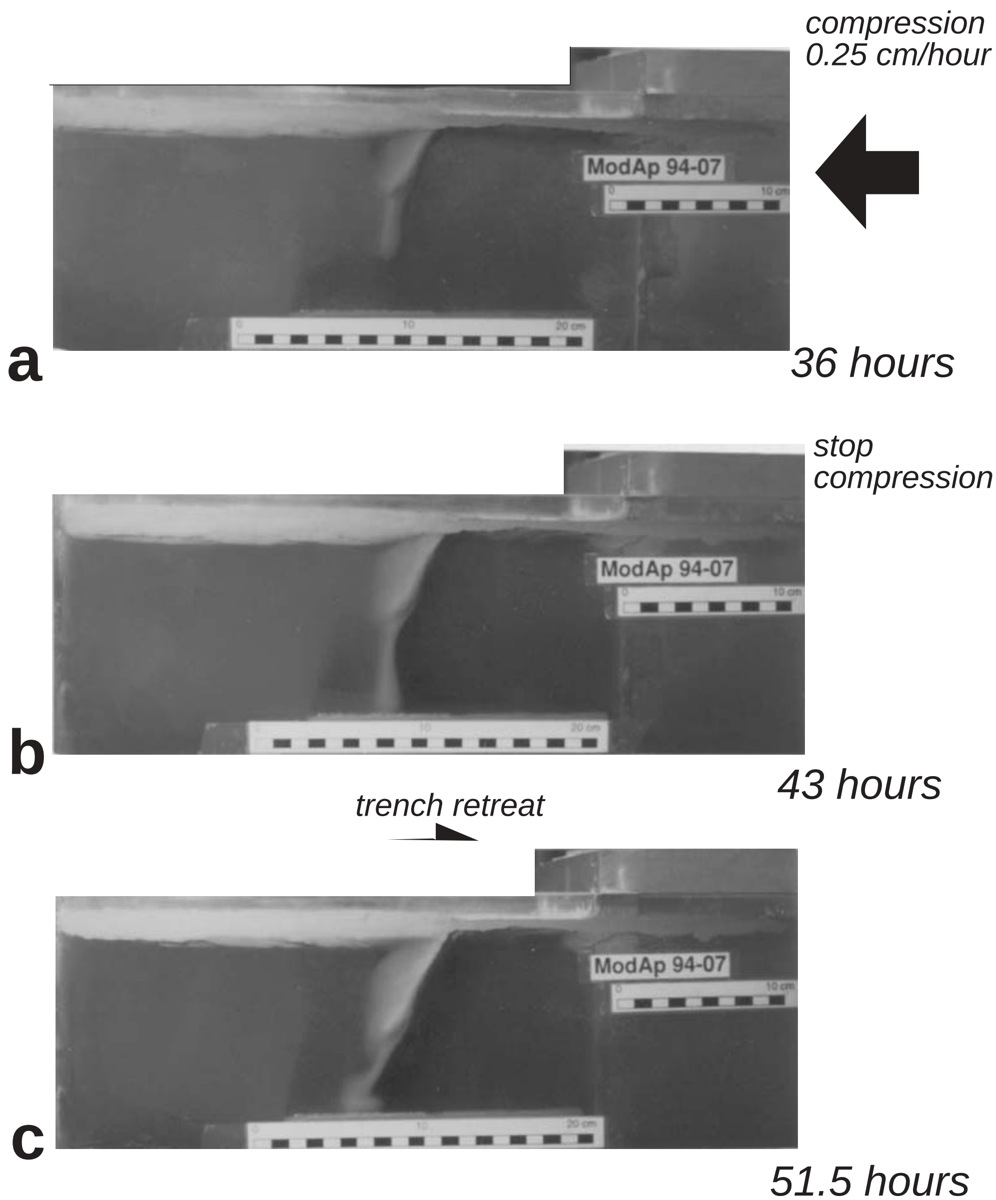

Figure 1.7: Three stages of subduction for laboratory reference experiment 7 ($F = 15.7$). The piston, acting on the oceanic plate, advances for the first 47 hours of deformation at a rate of 0.25 cm/h, equivalent to 3.2 cm/yr in nature (see the bold arrow for the sense of motion of the piston and also Table 1.1). The density contrast between oceanic plate and mantle is 64 kg/m^3. Note the decrease in the dip of the slab after anchoring at depth.

and r is the radius of bending. If the balancing term at each instance in time is roughly equal to the potential energy dissipation due to the negative buoyancy of the already subducted slab of height H ($\propto \Delta\rho g H R u$), then

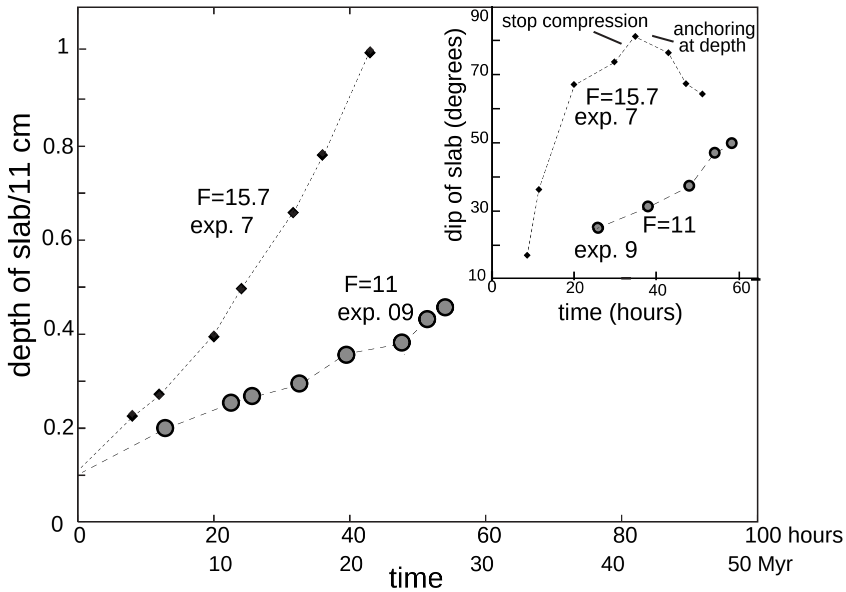

Figure 1.8: Depth of the slab versus time for the laboratory reference model 7 with $F = 15.7$ and for experiment 9 with $F = 11$. Figure 1.8 inset is dip of the slab versus time for experiments 7 and 9. Note the decrease in subduction angle after anchoring at depth for experiment 7.

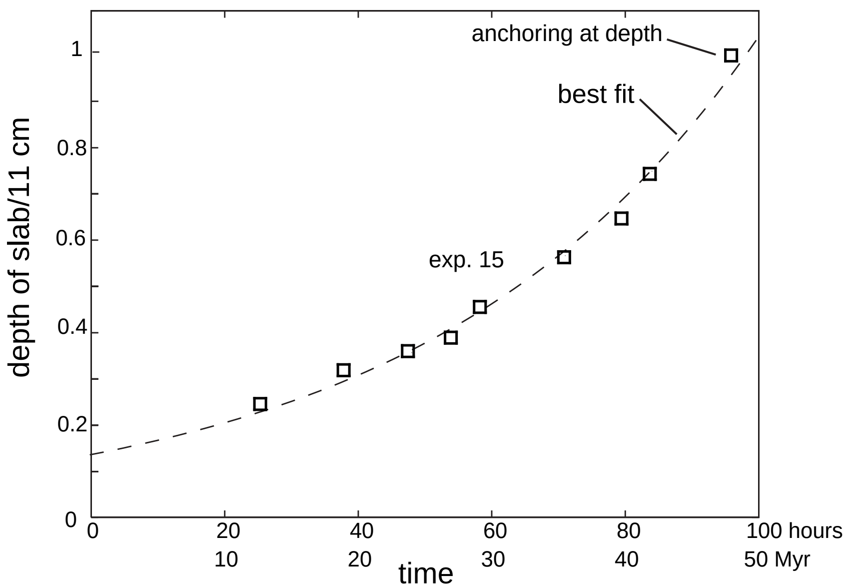

Figure 1.9: Free subduction model; depth of the slab versus time after the velocity of convergence (piston motion) was set to zero following the initiation of subduction. The best fit curve is used to estimate the effective viscosity of the experiment (7×10^5 Pa s for $C = 0.28$, $R = 6$ mm and $r = 9$ mm) from (1.4).

$u(t) \approx dH(t)/dt$ yields

$$H(t) \propto H_0 \exp\left(C \frac{\Delta\rho g r^3}{\mu_{oc} R^2} t\right). \tag{1.4}$$

Here C is a fitting constant of order unity and H_0 is the initial driving instability. Equation (1.4) is clearly only a first-order estimate since we have assumed that only the bending of the oceanic plate and the gain in buoyancy forces are relevant, that R and r are constant during subduction, and that the entrainment of upper plate lithosphere as well as the varying dip of the slab are not important. A more detailed treatment of the distribution of viscous dissipation between mantle and lithosphere is given by Conrad and Hager (1999a).

We have determined the geometry parameter r^3/R^2 numerically by tracing a midslab stream line and measuring the minimum radius of curvature at each time step. A fit of the data is then be obtained by using the time average of the approximately linearly increasing geometry parameters for each experiment (Figure 1.12). The values we obtain for C have remarkably small variations from model to model, and we use the average, $C = 0.28$, to establish an empirical relation for $H(t)$ for "free" subduction. All of our numerical data are thus consistent with the interpretation that the most important resisting force is the viscous dissipation in the oceanic plate, more

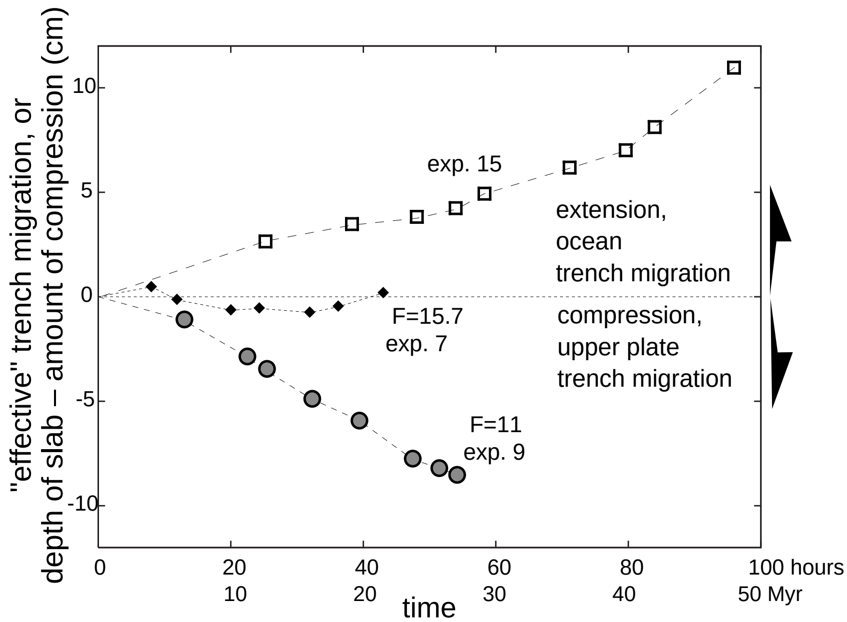

Figure 1.10: Effective trench motion, estimated by subtracting the amount of compression from the depth of the slab for laboratory experiments with $F = 15.7$, 11, and 18.4 for experiment 15, where the piston was stopped after 20 hours of compression. The effective trench motion is used to eliminate the effect of upper plate erosion from the data.

specifically in the trench region where the slab is bent.

In laboratory experiment 15 (not illustrated; see Faccenna *et al.*, 1996), the density contrast between oceanic plate and mantle is 75 kg/m^3. As for the numerical results above, the system is driven only by the weight of the slab after an initial piston advance (Figure 1.9). During the free subduction process, the laboratory model also shows slab hinge rollback, causing a retreat of the trench toward the ocean and extension in the overriding plate (Figure 1.10). We used the experimental data with the scaling relation (1.4) to arrive at an average viscosity estimate for the multilayered laboratory system. Figure 1.9 shows that an exponential fit like (1.4) is suitable for the free subduction data from the laboratory. Interpreting this fit quantitatively assumes that the factor C is approximately the same for both model setups. We consider this likely since we have observed qualitative and quantitative similarity as discussed in sec. 1.5.1. The estimated overall "effective viscosity" for the oceanic plate, $\overline{\mu}_{\mathrm{oc}}^{\mathrm{eff}}$, is $\sim 7 \times 10^5$ Pa s. This number is sensitive to the measurement of the radius of curvature and higher than the measured viscosity for the silicon putty ($\approx 7 \times 10^4$ Pa s; Table 1.2). We interpret the latter as a result of the presence of a stiffer upper sand layer that increases the bending resistance and use $\overline{\mu}_{\mathrm{oc}}^{\mathrm{eff}}$ to estimate the buoyancy number for the laboratory experiments. We find a value of $F \approx 15.7$ for the reference model (Table 1.1).

While the scaling relation that we discuss above for the exponential increase in subduction velocity is quite crude, it is remarkably successful: we are able to use the same relationship to fit estimates of subduction history in nature (sec. 2.1) and in further laboratory experiments with different geometries and without the brittle sand layer (Faccenna *et al.*, 2001b; Funiciello *et al.*, 2002).

1.5.4 Effects of the aspect ratio and weak zones

Two additional issues that can be addressed with the numerical experiments are the effect of the aspect ratio and that of a weak zone. Changing the aspect ratio of the computational domain from 1:2 to 1:4 leads to a delayed initiation of subduction and thus a shift in the slab depth versus time curves of ∼10–15 Myr. This is due to the way gravitational instabilities form in our models. They are advected in the upper oceanic plate and have to travel some distance to assist in the initiation of downwelling at the plate boundary. Another factor that might be of influence, but is difficult to quantify, is the effect of a longer oceanic plate on the work done by deflecting streamlines which could further delay the initiation of subduction. Hence the individual data points that we present are dependent on the geometry chosen for the model and the wavelength of the convective instabilities that result. However, our conclusions concerning the physical mechanisms of subduction are not affected, and our general findings are confirmed by all models.

The effect of a pre-existing fault at the plate boundary has been investigated by means of the introduction of a fixed 42 km × 42 km weak zone characterized by a 100-fold drop in viscosity. This configuration causes a

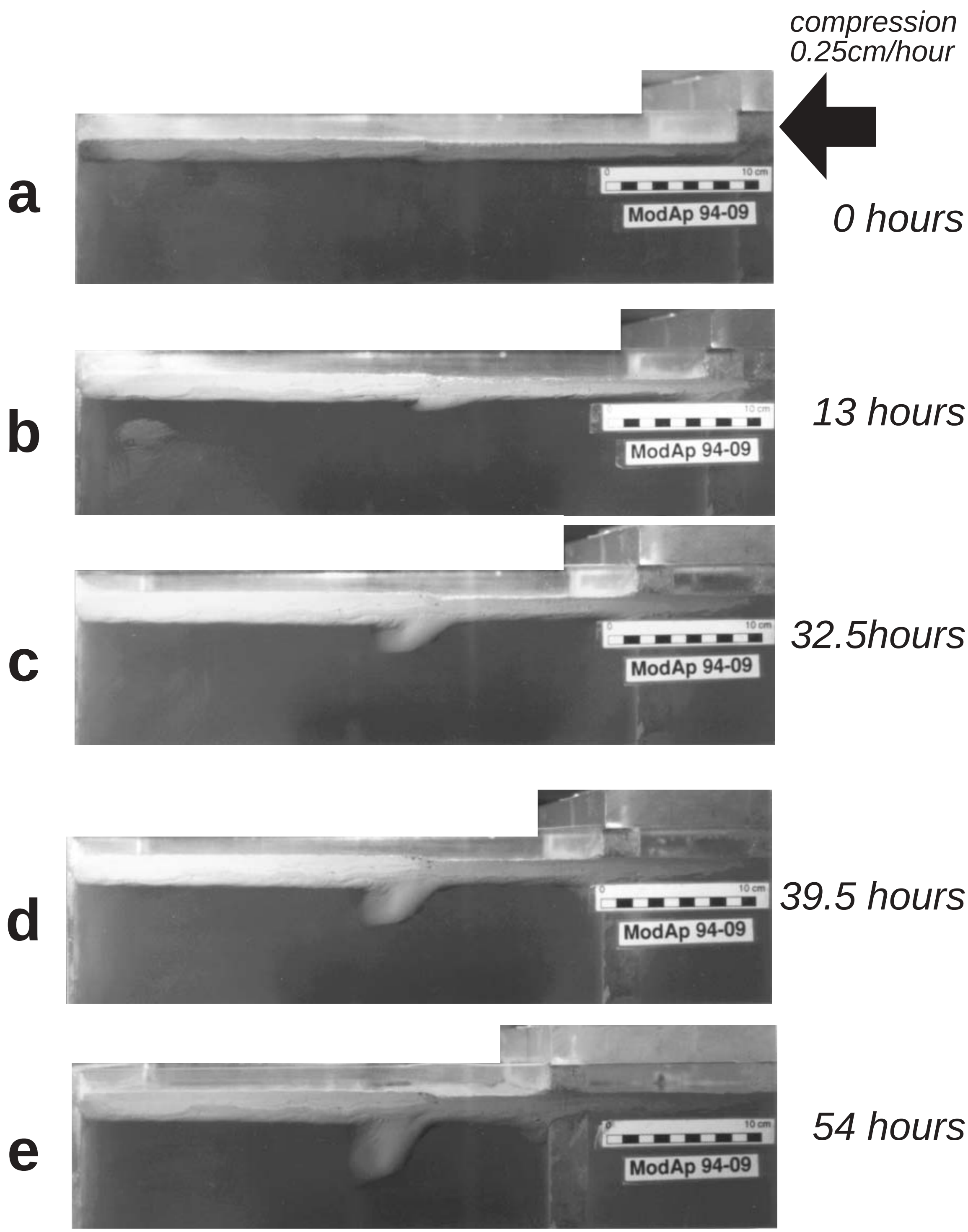

Figure 1.11: Five stages of the evolution of laboratory experiment 9 with $F = 11$ for a density contrast of 45 kg/m^3 between oceanic plate and mantle.

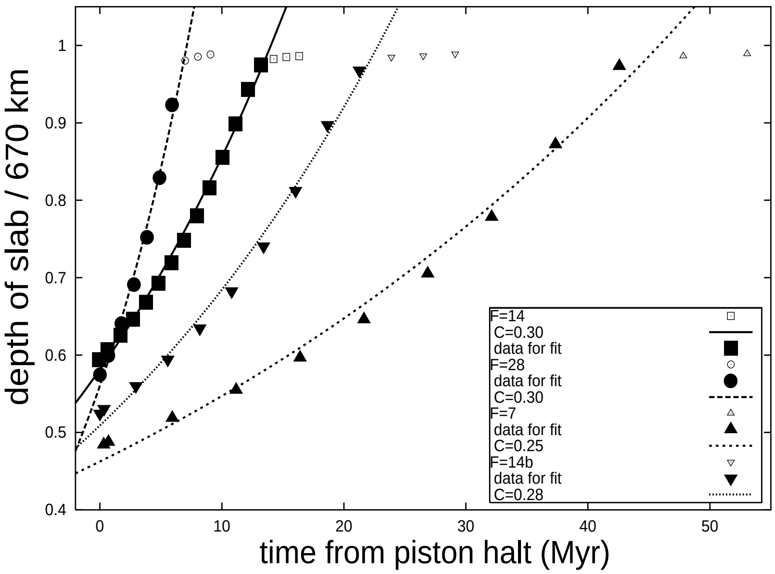

Figure 1.12: Free subduction models: depth of the slab versus time after the velocity of convergence at the right boundary was set to zero following the initiation of subduction. Data from three models with the geometry shown in Figure 1.1 ($F = 7$, 14, and 28) and one with a thicker oceanic plate, indicated by "14b." The data points (solid symbols) that were used for a least squares fit of (1.4) (lines) are shown together with the resulting values for the fitting constant C. Small open symbols (not used in the fit) indicate that the slab reached the bottom.

change in model behavior only insofar as the slab dips at a shallower angle in the early stages of subduction. By the time it reaches the bottom, the slab has steepened, and the shape of the subduction zone is similar to that in the other models. The absolute velocity of subduction is initially comparable to the ones observed in models without a weak zone and increases to $\sim$140% of these values during the final stages before the slab slows down. We note that the small effect that we find might be biased by our velocity boundary conditions and could be expected to increase with a larger weak zone (*e.g.* King and Hager, 1990).

1.6 Discussion

The style of subduction and its influence on the state of stress in the overriding plate represent a complex problem in plate tectonics, and many models have been proposed (sec. 2.2). In our experiments, subduction is mostly controlled by the buoyancy number. We now interpret the results by tracing the slab trajectory from the surface to the bottom of the upper mantle and comparing our findings to previous models and examples from nature.

1.6.1 Nucleation and development of the slab

We model subduction as a purely viscous process, based on the assumption that the slab behaves as a fluid over geological timescales. Within the investigated parameter range, the deformation is localized at the boundary due to the presence of a stiff resisting upper plate. Subduction does not initiate for F below a threshold: in this case the deformation is characterized by low-angle underthrusting of the oceanic plate, by thickening and collision at the trench, and, in the laboratory experiments, by diffuse folding of the entire oceanic plate (Faccenna *et al.*, 1999). If we express the F threshold as a viscosity contrast between ocean and mantle, we arrive at an upper value of $\sim$500–750 for the numerical experiments. This finding is in agreement with the range predicted by Conrad and Hager (1999a) and indicates a low effective lithospheric viscosity (sec. 2.3).

While our experiments are not meant to address the force balance for subduction initiation, the stresses that result from our prescribed convergence boundary condition are of interest. As Figures 1.2, 1.4, and 1.6 indicate, non-dimensionalized values are $\sim$15 in the middle part of the oceanic plate. This gives 11.3 MPa and 1.13×10^{12} N/m for a 100-km-thick lithosphere (Table 1.1). While this number depends on the choice of the absolute viscosity value, it is in the range that can result from ridge push forces (*e.g.* McKenzie, 1977). This implies that our boundary conditions with forced subduction do not necessarily lead to unrealistic forces applied to the plate.

For F above the initiation threshold the slab nucleates as a large instability, growing at a slow rate during the first 10–20 Myr. Afterward, the instability narrows and evolves, following the mantle trajectories and resembling the shape of a slab. The initial growth rate of the instability and the velocity of subduction that follows depend upon the buoyancy number; that is, for a given convergence velocity, they are proportional to the density contrast and inversely proportional to the viscosity of the oceanic plate.

The velocity of subduction

During the first stages of deformation for both numerical and laboratory models the subduction speed is only a small percentage of the convergence velocity u_r. Afterward, the slab accelerates until its speed becomes comparable to the velocity of convergence and the tip reaches the bottom at $\sim$40–50 Myr and 20–30 Myr in numerical and laboratory reference experiments, respectively. A common feature of all experiments is the exponential increase of the subduction rate and its dependence upon F. The scaling relation (1.4) can be used to fit both numerical and laboratory data for free subduction (sec. 1.5.3). Furthermore, the dependence of the subduction rate on the buoyancy number F indicates that the viscosity in our scaling law (1.3) is indeed the viscosity of the oceanic plate (sec. 1.5.2), and numerical experiments show that most of the viscous dissipation takes place in the trench region. We conclude that the major resisting force in our model is the viscous drag which arises mainly from the bending of the slab.

Comparison with nature and previous models

Recently, there has been some progress in modeling possible mechanisms for the initial stages of subduction starting from a homogeneous plate (*e.g.* Regenauer-Lieb *et al.*, 2001). However, all previous laboratory and numerical models that deal with the long-term evolution of slabs sinking in the upper mantle have either started with a predefined slab (*e.g.* Kincaid and Olson, 1987) or assumed the presence of a pre-existing fault zone crosscutting all or part of the lithosphere (*e.g.* Shemenda, 1993; Zhong and Gurnis, 1995; Moretta and Sabadini, 1995; Hassani *et al.*, 1997; Toth and Gurnis, 1998). In the latter class of models the subduction speed depends on the velocity of convergence and on the predefined characteristics of the weak zone (King and Hager, 1990). However, the velocity fields observed in the numerical models of viscous slabs sinking into the mantle (Moretta and Sabadini, 1995; Zhong and Gurnis, 1995) are consistent with our results. Since the deformation of a Newtonian fluid as in our experiments is more diffuse than that of a power law material (*e.g.* King and Hager, 1990), we expect that the localization, the growth, and the rate of subduction for a power law fluid will be more accentuated, further enhancing the time-dependent increase in the subduction velocity.

In nature, the lack of unambiguous present-day examples of trench nucleation and the difficulty in establishing the age of subduction do not allow us to verify our predictions directly. In some cases, subduction seems to initiate slowly, as in the central Mediterranean (sec. 2.1), whereas in other areas, as in New Zealand, subduction developed rapidly (Stern and Holt, 1994). Several parameters, such as the lateral propagation of the trench and the velocity of convergence, will determine the infant stage of subduction. However, the present-day velocities of most slabs, estimated by summing the velocity of plate motion and the velocity of trench migration, are usually of the order of 3–10 cm/yr (*e.g.* Jarrard, 1986). This value refers to subduction zones where thousands of kilometers of oceanic lithosphere have been consumed during the last 100 Myr (*e.g.* Cox *et al.*, 1989). In our time-dependent simulations we obtain similar velocities during the final stage of subduction, confirming the applicability of our approach for understanding natural subduction zones. With regard to slab nucleation, the results imply that the slow growth of the slab during the first stage of subduction should be taken into account in paleotectonic reconstruction.

Finally, the absence of a predefined and discrete subduction fault zone in our model results in upper plate being eroded and partially subducted (*e.g.* Tao and O'Connell, 1992a). This process is confined to the lower layer of the overriding plate in the numerical experiments, while the fraction of material entering the trench from both parts of the overriding plate ranges from 10% to 30% of the total amount of subducted material in the laboratory. These numbers might be higher than, but are of the same order of magnitude as, those estimated for Earth. In fact, trench subsidence and volcanic arc retreat, as defined for some of the trenches on the Pacific ring, indicate that the overriding arc is usually eroded at a rate of 8–10 km/Myr (for a review, see Lallemand, 1995).

1.6.2 The style of subduction and trench migration

In both numerical and laboratory experiments, contrasting styles of subduction have been observed as a function of the buoyancy number F. For low F, the slab is thicker and sinks at a lower angle, and the trench migrates toward the upper plate, accompanied by compression. For high F where subduction is favored, the slab is thinner and dips steeply, and the trench migrates toward the ocean, producing back-arc extension in the upper plate. In general, back-arc extension is observed in our models when the velocity of subduction and trench retreat is higher than the velocity of convergence (Figures 1.5 and 1.10). In this case, the hinge of the subducting plate rolls back leading to the retreat of the trench and extension in the upper plate.

As discussed in sec. 1.5.2, trench migration can be enhanced by the spreading tendency of the lighter upper plate toward the subducting one. This causes back-arc extension in all numerical experiments with $F > 14$ even during the first stage of deformation (see Figures 1.3 and 1.5). This result is similar to the laboratory experiments shown by Faccenna *et al.* (1996) in which trench migration and back-arc extension occur when the upper plate collapses under its own weight toward the oceanic plate. The nature of the “trench suction” in our experiments is related to the gravitational torque exerted by the downwelling motion of the denser subducting plate and the collapse of the upper plate. This can lead to effective back-arc extension when the horizontal push imposed by the plate convergence and the internal strength of the upper plate are overcome. The rate of trench migration ranges from 0.3 to 1 times the velocity of subduction. Our experiments indicate that a viscous slab, coupled to the upper plate, can indeed produce either extension or compression in the overriding plate as a result of the dynamical competition between driving (gravitational energy release) and resisting effects (viscous dissipation in the subducting plate).

Comparison with nature and previous models

Previous numerical models obtained comparable results using a viscoplastic rheology to simulate subduction (*e.g.* Whittaker *et al.*, 1992; Giunchi *et al.*, 1996). In those experiments, the stress in the upper plate depends mainly upon the equilibrium between the body forces and the coupling along a pre-existing fault zone. That is, unlocking of the fault zone will result in an increase in subduction velocity, producing an extensional horizontal relaxation of the upper plate. Other laboratory (Shemenda, 1993) and numerical (Hassani *et al.*, 1997) studies using elastoplastic rheology propose a different mechanism, connected to the suction hydrostatically produced along the subduction fault zone. In this latter class of models, the nature of trench suction is directly related to the increase in curvature and dip of the slab during its sinking into the mantle, which causes a downward force on the rigid subduction fault. Our models contrast with these studies in showing that trench migration can result from a viscous flow in a continuous medium with viscosity and density heterogeneities. Another class of models supports the idea that trench suction is related to a corner flow caused by the drag exerted on the mantle by the sinking slab (*e.g.* Andrews and Sleep, 1974; Bodri and Bodri, 1978; Toksöz and Hsui, 1978). Mantle drag and corner flow play a minor role in our experiments as trench migration occurs even before the slab starts sinking into the mantle. Furthermore, we find that mantle drag is not effective at determining the fate of the slab since viscous dissipation in the slab alone can account for the resisting effects (sec. 1.6.1).

In nature, back-arc compression or extension are well-documented end-members of more complex tectonic situations, showing variations both in space and time (Uyeda and Kanamori, 1979). Kinematic models indicate that back-arc extension can be connected with the absolute (Chase, 1978) or relative motion of plates (Dewey, 1980). Hence, when the velocity of trench retreat (possibly related to the body force on the descending slab) overcomes the velocity of convergence, the upper plate is submitted to extension and vice versa. These models seem appropriate for most natural cases, though exceptions exist (Taylor and Karner, 1983). Despite these results, the way in which the two plates interact and the mechanism of force transmission from the subducting slab toward the upper plate are still poorly understood (Taylor and Karner, 1983). On the basis of our results with a fixed upper plate and no background flow, we suggest that overriding plate compression or extension can be predicted using the buoyancy number F. It is difficult to test whether or not this mechanism can be applied to nature and to what extent other effects such as that of a background mantle flow (*e.g.* Tao and O’Connell, 1992a; Olbertz *et al.*, 1997; Becker *et al.*, 1998; van Hunen *et al.*, 2000) are important. However, the velocities of trench migration and back-arc extension in our experiments are in good agreement with the values observed in nature, where the velocity of back-arc spreading is about half that of subduction (Rodkin and Rodnikov, 1996). We will return to the problem of deformation in the overriding plate in sec. 2.2.

1.6.3 Dip of the slab

In both numerical and laboratory experiments the subduction angle increases until the slab reaches the transition zone. This again suggests that subduction is a time-dependent phenomenon and poorly characterized by steady-state parameters. In laboratory experiments, the velocity of steepening ranges from $\sim$1 – 2 $^\circ$/h, corresponding to 2 – 4°/Myr in nature, and is proportional to F. While the steepening rates given by Moretta and Sabadini (1995) are twice as high, a comparison of models with Earth is difficult, in general, as subduction in nature is long-lived and possibly interacts with density or viscosity barriers such as at 660 km (Jarrard, 1986).

With the boundary conditions we use, shallowing of the slab can only be obtained by anchoring the slab at a deep transition zone. In this case, the dip of the slab changes as a function of the velocity of trench motion. If the trench migrates oceanwards, as in experiment 7, the hinge of the slab rolls back with respect to its fixed tip inducing a decrease of the subduction angle. This result agrees with previous simulations using a more realistic increase in viscosity at the upper-lower mantle boundary (Tao and O'Connell, 1992a; Zhong and Gurnis, 1995; Griffiths *et al.*, 1995). Consistent with these models, we suggest that shallow-dipping subduction cannot be the result of the dynamic equilibrium between slab and upper mantle but rather is the result of other factors, such as age of subduction and interaction with a deep transition zone and/or background mantle flow.

1.6.4 Deformation within the slab

Our models indicate that the stress within the slab is usually downdip extension during its descent into the mantle regardless of the buoyancy number. When the slab reaches the transition zone, the area under tension is confined to the upper part of the slab, while the tip is submitted to compression. At half depth the stress field changes and decreases in magnitude forming a neutral downdip stress zone. Similar results have been obtained in earlier viscous flow models for the stress state in a fixed subduction geometry (Vassiliou and Hager, 1988) and for the strain field in a constant viscosity fluid (Tao and O'Connell, 1993). Here we have demonstrated that self-consistent viscous flow models with viscosity heterogeneities can reproduce the stress pattern that is common for many subduction zones (Isacks and Molnar, 1971), though the position of the neutral downdip stress zone might depend upon the slab morphology (Zhou, 1990) and the effect of phase transitions may complicate the picture (*e.g.* Yoshioka *et al.*, 1997). Our models support the interpretation that the seismicity in Benioff zones arises from a competition between slab pull and slab impediment in the lower mantle (Isacks and Molnar, 1971; Spence, 1987).

1.7 Conclusions

Our results from numerical and laboratory experiments demonstrate that it is possible to explain the major observations for subduction zones on Earth, such as trench migration and the stress pattern within the slab, with viscous models based on density and viscosity heterogeneities between the tectonic plates. The style of subduction is determined by the buoyancy number which measures the importance of the driving density contrasts versus resisting viscous dissipation. The existence of a buoyancy number threshold for subduction initiation yields an upper bound for the viscosity of the oceanic subducting plate. Our results support the view that subduction cannot be represented as a steady-state process since the state of stress, the velocity, and the dip of the slab evolve in space and time during its descent into the upper mantle.

Chapter 2

Observational constraints for subduction models

In chapter 1 we saw that our fluid-dynamical models can explain several first-order observations from subduction zones. Testable predictions of our models include the following: slow initiation with an exponential increase in the velocity of subduction before the slab reaches the 660-km phase boundary, dependence of the deformation state of the overriding plate on the buoyancy number, and, in general, a weak slab whose effective viscosity is not more than $\sim$750 times that of the surrounding mantle. The next sections will address observational support for these findings. First, we will examine the Central Mediterranean, where the time-dependence of subduction velocity can be reconstructed. We then consider constraints on the deformation of the overriding plate and observational support for weak slabs.

2.1 History of subduction and back-arc extension in the Central Mediterranean

2.1.1 Abstract

We present geological and geophysical constraints which we use to reconstruct the evolution of the Central Mediterranean subduction zone. Geological observations such as upper plate stratigraphy, high-pressure/low-temperature metamorphic assemblages, foredeep/trench stratigraphy, arc volcanism, and back-arc extension are used to define the different stages. Based on this data and upper mantle seismic tomography, we derive the time dependence of the amount of subducted material along two cross sections from the northern Apennines and from Calabria to the Gulf of Lyon. We unravel the main evolutionary trends of the subduction process; results of our analysis indicate that: 1) subduction in the Central Mediterranean is as old as 80 Ma, 2) the slab descended slowly into the mantle during the first 20–30 Myr (subduction speeds were probably less than 1 cm/yr), 3) subduction accelerated after 30 Myr, producing arc volcanism and back-arc extension, and 4) the slab reached the 660 km transition zone after 60–70 Myrs. There it flattened out to its present-day shape. This time-dependent descent velocity in which a slow initiation is followed by a roughly exponential increase in the subduction speed can be predicted by equating the viscous dissipation per unit length due to the bending of oceanic lithosphere to the rate of change of potential energy by slab-pull, according to the theory that was developed in chapter 1. The last stage is dominated by the interaction between the slab and the 660-km boundary. In the southern region, this results in a significant re-shaping of the slab and intermittent pulses of back-arc extension. In the northern region, the decrease in the trench retreat is amplified by the entrance of light continental material at the trench.

This section is based on a collaboration with Claudio Faccenna (University of Rome III) and has been published in modified form in the *Geophysical Journal International* (Faccenna, Becker, Lucente, Jolivet, and Rossetti, 2001a). The synthesis of geological data is based on C. Faccenna's work.

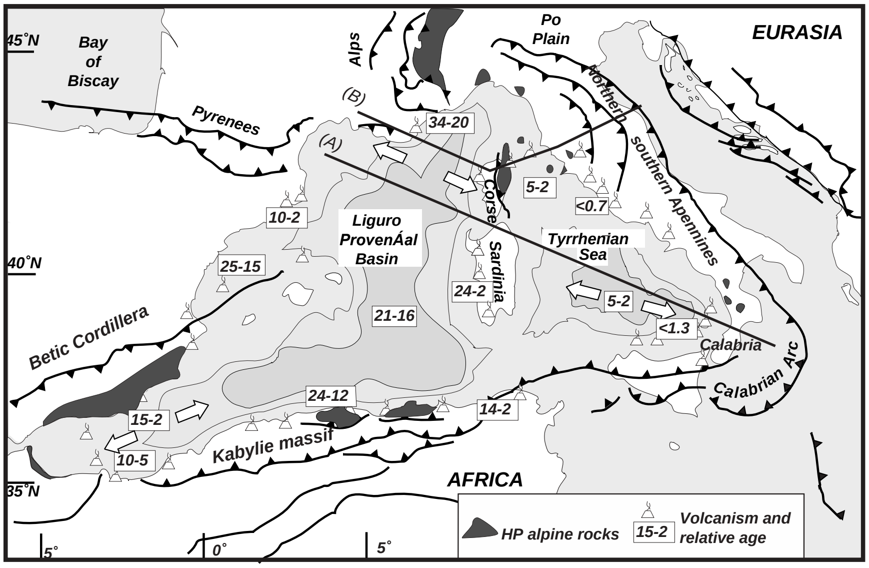

Figure 2.1: Simplified tectonic map of the Central Mediterranean. We show: the distribution of H*P* alpine metamorphism, the average ages in Myr, the distribution of volcanism (from Lonergan and White, 1997), and profiles A and B, along which we reconstruct the extensional geologic record (*cf.* Figure 2.2).

2.1.2 Introduction

Most of our knowledge about the geometry of subduction comes from two sources, earthquake hypocenters (*e.g.* Isacks and Molnar, 1971; Giardini and Woodhouse, 1984) and seismic tomography (*e.g.* van der Hilst *et al.*, 1997) which both yield snapshot images of slabs. Other constraints such as the geoid allow for indirect inferences about slab and mantle rheology (*e.g.* Hager, 1984; King and Hager, 1994; Moresi and Gurnis, 1996). Since seafloor is continuously consumed at trenches, surface accessible evidence is lost. The long-term evolution of subduction is therefore far more uncertain than its present state, yet knowledge about the history of subduction zones would provide important insight into subduction dynamics and help us understand the interaction between tectonics and mantle convection. In order to unravel the history of subduction, it is prudent to integrate different sets of data: tomographic models can provide information about the distribution of cold subducted material, plate tectonic reconstructions yield convergence rates at plate boundaries, and geological data can constrain the age and the style of subduction. In particular, prominent geological signals of subduction dynamics are the development of topography at the trench (*e.g.* Stern and Holt, 1994; Royden, 1993; Zhong and Gurnis, 1994), deep burial of crustal rocks, and initiation of arc magmatism (*e.g.* Jacob *et al.*, 1976). The uplift of continental material during subduction initiation will be followed by continental subsidence due to viscous coupling after the downwelling has picked up speed (*e.g.* Mitrovica *et al.*, 1989; Gurnis, 1992; Pysklywec and Mitrovica, 1997). When the slab reaches the 660-km discontinuity, impedance to flow will be accompanied by a decrease in subduction velocity and, possibly, trench migration rate (*e.g.* Christensen and Yuen, 1984; Kincaid and Olson, 1987; Zhong and Gurnis, 1995). Geological fingerprints of these dynamic effects that can be interpreted and used for reconstruction include large scale unconformities and marine deposits on the upper plate (*e.g.* Cohen, 1982; Mitrovica *et al.*, 1989; Gurnis, 1992), high pressure/low temperature (H*P*/L*T*) metamorphism (*e.g.* Peacock, 1996), and spatial, temporal, and chemical patterns of the volcanic arc (*e.g.* Jacob *et al.*, 1976; Keith, 1978).

Here, we will present a complete reconstruction of the history of subduction in the Central Mediterranean that uses a variety of geophysical and geological data and is tied into a consistent geodynamic framework. We are able to explain the evolution of subduction with a simple model of temporarily confined mantle convection. The examined subduction zone, presently located along the Apennine belt from the Calabrian arc to the northern Apennines (Figure 2.1), has been oriented roughly parallel to the direction of relative rigid-plate convergence during its whole lifetime (Dewey *et al.*, 1989; Patacca *et al.*, 1990). The rate of convergence at the trench has thus always been very low and the downwelling of the oceanic lithosphere probably driven mainly by its negative buoyancy, resulting in trench rollback (Malinverno and Ryan, 1986; Royden, 1993; Giunchi *et al.*, 1996; Faccenna *et al.*, 1996). This absence of significant plate convergence and the availability of geophysical and geological data make the Central Mediterranean a promising setting for unraveling the evolution of subduction zones. It is also one of the few settings in which we can test our model predictions directly for the free-subduction case (sec. 1.5.3).

The kinematics of the Central Mediterranean subduction zone will be reconstructed from its initial stage at $\sim$85 Ma to the present day along two cross-sections. The first (southern) section runs from Calabria via Sardinia to the Gulf of Lyon, while the second (northern) section runs from the northern Apennines via Corsica to the Gulf of Lyon (Figure 2.1). The constraints we use are present-day images of the slab as inferred from seismic tomography and geological data. Our model divides the evolution of subduction in the Central Mediterranean into three stages: (1) slow initiation, characterized by very low subduction speeds; (2) development of the slab, with an approximately exponential increase in subduction speed and opening of a first back-arc basin; and (3) deceleration due to interaction of the slab with the 660-km discontinuity. On the southern section, which is dominated by subduction of oceanic lithosphere, the last phase of the process is characterized by a transient slowing of subduction, followed by a resurgence in subduction speed and a second phase of back-arc spreading. On the northern section, we observe a permanent decrease of subduction speed that is most likely caused not only by the stagnant slab, but also by continental material (lighter than the mantle) entering the trench from 30 Ma onward.

2.1.3 Tomographic images of the upper mantle

Present-day subduction in the Central Mediterranean shows up in the Southern Tyrrhenian Sea as a NW-dipping Wadati-Benioff zone (Isacks and Molnar, 1971; Giardini and Velonà, 1988). Seismicity is distributed in a continuous 200-km wide, 40–50 km thick volume, plunging down to a depth of $\sim$450 km with a dip of 70 $^\circ$ (Selvaggi and Amato, 1992, and Figure 2.2a). Focal mechanisms show that the slab is subject to in-plane compression in its middle portion (165–370 km), whereas the stress state is heterogeneous in its upper portion (Frepoli *et al.*, 1996, and Figure 2.3). Active volcanic arcs related to the subducting slab are localized in the Eolian and Napolitan volcanic district.

Figure 2.2 shows images from a tomographic model of the upper mantle beneath the Italian Peninsula by Lucente *et al.* (1999). Their inversion was performed using a high quality data set of $\sim$6000 teleseismic *P* and *PKP*-phase travel times. The southern cross-section from Calabria to the Gulf of Lyon (Figure 2.2a) shows a high velocity body extending from the surface below Calabria with a NW dip of 70°–80°, it then becomes horizontal in the transition zone, continuing at least as far as Sardinia. At a depth of $\sim$500 km, the anomaly seems to be significantly thinned with respect to the shallower thickness and might be disrupted, whereas it appears to be thickened between 600 km and 700 km depth. The estimated total length of the high velocity zone, interpreted as subducted lithosphere (Lucente *et al.*, 1999), is $\sim$1200 km measured from the base of the lithosphere, including its lower-most flat portion. This interpretation implies that subducted material has piled up at a depth of 660 km and that slab penetration into the lower mantle has been delayed or prevented. Figure 2.2b shows the Lucente *et al.* (1999) model for our northern cross-section from the Apennines to the Gulf of Lyon. The images show a broad velocity anomaly ($d\ln v_P$ up to 3–4%) that dips toward the WSW at $\sim 70^\circ$–80° at shallower depths and seems to bend slightly in the transition zone. The slab anomaly is aligned with earthquake hypocenters whereas seismicity is limited to shallow depths ($\sim$90 km) in this region (Selvaggi and Amato, 1992). The structure of the lithosphere along the same cross sections reveals two thinned regions where the crustal rocks are oceanic, separated by the 80-km-thick Sardinia-Corsica continental block (Suhadolc and Panza, 1989).

As for all interpretations of tomographic models, there is some subjectivity involved in the description of structures. However, the presence of a large fast anomaly that can naturally be explained as an aseismic remnant of the Central Mediterranean slab appears to be a stable feature of several models. Using different data sets, Spakman *et al.* (1993) and Piromallo and Morelli (1997) obtained velocity models for the Mediterranean with high-velocity features that are similar in both geometry and total length to those of Lucente *et al.* (1999).

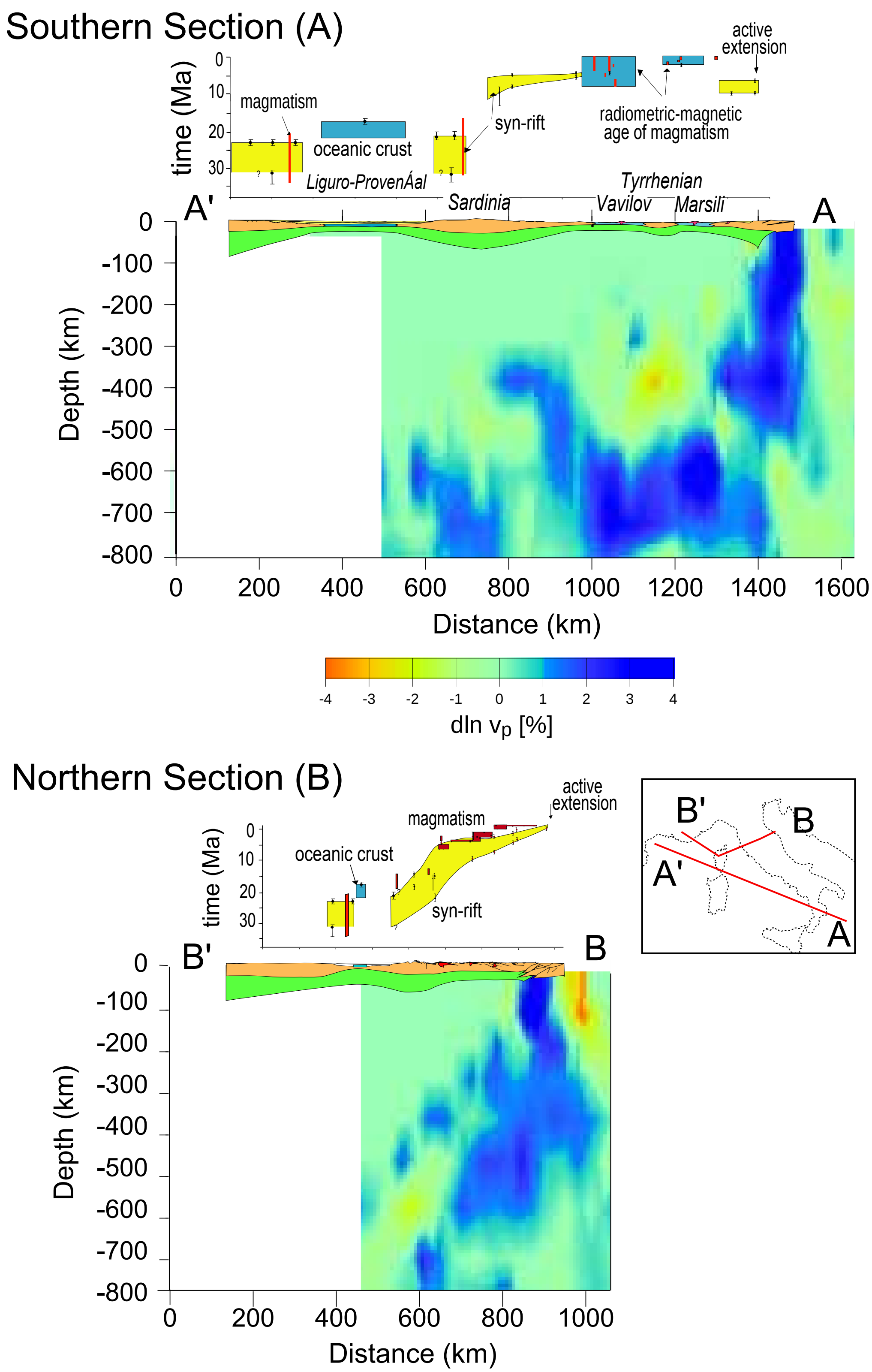

Figure 2.2: Tectonic cross-sections from a) Calabria to the Gulf of Lyon b) Northern Apennines to the Gulf of Lyon (for location see Figure 2.1), tomographic model is from Lucente *et al.* (1999). Lithospheric cross sections have been drawn using a lithospheric thickness from Suhadolc and Panza (1989) and crustal thicknesses from Finetti and del Ben (1986), Barchi *et al.* (1998), and Chamot-Rooke *et al.* (1999). Age of back-arc extension is from Faccenna *et al.* (1997).

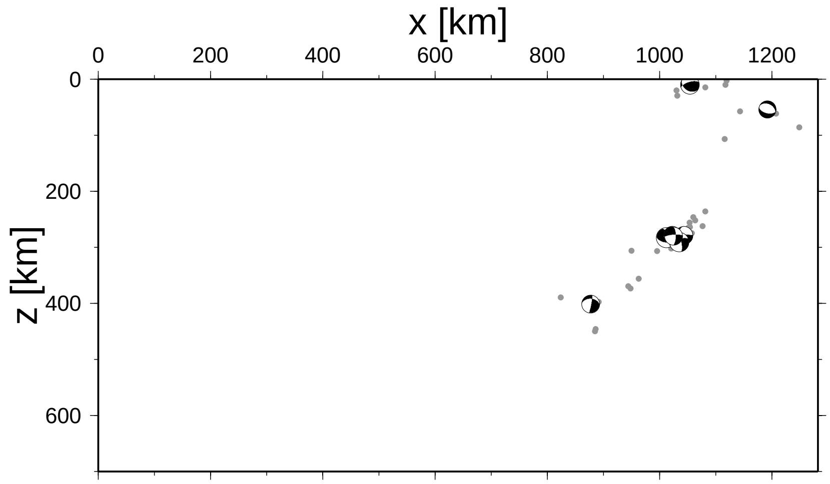

Figure 2.3: Harvard CMT solutions (Dziewonski *et al.*, 1981) (until 12/2001) from the Harvard web site for the southern section (profile A in Figure 2.2) from the gulf of Lyon to the Calabrian arc (best double couples); gray background seismicity is from the relocated catalog of Engdahl *et al.* (1998). Focal mechanisms are rotated into the plane; western hemisphere of the beach balls is shown (front-hemisphere projection).

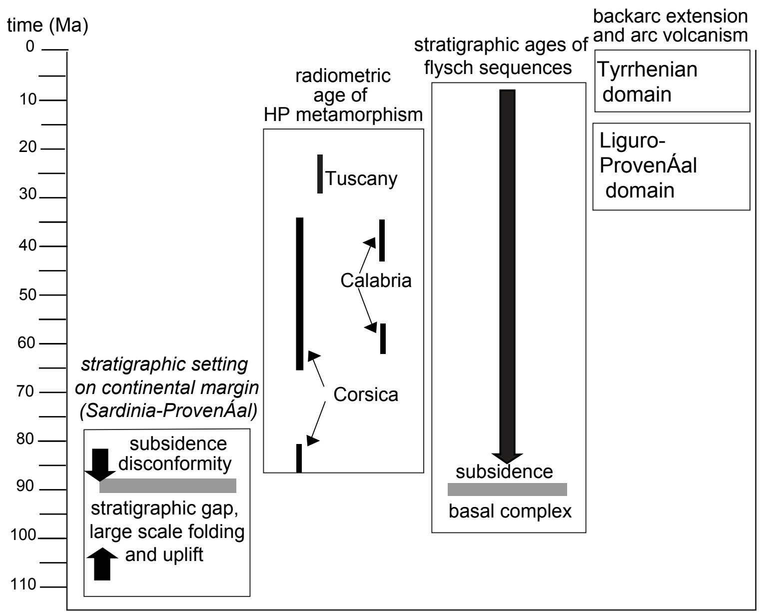

Figure 2.4: Geological data used to constrain the early stages of subduction in the Central Mediterranean area. Stratigraphic ages of Sardinia-Provençal unconformity are from D'Argenio and Mindszenty (1991). Radiometric ages of H*P* metamorphism from Borsi and Dubois (1968); Shenk (1980); Rossetti *et al.* (2001) for Calabria and Monié *et al.* (1996); Lahondère and Guerrot (1997); Jolivet *et al.* (1998) and Brunet *et al.* (2000), for Northern Apennines and Corsica. Stratigraphic ages of flysch from Marroni *et al.* (1992) and Monaco and Tortorici (1995).

2.1.4 Geological constraints

Geologically, we can discern two different phases for the evolution of the Central Mediterranean subduction zone: 1) formation of the first instability and development of the slab, and 2) the episodic opening of back-arc basins. In the following, we synthesize the geological data (summarized in Figure 2.4) that we consider pertinent to defining the age and style of subduction in the Apennines.

Formation and development of the slab

The whole Mediterranean region was subjected to a large-scale rapid pulse of horizontal in-plane compressional stress during the Late Cretaceous ($\sim$95–85 Ma). This event is marked by large-scale folding localized mainly along the southern North-African (Bosworth *et al.*, 1999) and northern Iberian-European (Guieu and Roussel, 1990; D'Argenio and Mindszenty, 1991) Tethyan passive margins of the Ligurian-Piedmont ocean (Dercourt *et al.*, 1986) and, subordinately, along the Apulia micro-plate (D'Argenio and Mindszenty, 1991). Along the northern margin, in particular in Sardinia and in the Provençal area, this event was followed by a rapid subsidence

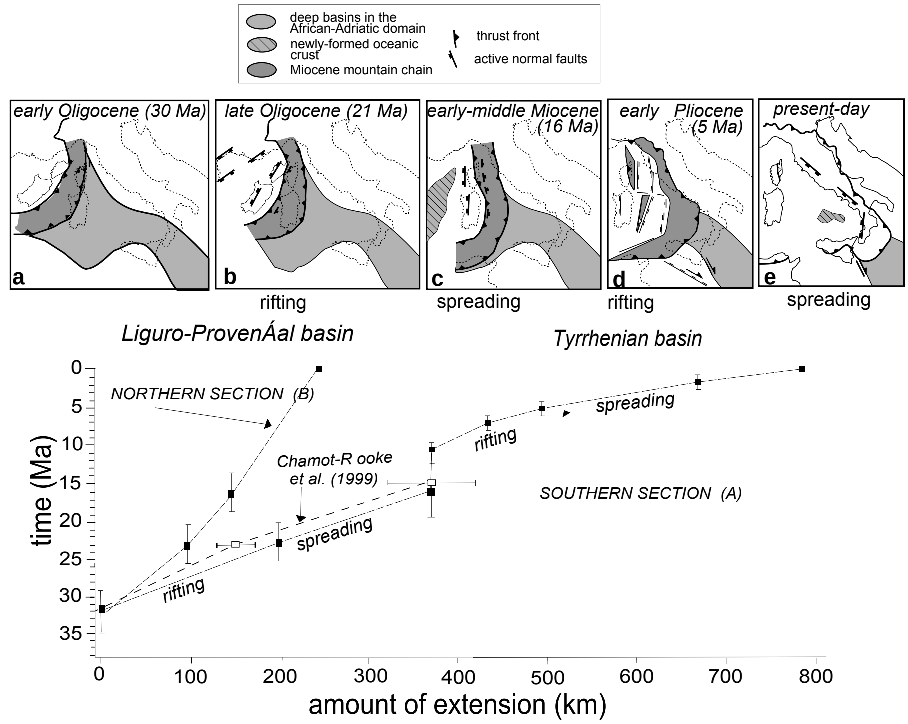

Figure 2.5: Paleogeographic reconstruction of back-arc extension in the Central Mediterranean (redrawn from Faccenna *et al.*, 1997) and estimation of the amount of extension in time along the cross sections of Figure 2.2.

as marked by the presence of a large-scale angular unconformity ($\sim$90–85 Ma, Figure 2.4; Guieu and Roussel, 1990; D'Argenio and Mindszenty, 1991). Soon after this widespread compressional episode, first evidence of the formation of a trench and of subduction along the northern, Iberian-European margin appears. This is marked by the formation of H*P* units in Corsica (Lahondère and Guerrot, 1997) and by the sudden and contemporaneous onset of siliciclastic deposition, presently outcropping in scattered sites along the Apennine chain ($\sim$85–80 Ma, Figure 2.4; Principi and Treves, 1984; Marroni *et al.*, 1992; Monaco and Tortorici, 1995). In particular, in the northern and central Apennines the older foredeep system shows locally continuous sedimentation for a duration of $\sim$15–20 Myr in the same basins from 85–80 Ma to 65 Ma (Marroni *et al.*, 1992). After 65 Ma, the life of the flysch basin is limited to a few Myr and the locus of deposition moved more rapidly toward the East up to the present-day deposition in the Adriatic foredeep (*e.g.* Patacca *et al.*, 1990). This suggests that during the first stage of slab evolution (Late Cretaceous-Paleogene) subduction progressed slowly ($\lesssim$ 1 cm/yr; Marroni *et al.*, 1992) and then accelerated.

During subduction, crustal material was dragged down into the sedimentary wedge suffering high pressure-low temperature metamorphism. In the Northern Tyrrhenian region, the H*P*/L*T* facies outcrop in Alpine Corsica and in the inner Northern Apennine (Figures 2.1 and 2.4), and are organized in a double-vergent wedge (Carmignani and Kligfield, 1990; Jolivet *et al.*, 1998). A maximum-pressure metamorphic peak of $\sim$1.6–2 GPa is recorded in the Corsica metapelites, and pressure decreases progressively to $\sim$1.5 GPa in the Tuscan archipelago, and to $\sim$1 GPa onshore Tuscany (Jolivet *et al.*, 1998). The oldest units are found in Corsica, with ages mostly ranging from 60 to 35 Ma, whereas in the inner Apennine the ages decrease to $\sim$25 Ma (Figure 2.4; Monié *et al.*, 1996; Jolivet *et al.*, 1998; Brunet *et al.*, 2000). The oldest reliable age in Corsica gives 85–80 Ma (Lahondère and Guerrot, 1997). Similarly, in Calabria, metamorphic units show radiometric ages of H*P* metamorphism ranging from $\sim$65–58 Ma (Borsi and Dubois, 1968) to $\sim$40 Ma (Shenk, 1980; Rossetti *et al.*, 2001) to $\sim$35 Ma (Monié *et al.*, 1996). These data indicate that the formation of H*P* metamorphic facies and their exhumation at the surface can be traced as a continuous process, from as early as the Paleocene up to the Miocene (Jolivet *et al.*, 1998), with metamorphism getting progressively younger toward the east.

In the Apennines, the passive continental margin of Apulia entered at the trench from 30 Ma (Figure 2.5), leading to subduction of continental lithosphere (Dercourt *et al.*, 1986) as attested by the incorporation of continental –passive margin– rocks into the Apennine accretionary wedge (*e.g.* Boccaletti *et al.*, 1971; Carmignani and Kligfield, 1990). The geometry of the Apulian-Adria plate is unknown. However, paleogeographic reconstruction

(Dercourt *et al.*, 1986) suggests that the width of the continental plate was reduced to few hundreds of km in the southern section due to its confinement to the east by the Ionian basin (Figure 2.5).

The opening of the back-arc basins

From $\sim$35–30 Ma, during the formation of HP/LT metamorphic facies and the deposition of siliciclastic deposits, arc volcanism and extension began behind the accretionary wedge (Beccaluva *et al.*, 1989). This indicates that the slab must have reached a minimum depth of 100–150 km to produce melting and arc-volcanism at the surface (Jacob *et al.*, 1976).

In order to estimate the amount and rate of back-arc extension, we plot the age of the syn-rift deposits and the age of oceanic crust and volcanism along the cross-sections shown in Figure 2.2, which run perpendicular to the strike of the basins. Arc volcanism first appeared at $\sim$34–32 Ma in Sardinia and in the Provençe, followed by the formation of the first extensional basins ($\sim$30–23 Ma, Beccaluva *et al.*, 1989; Cherchi and Montandert, 1982; Gorini *et al.*, 1994).

During the late Aquitanian ($\sim$20 Ma), post-rift deposits unconformably covered the syn-rift sequence (Gorini *et al.*, 1994; Seranne, 1999). Oceanic spreading occurred at this time (Burrus, 1984) as well as the $\sim 25^\circ$ counter-clockwise rotation of the Corsica-Sardinia block; the latter most probably occurred between 21 and 16 Ma (van der Voo, 1993). After a few million years, extension shifted to the Southern Tyrrhenian basin: syn-rift deposition started at $\sim$12–10 Ma in both Sardinia and Calabria (Kastens and Mascle, 1990; Sartori, 1990), followed by the formation of localized spreading centers (5–4 Ma: Vavilov basin, 2 Ma: Marsili basin) and drifting of the Calabria block (Sartori, 1990).

In the Northern Tyrrhenian Sea, extension is marked by a system of crustal shear zones, sedimentary basins, and magmatic activity that gets younger toward the east from Corsica to the Apennine chain (Figure 2.2b; Serri *et al.*, 1993; Bartole, 1995; Jolivet *et al.*, 1998). Syn-rift deposits are found from 20 Ma on in the Corsica basin (Mauffret and Contrucci, 1999) and 2 Ma along the Apennine watershed (for a review, see Bartole, 1995; Faccenna *et al.*, 1997), where normal faults are still active. Magmatic activity accompanied and post-dated the end of the syn-rift growth of the basin. Both the extensional basin and the magmatic center shifted eastward, away from the rift axis, at an average velocity of 1.5–2 cm/yr (Figure 2.2b) during this time period.

This data set allows us to determine the timing of the stretching and spreading events. We estimate the amount of back-arc extension by reconstructing the main tectonic events, at the scale of the crust, in several different steps. First, we subtract the oceanic-floored area of each basin from the sections of Figure 2.2, and then, using an area-balancing technique, we restore the crust to the thickness of the continental shoulders ($\sim$30 km, see Finetti and del Ben, 1986; Chamot-Rooke *et al.*, 1999), assuming that the locus of extension at the surface corresponds to the locus of maximum crustal thinning. The Northern Tyrrhenian section is restored to the slightly greater average minimum thickness of 35 km, to take the previous thickening event into account (Jolivet *et al.*, 1998). Figure 2.5 shows the amount of extension attained by the southern and northern Tyrrhenian, and the Liguro-Provençal basin at several ages.

With regard to the southern section, we note that:

– the total amount of extension ($\sim$780 km) is partitioned roughly equally between the two basins, with alternating episodes of rifting ($\sim$7 Myrs) and oceanic spreading ($\sim$5 Myrs);

– the rate of extension is reduced at the end of spreading of the Liguro-Provençal basin; rifting in the Tyrrhenian then initiated after a small pause of few Myr and progressively accelerated.

With regard the northern section, we note that:

– the total amount of extension ($\sim$240 km) is partitioned between the Liguro-Provençal basin ($\sim$140 km) and the Northern Tyrrhenian basin ($\sim$100 km). The oceanic spreading was confined to a narrow strip ($\sim$30 km) in the Ligurian basin (Mauffret and Contrucci, 1999);

– after the initial stretching event in the Liguro-Provençal basin, the rate of extension progressively decreased.

We also find from both sections that the volcanic arc-trench gap is rather wide ($\sim$400 km) in comparison to the present day. This suggests, in agreement with the paleo-reconstruction of Beccaluva *et al.* (1989) and Seranne (1999), that the slab dipped shallowly prior to and after the opening of the Liguro-Provençal basin. In addition, slab steepening has been proposed by Jolivet *et al.* (1999) and Brunet *et al.* (2000) along the northern section of

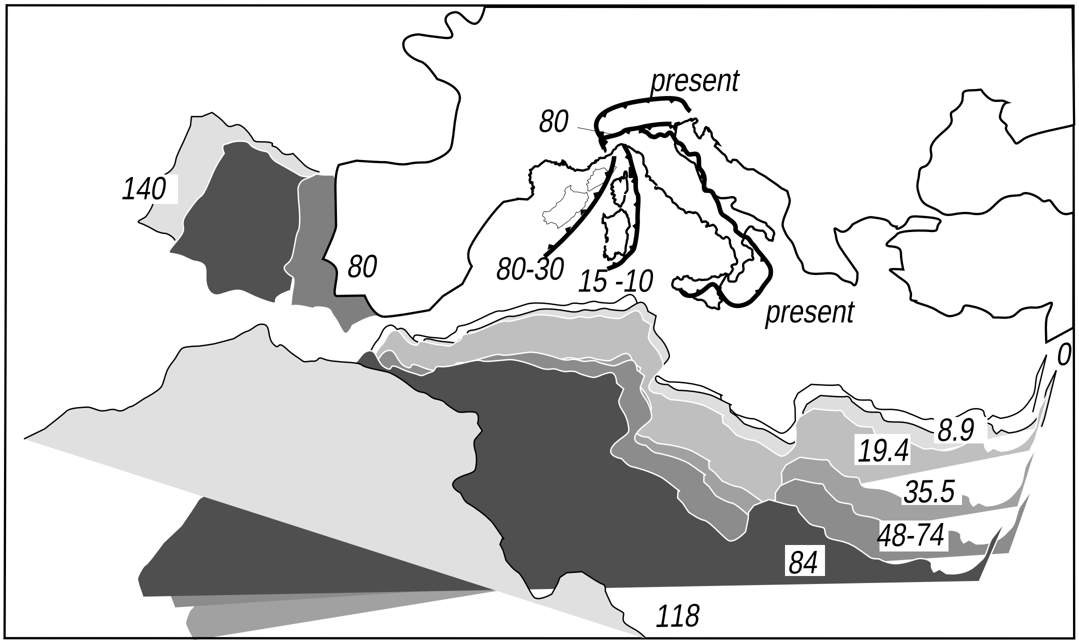

Figure 2.6: African motion with respect to fixed Eurasia as calculated by Dewey *et al.* (1989) and motion of Iberia (redrawn from Olivet, 1996). The orientation of the Central Mediterranean trench is also shown, numbers are Ma.

the Tyrrhenian Sea to account for the decreasing time gap between the H*P* compressional event and the onset of extension and magmatism as you go to the north.

The amount and velocity of extension we estimate are in good agreement with previous evaluations. Along the southern section of the Liguro-Provençal basin, the rifting has been estimated to account for 150$\pm$20 km of extension (Chamot-Rooke *et al.*, 1999) while the amount of spreading has been found to be 150 km (Mauffret *et al.*, 1995), 230 km (Burrus, 1984), and 230$\pm$20 km (Figure 2.5; Chamot-Rooke *et al.*, 1999). For the Tyrrhenian Sea, the total extension found by Malinverno and Ryan (1986) is $\sim$340 km. In the southern section of the Tyrrhenian Sea, similar values have been estimated by Patacca *et al.* (1990) and Spadini *et al.* (1995). Furthermore, the total amount of extension along the whole southern section agrees well with previous studies (Gueguen *et al.*, 1998).

2.1.5 African motion and trench orientation

Several kinematic reconstructions have been proposed for the Mediterranean to describe the convergence of Africa with respect to Eurasia (*e.g.* Dewey *et al.*, 1989; Dercourt *et al.*, 1993). All of these models suggest that Africa moved slowly relative to stable Eurasia, with counterclockwise rotation, moving NE until $\sim$40 Ma, then N, and finally NNW (Figure 2.6). The relative velocity of a point located half way along the northern African coast has probably been slower than 3 cm/yr during the last 80 Myr, decreasing by a factor of two during the last 30–20 Ma (Jolivet and Faccenna, 2000). These numbers are similar to an estimate of plate motions for Africa (Silver *et al.*, 1998). Geodetic data indicate that Africa currently moves N20° W at a rate of 0.7 cm/yr in the Central Mediterranean (Ward, 1994).

In order to estimate the net convergence rate (the rate at which the plate moves perpendicularly to the trench), we reconstruct the orientation of the trench in time (Figure 2.6). Paleomagnetic data indicate that Iberia rotated ($22^\circ \pm 14^\circ$) with respect to Europe between 132 Ma and 124 Ma (van der Voo, 1993; Moreau *et al.*, 1997). After this episode, the rotation of the Iberian peninsula slowed down and was followed by translation ($\sim$120 Ma) during the initial phase of the opening of the Bay of Biscay ($\sim$85 Ma; Olivet, 1996, and references therein). At that time, the trench was oriented NE-SW, running parallel to the former Iberian passive margin (Figure 2.6). Subsequently, the trench's position remained fairly stable, turning to N-S only after the rotation of the Sardinia-Corsica block ($\sim$21–16 Ma; van der Voo, 1993), and turning to its present-day position during the Southern Tyrrhenian spreading episodes ($\sim$5–2 Ma). The trench was therefore oriented roughly parallel to the motion of Africa during most of the subduction process. With the numbers from Dewey *et al.* (1989), we can estimate the

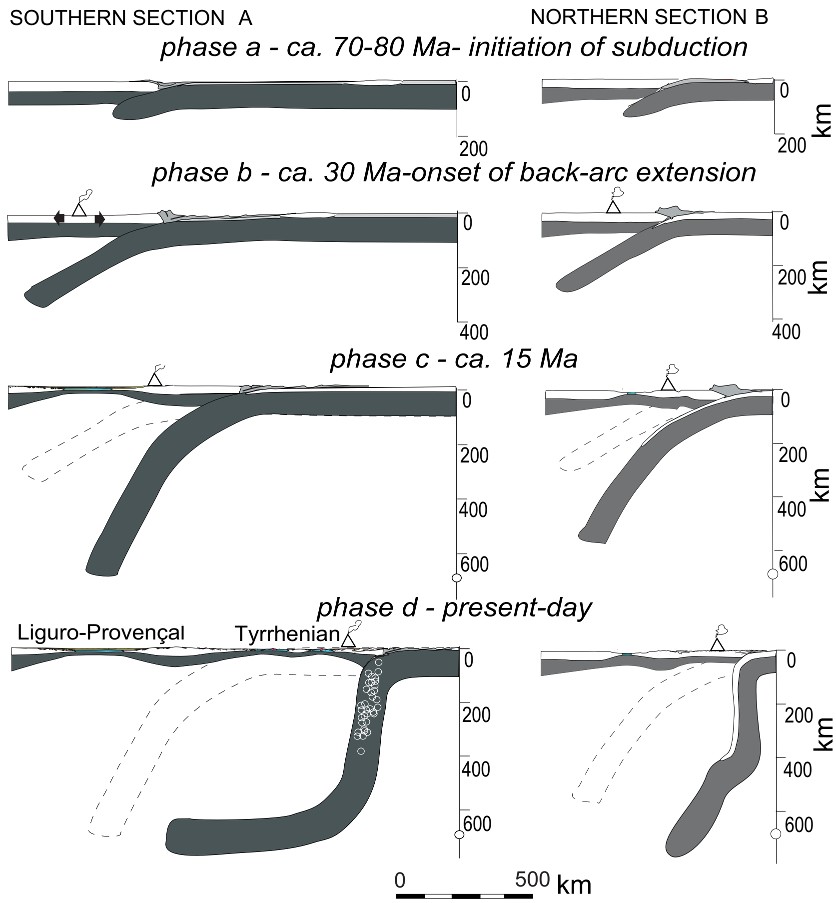

Figure 2.7: Four-phase reconstruction of subduction along the cross sections of Figure 2.2. White layers indicate crustal material; continental material is inferred to be dragged down into the upper mantle in stage d of the northern section. The dip of the deep slab portion at phase c is poorly constrained.

total amount of net convergence produced by the motion of Africa since 80 Ma as ∼240 km with an average rate of 3 mm/yr (Figure 2.8a). We note that taking into account the motion of the Adria microplate cannot increase the estimate of convergence significantly because its Tertiary motion has been coherent with Africa (Channell, 1986).

The net convergence velocity across the Central Mediterranean trench thus appears to be very low when compared with other subduction zones worldwide (Jarrard, 1986). As a consequence, subduction will be mostly driven by the negative buoyancy of the subducted slab. This type of setting has been studied in the models of Faccenna *et al.* (1996) and Giunchi *et al.* (1996) and in chapter 1.

2.1.6 Reconstructing subduction

We will now describe our reconstruction along the two cross-sections shown in Figures 2.1 and 2.2 (Figure 2.7). The present-day configuration of the slab was obtained from the upper-mantle velocity anomaly shown in Figure 2.2, assuming a continuous slab. As the rigid-plate convergence rate is considered negligible, the amount of back-arc extension shown in Figure 2.4 is directly related to the total amount of subduction. From the present-day configuration we subtract the total amount of material subducted during the opening of the back-arc basins. Phases b and c in Figure 2.7 show the slab configuration at the beginning of the Tyrrhenian and Liguro-Provençal rifting, respectively. The dip of the deeper part of the slab during phase c is inferred but not constrained by the available data.

We divide the subduction history in the Central Mediterranean into three stages (Figure 2.7):

1. Phases a–b, from 80 Ma to 35–30 Ma. In both sections, the amount of subduction, ∼400 km, was small cor-

responding to an average velocity of 0.8 cm/yr. Arc-volcanism developed when the slab, dipping shallowly, reached a depth of 200–300 km;

2. Phases b–c, from 35–30 Ma to 15 Ma. In both sections, the velocity of subduction and the slab dip increased rapidly during the opening of the Liguro-Provençal basin. By the end of the Sardinia drifting phase (Liguro-Provençal opening) the slab had reached a depth of $\sim$600 km. In the southern section, subduction halted at $\sim$15 Ma. In the northern section, the subduction velocity was slower than in the South at all times, and is observed to decrease progressively with time.

3. Phases c–d, from 15 Ma to the present. In the southern section, the slab becomes deformed, folding at the 660-km boundary. This is indicated by a $\sim$5 Myr pause in subduction and the subsequent acceleration of the rollback velocity to as much as 6 cm/yr during the opening of the Tyrrhenian back-arc basin. In the northern area, conversely, subduction ceases permanently.

In summary, we infer that subduction started very slowly. After the initiation phase, velocities increased rapidly with time during the descent of the slab into the upper mantle. The dip of the slab increased, and arc-volcanism developed 50 Myr after the onset of subduction. Soon after the opening of the Liguro-Provençal basin, the slab reached 660-km. Along the southern section, where only oceanic material was subducting, the subduction velocity decreased at this time, going to zero temporarily. After a few million years, however, the slab probably re-bent at depth, steepening again, the trench rolled back, and subduction velocity re-accelerated during the rifting and spreading of the Tyrrhenian basin. Along the northern section, conversely, we observe a progressive decrease of the subduction velocity and no re-acceleration.

This scenario with the opening of two back-arc basins is in agreement with previous models formulated on the base of different data sets (*e.g.* Bortolotti *et al.*, 1990; Principi and Treves, 1984; Knott, 1987; Jolivet *et al.*, 1998; Rossetti *et al.*, 2001). In our scenario, the consumed arc-perpendicular length of the oceanic lithosphere of the Jurassic Liguro-Piedmont ocean is $\sim$450 km in the North and $\sim$750 km in the South, consistent with paleogeographic reconstructions (Dercourt *et al.*, 1986; Schmid *et al.*, 1996).

Comparison with previous models

An alternative paleo-tectonic scenario envisions that subduction in the Central Mediterranean initiated at a later time than proposed here, and only after a polarity flip from an earlier southeast-dipping subduction zone. The timing of this flip has been put at 65 Ma (Dercourt *et al.*, 1986), 50 Ma (Boccaletti *et al.*, 1971), or 30 Ma (Doglioni *et al.*, 1997). The main objective of these alternative models is to explain the development of west-verging nappe structures in Alpine Corsica as well as the east-verging Apenninic structures. However, all of those models are at odds with the observations that H*P* metamorphic units are also found inside the internal Apenninic nappe, and that these units are progressively younger moving toward the East from 65 Ma up to 25–22 Ma. This indicates a continuous evolution from the development of subduction to back-arc extension (Jolivet *et al.*, 1998, and Figure 2.4). Furthermore, the east-verging siliciclastic deposition that began with the development of the Apenninic trench has been a continuous process, starting at $\sim$85 Ma and continuing to the present day (Principi and Treves, 1984, and Figure 2.4). All of these data support the model of a doubly vergent Alpine-Apenninic orogenic wedge, related to north-westward subduction from the very first stage of deformation, with an along-strike change in the dip of the subduction zone toward the Alps.

2.1.7 Discussion

Figure 2.7 can be recast in the form of a diagram showing the amount of subduction (*i.e.* the length of the subducted slab) versus time for the southern (Figure 2.8a) and northern (Figure 2.8b) cross-sections. Starting from the present, we first plot the current length of the slab as inferred from the tomographic model. The error bars that we show are conservative upper bounds. Other data in Figure 2.8 come from calculating the amount of extension. Under the assumption that convergence is negligible, the amount of extension is identical to the amount of subduction. Further constraints are the onset of arc volcanism, which gives a minimum amount of subduction of 150–200 km at that time (using 45° as a maximum slab-dip, as constrained by the arc–trench gap), and, in the northern section, the maximum amount of subduction during the deposition of the first foredeep deposits.

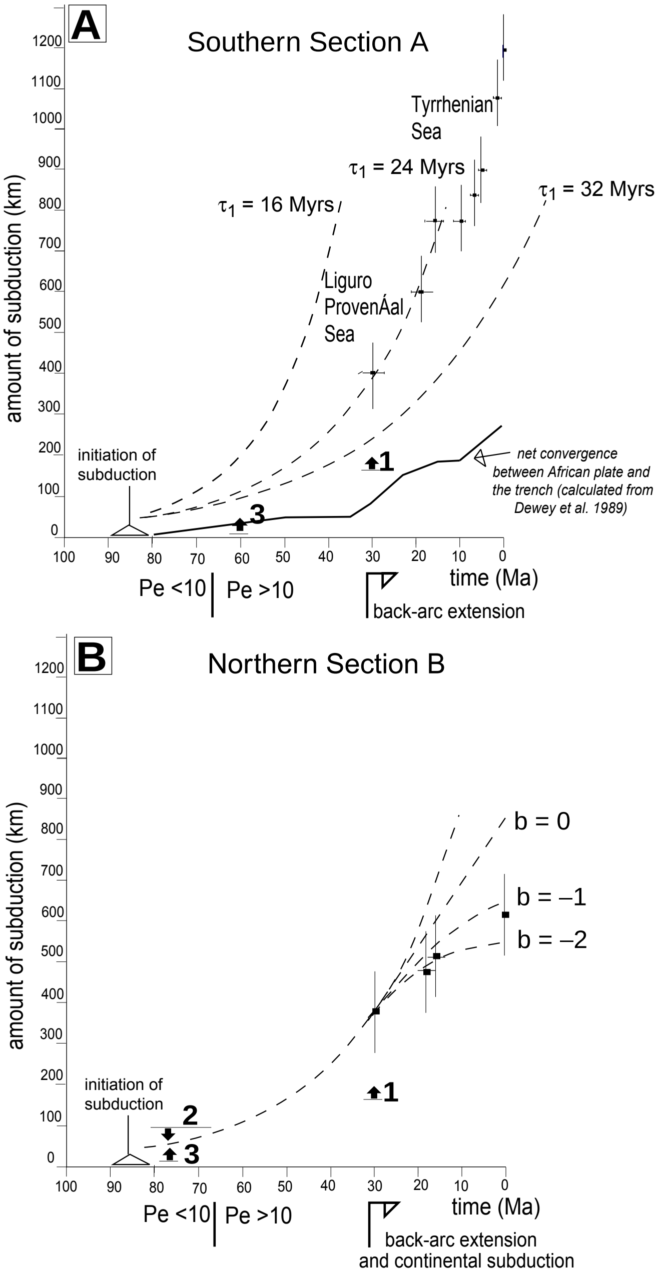

Figure 2.8: Amount of subduction (slab length) as a function of time for the Central Mediterranean subduction zone along the southern (a) and northern (b) cross-sections. Curves are drawn from (2.1) (left, exponential increase part) and (2.3) (right, slowdown of subduction after entrance of continental material) with the parameters mentioned in the text. Arrows denote the constraints from: (1) onset of volcanism, (2) the duration of the continuous foredeep deposition, and (3) first appearance of H*P* metamorphic assemblages. *Pe* refers to the Peclet number, see text.

The first stages: Initiation and development

We will start by discussing the primary, accelerating part of the subduction speed curve, which can be observed along both cross-sections.

Free subduction phase Before the slab reaches the 660-km discontinuity, the data in Figure 2.8 can be interpreted using our arguments from chapter 1. We observed that the subduction velocity increased roughly exponentially with time for slab instabilities that were free to sink under their negative buoyancy (*i.e.* no ridge-push) before impedance to flow at the transition zone became important. In both numerical and laboratory convection models, the data could be fit by equating the viscous dissipation per unit length due to the bending of oceanic lithosphere to the rate of potential energy change by slab pull. This approach was motivated by the work of Conrad and Hager (1999a).

The depth extent of the slab, $H(t)$, at time t then scales as

$$H(t) = H_0 \exp\left(\frac{t}{\tau_1}\right) \tag{2.1}$$

where H_0 is an initial length (to be determined from the data) and τ_1 is a characteristic time scale that follows from the scaling argument and is given by:

$$\tau_1 = \frac{\mu R^2}{C \Delta\rho_{oc} g r^3}. \tag{2.2}$$

Here, $\Delta\rho_{oc}$ is the density contrast between oceanic plate and mantle, μ is the effective viscosity of the bending plate, g is the gravitational acceleration, r is the bending radius, R is the half thickness of the plate, and C is a fitting constant that was found to be $\approx$0.28 for the numerical experiments of chapter 1; C is in a similar range for a slightly different laboratory setup (Funiciello *et al.*, 2002). For (2.1) it is assumed that only the viscous bending of the oceanic plate and the gain in buoyancy forces matter, that R and r are constant during subduction, and that the entrainment of upper-plate lithosphere and the varying dip of the slab are not important. Accordingly, (2.1) is only a first-order approximation.

In Figure 2.8a, we compare (2.1) with our data for a range of different timescales τ_1. The trend we observe for the Central Mediterranean subduction zone can be fit if τ_1 is equal to 24 Myrs. Using a value of 125 km for r (as measured from the present-day configuration), 45 km for R (Suhadolc and Panza, 1989), and 10^{23} Pas for the viscosity of the lithosphere, we solve for $\Delta\rho_{oc}$ in (2.2), and find $\Delta\rho_{oc} \sim 50$ kg/m^3. Considering the data uncertainties, we cannot argue for any particular non-linear functional dependence of H on t in a statistical sense. Furthermore, (2.2) shows that τ_1 depends strongly on the geometrical factor R^2/r^3, which is poorly constrained by geologic data, and might change substantially with time. This diminishes the resolution of our scaling argument with respect to parameters such as $\Delta\rho_{oc}$ and μ. Other, possibly important, effects we have not considered include viscous dissipation in the mantle and effects of non-Newtonian rheology that might be poorly described by our effective viscosity approach.

However, we note that our estimate of a timescale, $\tau_1 \approx 24$ Myr, is robust. Whatever process is responsible for the subduction dynamics must yield a similar number. Our viscous bending argument gives the correct timescale for a density contrast of around 50 kg/m^3 and a plate thickness of 90 km. Both are realistic estimates for the Central Mediterranean subduction zone (*e.g.* Cloos, 1993), where the plate was at least 70 Myrs old at initiation (*e.g.* Abbate, 1984). An effective viscosity of 10^{23} Pas for the lithosphere is consistent with estimates of a maximum factor of 100 to 500 contrast between lithospheric and mantle viscosities (Conrad and Hager, 1999a; Becker *et al.*, 1999a, and chapter 1), when a canonical post-glacial rebound value of 10^{21} Pas is used for the mantle. We thus have observational support that the theory developed in chapter 1 has relevance for dynamical processes in nature.

Slowdown due to continental entrainment Along the northern section we observe a decrease in the subduction speed from 30 Myr onward that could be due to the entrance of continental material at the trench (Faccenna *et al.*, 1997). Stretching our scaling argument from chapter 1 further, we modify the balance between viscous dissipation and slab-pull energy release that led to (2.1) to allow for the addition of a positive buoyancy anomaly to the slab column. If we keep all simplifications from above and assume that the change in the density contrast from oceanic ($\Delta\rho_{oc} > 0$) to continental ($\Delta\rho_{con} < 0$) material occurred at time t_1, we can derive an expression for the slab depth relative to $H(t = t_1)$ that will proceed as:

$$h'(t') = \frac{1}{b}\left(\exp\left(\frac{t'}{\tau_2}\right) - 1\right), \tag{2.3}$$

where $h'(t') = H(t')/H(t = t_1) - 1$, $t' = t - t_1$, $b = \Delta\rho_{con}/\Delta\rho_{oc}$, and τ_2 is a second timescale, related to τ_1 as:

$$\tau_2 = \frac{\Delta\rho_{oc}}{\Delta\rho_{con}}\tau_1 = \frac{\tau_1}{b}. \tag{2.4}$$

By taking 30 Ma as the time at which continental material entered the trench and assuming that all other parameters in the system remain constant, we find that the decrease of trench retreat (and hence the decrease in the amount of subducted material) can be modeled by continental material with $b \sim -1.5$ (Figure 2.8b). This corresponds to

$\Delta\rho_{\mathrm{con}} \sim -75$ kg/m^3 and is of the right order of magnitude for continental lithosphere.

The finding that our observations of subduction in the Mediterranean can be described by the simple scaling argument above lends credibility to the idea that the main resisting force for subduction arises from viscous dissipation within the bending oceanic plate at the trench (Conrad and Hager, 1999a; Faccenna *et al.*, 1999; Becker *et al.*, 1999a). The implication for subduction zones is that we should expect slow instability growth in non-converging margins, followed by an exponential increase of the subduction velocity before interaction with the boundary at 660 km becomes important. The entrance of continental material at the trench will, conversely, lead to a slowdown of subduction on timescales given by τ_2.

Instability timescales In settings with slow convergence, we can expect that thermal diffusion will broaden gravitational instabilities and so counteract subduction initiation. This effect will become important if convective timescales are greater than diffusive timescales. As a measure of this effect, we can use the Peclet number,

$$Pe = \frac{u_c l_c}{\varkappa}, \tag{2.5}$$

where u_c and l_c are characteristic velocity and length scales, respectively, and $\varkappa$ denotes thermal diffusivity. Thus, high Pe means that convection is efficient, and small Pe indicates that diffusion will tend to smear out buoyancy anomalies.

Arbitrarily picking $Pe = 10$ as a benchmark and taking $l_c = 100$ km and $\varkappa = 10^{-6}$ m^2/s, we find that velocities should be larger than $\sim$0.3 cm/yr for convection to dominate. More sophisticated treatments of similar problems can be found in the literature (*e.g.* Conrad and Molnar, 1997) but an order-of-magnitude estimate will suffice here. Therefore, diffusion can be expected to be important during the earliest, slow stages of subduction ($\sim$20 Myr). However, other effects such as strain-rate and/or grain-size dependent viscosity (*e.g.* Riedel and Karato, 1997) or the presence of a pre-existing weak zone might enhance the rate of instability growth and accelerate initiation. We note that in the Mediterranean slab pull must have been strong enough to overcome the limiting factors, since we know that subduction did initiate eventually. A comparison with other subduction zones indicates that our model applies strictly to a slowly converging setting because the onset of arc volcanism postdates the onset of subduction by only a few Myr in fast converging areas such as in New Zealand (Stern and Holt, 1994).

Episodic opening of back-arc basins and interaction with the 660-km discontinuity

In the southern cross-section, we observe that the initiation and development stage is followed by a decrease in subduction velocity when the slab reaches the 660-km phase boundary (Figure 2.8a). This coincides roughly with the end of the first episodes of back-arc spreading. Later, the velocity of subduction increases again with time, during the opening of the second back-arc basin. We interpret the opening of the first back-arc basin to have occurred as a consequence of the increased velocity of subduction. This increase was driven by the negative buoyancy of the oceanic plate: once the instability reached a significant depth (200–300 km), its total slab-pull increased, causing extension, rifting, and break-up of the overriding plate (Faccenna *et al.*, 1996, and chapter 1). In addition, the decrease in the African plate velocity at $\sim$35–30 Ma (*e.g.* Silver *et al.*, 1998) may have contributed further to the decrease the convergence velocity, allowing for a net increase in the velocity of trench retreat (Jolivet *et al.*, 1999).

In our model, the end of the first spreading episode and the initiation of the second spreading episode are due to the interaction between the slab and the 660-km boundary (Faccenna *et al.*, 2000). This is likely to produce a slowing of the subduction velocity (*e.g.* Christensen and Yuen, 1984; Zhong and Gurnis, 1995; Funiciello *et al.*, 2002) and a decrease in the dip of the slab, which can in turn cause a decrease in the in-plane extensional stress in the upper plate (Tao, 1991). After few million years, the slab steepens again and re-accelerates, leading to the opening of the second back-arc basin.

We have interpreted the seismic tomography models as showing a continuous flow of subducted material that has piled up temporarily at 660 km. This is congruent with the expectation that slab rollback will delay slab penetration into the lower mantle (*e.g.* Griffiths *et al.*, 1995; Christensen, 1996). In this trench rollback setting, we can therefore infer that restricted upper-mantle flow was the dominant mode of convection during the whole evolution of the slab, even though there is good evidence for the long-term ability of slabs to penetrate into the lower mantle.

2.1.8 Summary

The evolution of subduction in the Central Mediterranean represents a unique opportunity to unravel the way the upper mantle evolved over an 80-Myr timespan. We find that subduction was dominated by slab pull in a restricted, upper-mantle convection environment. Jointly interpreting geological constraints and seismic tomography allows the reconstruction of a non steady-state, three-stage process: 1) formation and nucleation of the first instability, 2) development of subduction in the upper mantle, and 3) episodic opening of back-arc basins as a result of the interaction between the slab and the 660-km phase boundary. The first stage is controlled by the onset of subduction with a slow growth of the instability. The second stage is characterized by the development of subduction, when the slab accelerates as it sinks into the upper mantle. This episode can be modeled by equating the viscous dissipation per unit length due to the bending of oceanic lithosphere to the rate of potential energy release by slab pull. Finally, the third stage is dominated by the interaction between the slab and the 660-km resulting, in the southern region, in an important re-shaping of the slab and intermittent pulses of back-arc extension. In the northern region, we can link the decrease in the trench retreat to the entrance of buoyant continental material at the trench.

2.2 Constraints on the deformation of the overriding plate

After discussing regional back-arc dynamics for models and the Central Mediterranean, we now turn to the question of whether we can predict the deformation state of the overriding plate globally. Back-arc regions in nature show varying styles of deformation and there are corresponding examples of pro or retrograde motion of the trench, *i.e.* of continentward or oceanward motion in a stationary, deep-mantle reference frame (*e.g.* Uyeda and Kanamori, 1979; Jarrard, 1986). The Pacific ocean margins are a case in point: in the West, extensional basins dominate, as in the Marianas and the Tonga trench, where the globally largest retrograde trench velocities are observed (Bevis *et al.*, 1995). In the East, we find the strongest compressional regimes in the overriding plate where the Nazca plate plunges underneath South America. Slab dynamics in that region have indeed been linked to the Andean orogeny by means of a slab "anchor" impeding mantle flow (Scholz and Campos, 1995; Russo and Silver, 1996; Silver *et al.*, 1998).

Some of the potential explanations for these contrasting styles of deformation have already been discussed in sec. 1.6.2. One idea invokes a relatively stiff slab that transmits stresses to the overriding plate depending on its direction of descent into a mantle in which there is a net rotation flow component with respect to a stationary lithosphere (*e.g.* Uyeda and Kanamori, 1979; Doglioni, 1990). Hotspot reference frame plate velocities such as HS2-NUVEL1 (Gripp and Gordon, 1990) have a net rotational component (*e.g.* Ricard *et al.*, 1991; O'Connell *et al.*, 1991) that corresponds to a NW-directed flow at the Marianas and a SW directed flow around South America. It is conceivable that the slab encounters a force that is either directed against or with it in those two locations, respectively, which could affect the normal stresses transmitted to the overriding plate. However, as we will argue in sec. 2.3, there are good reasons to believe that slabs are fairly weak. This implies that effects due to "slab anchoring" (*e.g.* Russo and Silver, 1994) might be of second order. Instead, a picture of a slab blowing in the mantle wind (*e.g.* Tao and O'Connell, 1992a,b) might be more appropriate. Indeed, as we showed in chapter 1, contrasting styles of deformation can be observed based on the dynamics of the bending lithosphere at the trench.

According to our scaling argument from chapter 1 in which the buoyancy number F emerged as the controlling parameter (sec. 1.3 and sec. 1.5.3), we should expect a more extensional style of deformation in the overriding plate when slab pull is strong, *i.e.* for old, cold plates. In contrast, for larger viscosities or relative velocities, we should expect a more compressional regime. Figure 2.9 shows a scatter plot of deformational regimes for a number of subduction zones (after Jarrard, 1986) against a proxy for F, the ratio between $\sqrt{\text{age}}$ (with which the slab pull scales, *e.g.* Turcotte and Schubert, 1982) and the velocity of convergence. This presumes that the age of the subducting plate does not affect its bending stiffness, clearly a simplification, since the thickness of the plate will exert a control on subduction, possibly a dominant one (Conrad and Hager, 1999b). However, as the scatter in Figure 2.9 suggests, a more elaborate treatment is probably not justified since there are a number of uncertainties in the dataset of Jarrard (1986) itself. For instance, the age of the subducting plate is poorly constrained in a number of regions (*cf.* Müller *et al.*, 1997). Furthermore, the deformation state of the overriding plate is measured with a qualitative scale. Other quantities such as the seismic coupling (Pacheco *et al.*, 1993; Scholz and Campos, 1995) might be a better proxy for a quantitative analysis, but coupling also depends on several properties of the subduction zone. Here, it suffices to state that there is some correlation between the predictions of the proxy

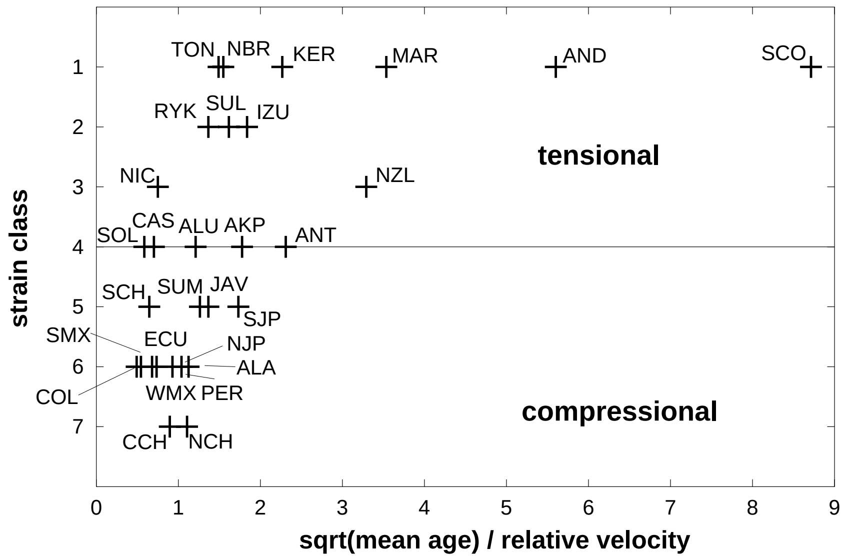

Figure 2.9: Square root of mean slab age (average of tip and trench age) over velocity of convergence versus overriding plate deformation (strain) class from Jarrard (1986). See this article also for a complete list of the abbreviations used for subduction zone regions such as CCH and NCH: Central and Northern Chile, PER: Peru, COL: Colombia, MAR: Marianas, SCO: South Sandwich, KER: Kermadec, TON: Tonga.

quantity we plot in Figure 2.9 and the deformation state. Most notably, the endmember cases of South America (*e.g.* CCH, NCH) and the Western Pacific (*e.g.* TON, MAR) are in the predicted regions of parameter space. Our buoyancy-number based correlation of slab dynamics with the deformation state ($r \approx 0.6$) is comparable in quality to those correlations that Jarrard (1986) discusses based on single quantities such as the rate of convergence. We cannot, however, argue that the introduction of a second variable has significantly improved the fit. A buoyancy number controlled deformation state of the overriding plate and the mode of trench migration are therefore in qualitative agreement with observations, but more work needs to be done to verify a quantitative relation.

In addition to the near-surface slab dynamics due to bending, we can expect that the interaction of the deep slab with the phase transition at 660 km will be of importance for surface deformation (*e.g.* Christensen and Yuen, 1984; Mitrovica and Jarvis, 1985; Tao and O'Connell, 1992b; Zhong and Gurnis, 1995; Pysklywec and Mitrovica, 1997; Karato *et al.*, 2001). Indeed, we argued in sec. 2.1.7 that we could relate the second phase of back-arc extension in the Mediterranean to the rebending of the slab at depth. Refolding may be a common phenomenon during transient slab holdup at the 660-km phase transition (*e.g.* Gaherty and Hager, 1994; Christensen, 1997), and there is evidence for complex slab morphologies from seismic tomography (*e.g.* van der Hilst, 1995). It should be noted that none of these effects require a stiff slab. Since the coupling due to flow driven by the sinking slab suffices to explain surface observables such as plate-velocities (sec. 4.5.2), it is not clear whether we should invoke a slab stress guide that is decoupled from the mantle flow that surrounds it.

The interaction between overriding plate deformation, trench migration, and the dynamics at 660 km are commonly discussed with a reversed sense of cause and effect. As tomographic images show various degrees of slab deflection at the phase transition (*e.g.* van der Hilst *et al.*, 1997; Kárason and van der Hilst, 2000), retrograde trench migration was identified as a major factor decreasing the propensity of a slab to penetrate straight through 660-km (*e.g.* Griffiths *et al.*, 1995; Christensen, 1996). Intuitively, this explanation is appealing because vertically piled up dense material will exert more force per unit area (and thus presumably sink faster) than a slab that is spread out over a large horizontal region. However, all of the previous models have prescribed the trench migration at a fixed rate; coupled models that fully explore the dynamic interactions between the deep phase transition and viscosity jump, self-consistent trench migration, and lithospheric deformation (Zhong and Gurnis, 1995) need further exploration. With a more complete understanding, trench migration might emerge rather as the result of slab interaction with 660-km than as the cause of transient layering.

2.3 Weak slabs

We have seen in chapter 1 and sec. 2.1 that purely viscous models of subduction are able to explain a wide range of observables. These results complement previous fluid dynamical models that were applied to data such as deep seismicity, both in terms of focal mechanisms and overall moment release (*e.g.* Vassiliou and Hager, 1988), and dynamic topography (*e.g.* Zhong and Gurnis, 1992, 1994). If slabs deform mainly as a viscous, and not as an elastic, medium at depth, what is their relative viscosity with respect to the mantle?

Lab-derived, temperature-dependent viscosity laws for olivine would predict many orders of magnitude viscosity difference for the several hundred degrees of temperature difference between the slab and the mantle (*e.g.* Ranalli, 1995). For the shallow lithosphere, faults or other weak zones therefore have to break the plates for a tectonic regime that resembles Earth's to develop rather than a stagnant lid regime (*e.g.* Moresi and Solomatov, 1998; Tackley, 2001a,b). At depth, we know from focal mechanisms and moment-release studies (*e.g.* Bevis, 1986, 1988) that strain rates in the slab are comparable to those in the mantle, implying similar viscosities at constant stress. Also, simply by inspection, slab morphologies as imaged by hypocenters alone (*e.g.* Giardini and Woodhouse, 1984, 1986) or seismic tomography (*e.g.* Kárason and van der Hilst, 2000) resemble those of fluid dynamical models, and not those of elastic beams sticking into the mantle.

Numerical constraints on the effective viscosity of the slab come from considering the viscous bending of the oceanic plate at the trench (Conrad and Hager, 1999a,b, and chapter 1) and regional (*e.g.* Moresi and Gurnis, 1996) or global geopotential (*e.g.* Zhong and Davies, 1999) studies. These studies agree that the effective viscosity of the subducting material cannot be larger than $\sim 500\times$ the viscosity of the surrounding mantle in order to fit the data. Given the wide range of viscosity contrasts that would be expected based on temperature dependence alone, we refer to this relatively small contrast between surrounding mantle and subducted lithosphere rheology as describing a "weak" slab. When we turn to plate-driving forces in chapter 4, we will also see that symmetric coupling by viscous drag of weak slab sinkers leads to better velocity predictions than models in which there is only a one-sided coupling of the slab pull to the subducting plate. If slabs were to present significant obstacles to a background mantle flow rather than mostly "go with the wind" (*e.g.* Tao and O'Connell, 1992a; Olbertz *et al.*, 1997) we should expect some behavior that attests to this divide between slab and mantle. Probably the most comprehensive argument for the existence of such data was put forward by Russo and Silver (1994). Based mostly on the approximately trench-parallel orientation of some fast shear-wave splitting axes, these authors argued for a lateral escape flow around the South American slab, caused by its interaction with large scale mantle currents. In chapter 5, we will show that trench parallel orientation of the largest finite stretching axes can be observed in some flow models with weak slabs. However, both the predicted and the observed anisotropy are quite complex so that we cannot rule out the possible importance of escape flow.

These arguments do not, of course, answer the question of what makes slabs appear effectively weak on long timescales. There are several possible explanations for why the overall viscosity might be smaller than that expected for a homogeneous olivine slab. Probable mechanisms include the presence of a multitude of possible slip planes for brittle deformation at intermediate depths that reduces the elastic stiffness, or, equivalently, the activation of plastic deformation (*e.g.* Karato *et al.*, 2001), shear weakening due to a power-law dependence on stress in the dislocation creep regime (*e.g.* Christensen, 1984), grainsize dependence of viscosity (*e.g.* Ranalli, 1995; Riedel and Karato, 1997), and/or the effect of shear heating (*e.g.* Turcotte and Schubert, 1973; van den Berg and Yuen, 1997; Kameyama *et al.*, 1997). Why slabs appear to be weak remains one of the outstanding questions in geodynamics.

2.3.1 Global circulation models

For the remainder of this thesis, we will proceed to treat slabs using the weak fluid end-member model. This section introduces a tool that will be important for a large part of this work (chapters 4 and 5): global flow models. We will then discuss a first application of such models, the prediction of individual slab shapes based on fluid flow. The backward-bent Indonesia slab will be presented as an argument that weakly deforming fluid slabs are a useful model for understanding subduction dynamics.

Convection in the mantle can be described by the infinite Prandtl number version of the Navier-Stokes equation (*e.g.* Jarvis and Peltier, 1989). The Boussinesq approximation is commonly adopted, such that density, ρ, varies only with temperature, T, and all other thermodynamic parameters and the gravitational acceleration g are independent of T and pressure, p. In this case, conservation of mass leads to the continuity equation

$$\nabla \cdot \mathbf{u} = 0, \tag{2.6}$$

where $\mathbf{u}$ is the velocity vector. Conservation of momentum simplifies to

$$\nabla \cdot \tau + \rho \mathbf{g} - \nabla p = \mathbf{0} \tag{2.7}$$

where τ is the deviatoric stress tensor. For thermal convection, the energy equation that governs the transport of heat by advection and diffusion must be solved simultaneously (see also sec. 5.4.2). Here, we will be concerned with the instantaneous flow solution given boundary conditions for either $\mathbf{u}$ or τ and a known distribution of density anomalies within the mantle. For all solutions of the convective flow problem we need a constitutive equation that relates the strain-rate tensor $\dot{\varepsilon}$ to the deviatoric stresses τ. Using the simplest possible fluid rheology, isotropic Newtonian creep with viscosity μ, $\tau = 2\mu\dot{\varepsilon}$, we arrive at

$$\mu \nabla^2 \mathbf{u} = \nabla p - \rho \mathbf{g}, \tag{2.8}$$

which was used for modeling flow in chapter 1, equation (1.1). There, we used a finite element method to solve (2.8). This was necessary since we wanted to allow for lateral variations in μ within the mantle and lithospheric plates. If it suffices to treat the viscosity of the mantle as varying only with depth, (2.8) can be solved analytically for a global spherical harmonic expansion of $\mathbf{u}$ and p using the propagator-matrix approach (Hager and O'Connell, 1979, 1981). When viscosity does not vary laterally, the harmonic modes decouple and (2.8) can be converted into a set of coupled ordinary differential equations. We denote the maximum degree (wavelength) of the expansion as $\ell_{\max}$ (for spherical harmonics convention, see sec. 3.4.1). Velocities are prescribed at the surface and a free-slip condition is applied at the core-mantle boundary (see Hager and Clayton, 1989, for additional details). All computations that refer to global flow models in this work were done using a computer program we slightly modified from Steinberger (1996).

The aforementioned method of solving for a simplified version of the mantle flow field will be referred to as the Hager and O'Connell (1981) method or as a *global circulation model* (to be distinguished from fully convective 3-D models like that of Bunge and Grand (2000)). Global circulation models have been successfully applied to the modeling of a number of geophysical observables, such as the geoid (*e.g.* Hager, 1984; Hager *et al.*, 1985; Hager and Clayton, 1989; Thoraval and Richards, 1997; Mitrovica and Forte, 1997; Forte and Mitrovica, 2001), dynamic topography (*e.g.* Lithgow-Bertelloni and Silver, 1998; Panasyuk and Hager, 2000), hotspot tracks (Steinberger, 2000a), slab distributions in the mantle (Steinberger, 2000a), true polar wander (*e.g.* Steinberger and O'Connell, 1997), plate velocities (*e.g.* Ricard and Vigny (1989); Forte *et al.* (1991); Lithgow-Bertelloni and Richards (1995, 1998); Deparis *et al.* (1995) and our chapter 4), and the lithospheric stress field (*e.g.* Bai *et al.*, 1992; Steinberger *et al.*, 2001; Guynn and Lithgow-Bertelloni, 2001; Becker and O'Connell, 2001a). Several of the simplifying assumptions that are needed to solve mantle flow with the Hager and O'Connell (1981) method have been critically evaluated (*e.g.* King *et al.*, 1992; King and Hager, 1994; Richards and Hager, 1989; Panasyuk *et al.*, 1996; Karpychev and Fleitout, 1996) and extensions to such flow models that include improvements such as iterative solution for lateral viscosity variations exist (*e.g.* Zhang and Christensen, 1993; Karpychev and Fleitout, 2000; Čadek and Fleitout, 2000). The major limitation of Hager and O'Connell (1981) type models appears to be the restriction that viscosity can vary only radially. One implication is that no toroidal flow can be generated by internal density anomalies; in particular, no $\ell = 1$ net rotation component of the lithosphere (O'Connell *et al.*, 1991; Ricard *et al.*, 1991) can be generated. To arrive at realistic, plate-like velocity fields we therefore have to either specify the surface plate motions completely or solve for a torque equilibrium for given plate geometries and interactions, as discussed at length in chapter 4.

If we had comprehensive knowledge of the lateral viscosity variations present in nature, a full solution of the convective problem with laterally varying viscosity (*e.g.* Zhang and Christensen, 1993; Čadek and Fleitout, 2000) would clearly be superior to one in which we have to treat each depth layer of the mantle and lithosphere as having a single average effective viscosity. Given the uncertainties that even simple flow models have to cope with (*e.g.* input model density, dealt with in chapter 3) and the poor constraints on lateral rheology contrasts in the upper mantle and lithosphere, it seems reasonable to proceed with a simplified model in order to expand the range of testable observables. Our philosophy will be to construct a flow model that fulfills as many observables as possible and see how well we can explain plate velocities (chapter 4), seismic anisotropy observations (chapter 5), and lithospheric stresses in a next step (Becker and O'Connell, 2001a). We find that flow models do a good job for a variety of datasets, providing a basis on which to build more complex and realistic models in the future.

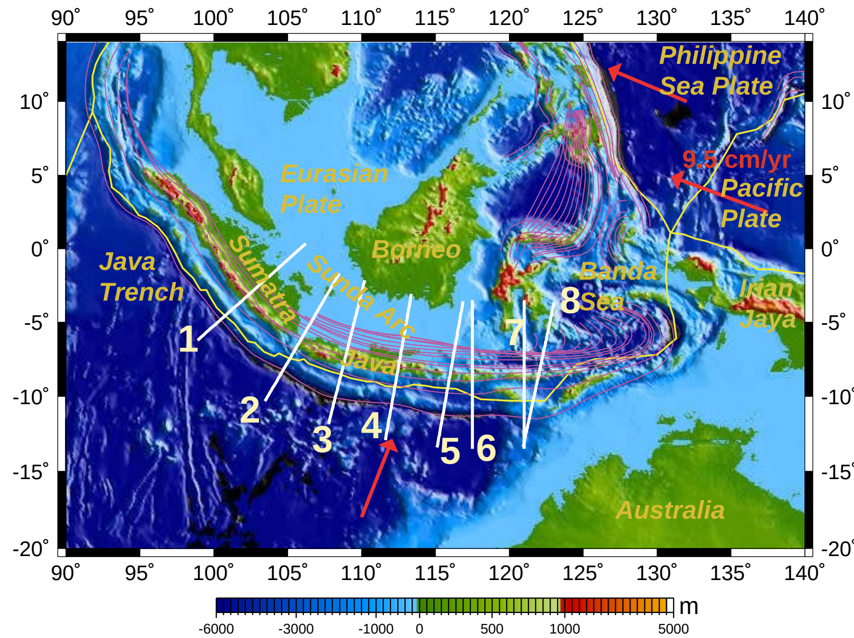

Figure 2.10: Overview map of the Indonesian subduction zone with focus on the Sunda arc; profiles for seismicity and tomography are shown. Vectors indicate NUVEL-1 (DeMets *et al.*, 1990) plate motion with respect to stable Eurasia, see Pacific plate vector for scale. Slab seismicity contours in 50 km intervals from *rum* (Gudmundsson and Sambridge, 1998).

2.3.2 The backward bent Indonesia slab

Our first application of global flow models in this work is the prediction of slab trajectories. Our approach is similar to that of Hager and O'Connell (1978) and Hager *et al.* (1983), who compared the shape of streamlines beneath subduction zones with the Wadati-Benioff zones of varying dip that are traced out by earthquake hypocenters. Hager and O'Connell (1978) concluded that a whole-mantle flow model leads to a better fit to slab trajectories than one in which flow is restricted to the upper mantle. The validity of this approach has been questioned by Garfunkel *et al.* (1986) who pointed out that in the case of trench migration, instantaneous flow lines are not identical to material trajectories. The question of the right reference frame is crucial (*e.g.* Tao and O'Connell, 1992a) but this does not invalidate the whole approach. As long as we perform flow calculations in a trench-fixed reference frame (which might, however, be difficult to establish when geodetic and geologic observations of migration rates are sparse), flow lines and particle trajectories underneath trenches should give us an idea of how slabs might be shaped. Slabs will deform to accommodate the large-scale mantle flow field, which they drive only partly themselves (*e.g.* Tao and O'Connell, 1992a; Olbertz *et al.*, 1997; van Hunen *et al.*, 2000). If global flow models without any lateral stiffness contrasts are able to predict slab shapes, this is another argument for the relative weakness of subducted lithosphere. In the following, we will show that such models are valid and that our flow calculations predict return flow at depth that could be responsible for the observed slab morphology beneath the Indonesian trench.

Observations

Stimulated by our work on the effect of background flow on slabs and in particular by a relocation study by Schöffel and Das (1998), we focus on the Indonesian subduction zone to see whether flow models can predict the backward bending that the slab appears to be undergoing at depth in the central portion of the Sunda arc (Figure 2.10). Along some of the indicated profiles, slices through a tomography model by Widiyantoro and van der Hilst (1996) are shown together with hypocenters from a global (Engdahl *et al.*, 1998) and a local (Schöffel and Das, 1999) relocation study (Figure 2.11). The seismicity contours in the overview map (Figure 2.10) indicate that we should expect considerable complexity of flow at depth since several subduction zones will interact. Other tectonic factors include the arrival of continental material at the trench such that oceanic, dense material that drives subduction is restricted to regions West of $\sim 120^\circ$ in the Sunda arc. The possible tectonic evolution of the region and its consequences for mantle dynamics have been studied by Widiyantoro and van der Hilst (1996, 1997).

As discussed most recently by Schöffel and Das (1998), seismicity in the Sunda Benioff zone (Figure 2.11)

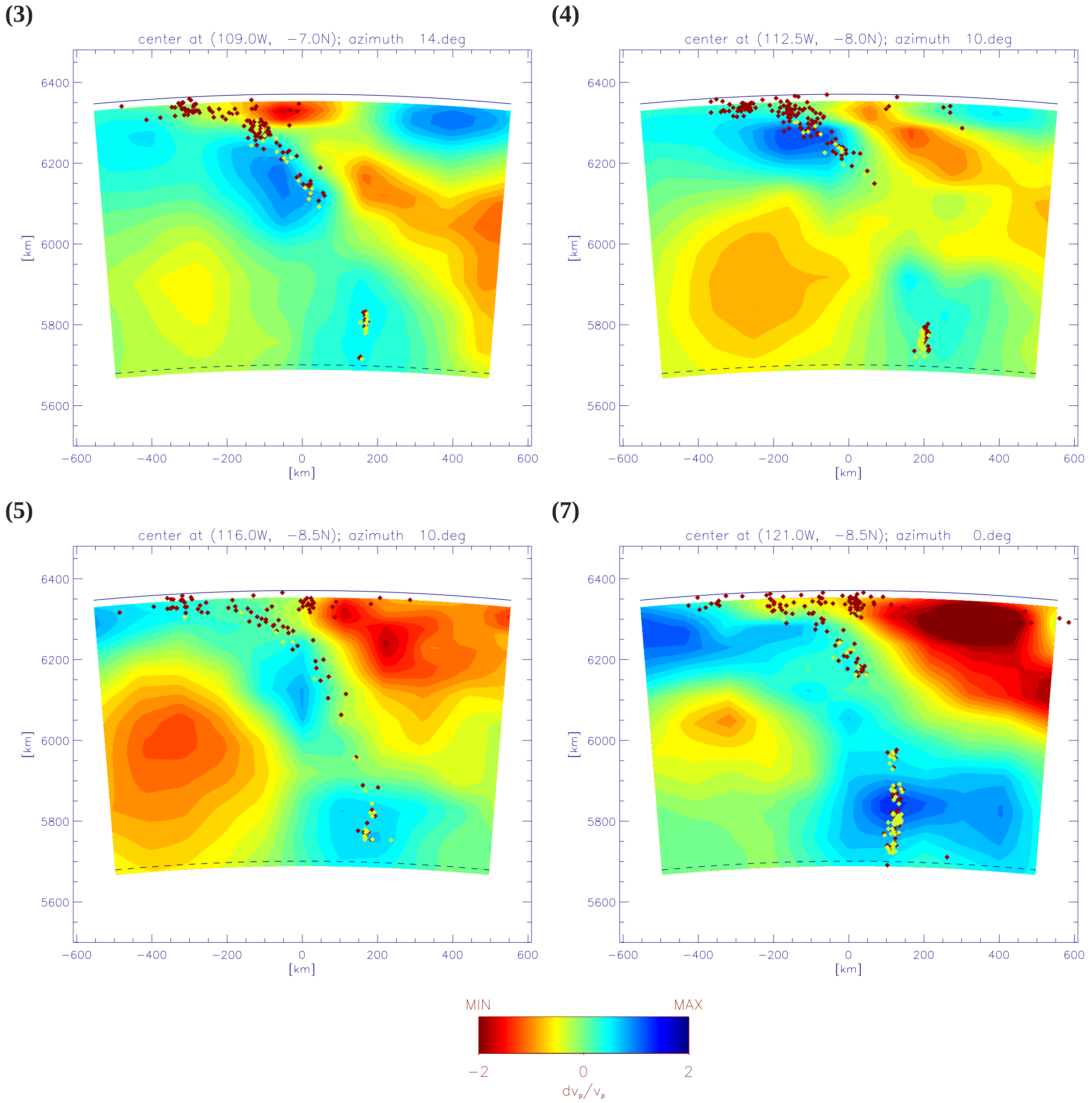

Figure 2.11: Slices through the local *P*-wave tomography model of Widiyantoro and van der Hilst (1996) underneath Indonesia corresponding to profiles 3, 4, 5, and 7 from Figure 2.10. Colorscale given below is relative deviation from ak135 (Kennett *et al.*, 1995) in %. We also show hypocenters within a 50 km range of the slices, dark dots are used for Engdahl *et al.*'s (1998) catalog and bright dots for Schöffel and Das (1999).

indicates a trend in which the slab rolls over, with the tip bent backward to varying degrees along strike. This effect is most pronounced between $\sim$110° and $\sim$ 120°. The easternmost profiles 7 and 8 are probably in a region where the slab starts to flatten out, as can be seen in the corresponding tomographic slice 7. In the examples of the flow profiles shown below, we will therefore focus on the 110° W region, somewhat removed from the other subduction zones in that area and approximately corresponding to profile 4 in Figures 2.10 and 2.11. The deformation of the slab at depth is indicated by moment tensors from the Harvard CMT project (Dziewonski *et al.*, 1981), shown in Figure 2.12, which can be interpreted as measuring the strain rate (Kostrov, 1974). First, the seismicity that is traced out by these large events (the CMT catalog is complete for M $\gtrsim$ 5.4, *e.g.* Ekström, 2000) also indicates the aforementioned backward-bending trend. Second, we can see that the deep moment release takes place mostly by

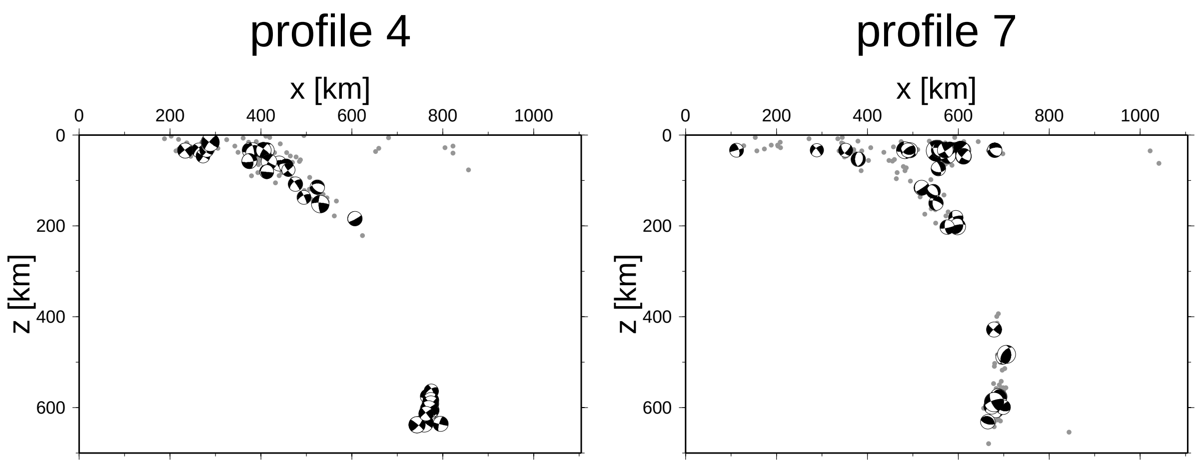

Figure 2.12: Harvard CMT solutions (Dziewonski *et al.*, 1981) as in Figure 2.3 for profiles 4 and 7 from Figure 2.10; we are viewing the eastern hemisphere of the beach balls.

downdip in-plane compression. This is the case for most subduction zones (*e.g.* Isacks and Molnar, 1971), and is an expected result for slab slowdown at 660-km (*e.g.* Vassiliou and Hager (1988) and chapter 1). The focal mechanisms display some complex second-order features that have been interpreted as indicating a slab pileup with significant in-slab deformation (Schöffel and Das, 1999).

Flow predictions

Figure 2.13 shows a slice through a global mantle flow model in which we have prescribed the surface velocities according to NUVEL-1 (DeMets *et al.*, 1990), with Eurasia assumed fixed to approximate a stable-trench reference frame. The radial viscosity structure we have used for the mantle is η_F from sec. 4.5, a best-fit profile from Steinberger (2000b). The spherical harmonic expansion was taken up to $\ell_{\max} = 63$ for computational convenience, corresponding to a resolution (half wavelength) of $\sim$320 km at the surface. We observe a return flow at depths of $\sim$ 700 km that is consistent with the tendency of the slab to fold backward.

To explore the additional effect of density anomalies due to the subducted material itself, we present results from a flow calculation for the upper-mantle slab model *rum* and plate motions (Figure 2.14). Model *rum* is based on assigning a density anomaly of 75 kg/m^3 to each location where Gudmundsson and Sambridge's (1998) RUM model places interpolated seismicity contours. The effective width of the slabs is determined by $\ell_{\max}$ and the $\cos^2$-taper that we apply for $\ell > 0.75\ell_{\max}$ (sec. 3.3.4). Since the flow problem is linear under the assumptions of sec. 2.3.1, the complete solution for flow can be obtained by superposition of the prescribed surface-velocities solution of Figure 2.13 and the flow solution corresponding to that driven only by density anomalies for zero velocities (no-slip) at the surface (see also sec. 4.3.3). Figure 2.14 shows that the flow that includes the effect of slab density exhibits larger downwelling velocities (scale same as in Figure 2.13) and a steeper descent, as would be expected by the Stokes sinker-like flow induced by the negative buoyancy anomalies of the slab material. There is still some tendency for backward flow, although it is not as pronounced as in the case where flow is driven by plate related motion only.

rum is clearly not the only possible model of density distribution in the mantle, and we could explore seismic tomography or subduction history models to determine the variations between models (*cf.* chapter 3). As with all density models of the mantle, there is also some uncertainty as to the scaling between observed and inferred density heterogeneity (sec. 4.4). This implies that the strength of the *rum*-related flow contribution might have to be adjusted. However, since we are only interested in demonstrating the general validity of the explanation that slab morphology in the Sunda arc is caused by large-scale mantle circulation, we will restrict our present investigation to the two flow models described above.

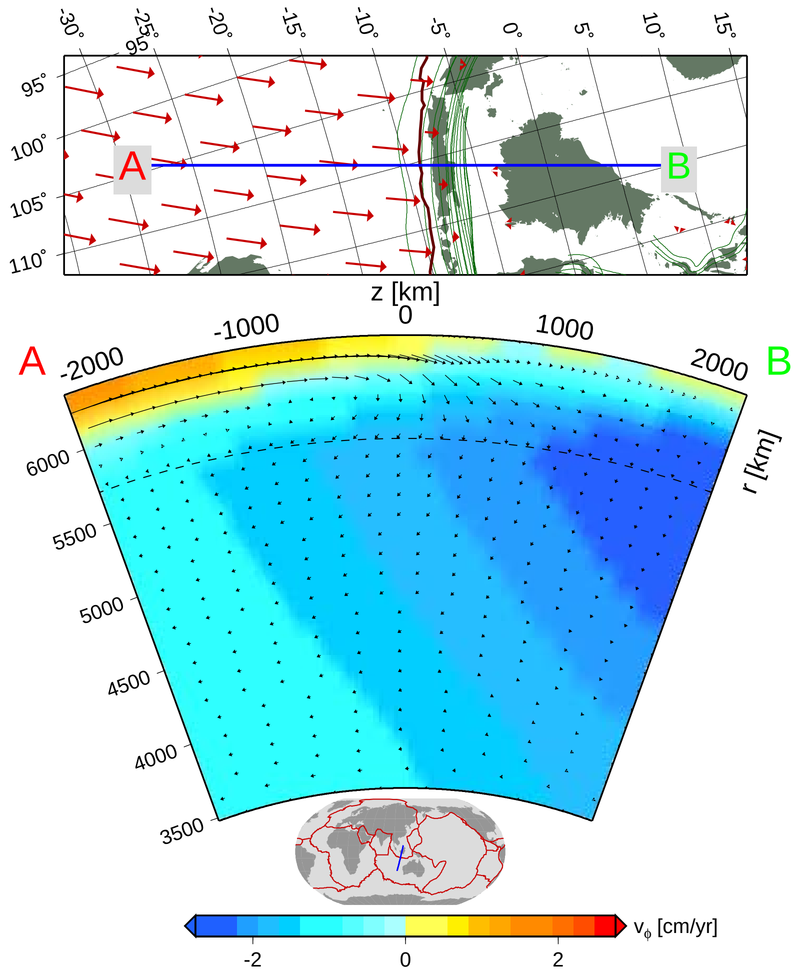

Figure 2.13: Global circulation model predictions for purely plate-motion driven flow. Top: surface velocity field around Borneo (vectors). Contour lines denote slab seismicity from Gudmundsson and Sambridge (1998). The profile marked from A to B is shown in the velocity slice underneath, roughly corresponding to profile 4 from Figure 2.10. Main plot: velocity profile, vectors indicate direction and magnitude of in-plane flow; background shading corresponds to flow into (negative values) and out of (positive values) the plane of the profile. Bottom: global overview map indicating location of the profile. All velocities are in an Eurasia-fixed reference frame.

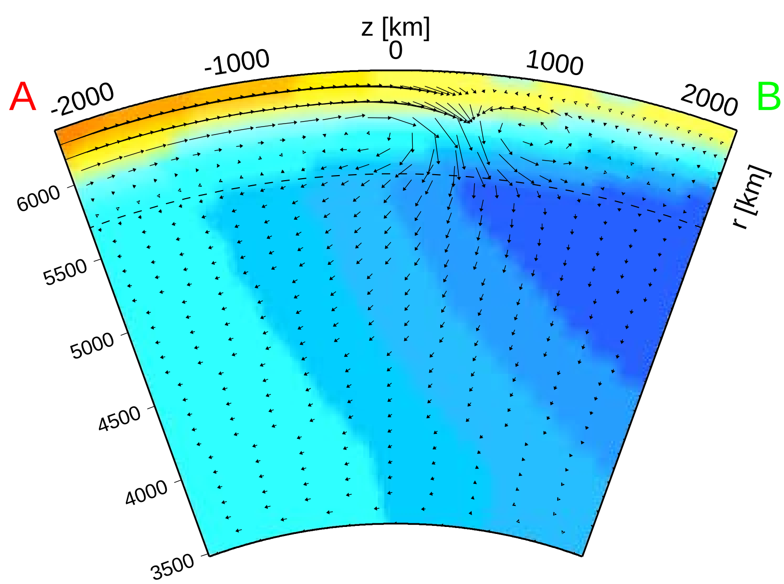

Figure 2.14: Global circulation model predictions for plate motions plus slab density (*rum* model) driven flow, profile and vector scale identical to Figure 2.13.

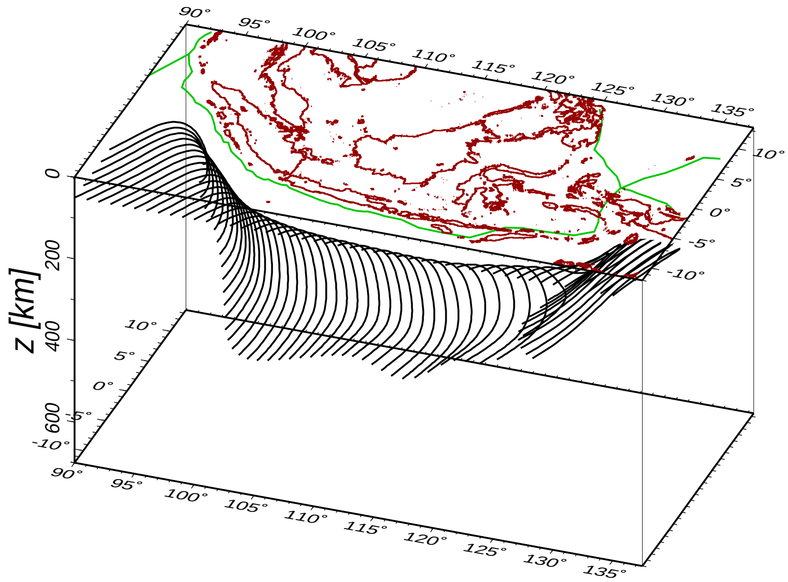

Figure 2.15: Particle trajectories for tracers in a plate-motion only flow field, advected for 60 Myr. Note that the distance tracers move horizontally before entering the trench varies such that final depths reflect both the effects of complex flow and initial position.

Material trajectories

What are the actual material trajectories for the Australian plate material during the descent of the slab in the 3-D flow field underneath Indonesia? To address this question, we trace particles in the velocity fields from above which are assumed to be in a steady-state, *i.e.* not changing significantly over the period over which we integrate the flow. If this condition holds approximately, and slabs are not much stiffer than the surrounding mantle, such predicted particle tracks should resemble the observed Wadati-Benioff zone geometry.

To integrate the path of a passive tracer numerically we use a 4th-order, adaptive stepsize Runge-Kutta scheme (*e.g.* Press *et al.*, 1993, p. 710), described in sec. 5.4.1. Figure 2.15 shows the material lines corresponding to the particle paths of a tracer distribution that was placed in the Indo-Australian plate at 50 km depth. The flow field is that of Figure 2.13 and includes plate motion driven circulation only. Figure 2.15 demonstrates that the downwellings at subduction zones to the northwest of Indonesia lead to a southward flow component that distorts the downwelling in the Sunda arc as already indicated in the profile of Figure 2.13. We also see that particle trajectories can be quite complex, even for flow that is driven only by plate motions.

For the flow underneath Indonesia, therefore, we find the backward tendency of flow confirmed for actual particle paths. The effective downward velocity of oceanic plate tracers is quite small for the plate-motions only model, and some tracers have not reached 660-km even after 60 Myr of advection. If we include the effect of slab density as derived from *rum* (Figure 2.16), we find, as expected, that the predicted slab trajectories are more vertical and the rate of subduction has been enhanced. However, we confirm that the slab should be expected to be almost vertical at mid-depth and then turn over toward the south below $\sim$550 km.

There are several shortcomings of these simple models, most importantly the assumption that the flow is steady-state. We should eventually include paleo plate-motions and also advect density anomalies (*e.g.* Steinberger, 2000b) to improve the realism. We will use such an enhanced model in our more extensive comparison of flow-model derived strains and anisotropy in chapter 5. However, we have seen that the observed Wadati-Benioff zone geometry underneath Indonesia is possibly related to large scale-fluid flow that deforms a weak slab. A more thorough, global re-investigation of the correlation between circulation-model predictions and observations of subduction zone geometries is beyond the scope of this work.

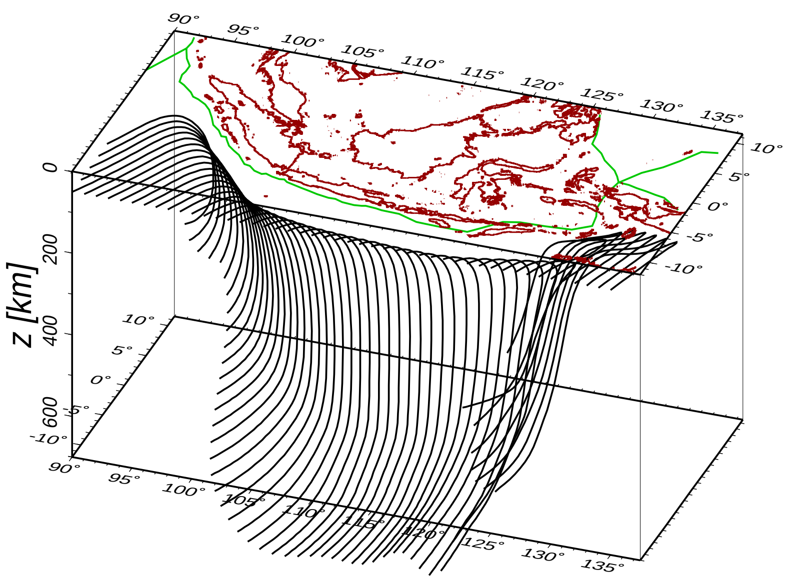

Figure 2.16: Particle trajectories for plate motion and effect of *rum* slab anomalies; tracers are advected for 60 Myr.

Chapter 3

A comparison of tomographic and geodynamic mantle models

After discussing the regional dynamic interactions between mantle convection and lithospheric deformation in subduction zones for fluid dynamical models (chapter 1) and a number of examples from nature (chapter 2), we will now move toward a global model of lithospheric deformation. The key ingredient for the mantle convection part of such a model will be a 3-D circulation calculation (sec. 2.3.1). While plate-related flow in the mantle can be estimated from the present-day plate velocities at the surface, density-driven motion at depth must be inferred by more indirect means. Mantle density models have been based on seismic tomography (*e.g.* Hager *et al.*, 1985; Mitrovica and Forte, 1997; Forte and Mitrovica, 2001), present-day seismically active slabs (*e.g.* Hager, 1984), or aseismic, reconstructed subduction zone distributions (*e.g.* Ricard *et al.*, 1993; Lithgow-Bertelloni and Richards, 1995; Steinberger, 2000b). It is therefore important to study carefully the similarities and differences between these various input models in order to understand the robustness of the model predictions that are inferred from them.

3.1 Abstract

We conduct a comprehensive and quantitative analysis of similarities and differences between recent seismic tomography models of the Earth's mantle in an attempt to determine a benchmark for geodynamic interpretation. After a spherical harmonic expansion, we find the spectral power and radial correlation of each tomographic model as a function of depth and harmonic degree. We then calculate the correlation, at the same depths and degrees, between all possible pairs of models, to identify stable and model-dependent features (the former being usually of longer spatial wavelength than the latter). We can therefore evaluate the degree of robust structure that seismologists have mapped so far and proceed to calculate *ad hoc* mean reference models. These insights will guide us later in our plate driving force inversions and finite-strain calculations.

Tomographic models are furthermore compared with two geodynamic subduction models that are based on plate motion reconstructions. We find systematically low intermediate-wavelength correlation between tomography and convective reconstruction models and suggest that inadequate treatment of the details of slab advection is responsible. However, we confirm the presence of stable, slab-like fast anomalies in the mid-mantle whose geographic pattern naturally associates them with subduction. This finding –in addition to our analysis of heterogeneity spectra and the absence of strong minima in the radial correlation functions besides the one at $\sim$ 700 km– supports the idea of whole mantle convection with slab penetration through the 660-km phase transition, possibly accompanied by a reorganization of flow.

The work presented in this chapter was done in collaboration with Lapo Boschi (Harvard University) and has been published previously in modified form in *Geochemistry, Geophysics, Geosystems* (Becker and Boschi, 2002) with additional online material at http://www.geophysics.harvard.edu/geodyn/tomography.

3.2 Introduction

Over the last two decades, numerous tomographic models of the Earth's interior have been derived from different types of seismological measurements and with different techniques (*e.g.* Dziewonski *et al.*, 1977; Masters *et al.*, 1982; Woodhouse and Dziewonski, 1984; Dziewonski, 1984; Inoue *et al.*, 1990; van der Hilst *et al.*, 1997). "Seismic tomography" denotes the result of inversions for the three-dimensional (3-D) wave speed anomalies in the Earth's mantle that lead to traveltime anomalies when compared with those predicted from 1-D reference models such as PREM (Dziewonski and Anderson, 1981). Methods and results of this CAT-scan like approach have been reviewed in a number of articles (*e.g.* Ritzwoller and Lavely, 1995; Dziewonski, 2000) and Boschi and Dziewonski (1999) give a brief account of the more technical aspects of the inversion procedures. Tomographic models can be seen as snapshots of the convecting mantle, thereby providing important constraints on the planet's dynamics (*e.g.* Hager *et al.*, 1985; Mitrovica and Forte, 1997). Here, we conduct a comparison between global 3-D mantle models, derived from seismological data, and theoretical geodynamic models. In order to proceed from mapping heterogeneity to testing geologically relevant hypotheses, such an undertaking is needed for a number of reasons:

1. Discrepancies between tomographic models often arise from differences in the modeling procedure (*e.g.* Boschi and Dziewonski, 1999). In particular, the choice of basis functions for the parameterization of the 3-D mantle anomalies (blocks, splines, or spherical harmonics are typically used) is important and each selection has its caveats. Directly related is the issue of damping since either total model size (norm damping) or smoothness (gradient damping) or both have to be constrained for an overdetermined system of equations with imperfect data (*e.g.* Parker, 1994). Using a systematic computation of the correlation between different models we attempt to distinguish stable features from those that depend on data selection and technical choices.
2. 3-D models of compressional (*P*) and shear (*S*) wave velocity in the Earth's mantle are derived from independent observations. The existence of a correlation between *P* and *S*-velocity anomalies might mean that they have a common origin, generally believed to be thermal and associated with mantle convection; on the other hand, where uncorrelated *P* and *S*-velocity heterogeneities are found, compositional heterogeneity can be invoked (*e.g.* Su and Dziewonski, 1997; Kennett *et al.*, 1998). It is therefore important to specifically measure the correlation between *P* and *S*-models.
3. Several authors have attempted to reconstruct the convective flow of the mantle (*e.g.* Ricard *et al.*, 1993; Lithgow-Bertelloni and Richards, 1995, 1998; Bunge *et al.*, 1998; Bunge and Grand, 2000; Steinberger, 2000a,b), and their results have been used to explain the current pattern of seismic heterogeneities. However, there is still some controversy on this subject; debated issues include the extent to which the phase transition at 660 km represents a barrier to mantle flow (*e.g.* Christensen, 1996; van der Hilst *et al.*, 1997; Puster and Jordan, 1997), and whether a layer or other large scale structure exists in the deep mantle (*e.g.* van der Hilst and Kárason, 1999; Kellogg *et al.*, 1999; Becker *et al.*, 1999b; Tackley, 2000). To contribute to this discussion, we carry out a quantitative comparison of seismological versus geodynamic results with the same algorithm used to find the correlation between tomographic models.

More than any previous comparative interpretation of global tomography (*e.g.* Grand *et al.*, 1997; Masters *et al.*, 1999) and geodynamics (*e.g.* Lithgow-Bertelloni and Richards, 1998; Bunge *et al.*, 1998), our study includes a comprehensive, consistent, and quantitative analysis of all recently published models, allowing the reader to make an informed choice as to which features and geodynamic inferences can be considered robust.

We follow Masters *et al.* (1999) and choose to measure the similarity between models in terms of the linear correlation between their spherical harmonic expansions. Only with a spectral analysis are we able to identify wavelength-dependent features and detect changes in the character of the spectrum of imaged heterogeneity (sec. 3.5.1). Our global measure of correlation suffers from certain drawbacks (*e.g.* Ray and Anderson, 1994), especially when narrow signals such as subducting slabs are studied. Wavelets might be better able to detect local features (*e.g.* Bergeron *et al.*, 2000); in sec. 3.5.4 we circumvent these problems with an additional spatial domain analysis.

We find that the correlation between modern global tomographic models is high at long wavelengths, even when *P* and *S*-wave models are compared with each other; in particular, slab-like structures extending below the 660-km phase transition are a stable feature of all models, and no other radial discontinuity is required at larger depths. Tomographic models are less similar at shorter wavelengths, and on a global intermediate-wavelength scale, do not yet correlate well with the slab signal of geodynamic models.

3.3 Models

Following is a brief description of all the models we study. Their abbreviated names, by which they are referred to hereafter, are given in italic font.

3.3.1 *P*-wave tomography

hwe97p: MIT model parameterized in terms of $2^\circ \times 2^\circ$ blocks of variable radial extent (van der Hilst *et al.*, 1997). *hwe97p* is undefined in areas where the data coverage was considered inadequate ("gaps").

kh00p: Derived similarly to *hwe97p* but a coarser parameterization ($3^\circ \times 3^\circ$ blocks) and additional travel time data (from core phases) has led to a model that is defined everywhere in the mantle (Kárason and van der Hilst, 2001).

bdp98: Harvard equal area block model BDP98 ($5^\circ \times 5^\circ$ at the equator, constant radial extent of ~ 200 km) (Boschi and Dziewonski, 1999).

bdp00: Unpublished improvement of *bdp98* based on further relocation efforts (see Antolik *et al.*, 2001).

All *P*-wave models are based on body-wave travel-time measurements collected by the International Seismological Centre (ISC). ISC data can be improved by source relocation; this has been done by both the Harvard group (Su and Dziewonski, 1997), and with a different method by Engdahl *et al.* (1998). Both MIT models were derived from Engdahl *et al.*'s (1998) data set.

3.3.2 *S*-wave tomography

Love and Rayleigh waves are mostly sensitive to anomalies in horizontally and vertically polarized shear velocity, v_{SH} and v_{SV} respectively, and only marginally affected by perturbations in *P*-velocity, v_P (*e.g.* Anderson and Dziewonski, 1982). Observations of surface waves are, therefore, usually taken into account in deriving *S*-models, while v_P heterogeneities are only constrained by the travel times of body waves whose ray geometry is generally nearly vertical within the upper mantle. As a result, the data coverage for v_S in the upper mantle is much more uniform than for v_P.

grand: equal-area block model as of Grand's ftp-site in fall 2000 (see Grand *et al.*, 1997), distributed on a $2^\circ \times 2^\circ$ grid. The model was derived from a combination of body and surface wave measurements with a two step process (Grand, 1994): first, observations are explained in terms of upper- and lower-most mantle structure only. Second, the authors invert the residual travel-time anomalies to find velocity heterogeneities in the rest of the mantle.

ngrand: Updated version of *grand*, as of Grand's ftp-site in June 2001. The inversion that led to *ngrand* was damped more strongly in the upper mantle than that of *grand* (S. Grand, pers. comm.); as a result, the new model is different from *grand* mostly in amplitude, rather than pattern, of heterogeneity (sec. 3.5.1).

s20rts: Caltech model S20RTS, parameterized horizontally in terms of spherical harmonics up to degree $\ell_{\max} = 20$, and radially with a set of cubic splines (Ritsema and van Heijst, 2000). Derived from a data set that, in addition to body and Rayleigh wave measurements, includes observations of normal mode splitting functions.

saw24b16: Berkeley v_{SH} model SAW24B16 (Mégnin and Romanowicz, 2000), derived by fitting body and surface wave transverse-component waveforms. Parameterized with spherical harmonics ($\ell_{\max} = 24$) and cubic splines.

sb4l18: Scripps model SB4L18, from observations of body, Love, and Rayleigh waves, and normal modes (Masters *et al.*, 1999). Parameterized in terms of equal-area blocks ($4^\circ \times 4^\circ$ at the equator) with 18 radial layers.

s20a: Harvard model S20A from observations of body, Love, and Rayleigh waves (Ekström and Dziewonski, 1998). v_{SH} and v_{SV} anomalies were treated as independent free parameters; δv_S is subsequently estimated from the Voigt-averaged *S* velocity (see Figure A.6). Spherical harmonics ($\ell_{\max} = 20$) horizontally; radially, upper and lower mantle are parameterized separately with two sets of Chebyshev polynomials.

s362d1: Harvard model S362D1, derived with a procedure analogous to *s20a* (including the discontinuity at 670 km) but described by a spline parameterization both horizontally and vertically (Gu *et al.*, 2001). Lateral resolution is equivalent to $\ell_{\max} \sim 18$.

In addition, we will also use lower resolution joint inversions for v_S and v_P in sec. 3.5.2. We consider MK12WM13 (Su and Dziewonski, 1997) (spherical harmonics, $\ell_{\max} = 12$, Chebyshev polynomials with depth, v_P and v_S anomalies denoted by *mk12wm13p* and *mk12wm13s*, respectively), SB10L18 by Masters *et al.* (2000) (similar to *sb4l18* but $10^\circ \times 10^\circ$ blocks, *pb10l18* and *sb10l18*), and Harvard model SPRD6 from normal mode splitting coefficients (Ishii and Tromp, 2001) (spherical harmonics, $\ell_{\max} = 6$, *sprd6p* and *sprd6s*).

3.3.3 Mean tomography models

While most tomographic models present significant discrepancies, they agree on certain, long-wavelength patterns. Efforts to define a 3-D reference Earth model from an inversion of geophysical observables are currently under way (see *e.g.* the Reference Earth Model (REM) web site, http://mahi.ucsd.edu/Gabi/rem.html). A REM would be a starting point for higher resolution models and provide the much needed benchmark to evaluate geodynamic hypotheses. Here, we adopt a pragmatic approach and calculate two mean models by taking a weighted average of several models, assuming that such "stacking" will amplify consistent features. The result is a largest common denominator model which we intend to update as tomographic research progresses.

pmean: Our mean *P*-wave model based on *bdp00* and *kh00p*.

smean: Our mean *S*-wave model, based on *ngrand*, *s20rts*, and *sb4l18*.

smean and *pmean* have been calculated by a weighted average of well correlated *S*-models with similar input data (*ngrand*, *s20rts* and *sb4l18*) and the newer *P*-wave models (*bdp00* and *kh00p*), respectively. We first determine depth averaged δv_{RMS} for each input model, and then scale the models such that they would lead to a mean model with a depth averaged δv_{RMS} that corresponds to the mean δv_{RMS} of all input models. This procedure maintains the depth-dependence of δv_{RMS} for each model but evens out total heterogeneity amplitude differences between models. (We have experimented with additional, ℓ-dependent average-correlation weighted models, results were not much different.) The spatial expansion of the resulting mean models is shown at selected depths in Figure 3.1 (for the spectral and δv_{RMS} character, see Figures 3.5 and 3.6).

3.3.4 Geodynamic models

We compare the velocity models with an upper mantle slab model, two models that account for inferred past subduction, and –in a statistical sense– with a thermal convection calculation.

rum: Our spherical harmonic expansion of slabs in the upper mantle obtained from the RUM seismicity contours (Gudmundsson and Sambridge, 1998) which are in turn based on the Engdahl *et al.* (1998) catalog. We integrate along the RUM contours at each layer using them as δ-functions such that the effective width of the slabs is determined by $\ell_{\max}$ and the $\cos^2$-taper that we apply for $\ell > 0.75\ell_{\max}$.

lrr98d: Density model by Lithgow-Bertelloni and Richards (1998) on spherical harmonics laterally ($\ell_{\max} = 25$) and layers with depth. *lrr98d* is based on "slablets", *i.e.* negative buoyancy anomalies, that sink at different speeds in the upper and lower mantle after starting at estimated past trench locations which are based on Mesozoic and Cenozoic plate reconstructions (Lithgow-Bertelloni *et al.*, 1993; Ricard *et al.*, 1993). The sinking rate was adjusted to fit geopotential fields, tomography, and plate motions.

stb00d: Density model by Steinberger (2000b) on spherical harmonics ($\ell_{\max} = 31$) and radial layers. *stb00d* is also based on past plate motions and subduction; Lithgow-Bertelloni *et al.*'s (1993) sets of plate boundaries were, however, interpolated at 2 Ma intervals while Lithgow-Bertelloni and Richards (1998) held boundaries fixed during individual plate-tectonic stages. *stb00d* is furthermore different from *lrr98d* in that it allows for lateral advection of slablets once they are below 380 km due to the flow that is generated by plate motion and slab buoyancy. *stb00d* can be considered more realistic than *lrr98d* with respect to the treatment of convective flow.

zmg00t: Temperature snapshot from a 3-D spherical convection calculation by Zhong *et al.* (2000); we use the non-adiabatic temperature variations from their case 7 at time $9.25 \cdot 10^{-4}$. Case 7 is an incompressible,

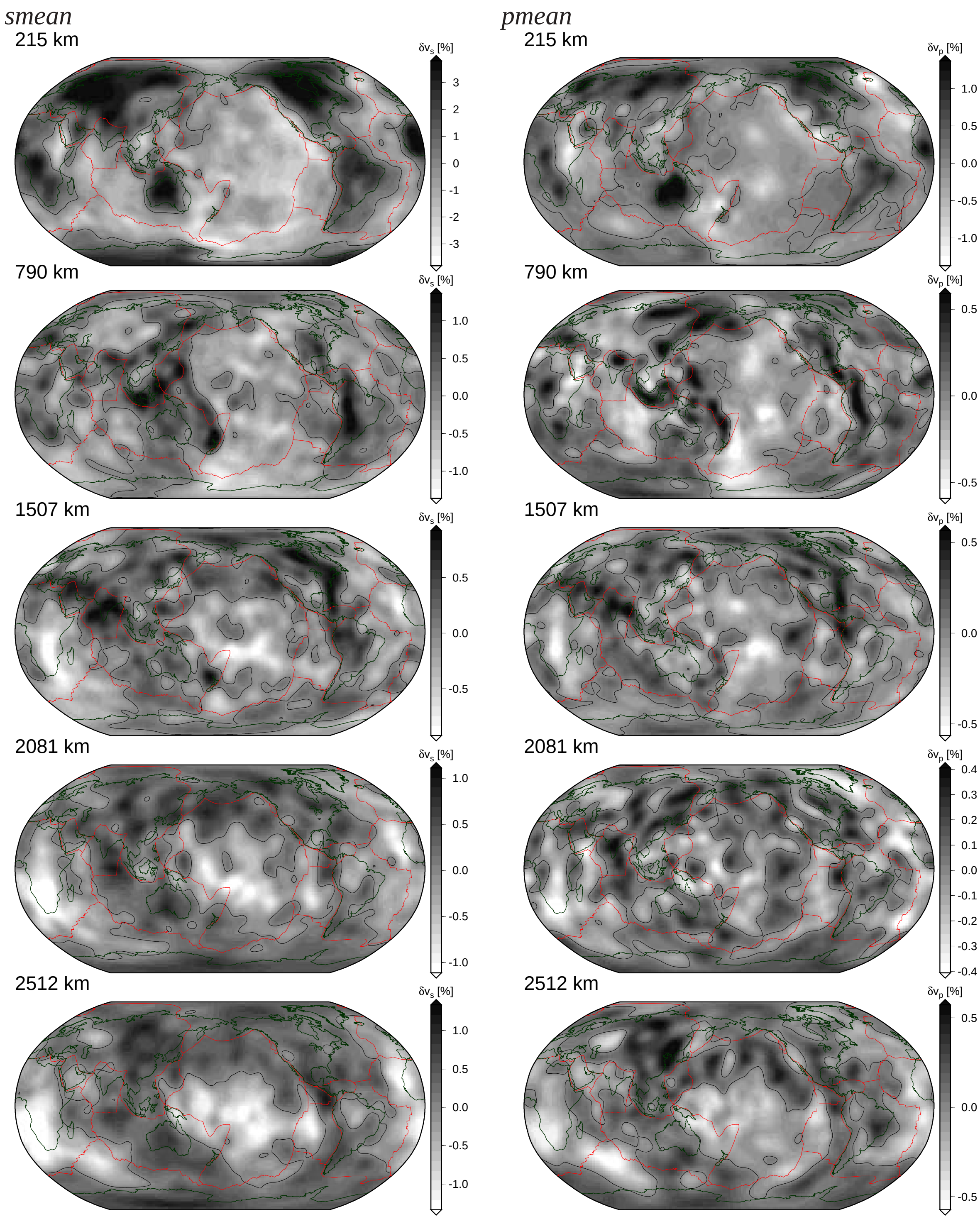

Figure 3.1: Maps of *smean* (δv_S, left) and *pmean* (δv_P, right) at the indicated depths ($\ell_{\max} = 31$), Pacific-centered Robinson projection. We trace out the zero anomaly contour.

temperature and depth-dependent viscosity calculation without phase transitions that allowed for plate-like flow through the inclusion of fixed weak zones (plates 2a and b of Zhong *et al.*, 2000). Assuming constant thermal expansivity, α, variations in non-dimensional temperature, $\overline{T}$, relate to density, ρ, as

$d\ln\rho = -\alpha\Delta T\ d\overline{T}$. With $\Delta T = 1800°$ K for the non-adiabatic mantle gradient and $\alpha = 1.4\cdot 10^{-5}$ K^{-1}, we scale with $\alpha\Delta T \approx 0.025$.

Current and past plate motions are some of the best indicators for the style of convective flow in the mantle. The derived slab sinker trajectories and density distributions of models such as *stb00d* should thus be amongst the best constrained geodynamic models. However, given the discrepancies that we observe between *lrr98d* and *stb00d* (sec. 3.5.4), we will not attempt to explore thermal convection models (*e.g.* Tackley, 1996; Bunge *et al.*, 1998; Zhong *et al.*, 2000) in greater detail at this point but only complement power spectra of tomography with one representative pattern from *zmg00t* (sec. 3.5.1).

3.4 Measuring model structure and similarity

Before carrying out any comparisons, we must find a consistent description. As tomographic models are expressed with respect to different 1-D reference profiles, we first scale heterogeneity to relative deviations from PREM, and define

$$\delta v_{P,S} = d\ln v_{P,S} = \frac{dv_{P,S}}{v_{P,S}}. \tag{3.1}$$

We then evaluate each model at a discrete set of depths z_i ($i = 1,2,\dots N$); at each z_i, we find the coefficients of a spherical harmonic expansion of the model –as a function of θ and ϕ– up to degree $\ell_{\max} = 31$ (see below). We set to zero all the $\ell = 0$ coefficients, corresponding to the constant offset from PREM at each depth. Correlation is usually computed for each harmonic degree up to $\ell = 20$, which is the nominal resolution limit of most long wavelength models (corresponding to a half wavelength of ~ 1000 km at the surface).

3.4.1 Spherical harmonic expansion

Using unity-norm real spherical harmonics (*e.g.* Dahlen and Tromp, 1998, B.8) we approximate any given field $\delta v(\theta,\phi)$ of velocity or density anomalies at a given depth with its expansion up to $\ell_{\max}$,

$$\delta v(\theta,\phi) \approx \sum_{\ell=0}^{\ell_{\max}} \left[a_{\ell 0} X_{\ell 0}(\theta) + \sqrt{2} \sum_{m=1}^{\ell} X_{\ell m}(\theta) \left(a_{\ell m} \cos m\phi + b_{\ell m} \sin m\phi \right) \right], \tag{3.2}$$

where $X_{\ell m}$ are the normalized associated Legendre functions

$$X_{\ell m}(\theta) = (-1)^m \left(\frac{2\ell+1}{4\pi} \right)^{\frac{1}{2}} \left[\frac{(\ell-m)!}{(\ell+m)!} \right]^{\frac{1}{2}} P_{\ell m}(\cos\theta) \tag{3.3}$$

with

$$P_{\ell m}(\mu) = \frac{1}{2^{\ell}\ell!} \left(1-\mu^2\right)^{\frac{m}{2}} \left(\frac{d}{d\mu} \right)^{\ell+m} \left(\mu^2-1\right)^{\ell}. \tag{3.4}$$

The set of coefficients $\{a_{\ell m}, b_{\ell m}\}$ is found by

$$a_{\ell 0} = \int_\Omega d\Omega\, X_{\ell 0}(\theta)\delta v(\theta,\phi) \quad \text{for} \quad m = 0 \quad \text{and} \tag{3.5}$$

$$\begin{pmatrix} a_{\ell m} \\ b_{\ell m} \end{pmatrix} = \sqrt{2}\int_\Omega d\Omega \left(X_{\ell m}(\theta) \begin{matrix} \cos m\phi \\ \sin m\phi \end{matrix} \right) \delta v(\theta,\phi) \quad \text{for} \quad 1 \le m \le \ell, \tag{3.6}$$

where $\int_\Omega d\Omega$ indicates integration over the unit sphere. Our experiments with different numerical integration methods and smoothly interpolated grids with spacings between $0.5°$ and $2°$ indicate that the spurious power which is introduced by the expansion of block models should be smaller than $\sim 2.5\%$ for degrees $\ell \le 20$.

Some tomography models are undefined in areas where the ray coverage was considered inadequate. The effect of these gaps is most extreme for *hwe97p*, where the areal coverage varies between $\sim 40\%$ at the surface and $\sim 95\%$ at the core mantle boundary (CMB). Since the size of gaps can be large, we set the velocity perturbations to zero in those regions before computing (3.5) and (3.6). This choice has the same effect as the imposition of a strong norm-minimization constraint in a least squares fit of $\{a_{\ell m}, b_{\ell m}\}$ (*i.e.* underestimation of RMS heterogeneity). While this approach is not ideal, we think that a more elaborate treatment is unnecessary since the gap-less *kh00p* has replaced *hwe97p*, and we will not base any of our conclusions upon *hwe97p*. Gaps in *grand* and *ngrand* occupy a fraction smaller than 1.1% and 0.3% at all depths, respectively; in these cases we have interpolated using the "surface" algorithm (Wessel and Smith, 1991) before expanding the fields.

3.4.2 Power as a function of wavelength

We define the spectral power of the field $\delta v(\theta,\phi)$ per degree ℓ and unit area as (*e.g.* Dahlen and Tromp, 1998, B.8):

$$\sigma_\ell^2 = \frac{1}{2\ell+1}\sum_{m=0}^{\ell}\left(a_{\ell m}^2 + b_{\ell m}^2\right), \tag{3.7}$$

such that a δ-function results in a flat spectrum (depth dependence will be assumed implicitly). The root-mean-square (RMS) power of the expansion is then:

$$\delta v_{\mathrm{RMS}} \approx \frac{1}{\sqrt{4\pi}}\sigma_{\mathrm{RMS}} = \sqrt{\frac{1}{4\pi}\sum_{\ell=1}^{\ell_{\max}}(2\ell+1)\sigma_\ell^2} \tag{3.8}$$

since

$$\int_\Omega [\delta v(\theta,\phi)]^2\, d\Omega = \sum_{\ell=0}^{\infty}\sum_{m=0}^{\ell}\left(a_{\ell m}^2 + b_{\ell m}^2\right). \tag{3.9}$$

We note that other definitions of spectral power can be found in the literature (*e.g.* Su and Dziewonski, 1991); our choice (normalization by $2\ell+1$ in eq. 3.7) emphasizes the wavelength dependence of heterogeneity.

3.4.3 Cross-model correlation

To evaluate the similarity of any two models at a given depth, we find the correlation r^ℓ between the spherical harmonic expansions $\{a_{\ell m}, b_{\ell m}\}$ and $\{c_{\ell m}, d_{\ell m}\}$ of the corresponding fields at each wavelength ℓ,

$$r^\ell = \frac{\sum_{m=0}^{\ell}\left(a_{\ell m}c_{\ell m} + b_{\ell m}d_{\ell m}\right)}{\sqrt{\sum_{m=0}^{\ell}\left(a_{\ell m}^2 + b_{\ell m}^2\right)}\sqrt{\sum_{m=0}^{\ell}\left(c_{\ell m}^2 + d_{\ell m}^2\right)}}. \tag{3.10}$$

The total correlation up to $\ell_{\max}$ is given by

$$r_{\ell_{\max}}^{\mathrm{tot}} = \frac{\sum_{\ell=1}^{\ell_{\max}}\sum_{m=0}^{\ell}\left(a_{\ell m}c_{\ell m} + b_{\ell m}d_{\ell m}\right)}{\sigma_{\mathrm{RMS}}^{\{a_{\ell m},b_{\ell m}\}}\,\sigma_{\mathrm{RMS}}^{\{c_{\ell m},d_{\ell m}\}}}, \tag{3.11}$$

where $\sigma_{\mathrm{RMS}}^{\{a_{\ell m},b_{\ell m}\}}$ and $\sigma_{\mathrm{RMS}}^{\{c_{\ell m},d_{\ell m}\}}$ denote the RMS sums for each model. Figure 3.2 shows a comparison of the normal, grid based (*e.g.* Press *et al.*, 1993, p. 636) and the spherical harmonics based estimates of total correlation between *bdp00* and *kh00p* as a function of depth. The area weighted, discrete data estimate is based on an expansion of the $\ell_{\max} = 31$ representation of both fields on $1.4^\circ \times 1.4^\circ$ blocks, and the spherical harmonics estimate is r_{31}, after (3.11). Both methods yield similar results in general, and we find no systematic deviations with depth. We have also included a r_{31}-correlation estimate that is based on a $k_{\max} = 20$ radial Chebyshev re-parameterization (sec. 3.4.4); features are similar but the curve is smoother, as expected.

After applying (3.10) and (3.11) to find the correlation between every combination of two models at M evenly spaced z_j where the models have been interpolated, we take the weighted average ($0 \le z_j \le 2871$ km):

$$\langle r_{\ell_{\max}}\rangle = \frac{\sum_{j=1}^{M} w_j r_{\ell_{\max}}^{\mathrm{tot}}(z_j)}{\sum_{j=1}^{M} w_j} \quad \text{with} \quad w_j = (a - z_j)^2, \tag{3.12}$$

where a is the Earth's radius; each layer enters the average according to its volume. While $\langle r\rangle$ is thus biased by

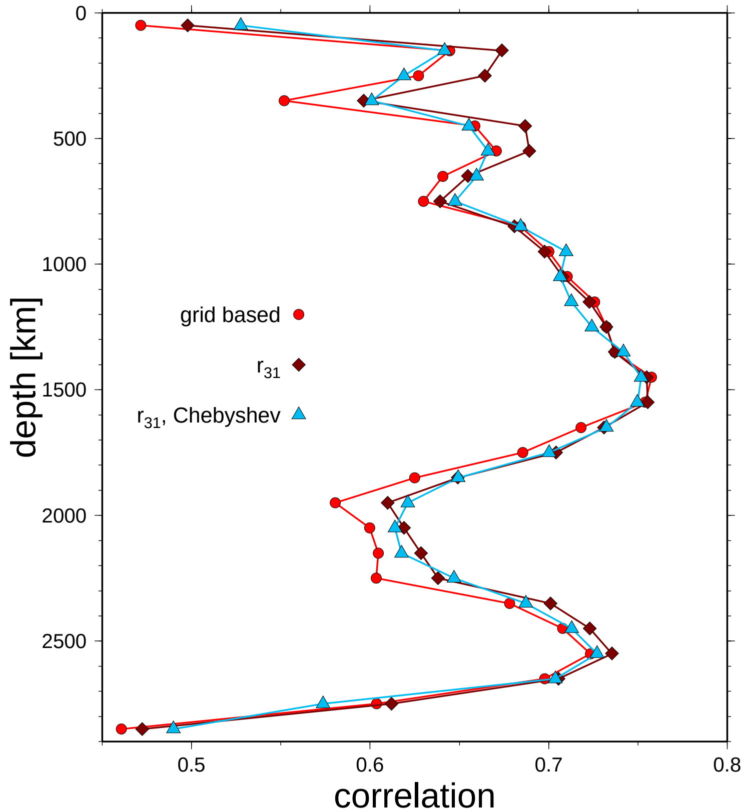

Figure 3.2: Comparison of total correlations between *bdp00* and *kh00p* based on grids (circles); with spherical harmonics, r_{31} (after eq. 3.11, diamonds); and spherical harmonics based on a $k_{\max} = 20$ Chebyshev re-parameterization (triangles, see sec. 3.4.4).

shallow structure, our approach seems appropriate for a global measure of similarity and we find that cross-model $\langle r \rangle$ does not depend strongly on this weighting.

Eqs. (3.10) – (3.12) are estimates of the similarity of two models in terms of global heterogeneity patterns; differences in amplitude do not affect r^{ℓ} or $r^{\text{tot}}_{\ell_{\max}}$. We find and compare r^{tot}_{8} and r^{tot}_{20} to evaluate separately the correlation between the long and intermediate spatial wavelength components of the models. Assuming a binormal distribution for the deviations from a linear trend, we can apply Student's t-test (Press *et al.*, 1993, p. 637) to evaluate the likelihood, P, that a correlation r between two sets of coefficients is caused by chance. The number of degrees of freedom is $(\ell_{\max}+1)^2 - 3$; for $\ell_{\max} = 20$ and $\ell_{\max} = 8$ the 99% significance levels ($p = 0.01$) for r are then given by 0.123 and 0.286, respectively. Most of the r values we find are therefore "significant" at the 99%-level, although care should be taken when interpreting such statements (*e.g.* Ray and Anderson, 1994).

3.4.4 Radial parameterization

We generally attempt to remain close to the original radial parameterization of all models: if models were described in terms of discrete layers, we first evaluate them at the original mid-layer depths, z_i. Likewise, we evaluate spline models at, roughly, the original spline knots and models that are parameterized with Chebyshev polynomials at constantly spaced ($\sim$ 150 km) intervals. Subsequently, if the value of the model is needed at any other depth z_j, we find it by linear interpolation. To explore how results are affected by different radial parameterizations, we will additionally show results from models that were re-parameterized in terms of normalized Chebyshev polynomials of order k (*e.g.* Su and Dziewonski, 1997). We obtain the Chebyshev coefficients by a least squares fit of the original expansion coefficients at the z_i using a combination of norm and roughness damping. This leads to a smoothed but faithful representation of the original models (see Figure 3.9): with $k_{\max} = 20$, we have a resolution of $\sim$ 150 km and achieve variance reductions typically better than 95%.

3.4.5 Radial correlation

Following Puster and Jordan (1997), we calculate the radial correlation matrix $r(z_1, z_2)$ between the lateral structure of the same model at any two depths z_1 and z_2. ($r(z_1, z_2)$ is simply the value of $r^{\mathrm{tot}}_{\ell_{\max}}$ found from the expansions $\{a^{z_1}_{\ell m}, b^{z_1}_{\ell m}\}$ and $\{a^{z_2}_{\ell m}, b^{z_2}_{\ell m}\}$ at the depths z_1 and z_2, respectively.) Two derived, closely related measures of radial coherence as a function of z are a) the correlation coefficient $r(z-\Delta z, z+\Delta z)$ for a fixed depth bracket Δz, and b) the value of Δz associated with a contour of constant $r(z-\Delta z, z+\Delta z)$. As outlined by Puster and Jordan (1997), radial correlation functions can be interpreted as a measure of mass flux between different depth ranges in the convecting mantle. In practice, we compute $r(z_1, z_2)$ for all z_i and interpolate on a smooth field at ~ 25 km grid spacing. For models whose spline parameterization density varies with depth, it is difficult to obtain adequate depth spacings; our discrete z_i estimate of the correlation functions suffers therefore from some oversampling, especially for *s20rts*. The resulting oscillations are, however, easily detected, and can be avoided if we choose a Chebyshev parameterization with depth (see Figure 3.9).

3.5 Results

3.5.1 Analysis of individual models

We study the spectral signal, δv_{RMS}, and radial correlation of each model before comparing models to one another. For consistency, all values of geodynamic models are scaled by

$$\Lambda = \frac{d \ln v_S}{d \ln \rho} = \frac{\delta v_S}{\delta \rho} = 3.6, \tag{3.13}$$

a weighted radial average (we neglect depth-dependence of Λ for simplicity) of Karato's (1993) profile.

Power spectra variation with depth

After computing the spectral power per degree σ^2_ℓ (eq. 3.7) we normalize it by its maximum at each depth in order to emphasize the dominant wavelengths and denote the resulting quantity $\widehat{\sigma}^2_\ell$. The first moment of a weighted sum of $\widehat{\sigma}^2_\ell$,

$$M(z) = \frac{\sum_{\ell=1}^{\ell_{\max}} \ell(2\ell+1)\widehat{\sigma}^2_\ell(z)}{\sum_{\ell=1}^{\ell_{\max}} (2\ell+1)\widehat{\sigma}^2_\ell(z)}, \tag{3.14}$$

is a measure of the z-dependence of the strongest wavelengths, *i.e.* the "color" of the heterogeneity spectrum. (Absolute values of $M(z)$ are only meaningful when $\widehat{\sigma}^2_\ell \to 0$ as $\ell \to \ell_{\max}$; most tomographic models approximately satisfy this condition.)

Figures 3.3 and Figure 3.4 show the normalized and absolute (σ^2_ℓ) spectrum for a selection of tomographic and geodynamic models. Most tomographic models are dominated by long wavelengths ("red", $\ell \lesssim 5$) at all depths (*e.g.* Su and Dziewonski, 1992). These low degree patterns roughly correspond to the continent/ocean function at the surface, the circum-Pacific subduction signal in the mid-mantle, and the "mega-plumes" toward the CMB. In other words, mantle convection appears to be organized by plate-scale flow with lengthscales as observed at the surface (*e.g.* Davies, 1988).

The P-models *kh00p* and *bdp00* have a different spectral character in the uppermost mantle (where $M(z)$ and δv_{RMS} from *bdp00* are smoother functions of depth) and for 1600–2400 km depths. *bdp00* furthermore indicates a stronger change in spectral character at $z \sim 800$ km than *kh00p* while *kh00p* and *bdp00* are consistent in that the absolute $\ell = 2$ power has a local minimum at ~ 2000 km depth (Figure 3.4). The $\widehat{\sigma}^2_\ell$-spectrum of *s20rts* is dominated by $\ell = 2$ everywhere in the lower mantle but weaker at intermediate ℓ than for the P-models. The δv_{RMS} of *s20rts*, minimum at ~ 1600 km depth, is focused in the uppermost mantle where $\widehat{\sigma}^2_\ell$ is strongest in degrees $\ell = 1$ and $\ell = 5$, as expected in an S-model with a well constrained ocean-continent signal (Su and Dziewonski, 1991). The spectrum of *s20rts* becomes continuously redder with increasing depth starting from ~ 1500 km. This is a common feature for S-models while P-models typically have intermediate wavelength power and a corresponding local maximum in $M(z)$ at ~ 2000 km. We find a minimum in absolute σ^2_2 for *s20rts* at ~ 1600 km (Figure 3.4), possibly related to the fading slab signal and to the uppermost boundary of the large slow anomalies that reach down to the CMB (Dziewonski, 1984). We also observe that the spectral power of *s20rts* is consistently higher

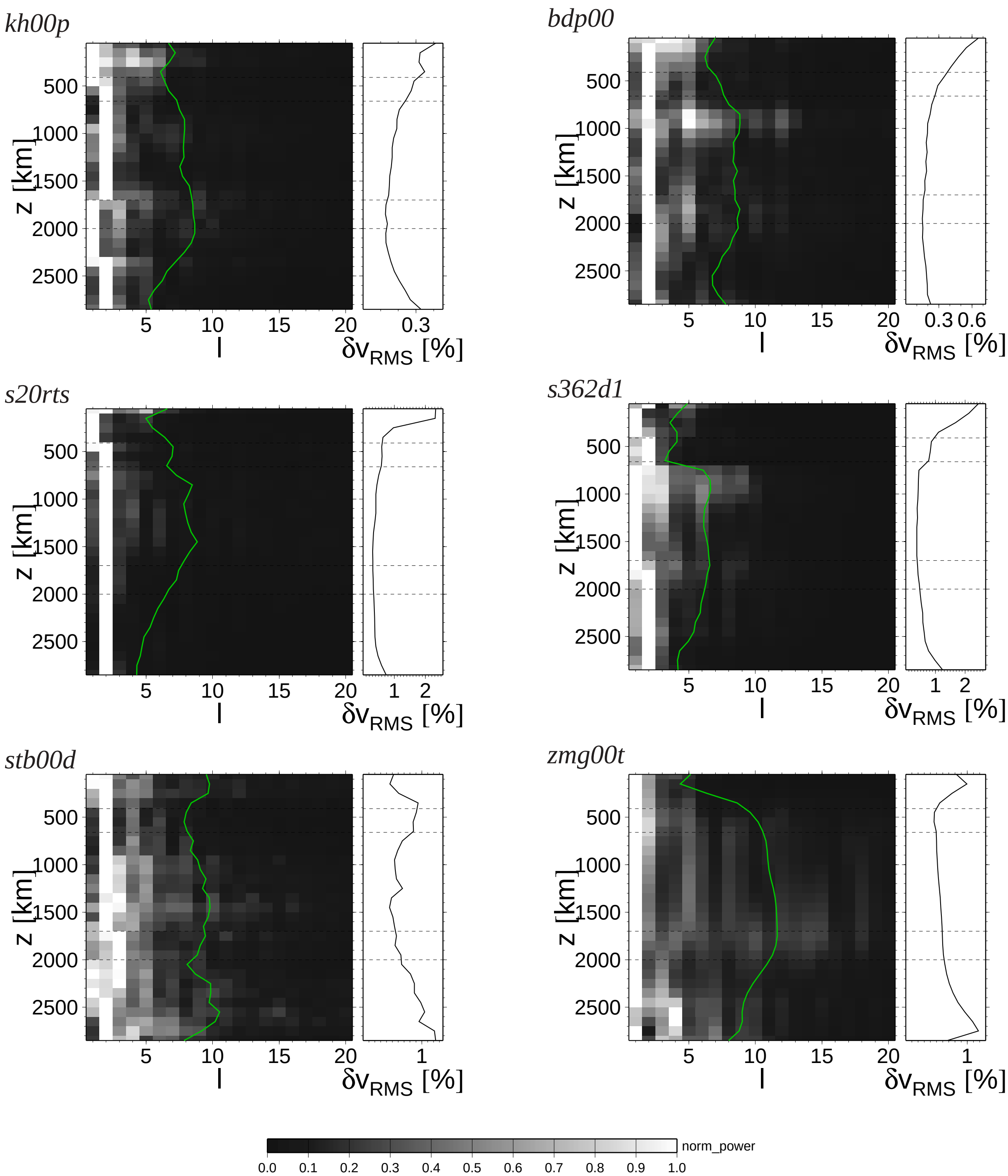

Figure 3.3: Normalized spectral power, $\widehat{\sigma}_\ell^2$, (left sub-plots) and RMS variations, δv_{RMS}, (variable scale with 0.1-tickmarks, right sub-plots) for *P*, *S*, subduction (*stb00d*) and thermal convection (*zmg00t*) models; curve in the left sub-plot indicates $M(z)$, (3.14). Dashed lines mark 410 km, 660 km, 1700 km, and 2000 km depths (compare Figure 3.4).

at even rather than odd ℓ, up to $\ell \sim 12$; one reason for this could be the ℓ-dependence of the sensitivity of normal mode splitting functions (used, among other data, to derive *s20rts*) to the Earth's structure. On the other hand, *s20a* and the subduction signal in *stb00d* and *lrr98d* indicate similar streaks in the power spectrum. The spectrum and δv_{RMS} of *s362d1* shows the effect of a 660-km deep discontinuity in the radial parameterization: the inversion shifts heterogeneity to the upper mantle and the sub 660-km spectrum gets whiter. Gu *et al.* (2001)

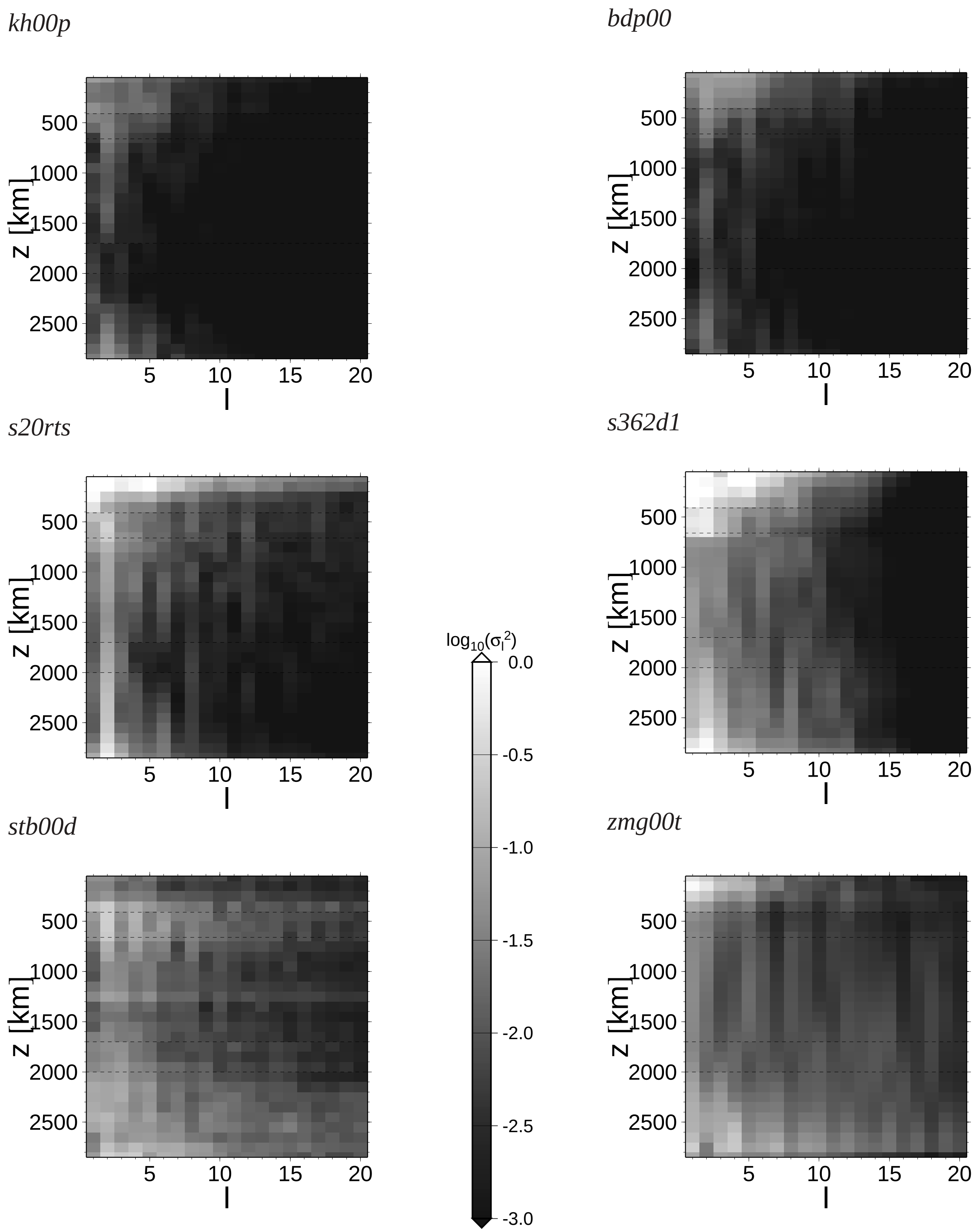

Figure 3.4: Absolute power per degree and unit area on a logarithmic scale, $\log_{10}\left(\sigma_\ell^2\right)$, for *P*, *S*, and geodynamic models (compare Figure 3.3).

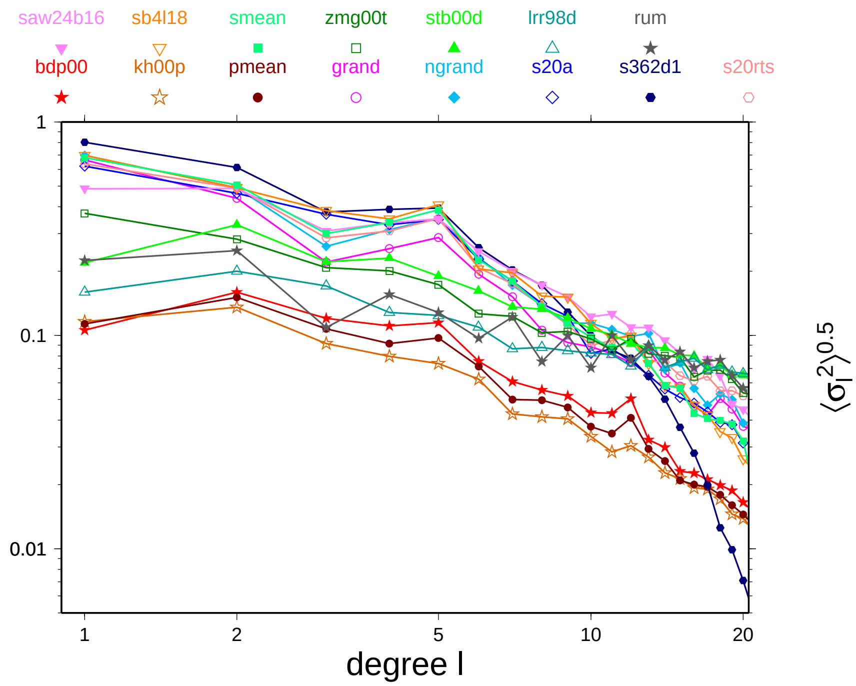

Figure 3.5: Depth averaged power spectra, $\sqrt{\langle\sigma_\ell^2\rangle}$.

find that such variations are not as pronounced when the parameterization discontinuity is placed at other depths. A change in spectral character below 660-km can also be found –to a lesser extent– in other models (*e.g. bdp00*); it might indicate the effect of a viscosity increase in the lower mantle (*e.g.* Mitrovica and Forte, 1997), leading to reorganization of flow and transient slab hold-up (sec. 3.5.1).

$\widehat{\sigma}_\ell^2$ of *stb00d* is strongest for $\ell \lesssim 3$ but differs from tomography in that it has relatively high power over a broad range of wavelengths as expected from the narrow slablet signal. Besides a trend toward a bluer spectrum below 660-km, there is no clear tendency of $M(z)$ of the subduction signal to vary with depth but –as noted above– we find that even ℓ is stronger in the mid-mantle than odd ℓ power for *stb00d* and *lrr98d* (see Figures 3.4 and 3.24). Thermal convection model *zmg00t* is similar to tomography regarding the low degree pattern of heterogeneity. Indeed, case 7 is Zhong *et al.*'s (2000) preferred model since the inclusion of "plates" lead to the characteristic red signal of seismological models in a temperature dependent viscosity calculation. *zmg00t* furthermore resembles tomography in that the signal is bluer in the mid-mantle than toward the thermal boundary layers (TBLs, $z \lesssim$ 500 km and at the CMB) where δv_{RMS} variations are strongest.

Figure 3.5 shows depth averaged $\sqrt{\langle\sigma_\ell^2\rangle}$ for a selection of models. In general, *S*-models are characterized by stronger heterogeneity than *P*-models (*e.g.* Anderson, 1987; Karato, 1993) (also see sec. 3.5.2). As noted above, spectral power for tomography is concentrated at low degrees ($\ell = 1$, $\ell = 2$, with a local maximum at $\ell = 5$) and rapidly decays when $\ell \gtrsim 5$ (*e.g.* Su and Dziewonski, 1991). *s362d1* is an outlier, in that it shows the most rapid decrease of $\widehat{\sigma}_\ell^2$ for $\ell \gtrsim 12$, mostly due to a relatively weak high frequency signal in the upper mantle (Figure 3.4). The geodynamic models *stb00d*, *lrr98d*, *rum*, and *zmg00t* have a stronger high frequency character than that mapped by tomography.

RMS heterogeneity

The aforementioned concentration of heterogeneity toward the boundary layers of the mantle, and the global minima at $\sim$ 1600 km (*S*-models) or $\sim$ 2000 km (*P*-models) depth, are common features of δv_{RMS} as a function of z (Figure 3.6). In the case of tomographic models, δv_{RMS} is a smooth function of depth; exceptions are *grand* and *ngrand* (whose high δv_{RMS} focusing is the result of the inversion procedure), as well as *s20a* and *s362d1* (based on a discontinuous radial parameterization sec. 3.3.2). *ngrand* is significantly closer in δv_{RMS} to the other *S*-models than its ancestor *grand* because of modified damping (sec. 3.3.2). The cross-model correlation between

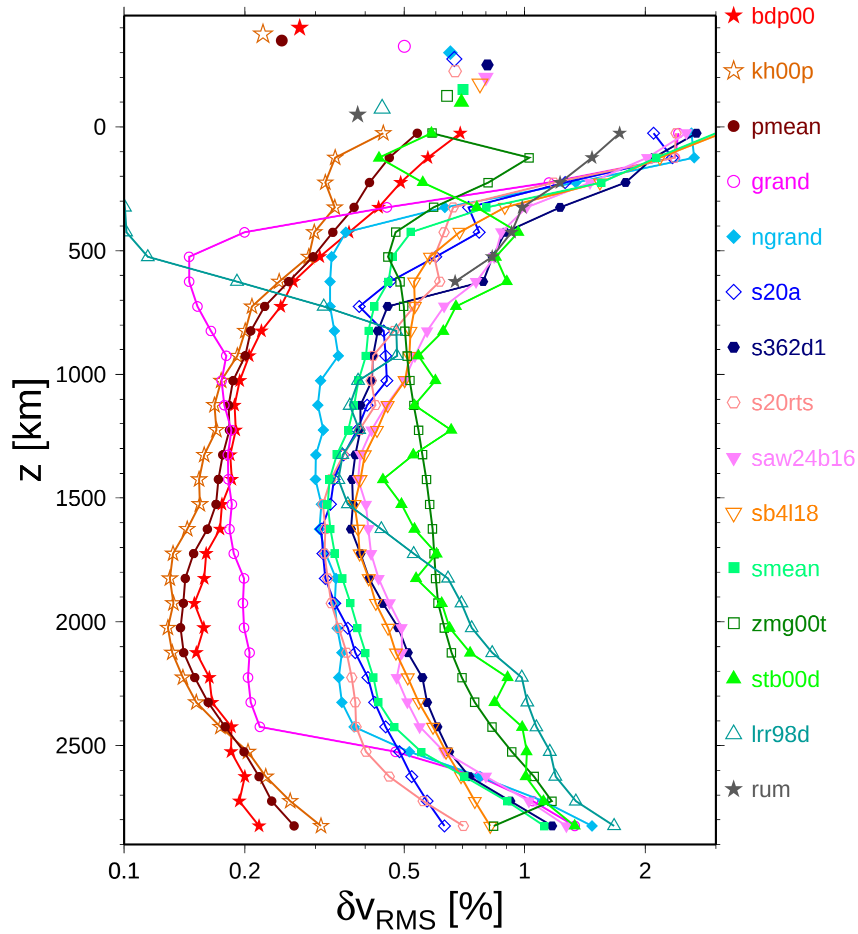

Figure 3.6: δv_{RMS} versus z, $\ell_{\max} = 31$. Symbols at $z < 0$ denote depth averaged $\langle \delta v_{\mathrm{RMS}} \rangle$.

grand and *ngrand* shows that patterns were only slightly affected by this modification ($\langle r_{20} \rangle = 0.9$).

The δv_{RMS} based on subduction models does not agree well with tomography in the upper mantle but shows a consistent increase in heterogeneity below ~ 1500 km. We furthermore find broad agreement between the thermal convection snapshot *zmg00t* and δv_{RMS} from tomography. However, seismological models indicate stronger variations of δv_{RMS} with z. Also, the upper boundary layer structure is generally more pronounced than the deep one for tomography. Reasons for these discrepancies are the continent/ocean differences and tectosphere (not included in any of the geodynamic models), the fact that $\delta\rho_{\mathrm{RMS}} \to 0$ at the surface and at the CMB are boundary conditions of *zmg00t*, and that Zhong *et al.*'s (2000) Rayleigh number is smaller than Earth's by a factor of ~ 10. We should therefore expect that the TBL thickness is overpredicted and $\bar{T}_{\mathrm{RMS}}$ is underpredicted for *zmg00t*. Variations in Λ or α (see sec. 3.5.1) and other effects such as compressibility will also affect the depth-dependence of δv_{RMS} and the spectrum as predicted by geodynamics (*e.g.* Tackley, 1996). However, a detailed discussion of dynamic convection models is beyond the scope of this work.

Radial correlation

Figure 3.7 shows three measures of the radial correlation of tomographic model *bdp00*: the correlation matrix, Δz at constant $r(z-\Delta z, z+\Delta z)$, and $r(z-\Delta z, z+\Delta z)$ at constant Δz (see sec. 3.4.5). All estimates in Figure 3.7 are based on $\ell_{\max} = 20$ expansions (see Figure 3.9 for $\ell_{\max}$-dependence). *bdp00* is characterized by a local minimum in Δz at ~ 600 km; correlation is then relatively high in the mid-mantle and decreases toward the CMB. For *kh00p* (Figure 3.8), local minima in radial correlation are found at ~ 400 km, ~ 800 km, ~ 1700 km, and ~ 2300 km.

Our results are similar (but not identical) to those of van der Hilst and Kárason (1999) who pointed out the decrease in correlation at ~ 1700 km. Since estimates of radial correlation are parameterization-dependent, we

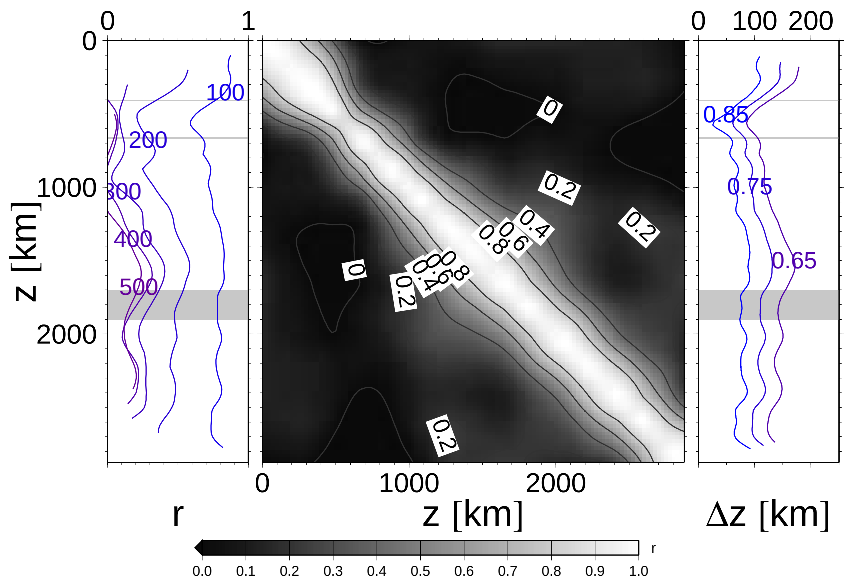

Figure 3.7: Radial correlation function for *bdp00*. We show r at fixed Δz of 100–500 km (left plot), the radial correlation matrix $r(z_1, z_2)$ with contours in 0.2 intervals (mid plot, colorscale clipped at 0), and Δz for fixed $r = 0.65$, $r = 0.75$, and $r = 0.85$ (right plot, if we were able to trace a continuous contour). 410-km, 660-km and the depth range from 1700 km to 1900 km are indicated.

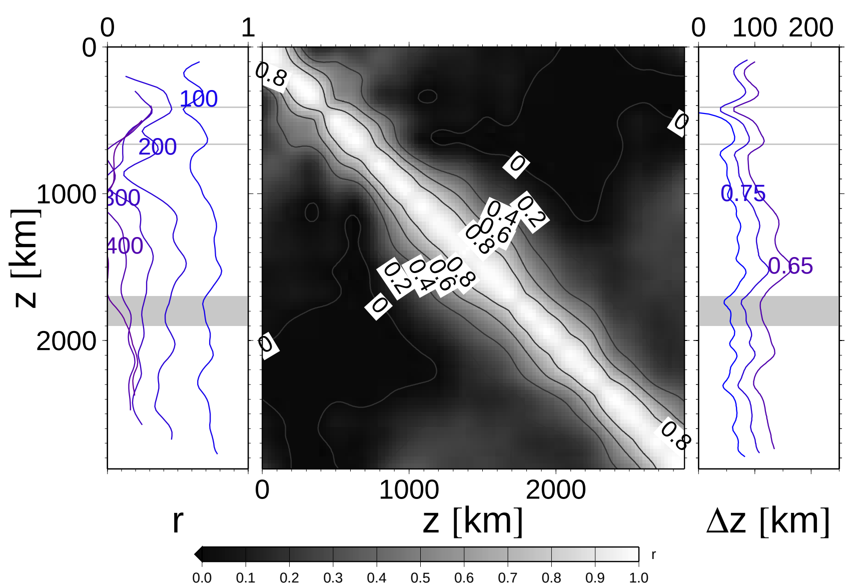

Figure 3.8: Radial correlation function for *kh00p*. See Figure 3.7 for description.

have repeated our calculation for *kh00p* using the original blocks or a radial Chebyshev re-parameterization. Figure 3.9 shows the radial correlation function estimate r at $\Delta z = 200$ km for different parameterizations of *kh00p*. We observe that radial features of our $\ell_{\max} = 20$ spherical harmonics based estimate as in Figure 3.8 are very similar to what we would obtain if we use original grid data (absolute numbers for r differ, however). The comparison of $\ell_{\max} = 8$ and $\ell_{\max} = 31$ estimates shows that small scale structure in r is found across all wavelengths. The Chebyshev radial parameterization introduces some smoothing but is otherwise able to recover the major features of the original model.

The radial correlation of S-models increases with increasing depth (*e.g. sb4l18* in Figure 3.10, with local minima in Δz at ~ 300 km and ~ 600 km). This effect is explained by the general tendency of S-models to become

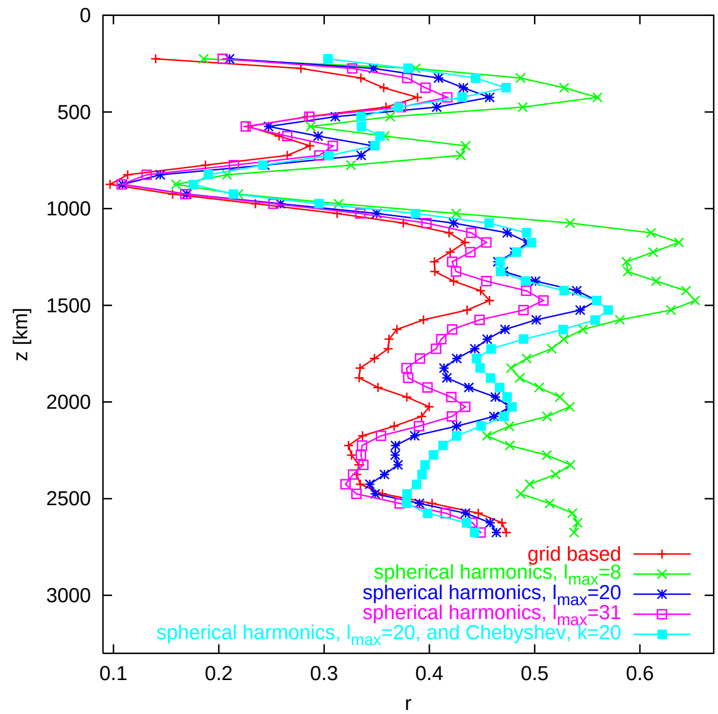

Figure 3.9: Radial correlation function estimates ($r(z-\Delta z, z+\Delta z)$ at $\Delta z = 200$ km) for different parameterizations of *kh00p*: grid based, spherical harmonics laterally for $\ell_{\max} = 8$, $\ell_{\max} = 20$ (identical to results in Figure 3.8), and $\ell_{\max} = 31$, as well as $\ell_{\max} = 20$ spherical harmonics and Chebyshev polynomials radially.

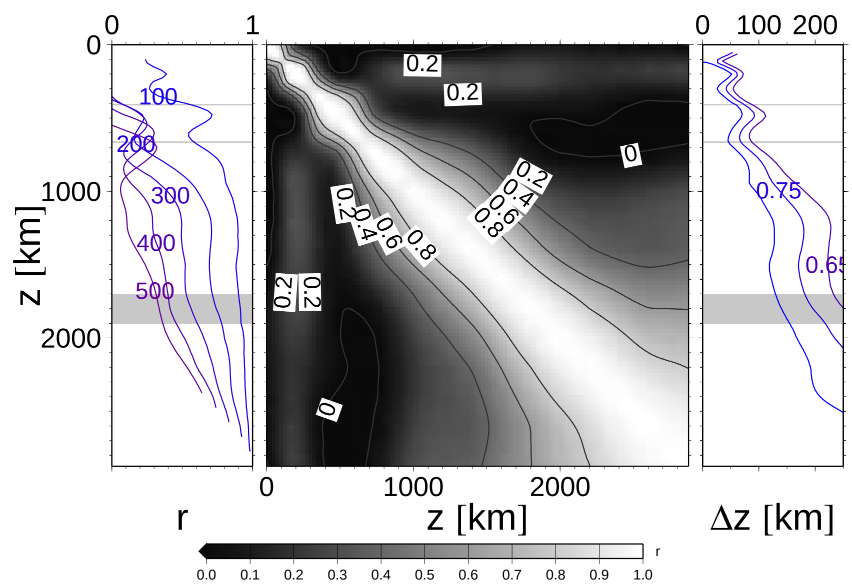

Figure 3.10: Radial correlation function for *sb4l18*. See Figure 3.7 for description.

redder with increasing depth (sec. 3.5.1): since long-wavelength features are better correlated, we then expect a more homogeneous radial correlation in the lower mantle. Indeed, if we damp out high frequency structure in the *P*-models for the lower mantle (typically concentrated at $z \sim 2000$ km), the resulting plots of the radial correlation function resemble those of *S*-wave models.

We show in Figures 3.11a and 3.12a the radial correlation r at $\Delta z = 200$ km of a selection of models as it results from our initial calculations with a discrete radial sampling. Then, we repeat the calculations after re-parameterizing the models over a radial Chebyshev polynomial basis, and show the results in Figures 3.11b and 3.12b. Consistent features of the *P*-models in Figure 3.11b are a broad global minimum in correlation for

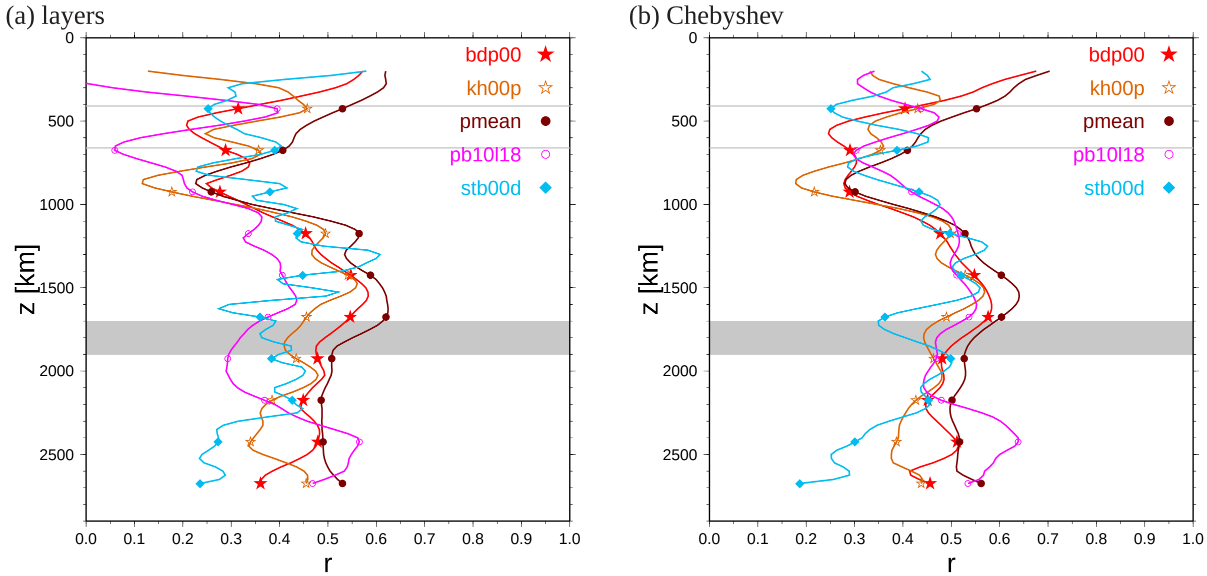

Figure 3.11: Radial correlation $r(z-\Delta z, z+\Delta z)$ at fixed $\Delta z = 200$ km for P-wave tomography with layers (a) and on radial Chebyshev parameterization (b), *stb00d* is shown for comparison.

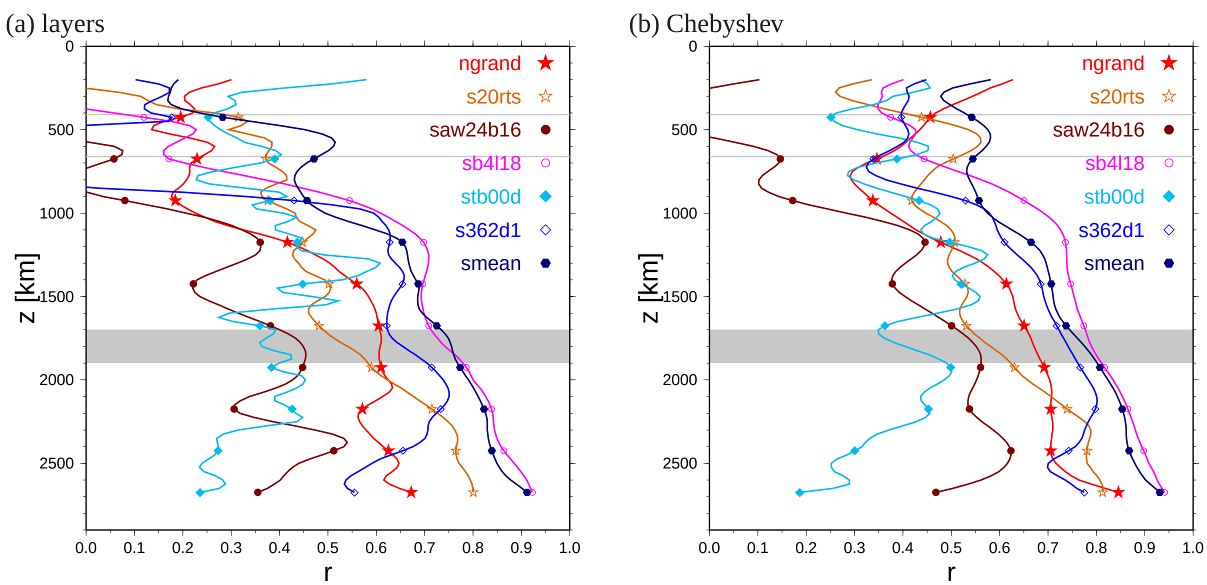

Figure 3.12: Radial correlation $r(z-\Delta z, z+\Delta z)$ at $\Delta z = 200$ km for S-wave tomography with layers (a) and on radial Chebyshev parameterization (b). The continuous Chebyshev parameterization is clearly not suited to represent discontinuities in *s362d1*.

400 km $\lesssim z \lesssim$ 700 km (possibly with a local maximum at $\sim$ 660 km), an increase in r toward 1500 km, and a decrease to a second minimum at 1700 km $\lesssim z \lesssim$ 2400 km. The latter feature is less pronounced in *pb10l18*. As anticipated above, S-models (Figure 3.12) are generally characterized by an increase in r with increasing z. Other notable features are local maxima at $\sim$ 660 km, artificial oscillations of the r versus z curve obtained from *s20rts* (explained in sec. 3.4.5), and the anomalously large (parameterization related, sec. 3.3.2) excursions of *s362d1* at 660-km.

Radial correlation estimates vary strongly with model parameterization (*e.g.* Ritzwoller and Lavely, 1995) and power spectra appear to be a more robust estimate of structural change than radial correlation functions. However, we find some indication for low radial correlation in P and S-models at $\sim$ 750 km, and in P-models at $\sim$ 2000 km, previously associated with reorganization of flow and possible deep mantle structure, respectively

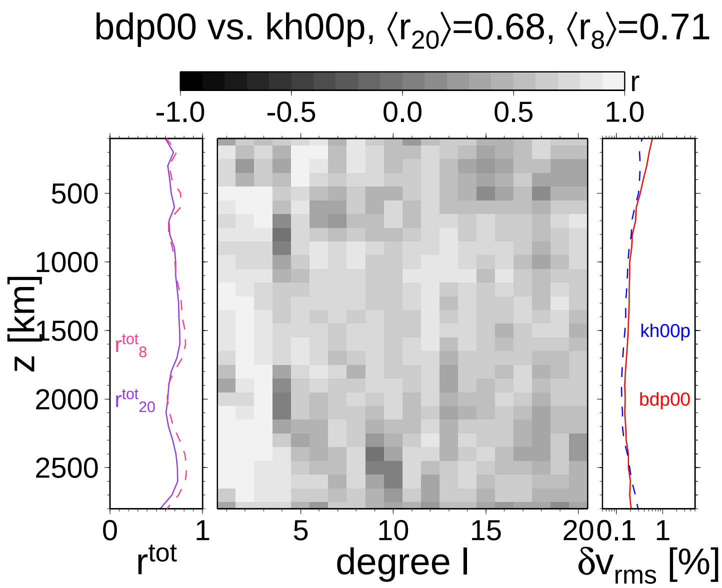

Figure 3.13: Cross-model correlation between *bdp00* and *kh00p*. We show total correlations r_8^{tot} and r_{20}^{tot} (dashed and solid curves, respectively, left plot), correlations per degree r^ℓ (mid plot), and δv_{RMS} for bdp00 (solid) and kh00p (dashed) on a log-scale (right plot).

(van der Hilst and Kárason, 1999). The work of Puster and Jordan (1997) and the *stb00d* (whole mantle flow) derived correlation profiles show that local minima in correlation are not necessarily indicative of a layered style of convection. Changes in slab morphology (*e.g.* van der Hilst *et al.*, 1997; van der Hilst and Kárason, 1999) and the general flow pattern due to the phase transition with a viscosity increase at 660-km (*e.g.* Mitrovica and Forte, 1997) are therefore likely explanations for the first minimum in correlation. Especially transient slab flattening and possible segmentation can be expected to yield structural changes below 660-km as indicated by some of the power spectra that were discussed in sec. 3.5.1.

The findings that $z \sim 2000$ km is a global minimum of δv_{RMS}, that the radial correlation of *S*-models shows no clear decrease at these depths, and the apparent absence of large scatterers in the lower mantle (Castle and van der Hilst, 2000), make the existence of a strong global structural change at ~ 2000 km seem unlikely at this point. However, the local minima in absolute $\ell = 2$ power that we found at ~ 1700 km (sec. 3.5.1) are consistent with a fade-out of the slab signal at these depths (*e.g.* van der Hilst and Kárason, 1999; Kárason and van der Hilst, 2000) and local compositional heterogeneity (*e.g.* Saltzer *et al.*, 2001) cannot be ruled out.

3.5.2 Cross-model comparisons

We now quantify similarities and discrepancies between models, focusing on a representative subset. The expanded online version of Becker and Boschi (2002) includes correlation plots for all possible pairs of models from sec. 3.3 with the exception of *zmg00t* which represents the current state of Earth's mantle only in a statistical sense.

P-wave models

Figure 3.13 shows r^ℓ between *bdp00* and *kh00p*, an example of the good correlation that generally characterizes *P*-models. The pattern and δv_{RMS} of *bdp00* and *kh00p* are mostly consistent throughout the lower mantle and up to $\ell = 20$; significant deviations are found in the uppermost mantle (where δv_{RMS} of *kh00p* is weaker) and at the CMB (where the inclusion of core phases has enhanced the δv_{RMS} of *kh00p* (Kárason and van der Hilst, 2001)). Other local minima in r_8^{tot} and r_{20}^{tot} are at $\sim$ 300 km, 700 km, and $\sim$ 1900 km. All three depths show a long wavelength breakdown in correlation ($r_8^{\mathrm{tot}} \to r_{20}^{\mathrm{tot}}$), especially at $\ell = 4$. The average correlation between *bdp00* and *kh00p* is high ($\langle r_8 \rangle = 0.71$), to be compared with $\langle r_8 \rangle = 0.85$ for *bdp00–bdp98*, and $\langle r_8 \rangle = 0.69$ for *kh00p–hwe97p* (but see sec. 3.4.1).

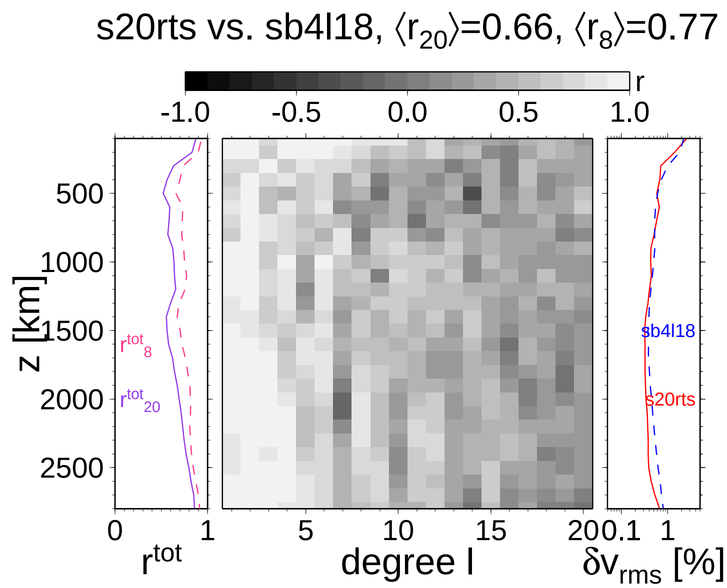

Figure 3.14: Cross-model correlation for *s20rts* (solid δv_{RMS}-line) and *sb4l18* (dashed δv_{RMS}-line), see Figure 3.13 for description.

S-wave models

Figure 3.14 shows r^ℓ for *s20rts* and *sb4l18*. Especially at low harmonic degrees, the two models are very consistent, more so than the *P*-models in Figure 3.13. However, at $\ell \gtrsim 12$ correlation degrades such that $\langle r_{20} \rangle$ is slightly lower than for *bdp00–kh00p*. These intermediate wavelength discrepancies that we find for most *S*-models are likely due to the greater variety in input data, while *P*-models are inverted from similar data sets (sec. 3.3). r_8^{tot} and r_{20}^{tot} for Figure 3.14 have a global maximum near the surface, decrease toward ~ 1500 km, and, as the low-degree portion of the spectrum becomes more important, grow monotonically thereafter while $r_{20}^{\mathrm{tot}} \to r_8^{\mathrm{tot}}$.

r^ℓ behaves as in Figure 3.14 for most combinations of *S*-models (sec. 3.5.3). Exceptions are *s20a* and *s362d1*: these models correlate well with other *S*-models in the upper mantle. Because of their inherent radial discontinuity, however, they are different from other models for $700 \text{ km} \lesssim z \lesssim 1500$ km. Yet, between *s362d1* and *smean*, r^2 and r^3 at $z = 800$ km are still > 0.68 and $\langle r_8 \rangle = 0.7$. As noted by Gu *et al.* (2001), the data-fit of their 660-km discontinuity model was not significantly better than that of their continuous parameterization inversion. This means that discontinuous descriptions of mantle structure are consistent with, but not required by, the data.

δv_S versus δv_P

Figure 3.15 is representative of comparisons between models of v_S and v_P. We find that those are generally not as well correlated with each other as models of the same kind. This result can partly be explained by the systematic differences in data distribution and sensitivity, especially in the upper mantle (sec. 3.3.2). r_{20}^{tot} in Figure 3.15 shows local minima at ~ 700 km and at ~ 1800 km, but only the former is accompanied by a broad $r_8^{\mathrm{tot}} \to r_{20}^{\mathrm{tot}}$ cross-wavelength breakdown (not as pronounced for comparisons with *kh00p*).

Figure 3.16 shows r_{20}^{tot} for a combination of *S*-models and *bdp00* and *kh00p*; Figure 3.17 allows a comparison of our mean models, long-wavelength joint inversions, and the normal mode model SPRD6 (secs. 3.3.2 and 3.3.3). We observe that correlation between δv_S and δv_P is low for all models between ~ 300 km and ~ 700 km; another minimum is found at ~ 2000 km for some models. r_{20}^{tot} between most *P*- and *S*-models has a local maximum at ~ 2500 km and then decreases, again, toward the CMB, hinting at compositional heterogeneity at the bottom of the mantle.

Comparisons of the δv_S–δv_P components of models derived from joint v_S–v_P inversions (Figure 3.17) can lead to quite different conclusions, depending on the model (Masters *et al.*, 2000): in the case of MK12WM13, the δv_S–δv_P correlation has a pronounced minimum at ~ 1000 km and is smaller at low ℓ than at intermediate ℓ. The correlations of *smean* versus *pmean* and δv_S versus δv_P components of SB10L18, on the other hand, are

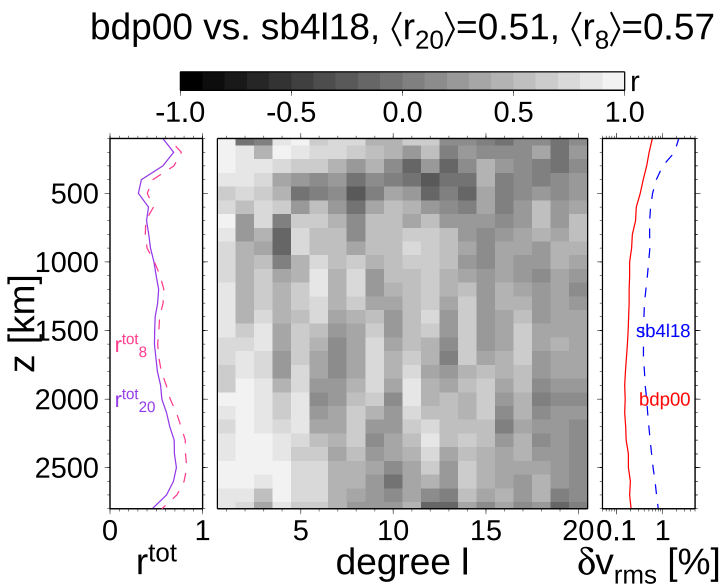

Figure 3.15: Cross-model correlation for *bdp00* (solid δv_{RMS}-line) and *sb4l18* (dashed δv_{RMS}-line), see Figure 3.13 for description.

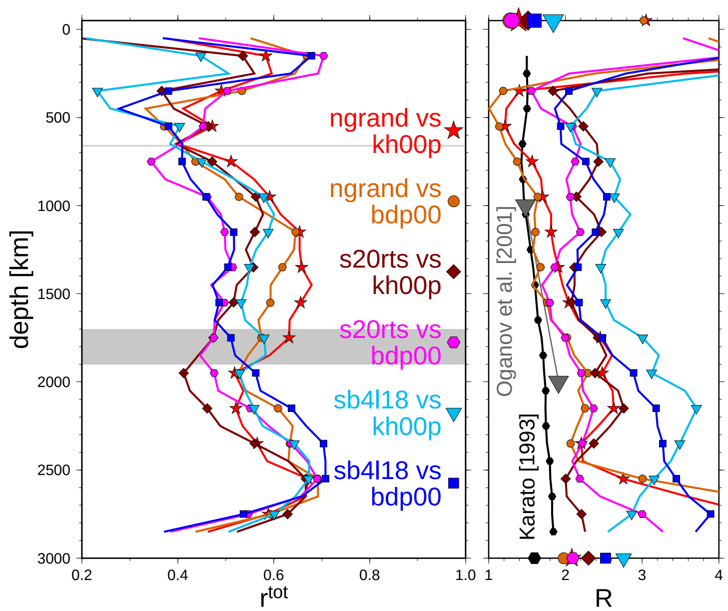

Figure 3.16: δv_S-δv_P correlation r^{tot} (left sub-plots) and $R = \delta v_S/\delta v_P$ (right sub-plots) for a combination of *S*- and *P*-models. Estimates of r^{tot} are based on $\ell_{\max} = 20$ (r^{tot}_{20}) and R is from the RMS ratio (solid lines). Symbols on R-axis indicate mean $\langle R \rangle$ for $z \geq 400$ km from the RMS ratio (at $z = 3000$ km) or lower and higher estimates from an iterative linear regression (at $z = 0$, large and small symbols, respectively).

consistent, with local minima at at $\sim$ 400 km and $\sim$ 2000 km (as before, only the former shows $r^{\mathrm{tot}}_8 \rightarrow r^{\mathrm{tot}}_{20}$). Absolute correlations are, however, higher for SB10L18.

We next determine

$$R = \frac{d \ln v_S}{d \ln v_P} = \frac{\delta v_S}{\delta v_P}, \tag{3.15}$$

first from the RMS heterogeneity ratio of the models (solid lines in Figures 3.16 and 3.17, mean $\langle R \rangle$ indicated

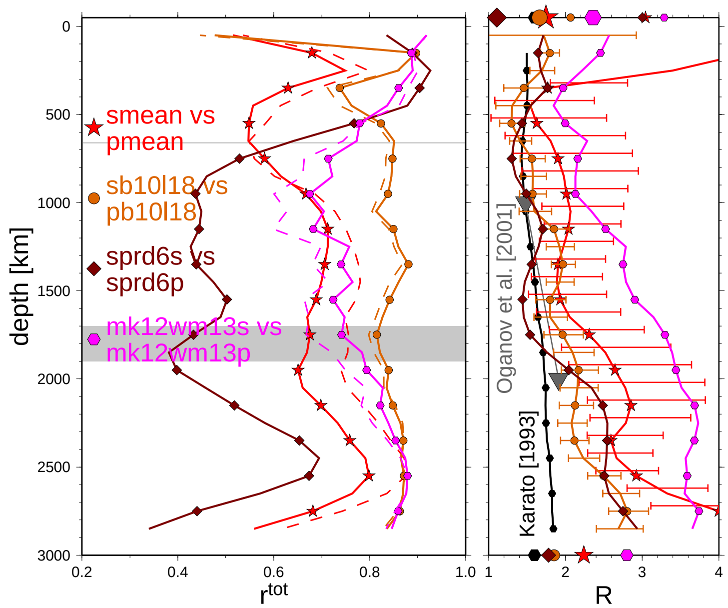

Figure 3.17: δv_S-δv_P correlation r^{tot} and $R = \delta v_S/\delta v_P$ for joint models MK12WM13, SB10L18, SPRD6, and our mean models *smean*/*pmean*. Estimates of r^{tot} based on $\ell_{\max} = 20$ (r^{tot}_{20}, solid) and $\ell_{\max} = 8$ (r^{tot}_{8}, dashed lines, except for SPRD6 which is always r^{tot}_{6}) and R is from the RMS ratio (solid lines) and an iterative linear regression (error bars, lower and higher estimates are for $\Sigma_{\delta v_S} = 2\Sigma_{\delta v_P}$ and $\Sigma_{\delta v_P} = 2\Sigma_{\delta v_S}$, respectively). Symbols on R-axis indicate mean $\langle R \rangle$ for $z \geq 400$ km as in Figure 3.16.

on the R-axis at the CMB). Secondly, we calculate R from a linear regression of the expansion coefficients of the models at each depth ($\ell_{\max} = 20$); an estimate whose reliability can be judged from the corresponding r^{tot}_{20}. In the absence of information about model uncertainties, R will vary depending on the assumed standard deviations, Σ, of each model. We therefore show a range of best-fit R values from an iterative linear regression (*e.g.* Press *et al.*, 1993, p. 666) where Σ of the S-model, $\Sigma_{\delta v_S}$, is assumed to be twice that of the P-model (leading to lower estimates for R) or vice versa, where $\Sigma_{\delta v_P} = 2\Sigma_{\delta v_S}$ (leading to higher estimates). The corresponding $\langle R \rangle$ values are indicated with different size symbols on the upper R axis in Figures 3.16 and 3.17. For comparison, we add the expected variation of R based on mineral physics if heterogeneity were purely thermal in origin, one estimate (black line) from Karato (1993), and the other (gray inverted triangles) from ab-initio calculations for $MgSiO_3$ perovskite by Oganov *et al.* (2001).

Measured R in Figure 3.16 typically increases for $z \gtrsim 400$ km, and is between 1 and 4 for RMS estimates. We note that $R \gtrsim 2.5$ implies a negative correlation between bulk sound and shear wave velocity (*e.g.* Masters *et al.*, 2000, eq. 4) which is usually interpreted as an indication of compositional heterogeneity. Mean $\langle R \rangle$ values based on δv_{RMS} are, indeed, in general larger than the mineral physics estimates for temperature and pressure effects in Figure 3.16, in agreement with findings from direct inversions for R (*e.g.* Robertson and Woodhouse, 1996). However, lower-end linear regression estimates and RMS $\langle R \rangle$ from *sprd6* and SB10L18 (Figure 3.17) fall close to the mineral physics values (see also Masters *et al.*, 2000) and recent estimates by Karato and Karki (2001) are larger than Karato's (1993) R values by ~ 0.4. Hence, the significance of the observed mid-mantle deviations from a homogeneous composition trend remains to be determined.

In synthesis, judging from r and R for δv_S–δv_P, regions of global deviation from the predictions of mineralogy for a chemically homogeneous mantle are likely to be limited to the tectosphere, the transition zone (where data coverage for P is inferior), the CMB region, and –less pronounced and with all the caveats from sec. 3.5.1– the depth range at ~ 2000 km.

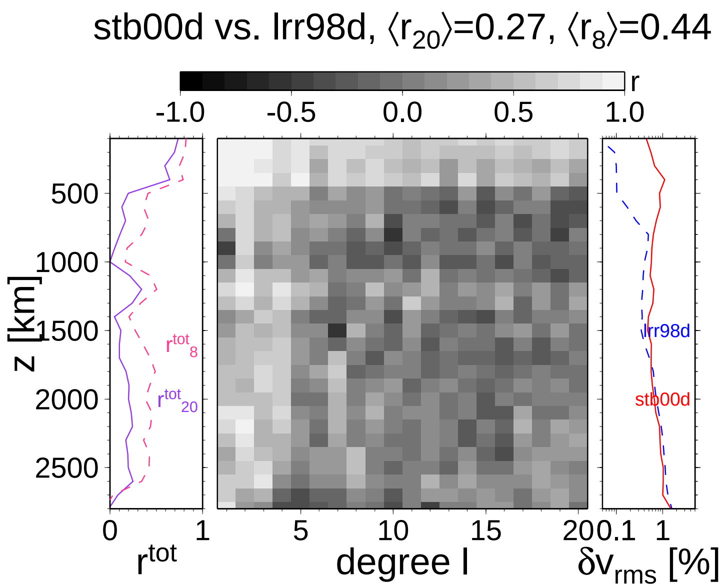

Figure 3.18: Cross-model correlation for *stb00d* (solid δv_{RMS}-line) and *lrr98d* (dashed δv_{RMS}-line). Compare with Figure 3.24 and see Figure 3.13 for description.

Geodynamic models

The correlation between two subduction models, *stb00d* and *lrr98d*, is shown in Figure 3.18. They are most consistent in the upper mantle where slab locations are well constrained by seismicity ($\langle r_8 \rangle$ with *rum* is 0.63 and 0.61 for *lrr98d* and *stb00d*, respectively). Moreover, advection is only active in *stb00d* once slabs sink below 380 km. Steinberger's (2000) and Lithgow-Bertelloni and Richards's (1998) approach should therefore lead to similar results for shallow structure. Once lateral advection becomes more important with depth, correlation decreases with z up to ~ 1000 km and stays low for $\ell \gtrsim 5$ throughout the lower mantle. The finding that the geodynamic models do not agree well with each other globally ($\langle r_8 \rangle = 0.44$) implies that differences in methodology and the effect of lateral advection on the narrow slab features affect the global measure r significantly (see sec. 3.5.4). This observation can also guide us as to how to judge the correlation of slab and tomography models.

r^ℓ between geodynamic and tomographic models is in fact high for long wavelengths ($\ell \lesssim 3$) (Ricard *et al.*, 1993; Lithgow-Bertelloni and Richards, 1998) throughout the mantle but r^ℓ is low for higher ℓ. We find that global $\langle r_8 \rangle$ is small on average ($\langle r_8 \rangle \sim 0.3$) and there is no clear depth-dependence of r_8^{tot} besides that correlation is usually largest below the transition zone at ~ 800 km and smallest at $z \sim 1500$ km depth. The best $\langle r_8 \rangle$–correlation between subduction and tomography models is $\langle r_8 \rangle = 0.33$ between *lrr98d* and *smean* (Figure 3.19 and sec. 3.5.3) but *lrr98d* and *stb00d* lead to similar $\langle r_{20} \rangle$–results ($\langle r_{20} \rangle = 0.18$ and $\langle r_{20} \rangle = 0.21$ with *smean*, respectively).

3.5.3 Correlation between *lrr98d* and *smean*

Figure 3.19 shows the cross-model correlation for the best $\langle r_8 \rangle$–pair of subduction and tomography models, *lrr98d* and *smean*. However, intermediate wavelength correlation with *smean* is slightly better for *stb00d* ($\langle r_{20} \rangle = 0.21$) than for *lrr98d* ($\langle r_{20} \rangle = 0.18$). The depth dependence of r_8^{tot} and r_{20}^{tot} in Figure 3.19 is similar to that shown in Figure 3.22 and shows a mid-mantle maximum.

Summary of average cross-model correlations

We summarize our findings in Figure 3.20 which shows the total depth-averaged correlations $\langle r_8 \rangle$ and the total cross-model correlations at 600 km, 1400 km, and 2750 km, for a selection of *P*, *S*, and geodynamic models. In general, agreement between tomographic structure is poor at $z \sim 600$ km (where *S*-models correlate fairly well with subduction models) and increases with larger depths. We find that our models *smean* and *pmean* correlate

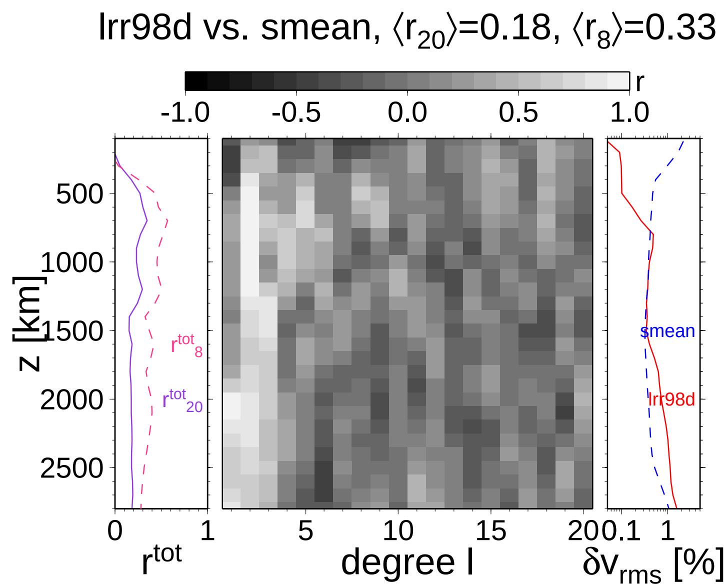

Figure 3.19: Cross-model correlation for *lrr98d* (solid δv_{RMS}-line) and *smean* (dashed δv_{RMS}-line), see Figure 3.13 for description.

better ($\langle r_8 \rangle = 0.71$) with each other than any other δv_S-δv_P combination in Figure 3.20a and achieve the highest $\langle r_8 \rangle$ with slab models *lrr98d* or *stb00d*. For the *S*-models that were not used for the construction of *smean* (see sec. 3.3.3), the discontinuity models *s20a* and *s362d1* are found to be more similar to *smean* than *saw24b16* which is δv_{SH} only. We cannot identify particular depth ranges where anisotropy in *S*-wave propagation might cause deviations. However, we note that correlation between *smean* and *saw24b16* has a local minimum in the lower mantle where Mégnin and Romanowicz (1999) argue that their approach has led to improved resolution over other *S*-models. From Figure 3.20 we can also see that subduction models correlate better with *S* than with *P*-models. On average, *lrr98d* is about as similar to tomographic models (mean $\langle r_8 \rangle / \langle r_{20} \rangle$ from Figure 3.20 is 0.24/0.13) as is *stb00d* (mean $\langle r_8 \rangle / \langle r_{20} \rangle$ is 0.23/0.16), even though *stb00d* is a more sophisticated model in terms of the treatment of mantle flow.

In a final step toward cross-model similarity synthesis, Figure 3.21 explores how similar *P*- (*bdp00* and *kh00p*), *S*- (*s362d1*, *s20a*, *sb4l18*, *saw24b16*, *s20rts*, and *ngrand*), and geodynamic models (*stb00d* and *lrr98d*) are on average. The highest correlations are generally associated with the longer wavelength component (*S*-models in particular) and –for tomography– larger depths. Subduction models become progressively uncorrelated with z.

3.5.4 Comparison of tomography and geodynamic models

We have seen that the geodynamic models *stb00d* and *lrr98d* do not correlate well globally with tomography for $\ell \gtrsim 5$. We now argue that this does not imply that there is no slab signal in the mantle but that our understanding of flow modeling has to be improved.

Subduction versus fast anomalies only

Slabs in the mantle will be colder than their surroundings and thus show up as fast anomalies only. Therefore, we set to zero all slow anomalies present in tomographic models, re-expand the models –thus “clipped”–, and recompute their correlation with the geodynamic models. This procedure leads to some increase in the correlation between *lrr98d*, *stb00d*, *rum*, and tomography models, particularly in the upper and mid-mantle. However, the depth-averaged correlation is still poor ($\langle r_8 \rangle \lesssim 0.4$). We thus infer that the low global correlation between tomography and subduction models cannot be explained as an effect of the lack of independent hot upwellings in subduction models. An alternative explanation is that our knowledge of mantle viscosity and of the velocity at which slabs sink is still incomplete. We will now analyze this possibility with additional calculations.

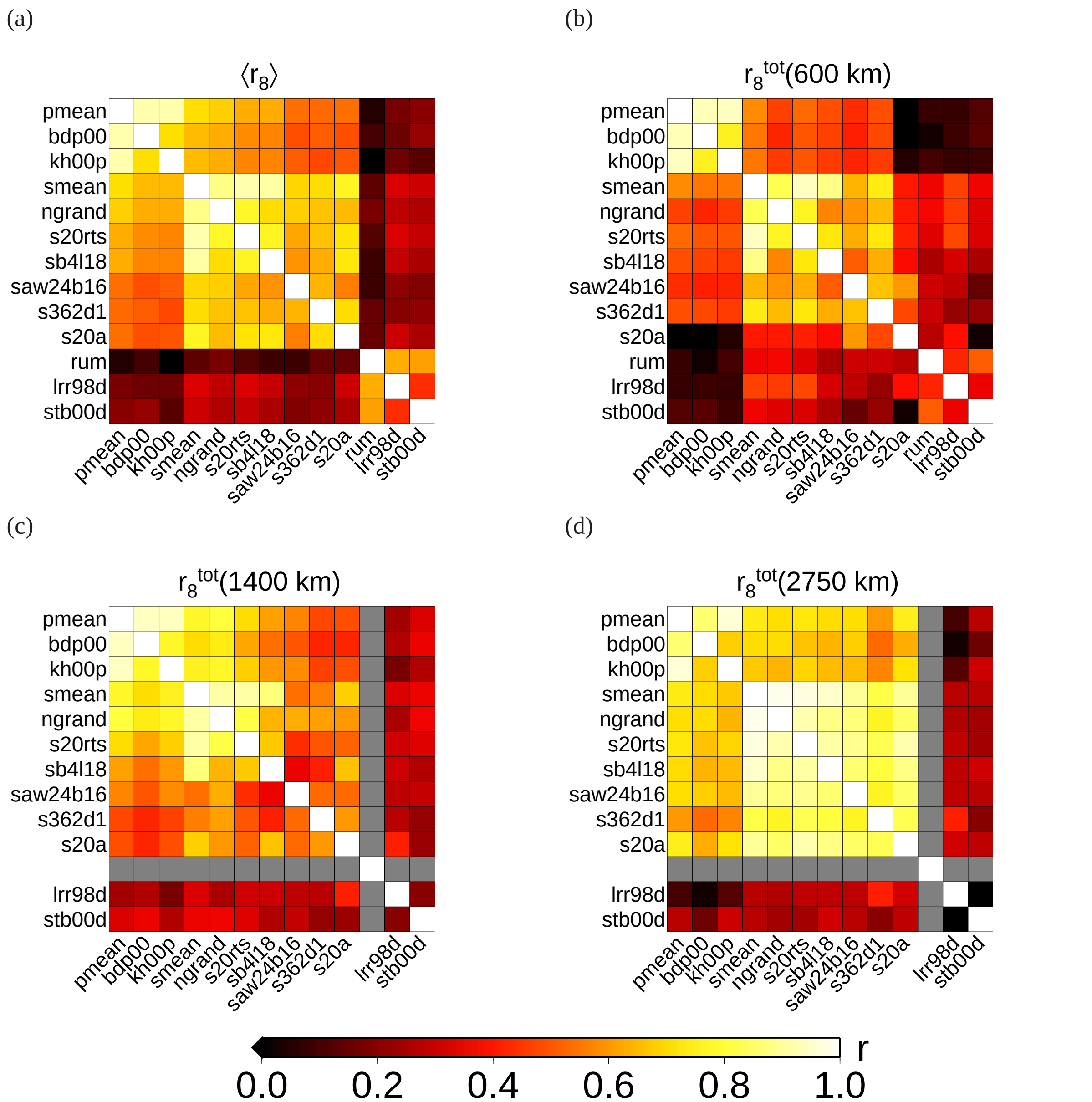

Figure 3.20: Average cross-model correlation up to $\ell_{\max} = 8$ ($\langle r_8 \rangle$, a) as well as r_8^{tot} at $z = 600$ km (b), $z = 1400$ km (c), and $z = 2750$ km (d).

We smooth the depth-dependence of *stb00d* and *lrr98d* by taking, for each expansion, a sliding boxcar average with depth extent δz_{box} up to 600 km (mean of $[z - \delta z_{\text{box}}/2; z + \delta z_{\text{box}}/2]$) and then find, again, the r_8^{tot} correlation between *stb00d* (Figure 3.22a) or *lrr98d* (Figure 3.22b) and several clipped ($\delta v > 0$) tomography models. The results, summarized in Figure 3.22, indicate that correlation becomes higher with increasing δz_{box}. Our radial smoothing filter, therefore, limits problems associated with the short radial correlation length Δz of subduction models. We find that correlations are higher with *S*-models, and the behavior of r_8^{tot} as a function of depth is different depending on the model (*stb00d* or *lrr98d*, see next section). In general, r_8^{tot} is negative in the shallow mantle ($z \lesssim 200$ km) due to the tectosphere and continent–ocean differences imaged by tomography but not included in the subduction models. r_8^{tot} then increases to its maximum in the mid-mantle ($z \sim 750$ km) where slabs might be more easily detected by tomography since an increase in viscosity at 660-km could lead to a broadening of the subduction signal in the lower mantle. Correlation then decreases toward the CMB.

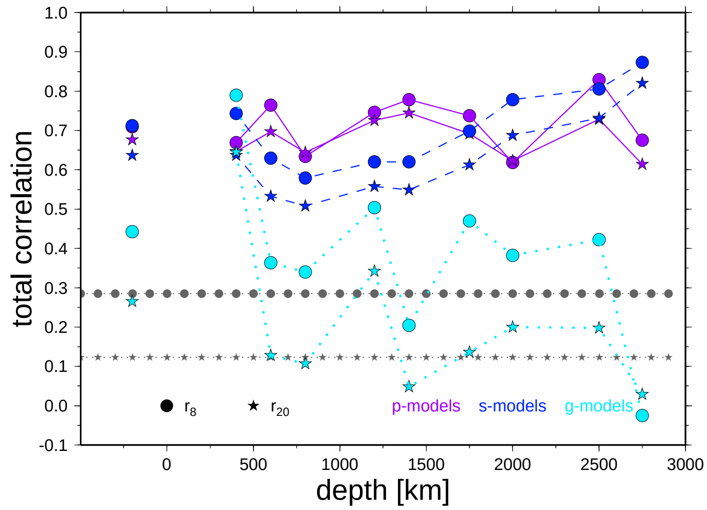

Figure 3.21: Cross-model correlations for *P*-models (solid lines), *S*-models (dashed lines), and geodynamic models (“g”, dotted lines). Symbols at negative depth indicate $\langle r \rangle$, and line-connected symbols are r^{tot}. Circles and stars denote r_8^{tot} and r_{20}^{tot}, respectively, and horizontal lines show the 99% significance levels (sec. 3.4.3).

(a) *stb00d* (b) *lrr98d*

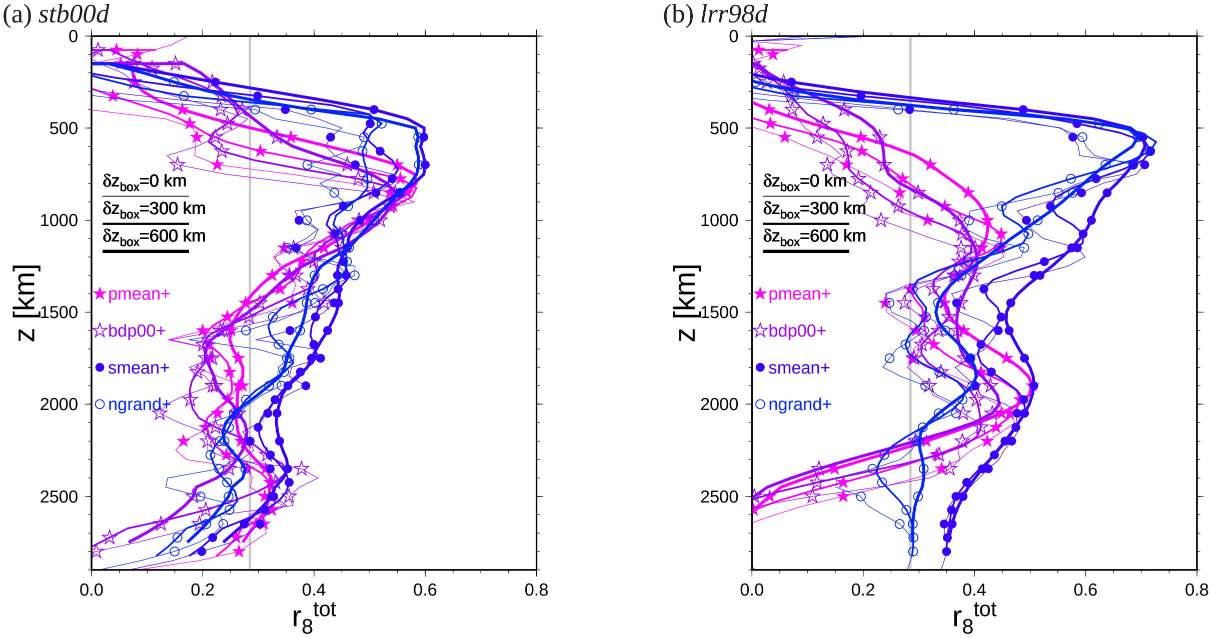

Figure 3.22: r_8^{tot} of *stb00d* (a) and *lrr98d* (b) with *P* and *S*-models for radial boxcar averaging. Line thickness indicates δz_{box}; the vertical gray line denotes the 99% confidence level.

Effect of slablet sinking speed

We simulate the effect that a wrong estimate of the sinking velocity of slablets would have on subduction models: neglecting lateral motion, upper/lower mantle differences, and upwellings, this can be done by “stretching” the models by a factor f, *i.e.* mapping the depth interval $[z_a, z_b]$ onto $[fz_a, fz_b]$ (Figure 3.23). For *stb00d*, $\langle r_8 \rangle$ with clipped tomography can be improved by up to 43% (Figure 3.23a) with the best $f_{\text{opt}} \sim 1.75$, corresponding to a higher sinking speed. Figure 3.24 shows the cross-model correlation for *lrr98d* and that $f_{\text{opt}} = 1.75$–stretched version of *stb00d*. Note that r^{ℓ} is consistently higher for even than for odd ℓ, especially below 700 km. From Figure 3.24 we see that *lrr98d* and the modified *stb00d* are more similar ($\langle r_8 \rangle = 0.66$) in this case, too. The even degrees –related to the circum-Pacific subduction– are prominent in the power spectra of *stb00d* and *lrr98d* (Figures 3.3 and 3.4) and appear to be best constrained at depth. However, individual $\langle r_8 \rangle$–correlations of the stretched *stb00d* with tomography ($\langle r_8 \rangle \leq 0.42$) are still not much better than for *lrr98d*, for which we find $f_{\text{opt}} \sim$

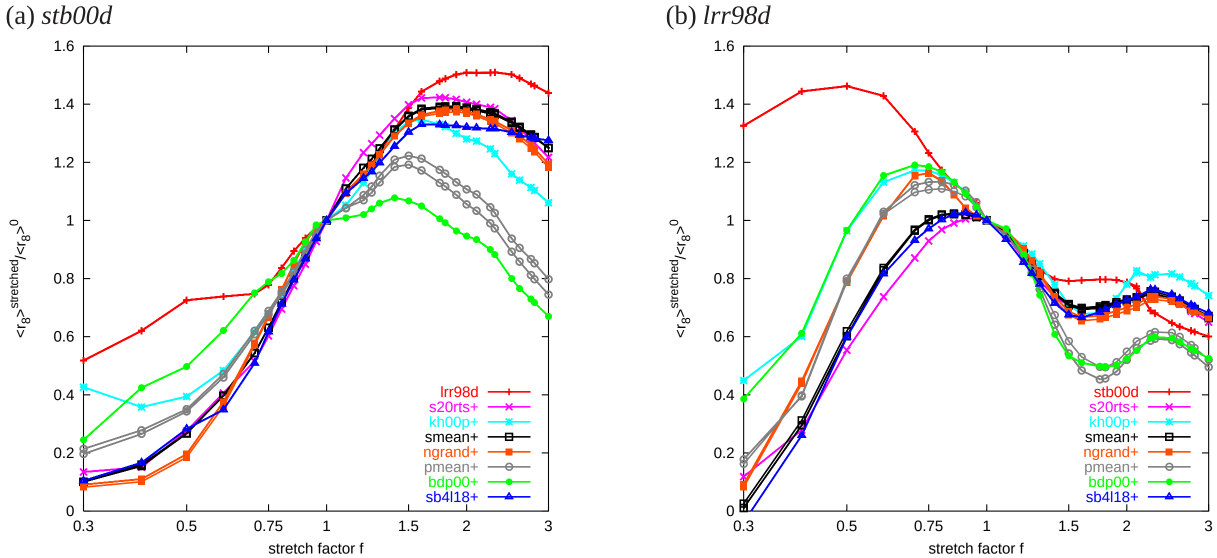

Figure 3.23: New cross-model $\langle r_8 \rangle$ over original $\langle r_8 \rangle$ if *stb00d* (a) or *lrr98d* (b) are stretched by f.

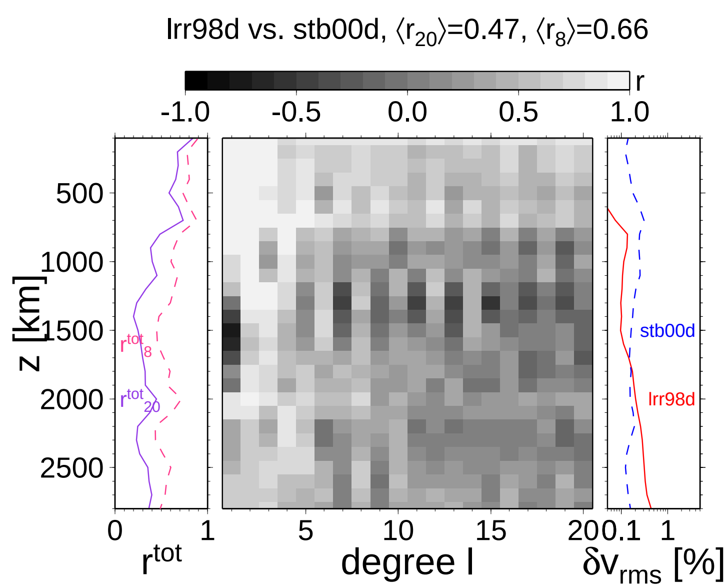

Figure 3.24: Cross-model correlation for *lrr98d* (solid δv_{RMS}-line) and $f_{\text{opt}} = 1.75$ stretched *stb00d* (dashed δv_{RMS}-line). Compare Figure 3.18 and see Figure 3.13 for description.

0.75 with a smaller relative increase of $\langle r_8 \rangle$ of $\lesssim 20\%$ ($\langle r_8 \rangle \leq 0.38$), most pronounced for *P*-models (Figure 3.23b). This implies that Lithgow-Bertelloni and Richards's (1998) optimization with respect to the sinking velocity was basically successful; Steinberger's (2000) more realistic subduction calculation with fewer free parameters and lateral advection did not produce a better model when global correlation with tomography is used as a measure.

In synthesis, we find that geodynamic models show some resemblance to tomographic models on a global scale. The correspondence is best at ~ 800 km depth, but not as good as between tomographic models. The reason for this could be that the subduction process is not yet modeled correctly; the lateral and depth offsets that might result from slab interaction with 660-km (*e.g.* Zhong and Gurnis, 1995; Christensen, 1996) could explain some of the weak correlation at intermediate ℓ. Especially transient slab flattening or segmentation (already invoked to account for changes in spectral characteristics) will degrade the global correlation as the comparison between the two, fairly similar, subduction models shows. Inaccuracies in the advection process are, of course,

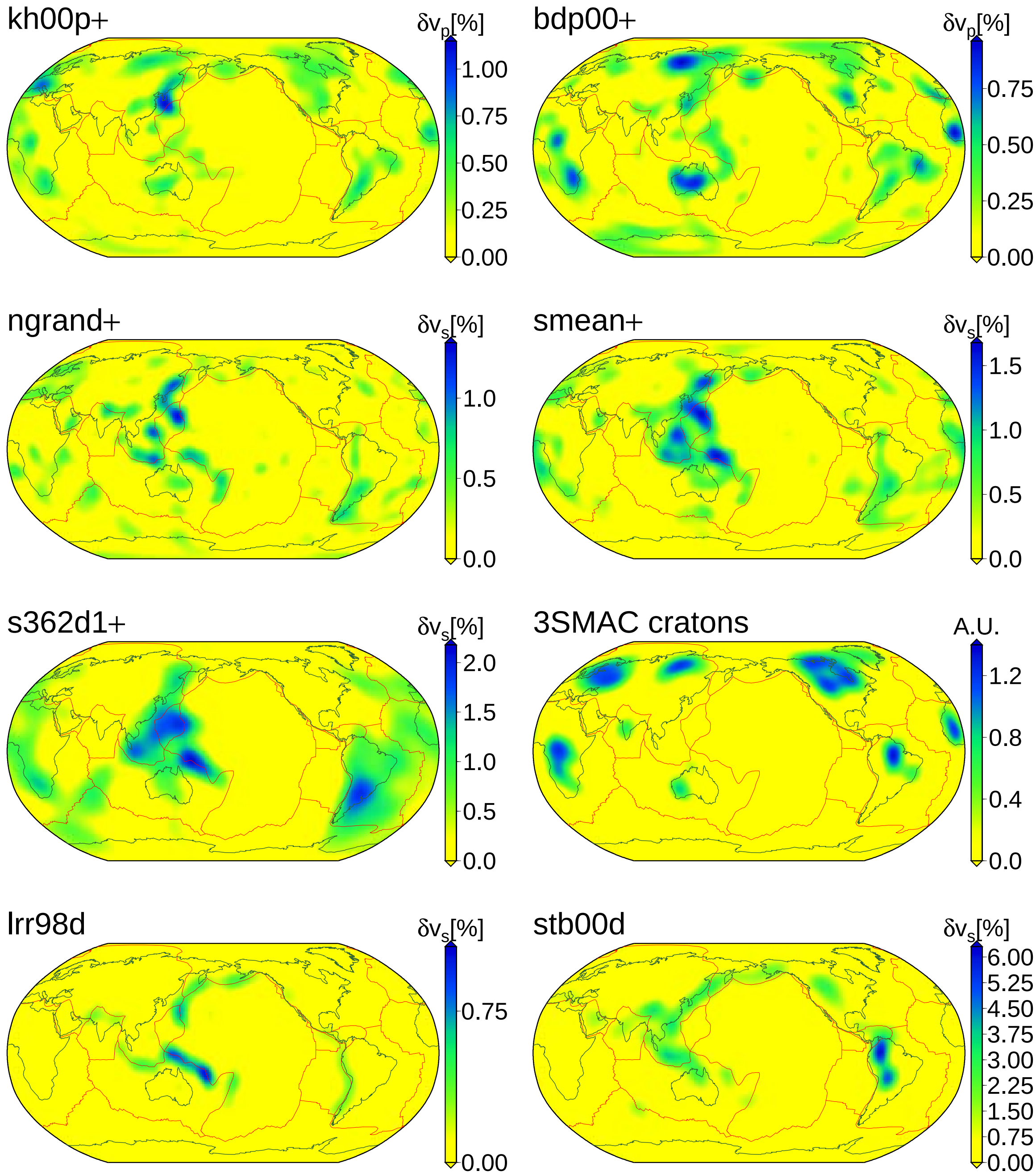

Figure 3.25: Comparison of tomographic models (positive δv only, "$+$"), old cratons from 3SMAC (Nataf and Ricard, 1996), and geodynamic models with $\ell_{\max} = 20$ at $z = 550$ km (average from 500 km to 600 km depth, $\delta z_{\text{box}} = 100$ km. Plate boundaries are from NUVEL-1 (DeMets *et al.*, 1990).

not the only possible explanation for the poor global agreement between subduction models and tomography. One question that needs to be considered is the precision to which we can infer past plate motions and how subsequent modifications in the reconstructions will map themselves into the large scale density field.

Mid-mantle slabs

Figures 3.25 and 3.26, including clipped tomographic and geodynamic maps above (550 km) and below 660 km (850 km), substantiate our finding that subduction models are most similar to tomographic ones at $z \sim 800$ km.

At 850 km depth (Figure 3.26), all models are remarkably consistent under the Americas, Indonesia, eastern Philippines, and Tonga, with a robust slab signal below 660 km. With the exception of the mantle below Africa, *s362d1* is the only model to include strong fast anomalies that are clearly not subduction-related. Some of the seismically active trenches (*e.g.* Japan, Kurile, Solomon, and Peru-Chile) are present at $z = 550$ km in all models (Figure 3.25). However, only *ngrand* includes a distinct image of the Tonga and Indonesia slabs; strong fast anomalies underneath North America appear only in the *P*-models. Also, older slab material might have accumulated in the Mediterranean (*e.g.* Wortel and Spakman, 2000): we can find such a signal most clearly in *kh00p*.

Figure 3.25 also shows that, at 550 km depth, all the *P*-models include other, probably not slab-related, fast anomalies beneath the cratonic regions of Canada, Africa, Eurasia and Australia. Since the tectosphere is believed to terminate at $z < 550$ km and *S*-models (well constrained in the upper mantle, see sec. 3.3.2) are not anomalously fast in the same regions, we suggest that these $\delta v_P > 0$ features are partly due to an artifact ("smearing") of the non-uniform coverage achieved by *P* body-wave data. Figures 3.27 – 3.29 show the correlation, at 550 km and 850 km, between clipped tomography models and, alternatively, *rum* (Figure 3.27), *stb00d* (Figure 3.28), and *lrr98d* (Figure 3.29). The correlation values that we find are statistically significant at the 99% level for most models at 850 km, and at least for *S*-models at 550 km depth. Again, we attribute the low correlation obtained from *P*-models in the upper mantle to the non-uniform ray coverage inherent to seismic observations of *P*-velocity (secs. 3.5.3 and 3.5.4). This is an important consideration if *P*-models are to be interpreted geodynamically as in the following chapters. In most cases, the highest values of tomography versus geodynamic correlation are found at ~ 850 km (sec. 3.5.4), confirming that most fast seismic anomalies found in the mid-mantle are slab-related.

Slow velocity anomalies

Identifying convective features in tomographic models is more difficult for slow than for fast wave speed anomalies. While slabs are of great importance for mantle convection (*e.g.* Davies and Richards, 1992) we also expect to see some trace of the upwellings, be it in the form of large scale swells or narrow plumes. It is not clear, however, if global tomography is able to image the latter features at this stage (*e.g.* Ritsema *et al.*, 1999).

To complement our correlation study for fast anomalies, we have expanded the hotspot lists of Steinberger (2000a) and 3SMAC (Nataf and Ricard, 1996) as negative δ-functions (damped with a $\cos^2$-taper for $\ell > 0.75\ell_{\max}$) and compared them to slow δv only tomography (r should be positive if hotspots are in $\delta v < 0$ regions). Figure 3.30 shows that we find only a weak correlation between surface observations of hotspots and slow anomalies that might be connected to rising plumes, consistent with earlier results (*e.g.* Ray and Anderson, 1994). The correlation is best near the surface, at ~ 1500 km, and at the CMB, the depths at which Figures 3.31 through 3.33 show the spatial expansions of the fields. As noted by Ray and Anderson (1994), there is no clear correlation between surface hotspot locations and tomographically mapped anomalies (the correlation is statistically significant only near the surface and at $z \sim 1500$ km). However, this does not imply that hotspots are not plume-related since plume conduits are likely to be deflected during their ascent (*e.g.* Steinberger, 2000a) and larger scale downwellings might affect the plume source locations in the deep mantle (*e.g.* Richards *et al.*, 1988; Steinberger and O'Connell, 1998).

Certain slow anomalies that are not ridge-related appear systematically in all tomographic models at $z =$ 300 km (see Figure 3.31): around the Afar region and Iceland (possibly related to plumes), in the south-western Pacific (possibly related to the superswell), and in the central Pacific region. The latter anomaly is of complex structure, widespread, and lies in a region where seismic observations are affected by strong radial anisotropy (Ekström and Dziewonski, 1998; Boschi and Ekström, 2002). At $z = 1500$ km (Figure 3.32), all models are dominated by two large anomalies centered on south-west Africa and the central Pacific (thus characterized by a strong $\ell = 2$ component); of these, at least the African one stretches down to the CMB in more than one model (*e.g.* Dziewonski, 1984). At 2500 km depth (Figure 3.33), we find that the African anomaly is accompanied by one underneath the Antarctic plate at 60°/60°S. The Pacific part of the $\ell = 2$ pattern can also be separated into three sub-anomalies, the western-most lying underneath the Nazca plate (see also Figure 3.1).

3.6 Conclusions

The spectra of seismic models of the Earth's mantle are predominantly of long spatial wavelength (*e.g.* Su and Dziewonski, 1992). We have found that the long-wavelength components of most tomographic models published

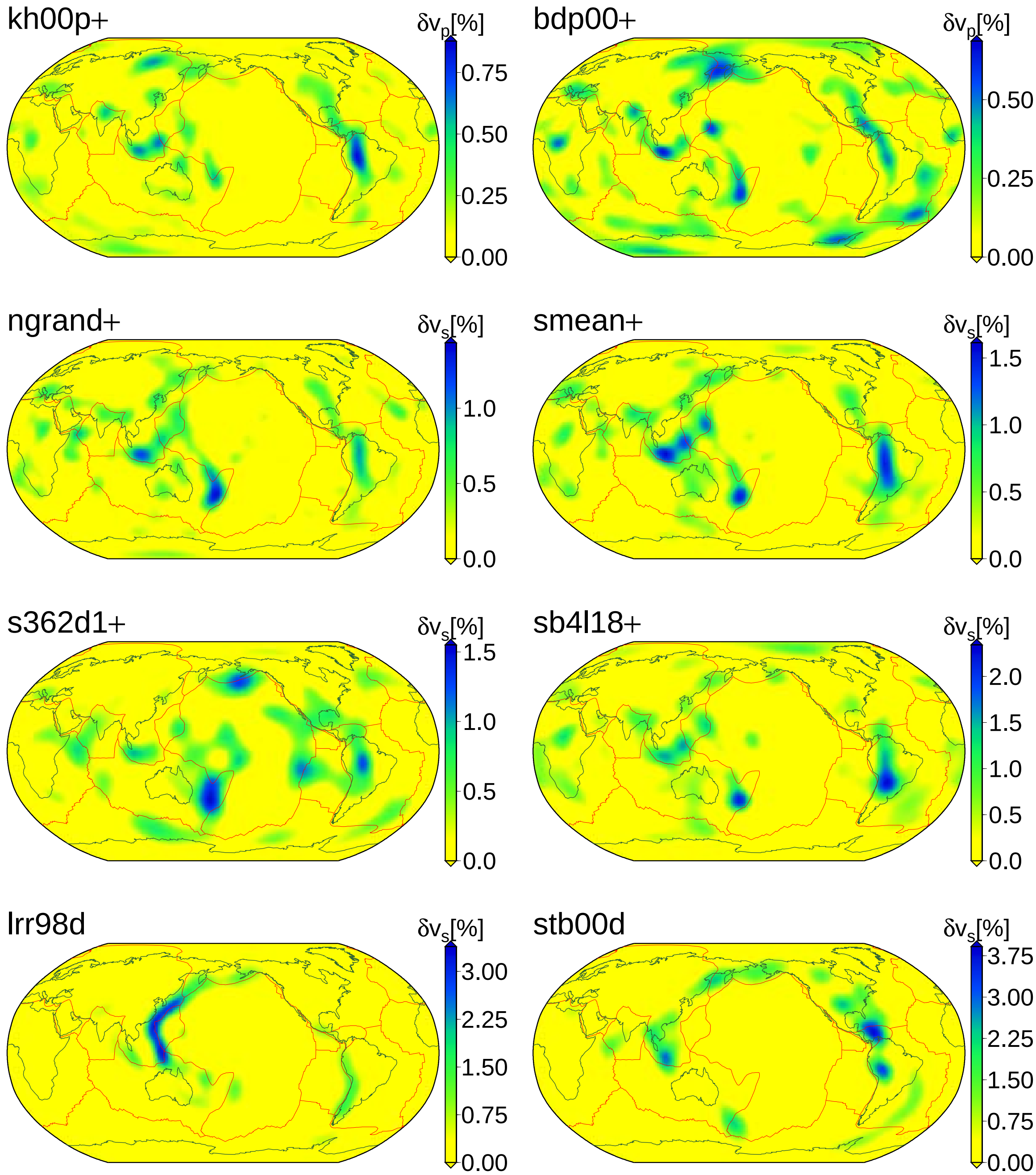

Figure 3.26: Comparison of positive δv only tomography and geodynamic models, $z = 850$ km (average from 800 km to 900 km). 3SMAC cratons were replaced with *sb4l18+*.

within the last decade are systematically well correlated with each other, indicating a substantial agreement between different techniques. As a general rule, correlation is highest in the lowermost mantle, where the coverage of teleseismic travel-time data is most uniform (*e.g.* van der Hilst *et al.*, 1997). Although most models are described with a fine lateral parameterization (at least up to spherical harmonic degree $\ell = 20$, or equivalent), correlation is always lower for shorter spatial wavelengths, especially for *S*-models. This suggests that, so far, attempts to image the smaller ($\sim$ 1000 km) scale structure of the mantle have not been equally successful. The correlation between models of the same type is significantly higher than when *P* and *S*-models are compared with each other. This discrepancy can partly be explained in terms of different sensitivities of the *P* and *S*-data sets to lateral structure

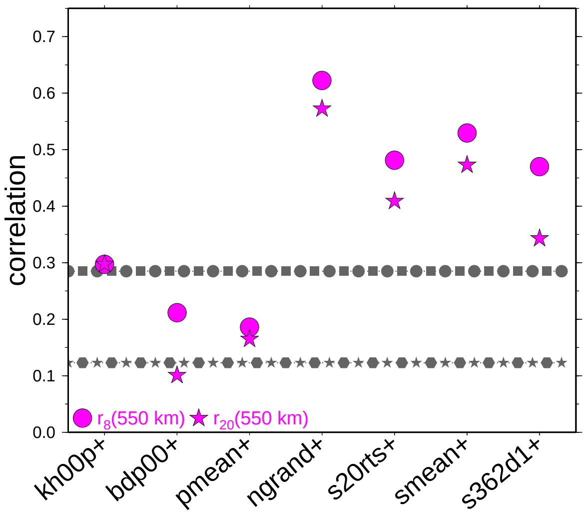

Figure 3.27: Correlation of fast anomaly only tomography and *rum* slab model. Symbols denote r_8^{tot} and r_{20}^{tot} for layer correlations at $z = 550$ km with $\delta z_{\text{box}} = 100$ km. Horizontal lines are 99% confidence levels.

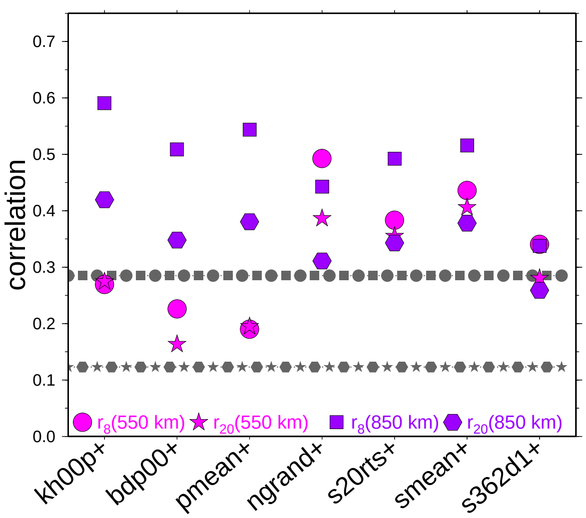

Figure 3.28: Correlation of fast anomaly only tomography and *stb00d* slab model. Symbols denote r_8^{tot} and r_{20}^{tot} for layer correlations at $z = 550$ km and $z = 850$ km with $\delta z_{\text{box}} = 100$ km.

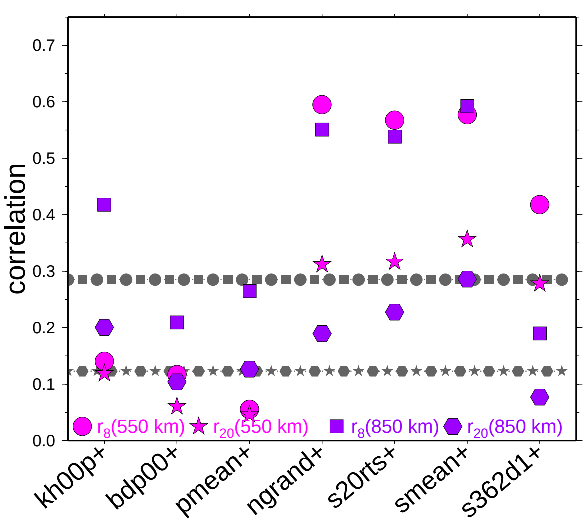

Figure 3.29: Correlation of fast anomaly only tomography and *lrr98d* slab model, see Figure 3.28.

(a) Steinberger (2000a) (b) 3SMAC

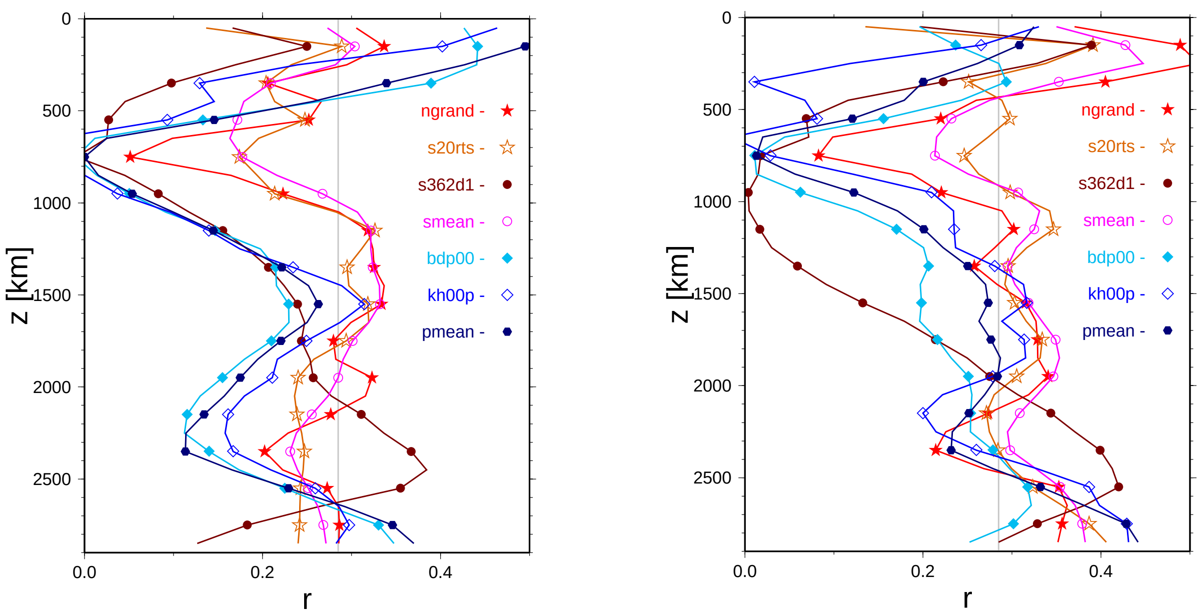

Figure 3.30: r_8^{tot} correlation between negative δv only tomography (appended "$-$") and hotspot function based on Steinberger (2000a) (a) and 3SMAC (b). Gray lines indicate 99% confidence levels. Compare with Figures 3.31 – 3.33.

at different depths. Correlation between δv_S and δv_P anomalies is lowest in the upper mantle and at the CMB where a common thermal origin might not be sufficient to explain the imaged heterogeneities but compositional anomalies could be invoked.

We found evidence for a change of the spectral character of heterogeneity below 660 km and local minima in the radial correlation function at $\sim$ 700 km for *S* and *P*-models but failed to detect strong layering or global discontinuities at other depths in the mantle. However, as the 660-km discontinuity model *s362d1* and cross-model discrepancies at $\sim$ 2000 km show, interesting depth ranges in the mantle coincide with those depths where tomographic model consistency is still limited. Tomography does not correlate well globally with models based upon geodynamic reconstructions of mantle flow for $\ell \gtrsim 5$; seismic observations and subduction history models do not yet produce identical images. We have, however, found that fast anomalies are imaged consistently in the mid-mantle where we would expect slabs in the absence of a long-term barrier to flow at 660 km. This substantiates previous studies (van der Hilst *et al.*, 1997; Čížková *et al.*, 1998; Bunge *et al.*, 1998), and slab penetration is found to be a common phenomenon. As discussed, it can be expected that future flow models will do a better job in predicting slab locations, and current discrepancies should lead to a better understanding of the nature of the subduction process.

Our results are consistent with an emerging whole mantle convection paradigm in which the phase transition –with a probable viscosity increase– at 660 km can lead to transient slab flattening and flow reorganization but, in the long term, subduction maintains a high mass flux between the upper and lower mantle.

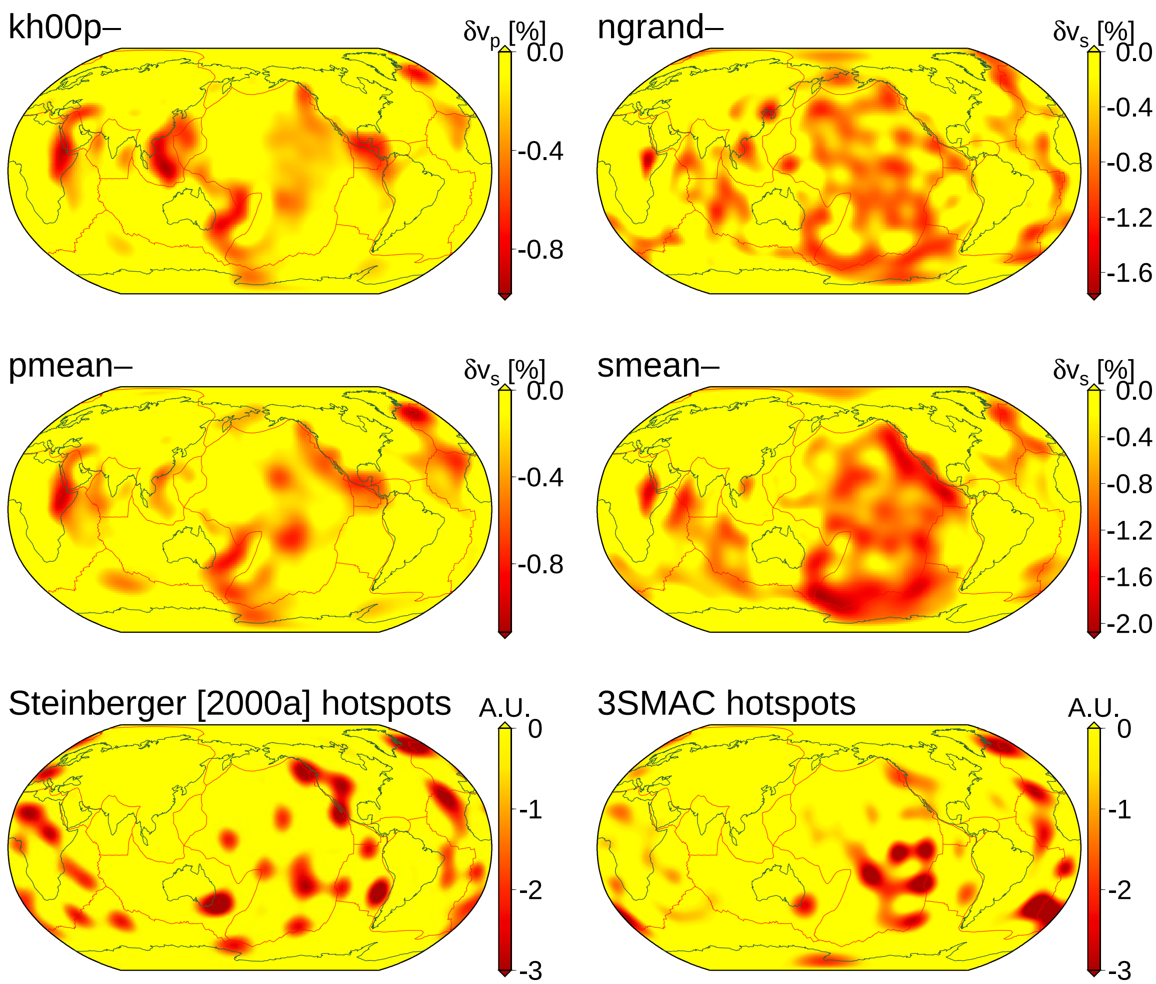

Figure 3.31: Comparison of negative δv only tomography and hotspot distributions (arbitrary units). $\ell_{\max} = 20$, and depth of tomography is $z = 300$ km. Hotspot fields are based on δ-function expansions of hotspot locations from Steinberger (2000a) and 3SMAC (Nataf and Ricard, 1996).

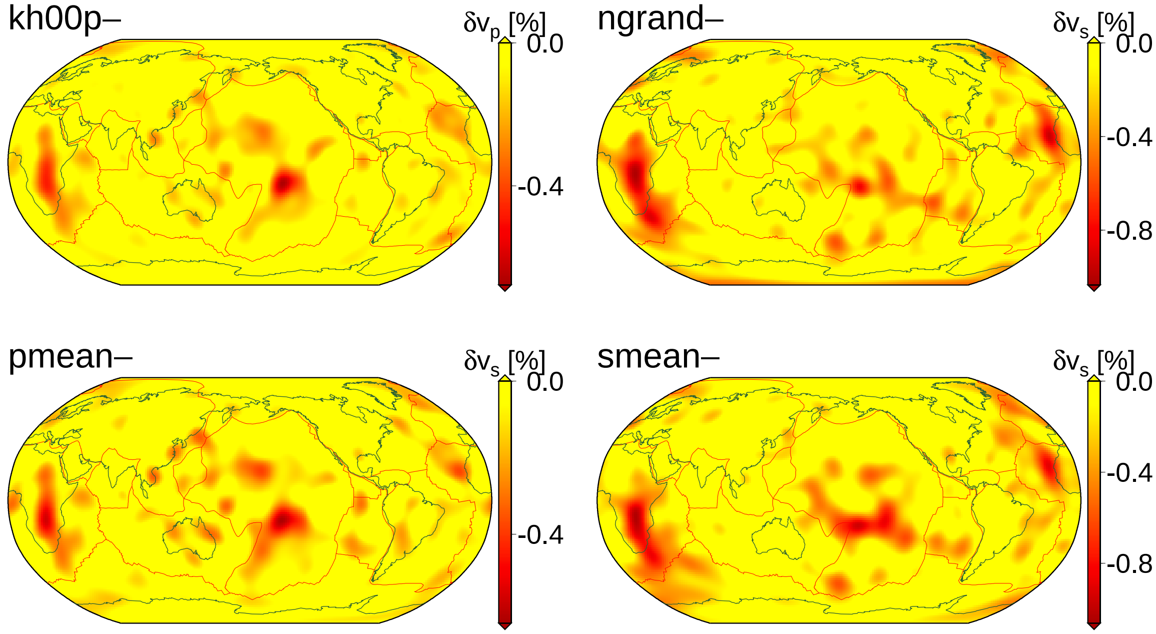

Figure 3.32: Negative δv only tomography at $z = 1500$ km.

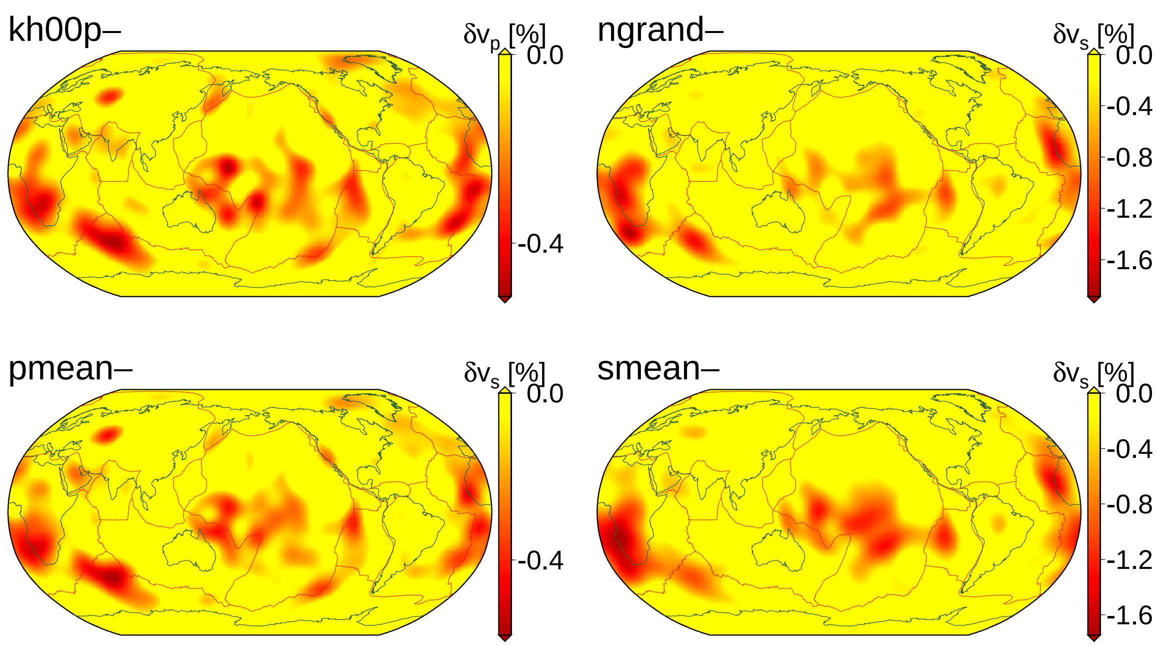

Figure 3.33: Negative δv only tomography at $z = 2500$ km.

Chapter 4

Predicting plate velocities with mantle circulation models

After studying the differences and similarities of various mantle models, we will now proceed to discuss plate driving forces. This will ensure that the global circulation models we construct are dynamically self-consistent.

4.1 Abstract

We predict plate motions from a comprehensive inversion of theoretical estimates of tectonic forces in order to evaluate the relative importance of these and the uncertainties of such models. Plate-driving forces from the mantle are calculated using global flow-models that are driven by tomography and subduction-derived density fields. Observed and predicted plate velocities agree well for a variety of models, leading to varied conclusions about the relative importance of forces. The importance of the subduction related density pattern in the mantle for driving plates is confirmed; it appears that *P*-wave models do not satisfactorily image all of the slab-associated anomalies in the upper mantle. Furthermore, lower mantle structure always improves the plate-motion fit with respect to models that are based on upper mantle anomalies and lithospheric thickening only. We show that the average torques from the lower mantle scale with the radial flow through the 660-km phase transition; the amplitude of the lower mantle torques will be significant for a range of models if there is mass flux through 660-km. We also evaluate parameterized edge forces and find that the additional inclusion of such torques does not significantly improve the model fit. The main reason for the non-uniqueness of the inversions is plate boundary geometry since all plate motions are dominated by the trench–ridge system, and plates move from ridges to trenches.

4.2 Introduction

It is now commonly accepted that plate motions are the surface expression of mantle convection. How the dynamic system plate tectonics should be broken down into parts to identify, isolate, and analyze the driving forces has, however, been debated for the last 30 years. As a recent AGU session shows (Bokelmann and Humphreys, 2000), there is continuing controversy with regard to the most basic issues and a division between seemingly distinct approaches persists. These modeling approaches can be roughly classified into two types: the force balance type (where the goal is to achieve a force equilibrium for each plate given the observed plate motions) or the velocity model type (where driving forces and resulting tractions are calculated first and model quality is subsequently judged from the plate motion predictions). Both approaches can be understood as alternative solutions to a boundary value problem but it is not known *a priori* if they give the same answer. However, one expects that they would approach one another as the errors in each became small (which would be the case for a completely linear model). In our study, we attempt to combine both approaches to understand why different combinations of plate driving forces are successful in predicting plate velocities.

Material in this chapter has been previously published in modified form in *Geochemistry, Geophysics, Geosystems* (Becker and O'Connell, 2001b).

Given its long-standing history, it is not feasible to give an exhaustive review of the problem here; the following account of previous work is necessarily incomplete. With regard to the quantifying of individual plate-driving forces, the role of sinking slabs and sub-lithospheric convection was mentioned by Isacks *et al.* (1968). McKenzie (1967, 1968) estimated the cooling of the oceanic lithosphere and the temperature structure of subducted slabs which provided the basis for subsequent calculation of driving forces. The role of horizontal structural variations and a low viscosity asthenosphere in driving plate motions was discussed by Hales (1969) and Lliboutry (1969); both considered plates sliding on topographic swells and neither explicitly considered the cooling lithosphere. However, cooling lithosphere, sinking slabs and sub-lithospheric convection were all implicitly included in the boundary layer model of Turcotte and Oxburgh (1967). Elsasser (1969) pointed out the importance of the lithosphere as a stress guide that integrates tractions acting over its surface. Richter (1973) then analyzed models of upper mantle convection beneath a plate, and emphasized the importance of subducted slabs for driving plate motions. The effect of the cooling lithosphere in providing a plate-driving force was clarified by Lister (1975).

The first to consider plate motions on a global scale were Solomon and Sleep (1974) who discussed the no net torque concept for the force equilibrium on the plates, Harper (1975) who calculated the forces from lithospheric cooling and sinking slabs for specific plates and used them to calculate plate velocities, and Forsyth and Uyeda (1975) who considered parameterized forces acting on all the plates and sought a force balance to constrain their estimates (Figure 4.1). The parameterized force model was broadened by Chapple and Tullis (1977) who included an explicit calculation of the sinking force from subducted slabs, thus constraining the magnitudes of the parameterized forces. Solomon *et al.* (1975) and Richardson *et al.* (1979) introduced the use of the intraplate stress field to test force models and found that ridge push was as important as other forces such as slab pull.

The three dimensional flow in the mantle associated with plate motions was calculated by Hager and O'Connell (1979) and included in a force balance model by Hager and O'Connell (1981). This model explicitly included forces from lithospheric cooling, density in subducted slabs, and flow in the mantle excited by sinking slabs and by the motions of plates, including the return flow from subduction zones to ridges. Forces on plate boundaries were parameterized (after Forsyth and Uyeda, 1975) and chosen to minimize the net force on each plate. The complementary approach –a velocity model– was presented by Ricard and Vigny (1989) who calculated forces from density heterogeneities associated with subducted slabs, and seismic tomography in the upper and lower mantle. They did not consider any forces on plate boundaries. The use of seismic tomography to estimate mantle density heterogeneity was introduced by Hager *et al.* (1985) in a study of the origin of the geoid, and Forte and Peltier (1987) used plate velocities to constrain the mantle viscosity. Among the more recent studies are those of Deparis *et al.* (1995) and Lithgow-Bertelloni and Richards (1995, 1998), who estimated density variations in the lower mantle from a model based on the locations of past subduction, and also considered the balance of forces acting on different plate configurations during the Cenozoic.

4.2.1 Objective of this study

Plausible models for forces causing plate motions can be found. The earlier models (Harper, 1975; Forsyth and Uyeda, 1975; Hager and O'Connell, 1981) all indicated that subducted slabs were important, but that other forces were comparable to the net force transmitted to the plate by the sinking slab. Later, Lithgow-Bertelloni and Richards (1998) found that for their best-fit model, lower mantle density variations resulting from past subduction were most important. Evaluating these studies is difficult because each uses different combinations of forces. We will therefore systematically investigate the role of all the forces that have been proposed in order to explore the range of uncertainty in the models. A velocity model will be used to test if candidates produce realistic plate motions in a simplified spherical flow-model, using rigid plates with the current geometry and radial viscosity profiles from the literature. As driving torques, we consider several models of lithospheric and mantle density structures, either based on seismic tomography or past subduction, and edge forces.

We find that models that account for mantle-based forces always achieve a better fit than models driven by lithospheric thickening and slab pull only. This result is insensitive to the details of the viscosity structure with depth, and the lower mantle will have a significant effect as long as there is mass flux through the 660-km discontinuity. We confirm earlier studies that indicate the importance of deep mantle density anomalies resulting from subduction (Deparis *et al.*, 1995; Lithgow-Bertelloni and Richards, 1998) and find that plate motions based on slab models are not significantly different from models that use seismic tomography to infer lower mantle densities. However, we demonstrate that estimates of the relative importance of different forces change with input model choice. This ambiguity is not resolved if parameterized plate boundary forces are introduced. While the

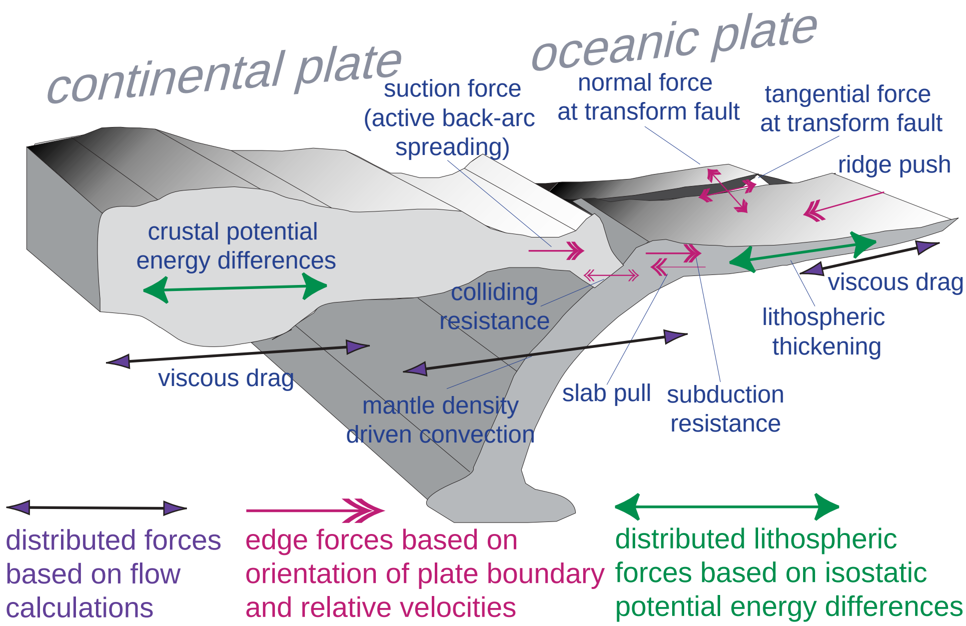

Figure 4.1: Forces acting on plates, modified after Forsyth and Uyeda (1975).

model fit can be improved when such forces are considered, the gain is small. We show that this is due to plate geometry, leading to strong (anti-)correlations between several driving and resisting forces. These trade-offs were noted before for the slab pull/subduction resistance pair (Forsyth and Uyeda, 1975); we demonstrate that all forces except the back-arc suction and the transform fault normal forces can be classified as either driving or resisting in a roughly uniform fashion.

4.3 Method

Our basic method of solving for plate velocities has been used for a thermal convection model with plates (Gable *et al.*, 1991), is similar to that of Ricard and Vigny (1989), and described in some detail by Lithgow-Bertelloni and Richards (1998). The discussion will therefore be brief.

4.3.1 Observed plate motions

We treat plate tectonics as a system of rigid plates and use the boundaries and Euler poles from NUVEL-1 (DeMets *et al.*, 1990) to define the individual plates (Figures A.1 – A.3). Since the no net torque condition for the force equilibrium of the plate motions can be fulfilled with any arbitrary rigid body rotation, we set this rotation to zero and use the no net rotation (NNR) reference frame for velocities. It has been shown that a net rotation of the lithosphere with respect to the mantle can only be excited in the presence of lateral viscosity variations (O'Connell *et al.*, 1991). As such variations are missing from our model, the NNR frame is the natural choice. Out of the original 14 plates of NUVEL-1, we ignore the Juan de Fuca plate since it is too small to yield a reliable velocity prediction. We treat the Australian(AUS)-Indian(IND) system as two plates, divided along an inferred plate boundary in the Indian ocean. We find that the inversion is not sensitive to this distinction since AUS and IND move in nearly the same direction.

4.3.2 Global flow-models

We model mantle convection as the instantaneous flow that solves the Navier–Stokes and continuity equations for the incompressible, infinite Prandtl number case given a known density anomaly distribution. If the viscosity varies only radially, the equations can be solved by the propagator matrix method (Hager and O'Connell, 1979, 1981), see sec. 2.3.1. Such an approach involves expanding fields into spherical harmonics, leading to well known problems: since velocities are discontinuous at the plate boundaries, theoretical stresses there are singular; the amplitude of the resolved stress depends on the maximum degree $\ell_{\max}$ of the expansion (Hager and O'Connell, 1981). Following Hager and O'Connell we circumvent this problem by evaluating all stresses below the viscous lithosphere at depth $z = 100$ km. It has been shown that the integrated torques using this approach are insensitive to $\ell_{\max}$ (Hager and O'Connell, 1981; Lithgow-Bertelloni and Richards, 1998). Our theoretical resolution is then limited mainly by the seismic tomography models, since we know plate boundaries and upper mantle slab locations to higher precision, and we will use $\ell_{\max} = 31$ for computational efficiency.

4.3.3 Torque balance and plate velocity solution

We interpret fast and slow regions of seismic anomalies as being purely thermal in origin (*e.g.* Hager *et al.*, 1985) except for the continental tectosphere. Thermal density anomalies then drive flow in the mantle and exert torques on the overlying lithosphere. The solution for plate velocities depends on the linearity of the momentum equation (*cf.* Gable *et al.*, 1991). Firstly, flow driven by density anomalies is calculated with a fixed surface (*i.e.* no plate motion), and the tractions on the base of each plate are evaluated. Secondly, the motions of plates will also cause flow that exerts viscous drag on their base; the corresponding tractions are evaluated for the motion of each individual plate. Thirdly, the plate velocities that are driven by internal flow are found from the superposition of these solutions that results in zero net torque on each plate. We write this condition as

$$\mathbf{T}_{\mathrm{vd}} = \mathbf{P} \cdot \omega = \sum_{i}^{M} \mathbf{T}_i, \tag{4.1}$$

where we have expressed the torque due to viscous drag $\mathbf{T}_{\mathrm{vd}}$ as the product of the interaction matrix $\mathbf{P}$ ($3N \times 3N$ components) with the plate rotation vector ω ($3N$ components), where N is the number of plates (13 in our case). $\mathbf{P}$ is calculated by prescribing unity velocities for each plate and calculating the resulting drag torques on all other plates (Gable, 1989). $\mathbf{T}_i$ are the driving torques from M various sources, such as lower and upper mantle flow, lithospheric contributions, and edge forces. Equation (4.1) is then solved for the plate rotations ω assuming that the $\mathbf{T}_i$ are known. We use singular value decomposition (*e.g.* Press *et al.*, 1993) and neglect small singular values to avoid the singularity of $\mathbf{P}$ (a rigid body rotation can be added to ω without affecting $\mathbf{P} \cdot \omega$). We therefore enforce the no net rotation reference frame for plate motions ω.

To determine torques that are based on tractions, σ, beneath plates we evaluate surface integrals of the type

$$\mathbf{T}_i = \int_{\mathrm{plate}} dA \, \mathbf{r} \times \sigma \tag{4.2}$$

numerically at 0.5 degree spacing. Here, $\mathbf{r}$ is the location vector, and dA indicates the plate area. Karpychev and Fleitout (1996) have argued that the detailed location of density anomalies is important when plate velocities are to be predicted because strong lateral variations of viscosity can be expected at plate margins. While we cannot treat such lateral variations with our model, we have explored a simplified scenario: the outcome if we do not consider tractions that are closer than ~ 200 km to a plate boundary. The torques that we calculate with this constraint are similar to those that use all tractions, implying that at least our large scale integrated torques are insensitive to the details of the density structure near plate boundaries.

Recently, Steinberger *et al.* (2001) developed a thin shell formulation for the elastic and viscous deformation of the lithosphere due to basal tractions, an extension of work by Bai *et al.* (1992). We found that the torques calculated when such deformation is included are larger in amplitude than our rigid plate torques by $\sim 15\%$ but similar in direction. Since the role of the deforming lithosphere can ultimately only be resolved if we allow for faulted margins and a more realistic rheology we will neglect the deformation of the lithosphere and rheological complexity in our current calculations.

4.3.4 Inversion for scaling parameters

The amplitude of torques that result from tomography-based flow calculations is proportional to the factor

$$R_{\rho}^{P,S} = \frac{d \ln \rho}{d \ln v_{P,S}} \tag{4.3}$$

that relates density anomalies, $d\ln\rho$, to P and S-wave anomalies, $d\ln v_{P,S}$, and all plate motion derived viscous drag torques scale with the absolute value of the viscosity, η_0. We allow these scaling factors to vary in order to minimize the difference between the calculated, ω^{mod}, and observed, ω^{obs}, plate rotation vectors. We use the downhill simplex method of Nelder and Mead (1965) for optimization (*e.g.* Press *et al.*, 1993, p. 408), and minimize the misfit by varying the scalar weight of $\mathbf{P}$ (factor w_1) and the driving torques $\mathbf{T}_i$ (factors $w_2 \ldots w_{M+1}$). The quality of fit is measured by the linear correlation coefficient, r, of the Cartesian components of the rotation vectors and the variance reduction, VR:

$$\mathrm{VR} = 1 - \xi^2/|\omega^{\mathrm{obs}}|^2 \quad \text{with} \quad \xi^2 = \sum_i^{3N} \left(\omega_i^{\mathrm{obs}} - \omega_i^{\mathrm{mod}}\right)^2. \tag{4.4}$$

We will present results in terms of the unweighted quantities r and VR and the plate-area weighted values r_w and VR_w. r_w is equivalent to the point by point correlation for surface velocities and, as noted by Lithgow-Bertelloni and Richards (1995), dominated by the large, fast plates like PAC.

The objective of the simplex method is to minimize VR_w (and therefore to maximize r_w). The final weights are then normalized such that $\sum_i w_i^2 = 1$ and, using a penalty formulation, we usually enforce that all weights $w_i \geq 0$. (This prohibits driving forces from changing sign and becoming resisting forces.) We tested our simplex procedure by comparison with a grid search for $M \leq 3$ and were able to find the global minimum to within $|\Delta r_w| \lesssim 0.003$. However, as we will show in sec. 4.4.4, many of the driving torques are highly correlated. This results in trade-offs that are responsible for the existence of numerous local minima in w_i-space that correspond to solutions of the inverse problem with only slightly poorer fits to plate motions than the global minimum.

4.4 Input models

We now analyze the input models that are used to derive estimates of the various types of plate-driving forces. Firstly, we discuss the mantle density fields as inferred from tomography and geodynamic models and, secondly, we study their degree of similarity. Thirdly, we explore different models of lithospheric thickening and ridge push. Lastly, we describe how we derive edge forces based on NUVEL-1 plate boundaries.

4.4.1 Seismic tomography

We assume that the anomalies that are imaged by seismic tomography are thermal in origin throughout all but the shallowest mantle (*e.g.* Hager *et al.*, 1985; Mitrovica and Forte, 1997). This is a simplification since velocity heterogeneities may well be due to compositional variations (*e.g.* Ishii and Tromp, 2001), although there is no consensus on this issue at present (*e.g.* Masters *et al.*, 2000; Tackley, 2000, and chapter 3). We also neglect depth-dependence of R_ρ (*e.g.* Karato, 1993) for simplicity but use typical starting values of $R_\rho^P = 0.4$ and $R_\rho^S = 0.2$. R_ρ can then be adjusted via the optimized weights w_i (sec. 4.3.4). We furthermore remove all structure shallower than 220 km depth from the tomographic models to account for the effect of the tectosphere where compositional differences are likely to cancel out the fast anomalies beneath cratons (*e.g.* Jordan, 1978; Forte *et al.*, 1995). For P-wave tomography, craton related structures are probably imaged at depths larger than 220 km (*e.g.* sec. 3.5.4); our cutoff value might therefore be too low for these models. In any case, we will see that best-fit inversions tend to include only lower mantle for P-wave models. Removing shallow structure also avoids counting lithospheric thickening twice since it is explicitly included as a separate torque. Several tomographic models were selected as representative of the current state of the art; they have been described in sec. 3.3.

4.4.2 Subduction models

Geodynamic subduction models are an alternative to tomography models, and if the assumptions that go into these models are correct, they should directly predict the location of density anomalies caused by sinking slabs, though not those due to independent upwellings. We consider two whole, and one upper mantle subduction model. Whole mantle model one (*lrr98d*) is by Lithgow-Bertelloni and Richards (1998), model two (*stb00d*) by Steinberger (2000b), and for the upper mantle part of the slab pull forces, we consider a third model that attributes a density anomaly of $\Delta\rho = 75\ \mathrm{kg/m^3}$ to each location where we observe seismicity in subducted lithosphere (*rum*). Wadati-Benioff zones were converted to a spherical harmonics model by integrating along the RUM slab contours

Table 4.1: Average densities of the lithospheric model for layers ic: ice, wa: water, $^{co}_{cr}$: continental crust, $^{co}_{ma}$: sub-continental mantle, $^{oc}_{ma}$: sub-oceanic mantle, $^{oc}_{li}$: oceanic lithosphere, and $^{oc}_{cr}$: oceanic crust.

type	*value* [kg/m^3]
ρ_{ic}	920
ρ_{wa}	1020
ρ^{co}_{cr}	2861
ρ^{co}_{ma}	3380
ρ^{oc}_{ma}	3350
ρ^{oc}_{li}	3412
ρ^{oc}_{cr}	2868

(Gudmundsson and Sambridge, 1998). We will furthermore contrast this seismically active upper mantle slab model with the upper mantle part of *lrr98d* to study the possible effect of older, aseismic slab material. All input models were discussed at length in chapter 3.

The slab pull that follows from flow calculations based on models like *rum* is a force that acts on both the subducting and the overriding plate because of the viscous drag of sinking slabs that is transferred to the base of the lithosphere. This is different from the common notion of a stress guide coupling the negative buoyancy of the subducting lithosphere to the oceanic plate only (*cf.* King *et al.*, 1992, for a comparison of different ways of treating slab forces). We find that our model predictions are actually better if we apply a two-sided drag force instead of a one-sided slab pull (see sec. 4.5.2). This might be because slabs are comparable in strength to the surrounding mantle (sec. 2.3) and it is the mantle flow that couples slab forces to the overlying plates.

4.4.3 Lithospheric contributions

Lateral variations in the density structure of the lithosphere can lead to deviatoric stresses and drive plate motions (*e.g.* Artyushkov, 1973; Lister, 1975; Hager, 1978; Fleitout and Froidevaux, 1982). These stresses can be derived from the gradient of the vertically averaged normal stress, $\bar{\sigma}_{rr}$, or equivalently from the potential energy per unit area, U. Variations in U for the oceanic plates are mainly due to sea-floor spreading and the age progression of the lithosphere which results in a distributed lithospheric thickening force (*e.g.* Hager, 1978). In continents, lateral gradients in U, ∇U, can be expected to be most pronounced around regions of high topography where forces arise from the tendency of orogens to collapse and spread. The effectiveness of intra-continental ∇U for plate-driving forces will depend on the rheology of the lower lithosphere; it will be most pronounced for regions where lateral variations are important down to the asthenosphere in young tectonic settings. Moreover, intraplate continental stresses that are not active across plate boundaries will tend to have little net effect on driving a plate. Hence, we will make a distinction between lithospheric models that are only based on oceanic contributions and global models that incorporate continental contributions as well.

Our approach is similar to that of Coblentz *et al.* (1994): We use an isostatic, long-wavelength and thin sheet approximation for the lithosphere. Solving for vertically averaged stresses, we can then relate the gradient in U to equivalent basal tractions, $\sigma_{\{r\theta,r\phi\}}$, (Fleitout and Froidevaux, 1983):

$$U(\theta,\phi) = \int_0^{L+\varepsilon} dr\, g\rho(r)r \tag{4.5}$$

$$\sigma_{\{r\theta,r\phi\}} \approx -L_0\nabla_{\{\theta,\phi\}}\bar{\sigma}_{rr} \tag{4.6}$$

$$= -\frac{L_0}{L}\nabla_{\{\theta,\phi\}}U \tag{4.7}$$

where L is the isostatic compensation depth ($L = 130$ km), L_0 is the lithospheric shell thickness ($L_0 = 100$ km), ε is elevation, g is gravitational acceleration ($g = 9.81$ m/s^2), ρ density, and $\nabla_{\{\theta,\phi\}}$ are the θ and ϕ components of the horizontal gradient operator, respectively.

We have used the 3SMAC model (Nataf and Ricard, 1996) to obtain ice thickness and extrapolated $2^\circ \times 2^\circ$ sea-floor ages from which we calculate an oceanic lithosphere model, using a modified half-space cooling progression for the water depth d_w:

$$d_w = 2600\,\text{m} + 345\,\text{m}\sqrt{t[\text{Ma}]} \quad \text{for} \quad t \leq 81\ \text{Ma} \quad \text{and} \tag{4.8}$$

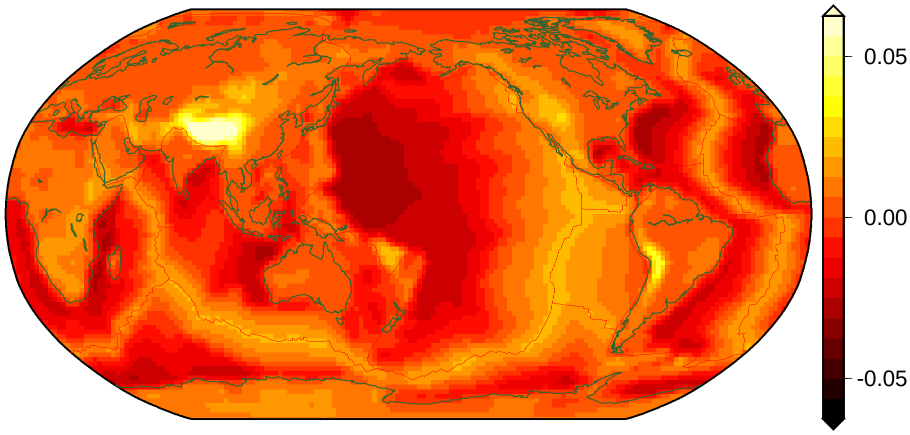

Figure 4.2: Differential potential energy $\Delta U = U - \bar{U}$ ($\bar{U} = 2.616 \cdot 10^{14}$ Jm^{-2}) of our $2^\circ \times 2^\circ$ model in units of 10^{14} Jm^{-2}. Min/mean/max values of ΔU for oceanic and continental lithosphere are $-0.03/-0.004/0.023$ and $-0.013/0.007/0.078$, respectively.

$$d_w = 6586\,\text{m} - 3200\,\text{m}\exp\left(\frac{-t[\text{Ma}]}{62.8}\right) \quad \text{for} \quad t > 81\text{ Ma} \tag{4.9}$$

(Parsons and Sclater, 1977; Carlson and Johnson, 1994). The thickness of the oceanic lithosphere, d_{li}^{oc}, is found from isostasy for constant ρ_{li}^{oc} and crustal thickness $d_{cr}^{oc} = 8$ km. This leads to a simplified model for the lithospheric thickening force with $d_{li}^{oc} \leq 100$ km. For continental areas, we correct a 2° smoothed ETOPO5 topography (NOAA, 1988) for the iceload and again determine an isostatic crustal thickness using average densities as given in Table 4.1. The resulting potential energy differences from a global mean of $\bar{U} = 2.616 \cdot 10^{14}$ J/m^2 are shown in Figure 4.2. As expected, the main variations are due to sea-floor age and large orogens.

Our model is a simplification of the actual lithospheric density variations, and we have strived to emphasize well constrained features like the sea-floor age. In addition, we have experimented with more detailed models of the continental crust such as CRUST 5.1 (Mooney *et al.*, 1998). We note, however, that CRUST 5.1 is not an isostatic model, but the topography has to be dynamically (Pari and Peltier, 2000) or compositionally supported in the mantle. Since we attempt to include dynamic effects in our flow-models and want to exclude cratonic tectosphere, we will limit ourselves to isostatic models at this point.

After taking the gradient of U we derive tractions from (4.7); integration yields the driving torques that are shown together with Coblentz *et al.*'s (1994) results in Figure 4.3. We have chosen to evaluate the torques as equivalent forces at the plate centroids instead of showing a force field to allow for easier comparison between different driving torques. The predictions from our model are similar to those of Coblentz *et al.* (1994), especially for the torques that are based solely on oceanic lithosphere. There are some differences, however, and correlations of torque directions with NNR plate velocities are better (worse) for Coblentz *et al.*'s (1994) model for oceanic-only (continental topography included) torques. Discrepancies might in part be due the plate boundaries used by Coblentz *et al.* which are somewhat different from ours (*e.g.* AUS/IND was treated as one plate). We have attempted a first-order correction by scaling with modified plate areas when given but some of the remaining differences might simply have a geometric origin.

We furthermore find that the ridge push torques in Figure 4.3, which are based on parameterized edge forces, are similar to sea-floor age derived lithospheric thickening. Ridge push actually leads to a better correlation with plate motions than the field derived torques. This implies that plate motion changes in the last 180 Ma have little effect with regard to integrated, age-based torques. For most plates with a substantial oceanic part, the resolved forces agree well with plate motions (*c.f.* Richardson *et al.*, 1979; Richardson, 1992) although SAM and PHI are exceptions. For the latter plate, this might be due to the poorly constrained age structure.

The correlation of resolved forces with NNR-NUVEL-1 velocities is one measure of the degree of alignment between torques and observed velocities, and it is appropriate to compare NNR reference frame derived torques

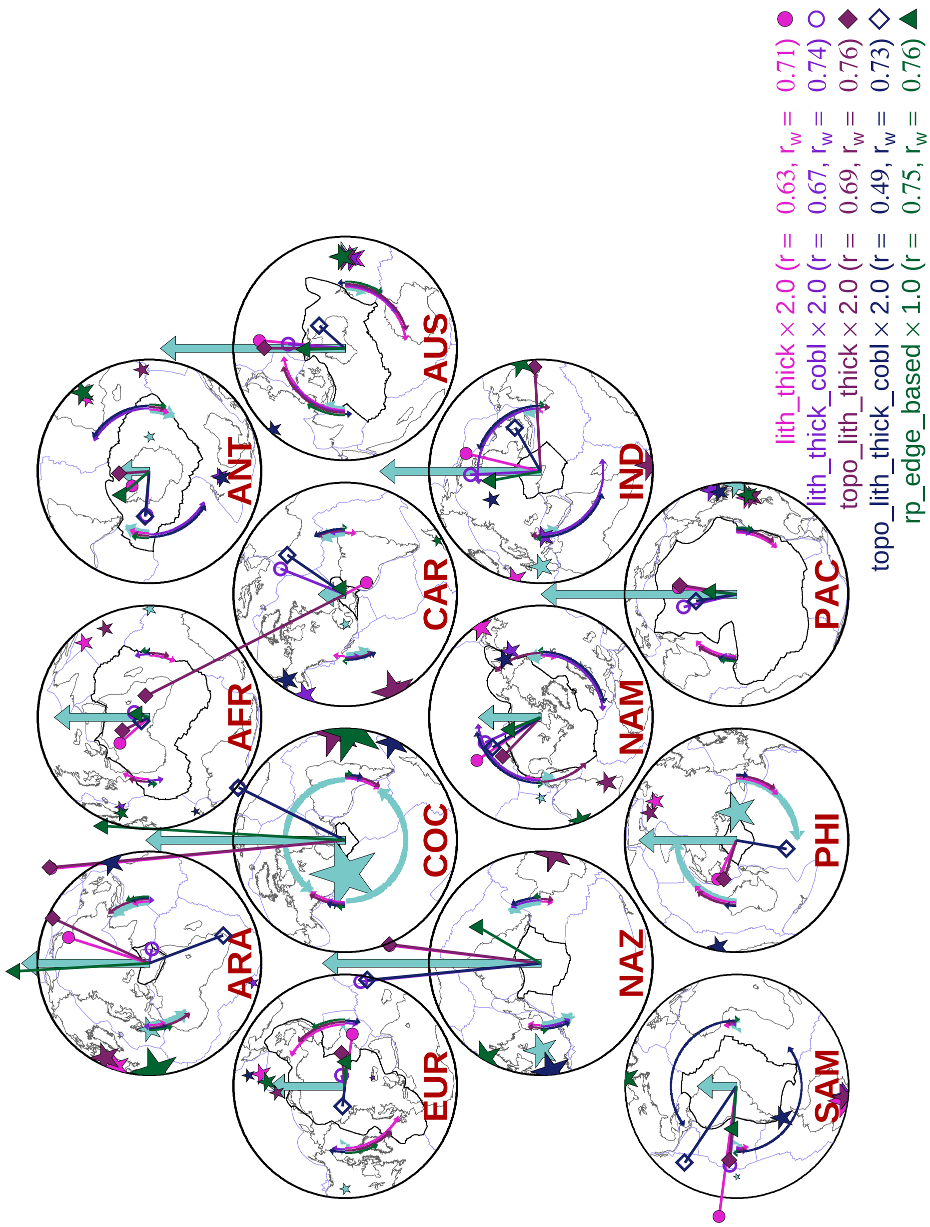

Figure 4.3: Lithospheric torques per plate area based on our lithospheric model (oceans only, *lith_thick*, or whole Earth including continental topography, *topo_lith_thick*), Coblentz *et al.* (1994) (*lith_thick_cobl* and *topo_lith_thick_cobl*), and our ridge push estimate from edge forces (sec. 4.4.4). We show NNR-NUVEL-1 plate motions (thick vectors, maps are rotated accordingly to aid comparison) and boundaries; vectors indicate velocity/horizontal force if the Euler poles/torque vectors are evaluated at the plate centroid. The rotational component of the Euler pole/torque vector is indicated by two arc segments; while arc lengths have the same scaling in all plots they are not drawn to scale compared to the force vectors. Also shown are the Euler/torque pole axes (stars); sizes scale with the magnitude. The legend lists torque scaling factors, w_i, and the overall (plate area weighted) correlation r (r_w) of the normalized resolved forces and plate velocities at the centroid.

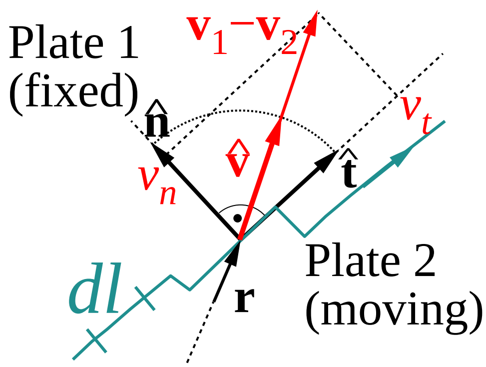

Figure 4.4: Geometric quantities for the integration of edge forces acting on plate 1.

with NNR plate velocities. However, if the model would be able to produce a net rotation of the lithosphere, other reference frames could be realized. We can indeed find a rigid body rotation such that the resulting correlations are improved up to $r_w = 0.92$ for our and Coblentz *et al.*'s (1994) lithospheric thickening model. This optimal reference frame minimizes the motion of continental areas and causes the oceanic plate cooling derived torques to align better with absolute plate velocities.

We note that the basic observation that the ridge–trench geometry is directly related to tectonic plate motions (Gordon *et al.*, 1978) explains the good correlation between all ridge push torques and plate velocities. This relationship makes it hard to distinguish between the various contributions of driving forces, as we will discuss below.

4.4.4 Plate boundary forces

In addition to traction based torques, we also consider globally parameterized edge forces that act along plate boundaries. Such torques have been neglected in previous plate velocity inversions although they were included in force balance models (Forsyth and Uyeda, 1975; Chapple and Tullis, 1977; Hager and O'Connell, 1981). Based on the classification by Forsyth and Uyeda (1975), we calculate the following contributions for all plates, listed in Table 4.2 (see Figures 4.1 and A.1 – A.3):

$$\begin{Bmatrix} T_{\text{tft}} \\ T_{\text{tftw}} \end{Bmatrix} = C_1 \quad \int_{\text{TF}} \, dl \begin{Bmatrix} sgn(v_t) \\ \frac{v_t}{v_t^{\max}} \end{Bmatrix} (\mathbf{r} \times \hat{\mathbf{t}}) \tag{4.10}$$

$$T_{\text{tfn}} = C_1 \quad \int_{\text{TF}} \, dl \; \mathbf{r} \times \hat{\mathbf{n}} \tag{4.11}$$

$$\begin{Bmatrix} T_{\text{sp}} \\ T_{\text{spw}} \\ T_{\text{sdr}} \\ T_{\text{sdrw}} \end{Bmatrix} = \quad \int_{\text{SP}} \, dl \begin{Bmatrix} -C_2 \\ -C_2 \sqrt{\frac{t[\text{Ma}]}{180}} \\ C_1 \\ C_1 \frac{v_n}{v_n^{\max}} \end{Bmatrix} (\mathbf{r} \times \hat{\mathbf{n}}) \tag{4.12}$$

$$\begin{Bmatrix} T_{\text{crnv}} \\ T_{\text{cr}} \\ T_{\text{crw}} \end{Bmatrix} = C_1 \quad \int_{\text{TR}} \, dl \; \mathbf{r} \times \begin{Bmatrix} \hat{\mathbf{n}} \\ \hat{\mathbf{v}} \\ \frac{\mathbf{v}}{|\mathbf{v}|^{\max}} \end{Bmatrix} \tag{4.13}$$

$$T_{\text{bas}} = -C_1 \quad \int_{\text{OP}} \, dl \; \mathbf{r} \times \hat{\mathbf{n}} \tag{4.14}$$

$$T_{\text{rp}} = C_1 \quad \int_{\text{SR}} \, dl \; \mathbf{r} \times \hat{\mathbf{n}} \tag{4.15}$$

Here, $\int dl$ means integration along the appropriate plate boundary segments, $\hat{\mathbf{n}}$ and $\hat{\mathbf{t}}$ are unit vectors normal and tangent to the boundary, $\hat{\mathbf{v}}$ is the unity relative motion vector, and v_n and v_t are the relative motion components in the the $\hat{\mathbf{n}}$ and $\hat{\mathbf{t}}$ directions, respectively (Figure 4.4). The boundary types are TF: transform fault; SP: trench, acting only at the subducting plate; TR: trench, at both plates; OP: trench, only at overriding plate; and SR: spreading ridge.

The force magnitudes are poorly constrained *a priori*; we have therefore set the factors $C_1 = 2 \cdot 10^{12}$ N/m and $C_2 = 2 \cdot 10^{13}$ N/m, on the order of typical estimates for lithospheric thickening and slab pull, respectively (*e.g.*

Table 4.2: Torque type abbreviations, compare (4.10) – (4.15).

abbreviation	*description*
tft	transform fault tangential
tftw	weighted *tft*
tfn	transform normal
sp	slab pull
spw	weighted *sp*
sdr	subduction resistance
sdrw	weighted *sdr*
cr	colliding resistance
crnv	*cr* no velocity dependence
crw	weighted *cr*
bas	back-arc suction
rp	ridge push

Turcotte and Schubert, 1982). C_1 and C_2 are also equivalent to the integrated strength of a plate margin with a yield stress of 200 MPa and depth extents of 10 km and 100 km, respectively. We have chosen the signs of the edge forces such that *sp*, *spw*, *bas*, and *rp* are driving, and *tft*, *tftw*, *tfn*, *sdr*, *sdrw*, *cr*, *crnv*, and *crw* are resisting plate motion.

We numerically compute the integrals in (4.10) through (4.15) along the NUVEL-1 boundaries using segment lengths of 0.2°. Since plate boundaries and Euler poles are better determined now than 25 years ago, our torques should be an improvement over the work of Forsyth and Uyeda (1975). There is, however, some arbitrariness in the definition of the margin types: Our rule for discerning between transform and convergent/divergent margins is that boundaries are of the transform type when relative motion is at an angle smaller than 25 ° to the tangential. We use the RUM Wadati-Benioff zone model to decide if the plate boundary is converging with or without a seismic slab and which plate is subducting. For *spw*, we need the sea-floor age at the trench which is poorly constrained at some subduction zones (*cf.* Müller *et al.*, 1997). We therefore extrapolate ages based on the 3SMAC model. All relative velocities $\mathbf{v}_1 - \mathbf{v}_2$ are calculated from NUVEL-1 and are then used to calculate edge torques for plate motion inversions. If those torques depend on the observed velocities, this procedure is not self-consistent. However, as we show in sec. 4.5.2, parameterized edge forces do not improve the plate motion fit significantly. Thus, we will not attempt to find a more consistent solution by including the velocity dependent torques on the left hand side of (4.1).

Figure 4.5 shows a comparison between some of the edge torques. A quantitative analysis of the interdependence of the different forces can be done by calculating the correlation matrix of the torque vectors. Forsyth and Uyeda (1975) pointed out that the strongest (anti-)correlation is that between the slab pull (*sp*) and the weighted subduction resistance at the trench (*sdrw*). If we consider (4.12), it is clear why this is the case: *sp* and *sdrw* are derived from integrating the same plate boundaries; their only difference is the pre-factor, $C_1 v_n / v_n^{\max}$ for *sdrw*. If the small deviations that are introduced by the velocities are neglected, *sp* and *sdrw* are exactly anti-correlated. The dominance of such strong correlations between different components of the plate-driving force inversion has been noted before (Forsyth and Uyeda, 1975; Backus *et al.*, 1981) but it is worthwhile to point out that they are simply geometric in origin. Any force balance model that is based on similar integration rules will be dominated by plate geometry effects that render the analysis of the physical processes at plate boundaries extremely difficult.

Figure 4.6 shows the correlations for some of the edge and area-based torques: "plate_motion_D" is the viscous drag resistance to plate motion that we find for a 3-D flow calculation using viscosity profile η_D (sec. 4.5) and prescribing the NUVEL-1 NNR plate motions, $\mathbf{v}_{\mathrm{NNR}}$, at the surface (sec. 4.5.2). In comparison, we can resort to a simplified estimate of the viscous drag by assuming that tractions are given directly by $-\mathbf{v}_{\mathrm{NNR}}$, either underneath all plates ("visc_dragnnr") or only under cratons ("visc_dragnnr_craton"). It has been pointed out that these viscous drags are not identical (Hager and O'Connell, 1981); deviations vary between plates, and are strongest for SAM, NAM, EUR, and ARA. In Figure 4.6, we also show correlations for driving torques for *rum* ("rum_D") and tomographic model *s20rts* ("s20rts_whole_mantle_D") that can be compared to the edge based slab pull (*sp*), the lithospheric thickening ("lith_thick"), and the ridge push edge force (*rp*). This analysis shows that only the suction

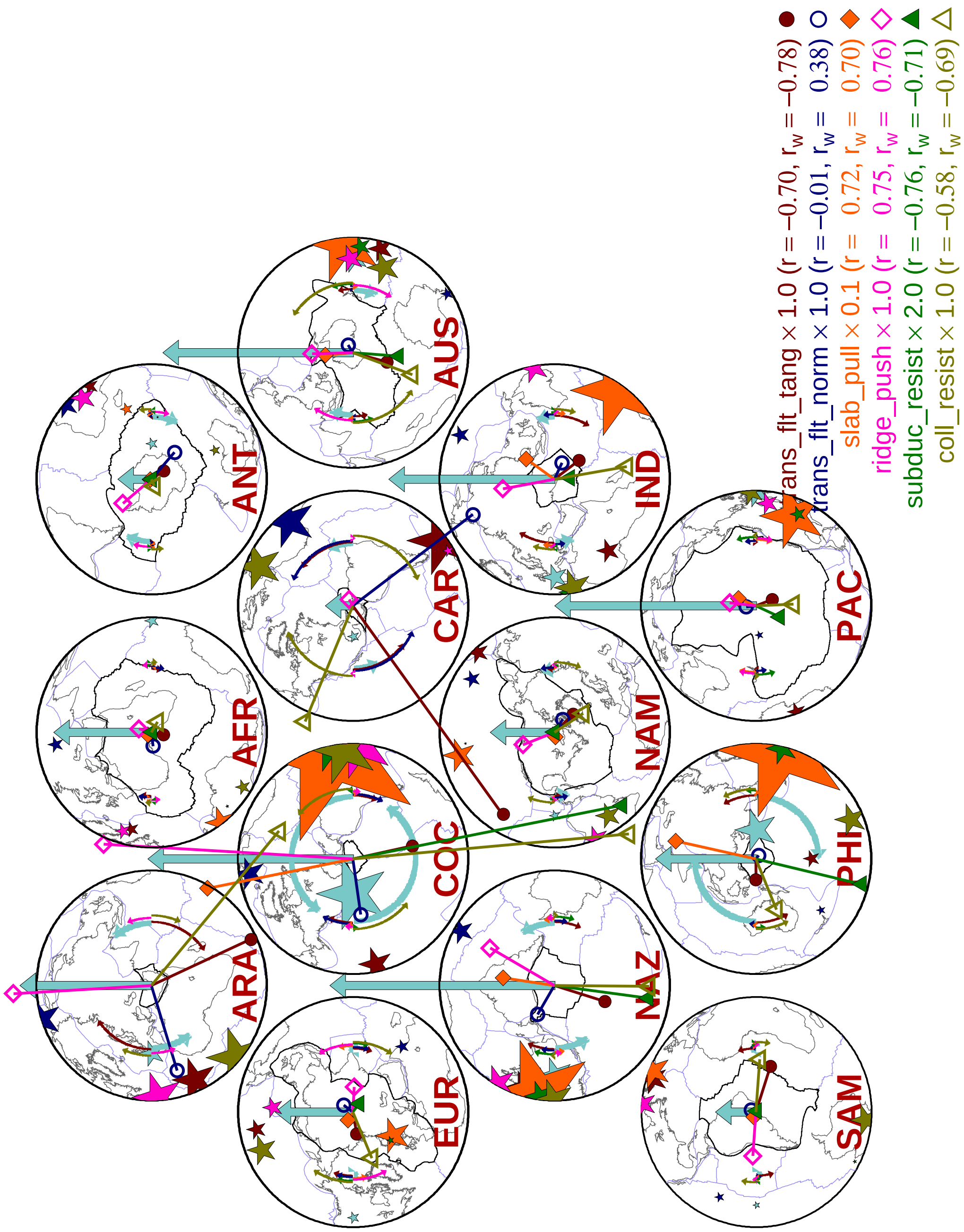

Figure 4.5: Comparison of edge force derived driving torques, for explanation see Figure 4.3.

force (*bas*) and the force that is normal to transform faults (*tfn*) do not consistently correlate with any of the other forces. It also implies that a number of different models of driving forces can be expected to yield good plate motion fits.

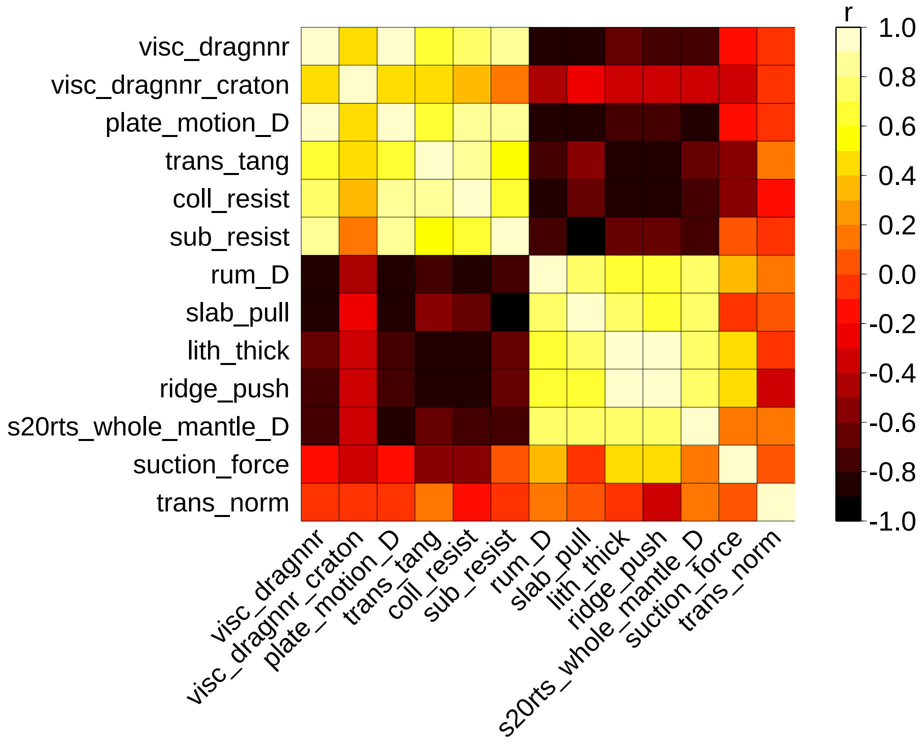

Figure 4.6: Correlation matrix for driving and resisting torques calculated by comparing the $3N$ components of the torque vectors.

4.5 Results and discussion

We now discuss flow-model based torques which represent the driving effect of the mantle. Subsequently, we will use these torques in plate motion inversions. At this point, we do not invert for other geophysical observables such as the geoid or intraplate stresses but use typical scalings and viscosity profiles that have been determined by other studies. Figure 4.7 shows the viscosity structures we consider: η_C is a generic model with an increase in viscosity in the lower mantle, η_D has an asthenospheric channel, η_E a weaker lithosphere than η_C, η_F has been used by Steinberger (2000b) for *stb00d*, and η_G and η_H are from an inversion by Mitrovica and Forte (1997). η_E is similar to the best-fit viscosity structure from Lithgow-Bertelloni and Richards (1998) and has the factor 50 increase in the lower mantle as used to construct *lrr98d*. We will discuss model resolution with respect to viscosity structure in sec. 4.5.2.

4.5.1 Mantle driving torques

Figure 4.8 shows an example of driving torques that result from flow-models; we have used viscosity η_D and the density models as described in sec. 4.4. We note that using slab model derived torques that are based on viscosity structures other than that used in the slab advection calculations itself (upper/lower mantle jump as in η_E for *lrr98d*, η_F for *stb00d*) is slightly inconsistent. Deviations should be small, however, as we will see in sec. 4.5.2. The whole-mantle torques of Figure 4.8 can be compared with Figure 4.9, which shows the torques that result from lower mantle structure only.

Table 4.3 gives the average fraction of the torque contribution of the lower mantle when we use different viscosity profiles. We use two measures for the strength of the driving forces: mean absolute torque, $\overline{T}_{\text{abs}}$, which is obtained by averaging all local torque magnitudes, $|\mathbf{T}|$, on the surface of the Earth ($\overline{T}_{\text{abs}}$ is Earth's radius times the mean horizontal traction magnitude), and average torque, T_{avg}, which is determined by plate-area weighted averaging of the integrated plate torques. T_{avg} contains information about the current plate geometry.

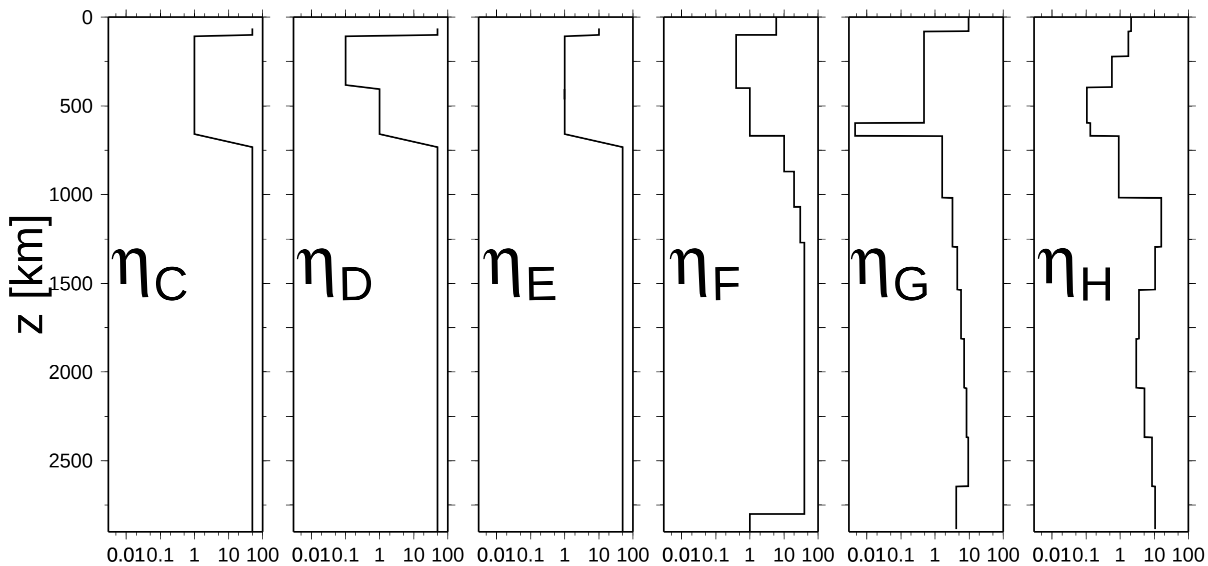

Figure 4.7: Viscosity profiles as used in the flow-models, units are 10^{21} Pas.

model	$\bar{T}_{\text{abs}}$ [%]	T_{avg} [%]
bdp00	59 ± 7	52 ± 6
kh00p	59 ± 2	68 ± 6
s20rts	68 ± 2	71 ± 2
sb4l18	68 ± 5	69 ± 5
ngrand	74 ± 3	85 ± 2
lrr98d	91 ± 1	84 ± 1
stb00d	63 ± 4	56 ± 4

Table 4.3: Average $\pm$ standard deviation of the fractions of $\bar{T}_{\text{abs}}$ and T_{avg} that are caused by the lower mantle for different viscosity profiles η_i as in Figure 4.7.

We find that a substantial fraction ($\sim$ 70%) of the absolute mantle based torques on the plates result from lower mantle structure (comparable to the volumetric fraction of the lower mantle, 66%), with small variations with the viscosity structure and moderate dependence on the model type. *lrr98d*'s lower mantle fraction is the largest overall; this is likely due to the strong increase in the density heterogeneity signal from upper to lower mantle (sec. 3.5.1).

Figure 4.8 indicates that, for some plates, different mantle models result in substantial variations in driving torque directions. For the smaller plates such as ARA, COC, and CAR, these differences are emphasized since we normalize by the plate area, and small plates are also at the limit of our model resolution. In general, however, correlations between resolved forces and plate velocities are again found to be good (AFR, CAR, NAM, and SAM being the exceptions). They are best for geodynamic models ($r_w \approx 0.83$), slightly poorer for *S*-wave models ($r_w \approx 0.67$), and poorest for *P*-wave models ($r_w \approx 0.29$).

We can compare the global correlation of individual torques (Figure 4.10) with the correlations between the input models (Figure 3.20) to observe that the driving torques show a higher correlation with each other than do the input models. This can be expected since torques are integrated tractions and are therefore smoother than the density variations. We also find that *S*-wave and subduction-model derived torques are more similar than *P*-wave model torques, an observation that is mirrored in the model performance in terms of plate motion inversions (sec. 4.5.2). The reason for this appears to be structure in the upper mantle that is important for slab pull forces. While *P*-wave tomography images slabs in some subduction zones (*e.g.* van der Hilst *et al.*, 1997), other seismically fast structure in the *P*-models –mostly correlated with cratons– probably offsets the upper mantle slab signature when tomography is scaled to density anomalies. *S*-wave models have a more even data coverage in the upper mantle since they can rely on surface wave observations which are not limited by the ray-path incidence which is nearly vertical at shallow depths (see sections 3.3.2 and 3.5.2).

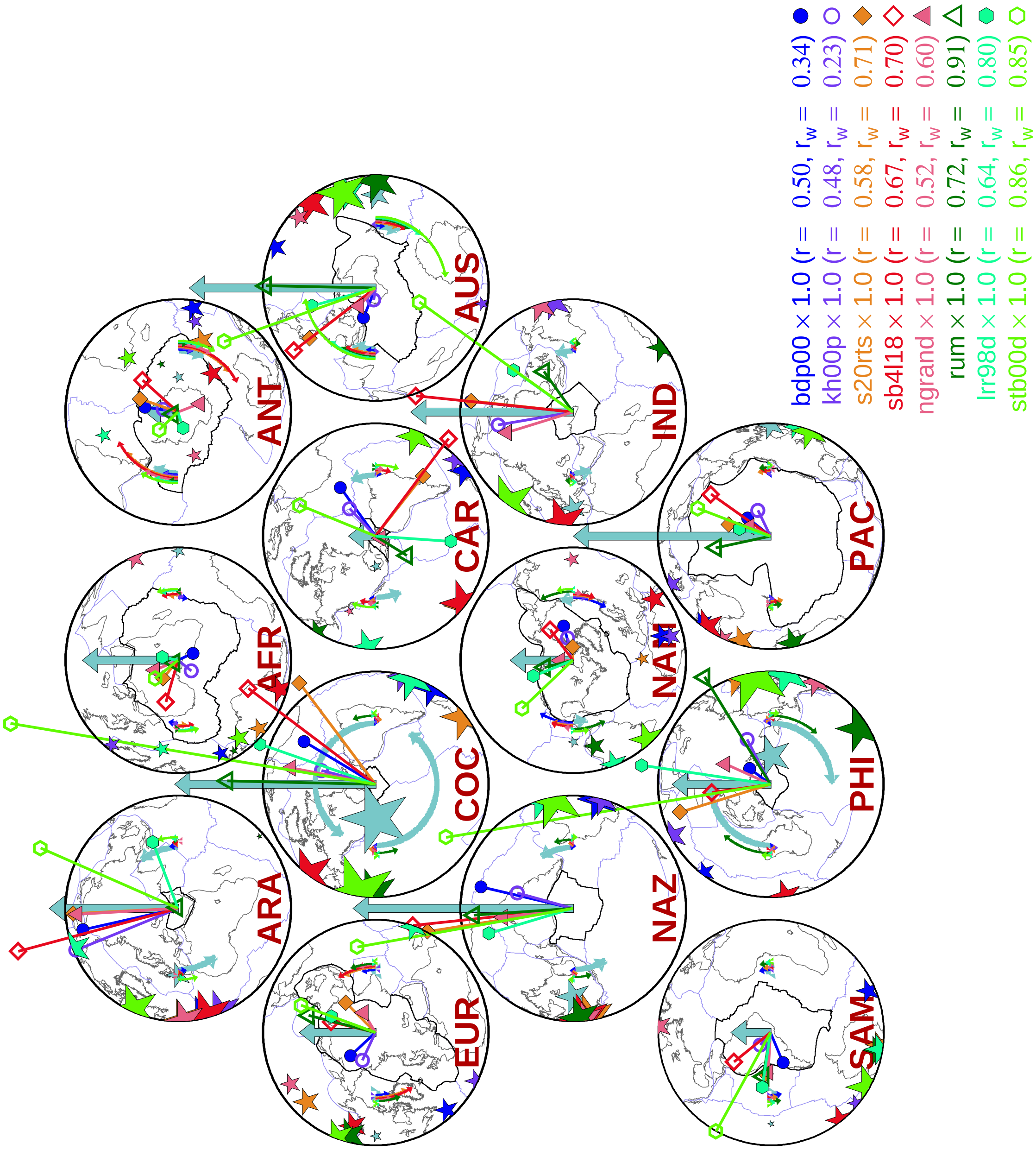

Figure 4.8: Comparison of mantle based driving torques for viscosity profile η_D. For explanation see Figure 4.3.

4.5.2 Plate motion inversions

We conducted numerous plate velocity inversions using different combinations of input models and viscosity structures and will now describe some of the successful models. By introducing different types of driving forces step by step, we attempt to develop a deeper understanding of their role in driving the plates and try to assess

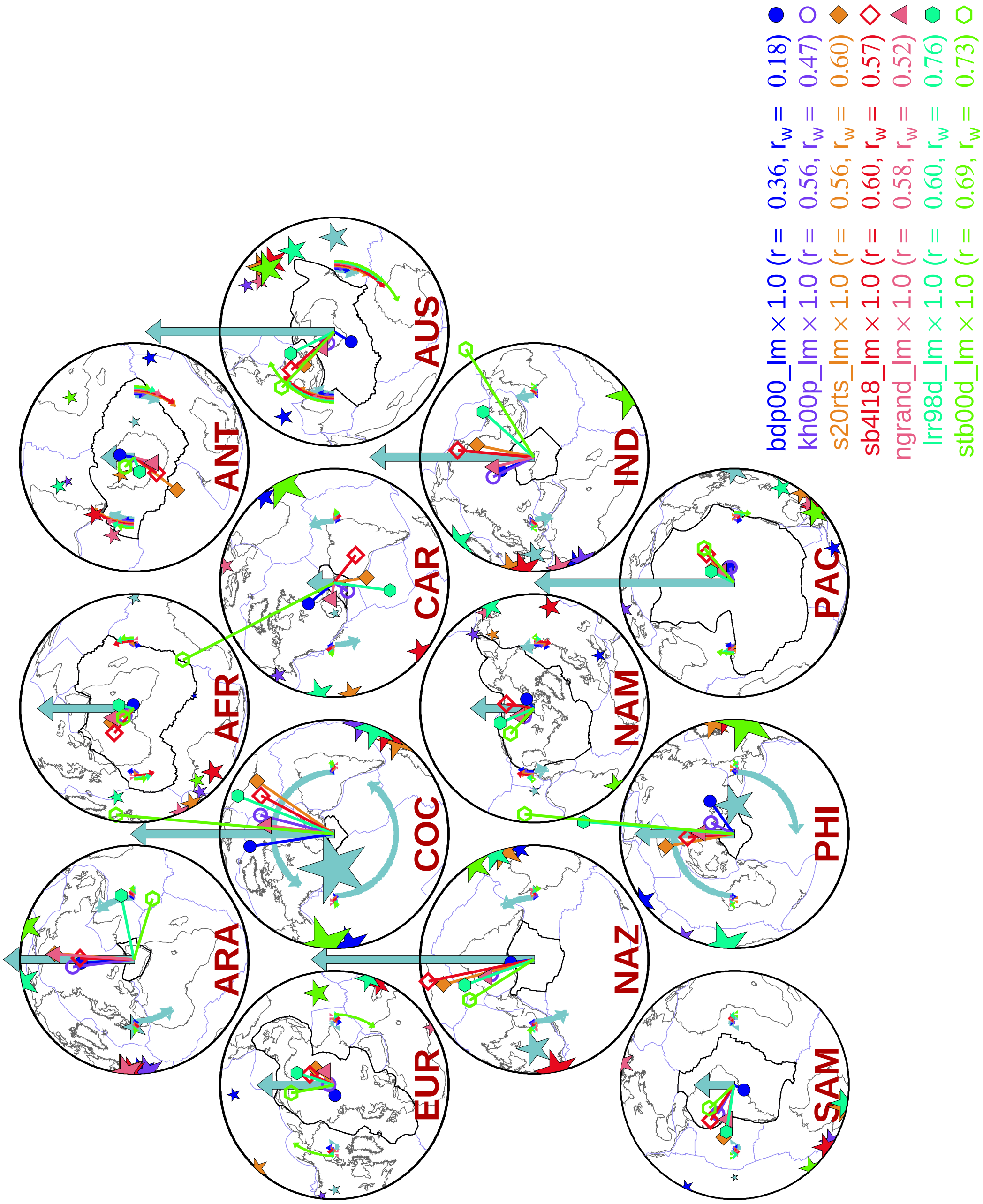

Figure 4.9: Comparison of lower mantle based driving torques for viscosity profile η_D; compare with Figure 4.8 and see Figure 4.3 for explanation.

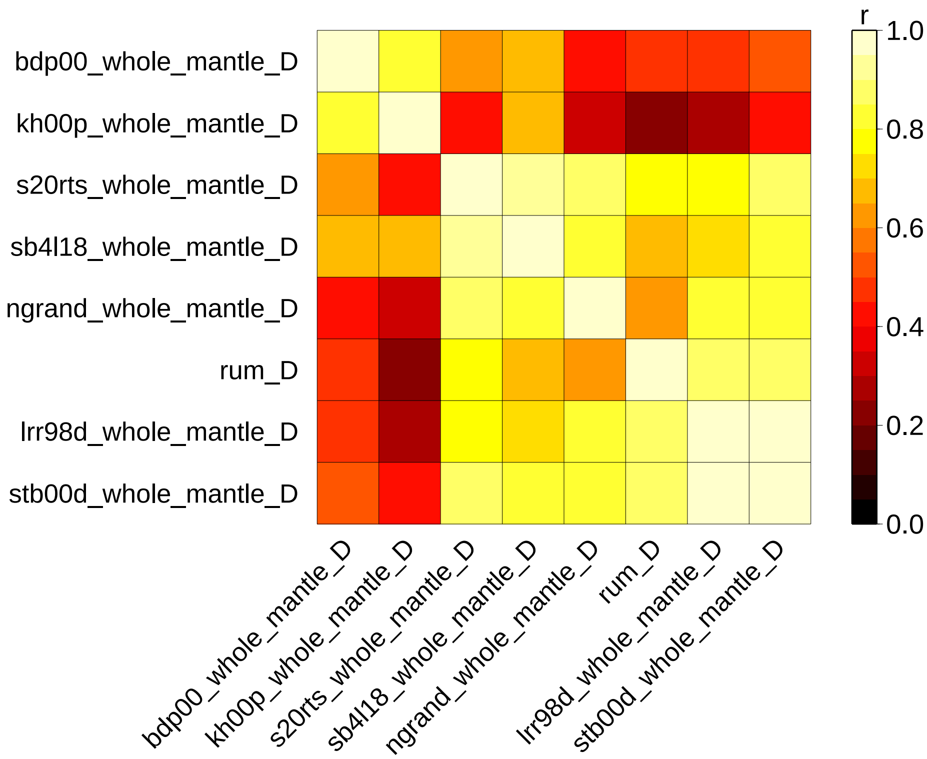

Figure 4.10: Correlation matrix for driving torques based on whole mantle density models and flow calculations with η_D.

which degree of model complexity is warranted.

Effect of viscosity structure

An increase of mantle viscosity with depth is likely (*e.g.* Hager, 1984; Hager and Clayton, 1989; Mitrovica and Forte, 1997) and plate velocities have indeed been used to deduce such an increase (Forte and Peltier, 1987). The differences between our radial viscosity profiles (Figure 4.7) are therefore of second order compared to this general trend; consistent with Lithgow-Bertelloni and Richards (1998), we find that the inversions are insensitive to such details. If we use our starting values for the scaling factors (Figure 4.11), we observe that viscosity profiles η_D, η_G, and η_H lead to the best mean model performance in terms of r_w. Individual best models lead to velocity predictions that are correlated as $r_w \approx 0.9$ with NUVEL1-NNR. If the scalar pre-factors of the driving and resisting torques are optimized to reduce the misfit in plate motion predictions (sec. 4.3.4), the performance of the models is as shown in Figure 4.12.

We see that all combinations of models and viscosity profiles can be adjusted to yield good fits, that there is not much variation with respect to mean model correlation, $\bar{r}_w$, and that the best models of each η-type all give $r_w \approx 0.9$ with best overall results for η_D, η_G, and η_H. This implies that our original choices for scaling factors led to reasonable plate motion predictions, especially for viscosity profiles of the η_D type. The mean $\bar{r}_w$ of optimized models is, however, in general ≈ 0.07 higher than the non-optimized models (*cf.* Figures 4.11 and 4.12).

If we compare optimized and non-optimized variance reduction histograms (Figures 4.13 and 4.14), we can see that improvements in mean VR vary by a larger extent between η-structures than for r_w, and adjustment of scaling factors leads to a larger improvement for VR overall. For η_G and η_H, mean VR is improved substantially over fixed weight models. Since variance reduction is affected by the plate velocity magnitude and not only the directions, as is the case for r_w, this implies that we have some resolution in terms of the absolute value of the viscosity, η_0, which controls the viscous drag amplitudes (Forte *et al.*, 1991; Lithgow-Bertelloni and Richards, 1998). In particular, viscosity profile η_G leads to models whose velocities are too high such that the optimized viscosity η_0 is increased by a factor of ~ 3 (Table A.2).

The finding that predicted plate motions are insensitive to the depth dependence of η is consistent with work by

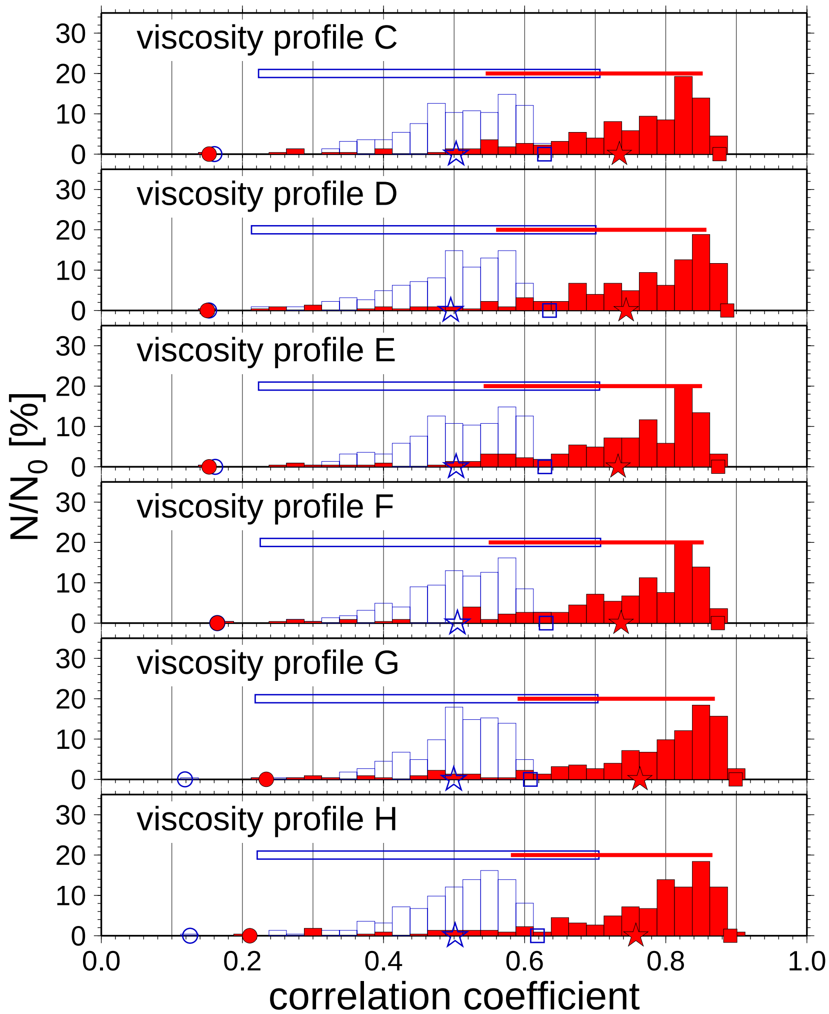

Figure 4.11: Histogram of non-optimized model performance as a function of r (open bars) and r_w (filled bars). N/N_0 denotes the fraction of all models that fall into a certain quality bin when models are sorted by viscosity structure. Circles, stars, and boxes indicate minimum, mean, and maximum performance of the models, respectively. Horizontal bars centered on the mean indicate the 95%-confidence interval were the mean r the true correlation of the inversion, determined from Fisher's z-transformation (*e.g.* Press *et al.*, 1993). Variations are small between results with different viscosity profiles. (*cf.* Figures 4.12, 4.14, and 4.13.)

Lithgow-Bertelloni and Richards (1995) who explored the role of a low viscosity asthenospheric channel similar to that in our profile η_D. Such a decoupling zone could be expected to diminish the plate-driving force of the mantle. However, Lithgow-Bertelloni and Richards showed that a viscosity drop of several orders of magnitude will still lead to large mantle contributions, and some of our best fitting models actually have such low viscosity channels (η_D and η_G). The explanation for this apparent paradox is conservation of mass: while a low viscosity channel will reduce the shear stresses that are transmitted across such a zone, radial flow will maintain communication between the layers. Figure 4.15 explores this: we studied the effect of models with only lower mantle density variations (based on *bdp00*, *ngrand*, *s20rts*, and *lrr98d*) on the magnitude (RMS) of the radial flow through the transition zone at 660 km, $u_r^{660}|_{\mathrm{RMS}}$, and the torques on the plates when the viscosity of the lower mantle, η_{lm}, is varied for an η_E-type viscosity profile. As expected, radial flow decreases when convection becomes more sluggish in the lower mantle; we can fit all models with a power law $u_r^{660}|_{\mathrm{RMS}} \propto \eta_{\mathrm{lm}}^{-0.62}$ (Figure 4.15, top). Correspondingly, the torque amplitudes are smaller, and for the average plate-integrated torques, T_{avg}, we fit $T_{\mathrm{avg}} \propto \eta_{\mathrm{lm}}^{-0.29}$ (Figure 4.15, bottom).

The considerations above hold for constant density anomalies in the lower mantle. As noted before, η_{lm} strictly cannot be varied independently for geodynamic models like *lrr98d* since the density field of those models depends on the viscosity structure itself. For *lrr98d*, we can estimate that the total slab density that can be sustained will scale with the inverse of the sinking velocity of subducted material in the lower mantle since the influx is constrained by the plate tectonic reconstruction. Depending on the functional relationship between the sinking velocity and η_{lm}, we can therefore expect that the decrease of T_{avg} with increasing η_{lm} will be diminished

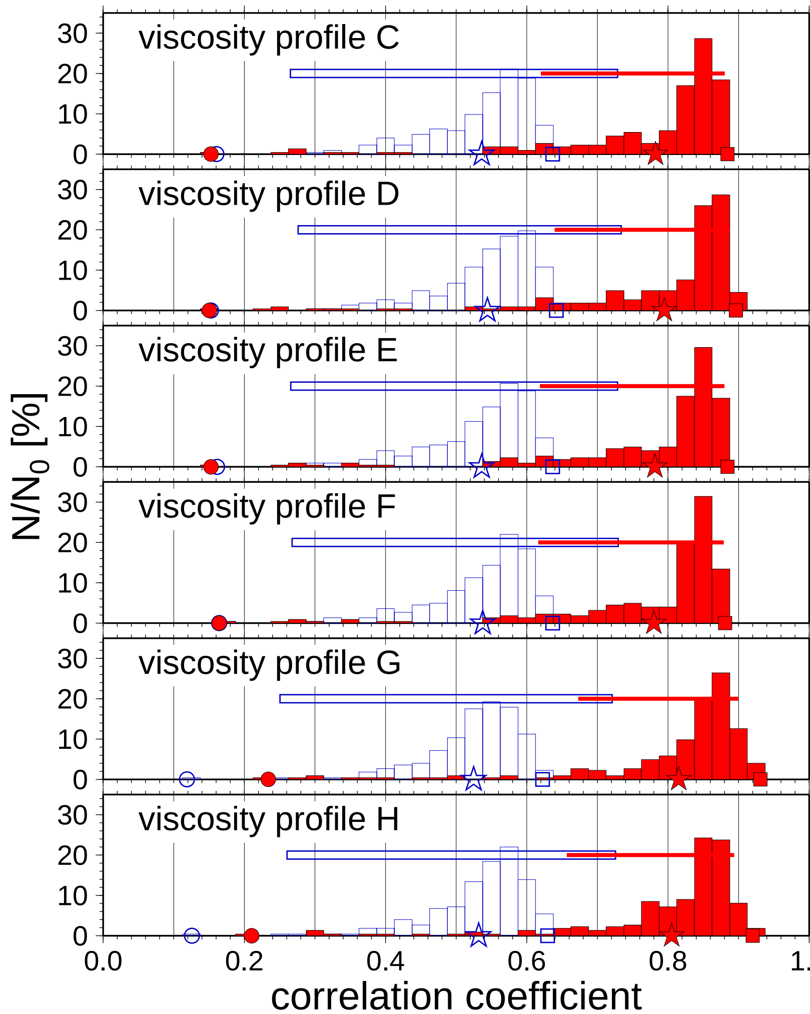

Figure 4.12: Histogram of optimized model performance in terms of correlation. In contrast to Figure 4.11, all scaling factors, w_i, were allowed to vary. All viscosity profiles give similar results.

from that shown in Figure 4.15. However, torques due to lower mantle density are always large when compared, for example, to those due to lithospheric thickening. Independent of the absolute magnitude of T_{avg}, we find that the torques relate to the flow through the transition zone roughly as $T_{\text{avg}} \propto \sqrt{u_r^{660}|_{\text{RMS}}}$ for the current plate geometry; this appears to be valid for many density models. Our results therefore illustrate how lower mantle density variations can play a role in driving the plates in any style of convection that allows for substantial mass flux through 660-km, as is likely the case for the present-day Earth (chapter 3).

Lithosphere and upper mantle driving forces only

For the discussion of the best fitting models of plate motions in terms of model quality we fix the viscosity structure to be η_D. While η_G yields results that are slightly better most of the time, we constrain ourselves to the simpler viscosity profile since we have seen that differences are small. We also proceed to show models with adjusted, non-negative scalar torque weights w_i but –as discussed in sec. 4.5.2– optimization gains are small, too.

First, we present models that are based on lithospheric structure only, testing the hypothesis that lithospheric thickening forces alone counterbalance the viscous drag due to plate motion. Figure 4.16 shows the quality of plate velocity fit for a combination of driving torques. We find that our lithospheric model ("lith_thick") performs better if tested against Coblentz *et al.*'s (1994) model ("lith_thick_cobl") for lithospheric thickening only ($r_w = 0.62$ vs. $r_w = 0.52$). Models that further include continental topography ("topo_lith_thick") are not necessarily in better agreement with plate motions than oceanic plate only models; while topography-included

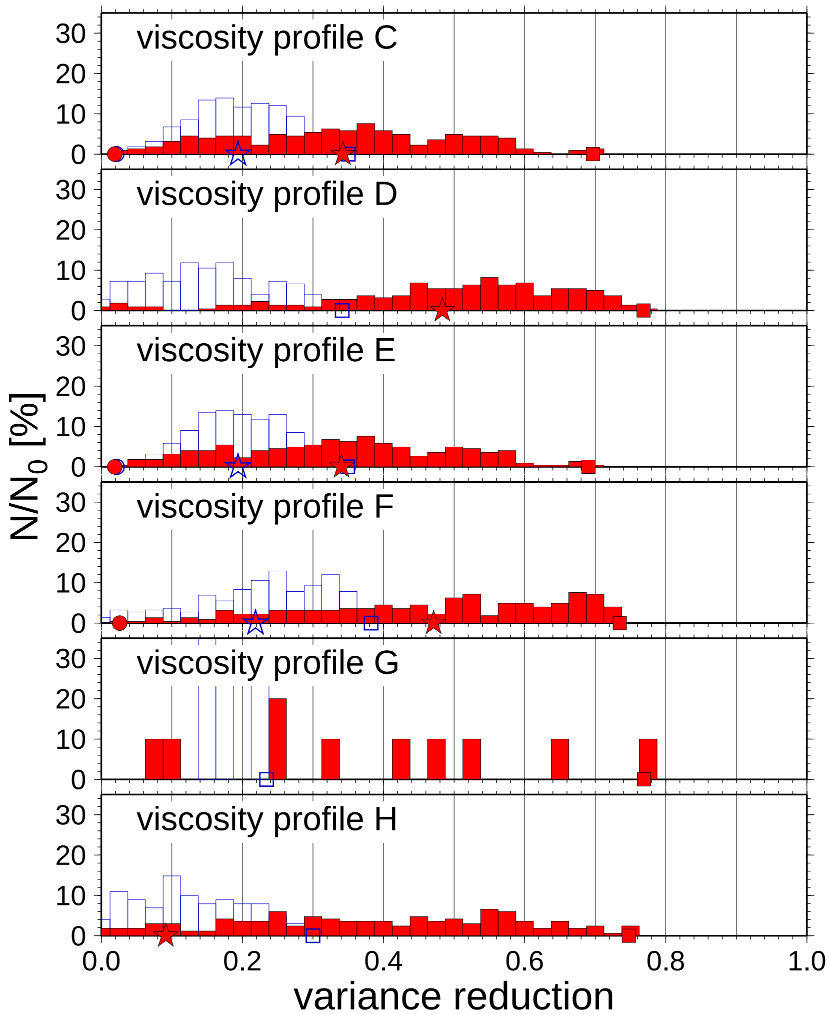

Figure 4.13: Histogram of non-optimized model performance in terms of variance reduction.

torques yield better results for our model ($r_w = 0.72$), the opposite is true for Coblentz *et al.*'s (1994) torques ($r_w = 0.22$).

We next consider only slab pull driving plate motions, in the form of *rum*, our seismic slab model, or the upper mantle part of *lrr98d*, as an approximate "total" upper mantle slab model. With viscosity η_D we achieve $r_w = 0.82$ for *rum* which is not much lower than the fit for more complex models. Upper mantle slabs based on *lrr98d* lead to a poorer performance than *rum*. If we combine *rum* or upper mantle *lrr98d* slab pull with the lithospheric models, the fit to plate motions is slightly improved to $r_w \approx 0.83$. These numbers are, however, lower than for models that include lower mantle based forces, considered in the next section.

Mantle structure

We now turn to plate motion models that are based on lower and/or whole mantle density anomalies and include other driving forces successively. Results in Figure 4.17 are based on *P* and *S*-wave tomography and subduction models *stb00d* and *lrr98d*. As above, we test seismic (*rum*) and "total" (*lrr98d*) upper mantle slab configurations. For flow driven by mantle density structure only, we observe that *P*-wave models do a poorer job than *S*-wave models. Both are inferior to subduction models, such as *stb00d*, which yields $r_w = 0.84$. When we allow for lithospheric contributions, plate motion fits are improved, and the best model is again *stb00d*, although it is not substantially better than *lrr98d* or *s20rts*. Table A.1 lists the performance parameters for the best mantle plus lithospheric thickening models with the corresponding optimized values for η_0 and R_ρ.

Focusing on the lithospheric structure models, we find that for η_D the mean model performances of all model

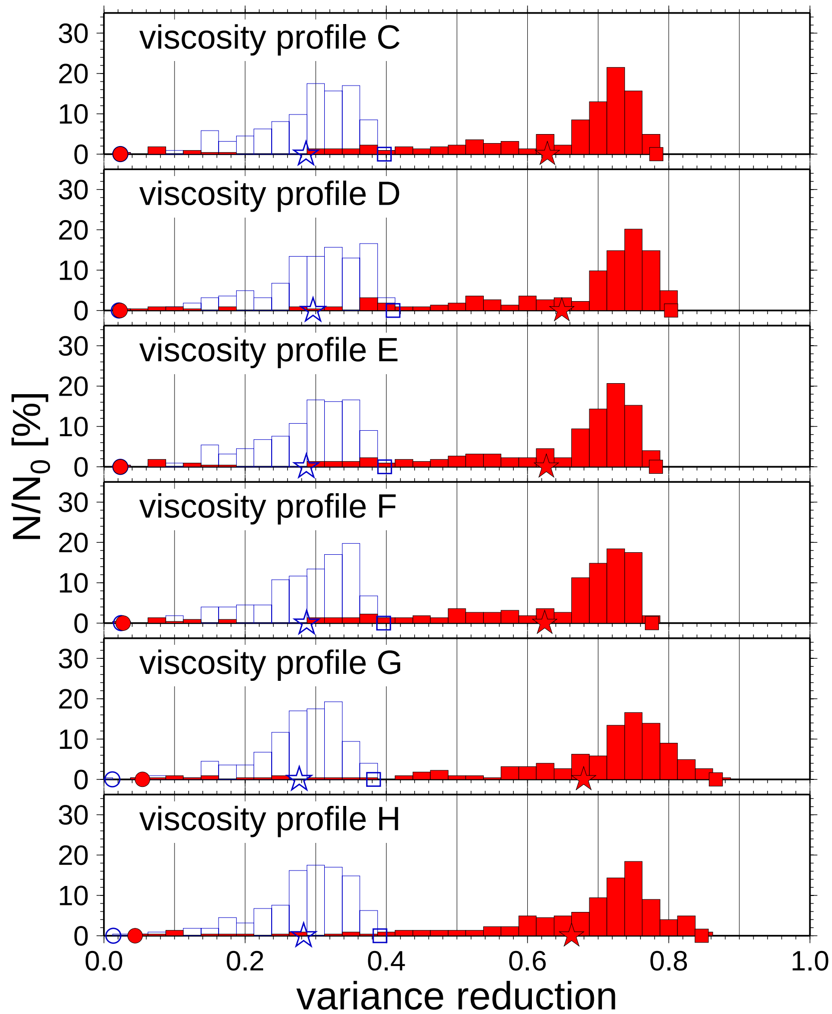

Figure 4.14: Histogram of optimized model performance in terms of variance reduction. In contrast to Figure 4.13, all scaling factors were allowed to vary.

combinations, $\bar{r}_w$, are 0.80/0.83 for oceanic-only/global lithospheric contributions from our model and 0.79/0.75 for the Coblentz *et al.* (1994) torques. Consistent with our findings in sec. 4.5.2, we find that our lithospheric torques lead to slightly better predictions than Coblentz *et al.*'s (1994), and the inclusion of continental crustal structure has led to a small improvement of plate motion fits. However, as mentioned before, it is not clear if potential energy differences in old continental regions will contribute much to driving plates such that the relevance of this improvement is doubtful.

We next test the effect of replacing all upper mantle structure with the seismic slab model *rum* (Figure 4.17). This approach improves *P*-wave models substantially, *S*-wave models, *stb00d*, and *lrr98d* slightly. When we use slabs as derived from the upper mantle part of *lrr98d* instead, results are comparable. For other viscosities (markedly η_G) we find that "total" slabs based on *lrr98d* lead to models that are slightly better than those for *rum* ($\Delta r_w \sim 0.03$). (Scaling factors for the upper mantle part of *lrr98d* are then larger than those for the lower mantle, most likely since *lrr98d* has small density amplitude in the upper mantle.) We might therefore slightly underestimate the upper mantle slab driving force by restricting ourselves to the seismic *rum*. Since differences are not great, we nonetheless use *rum* for upper mantle slabs in the following for simplicity.

Finally, we search for the best models using whole or lower mantle only structure, lithospheric thickening due to seafloor spreading, and additional *rum* slabs (assuming that tomographic models fail to image some slab signal). With this combination, all types of models achieve $r_w \approx 0.89$ ($\mathrm{VR}_w \approx 80\%$) and none is significantly better than the other. (A list of best-fit models with the scaling parameters is given in Table A.2.) For *P*-wave models, the best fit is achieved with lower mantle structure from tomography, replacing the upper mantle completely with

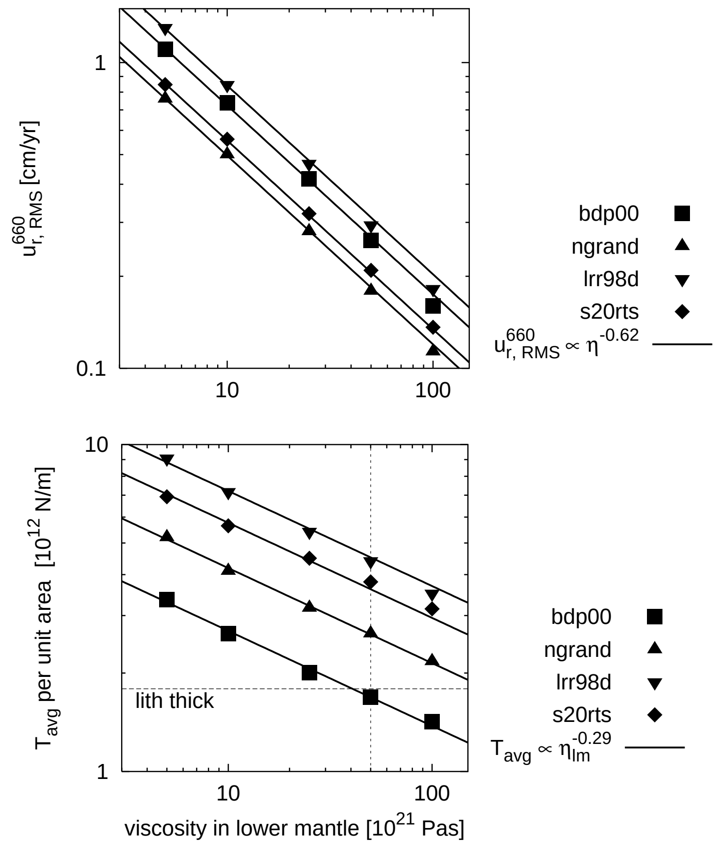

Figure 4.15: RMS of the radial velocity, $u_r^{660}|_{\mathrm{RMS}}$, driven by lower mantle only density models in a no-slip surface boundary condition flow-model (top) and plate averaged torques per area, T_{avg} (bottom) as a function of lower mantle viscosity η_{lm} for η_E-type profiles. Horizontal dashed line indicates the lithospheric torque contribution from our model and vertical dotted line $\eta_{\mathrm{lm}} = 50$, as used in the construction of *lrr98d*.

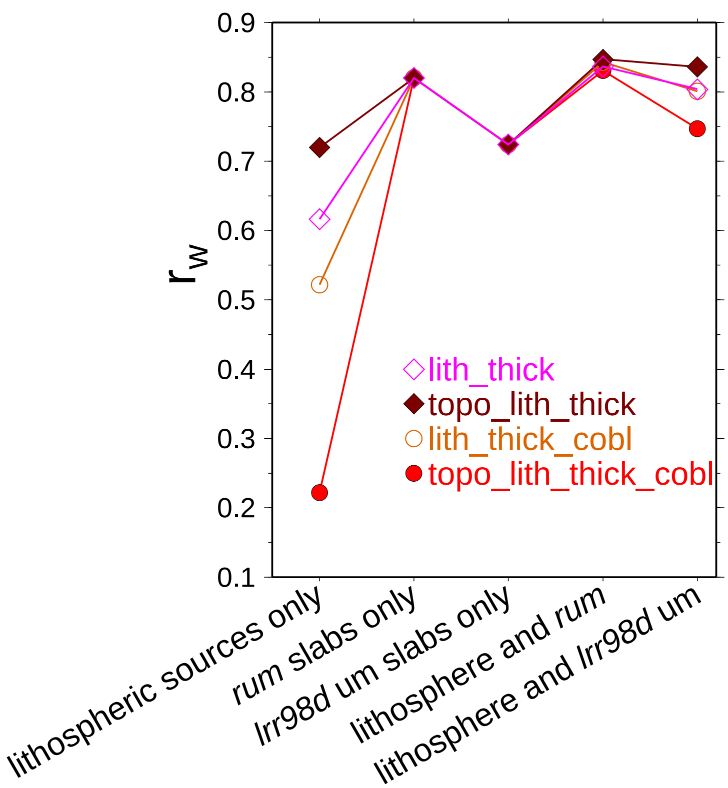

Figure 4.16: r_w for best-fit models using viscosity profile η_D and lithospheric driving forces only, upper mantle seismic slabs from *rum* only, upper mantle "total" slabs from *lrr98d* only, lithosphere plus *rum*, and lithosphere plus *lrr98d* upper mantle slabs.

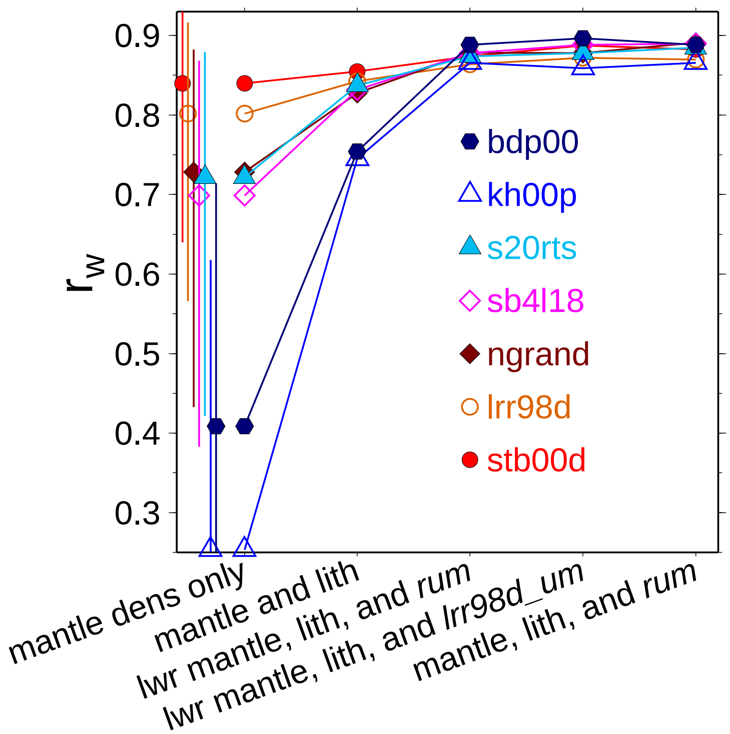

Figure 4.17: r_w for best-fit models with mantle density driven flow and η_D. Error bars on the left indicate the range outside which models can be considered significantly better or worse than mantle only models at the 95%-confidence level according to Fisher's z-transformation.

rum. This is consistent with our previous finding that the upper mantle structure imaged by *P*-wave models is different from the slab signature that appears to be included in *S*-wave models (sec. 4.5.1). Accordingly, the best *S*-wave model inversion uses the whole mantle structure and adds some *rum* signal to the upper mantle part. If we consider only the exact viscosity structures that have led to the geodynamic models *lrr98d* and *stb00d* for consistency, the best models are slightly worse and $r_w \approx 0.86$.

For illustration, we include the predicted plate velocities for the best fitting *S*-wave model and *lrr98d* in Figure 4.18 and for the best-fit *P*-model and *stb00d* in Figure 4.19. Model scaling factors are given in Table A.2. Inspection of the plate velocities shows fairly good agreement between models and observations, as in earlier work. Discrepancies differ between models, with some consistent failures like the underprediction of the northward motion of SAM. The velocities we find for *lrr98d* are similar, but not identical, to those of Lithgow-Bertelloni and Richards (1995) and we attribute this to small differences in the viscosity structure and the lithospheric model. Quality measures such as r_w (~ 0.9) are comparable, however.

We conclude that a range of models, based on tomography or subduction history, can reproduce plate motions, indicating that the sinking slabs are the most important contribution to the mantle driving forces as far as tomography and our models can resolve them. All models that include lower mantle structure perform better than the upper-mantle only models of sec. 4.5.2. For some models and viscosity profiles, the difference is up to $\Delta r_w \approx 0.1$ which is statistically significant at the 95%-level using Fisher's z-transformation. This improvement in fit when lower mantle sources are included is in agreement with the notion that slab related structures in the lower mantle are the most important features of mantle convection (*e.g.* Chase, 1979), that they correlate relatively well with fast regions of tomography (chapter 3), and are responsible for major driving forces (*e.g.* Davies and Richards, 1992; Ricard *et al.*, 1993; Deparis *et al.*, 1995; Lithgow-Bertelloni and Richards, 1995).

What differs between the best-fitting mantle models, however, are the relative contributions of the different components to the total torque, T_{avg}. Figure 4.20 shows that the contribution of the lithosphere for the best-fit models with η_D with optimized weight factors varies between $\sim 30\%$ for most models and $\sim 10\%$ for *stb00d*. While all inversions include substantial additional *rum* slab pull, *lrr98d* does so to the smallest extent for η_D and rejects it completely for other viscosity structures such as η_G. We also observe that the fraction of the mantle driving force that comes from the lower mantle is between $\sim 20\%$ and $\sim 35\%$ for η_D. There is some variation of the individual contributions between viscosity profiles, and the lower mantle contribution can be as high as $\sim 50\%$ for *lrr98d* and η_G.

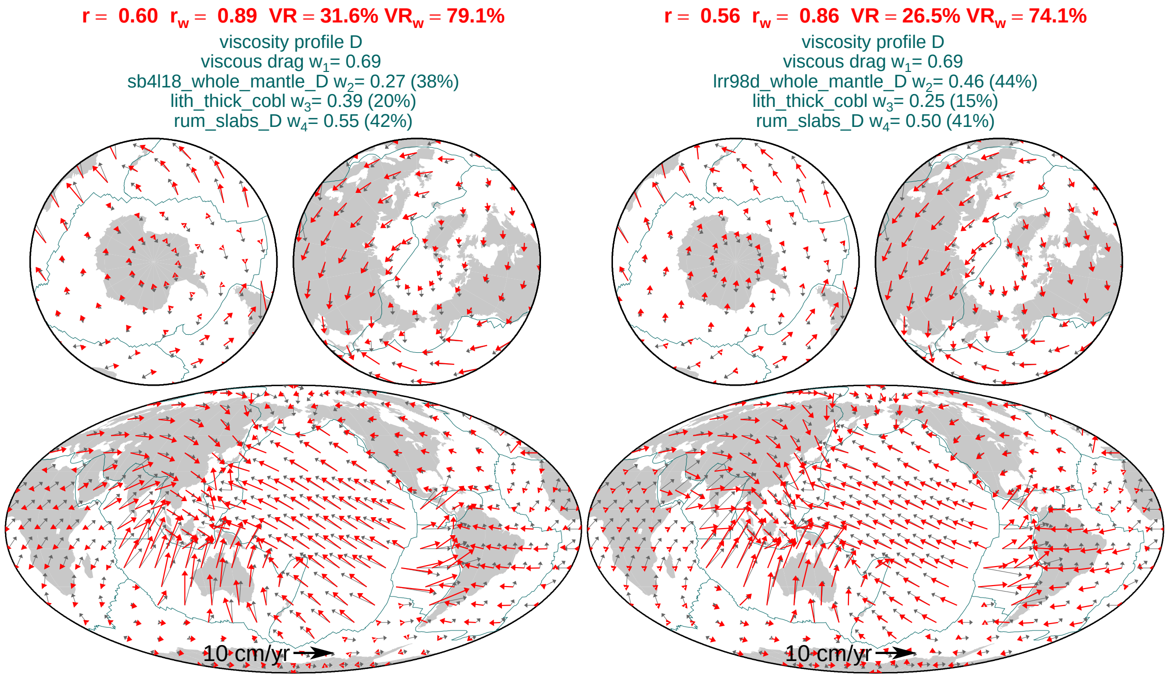

Figure 4.18: Predicted plate velocities (dark, thick vectors) based on the best fitting *S*-wave model for η_D, *sb4l18*, (left), *lrr98d* (right) and observed NNR-NUVEL-1 velocities (thin vectors). w_i-values indicate the scalar factors that were adjusted to minimize the misfit. (If we assume that the lithospheric model is best constrained for *sb4l18*, $w_3 \equiv 1$, the absolute viscosity of η_D should be scaled by 1.78, and mantle and slab density fields by 0.7 and 1.41, respectively. See also Table A.2.) Numbers in parentheses are the relative contributions of the driving torques to T_{avg}.

There is, of course, *a priori* information about the presence and, to some extent, the amplitudes of the individual driving torques. Not all combinations of our optimized weights models correspond, therefore, to realistic absolute viscosity values and scaling factors. We have also seen that optimization gains are small since good velocity predictions can be found for a range of models and viscosity structures; the non-uniqueness of driving force inversions is, in fact, one of our main conclusions. However, if we examine models where we fix the, probably best constrained, lithospheric thickening contribution and let only the absolute viscosity values vary, or if we fix all weights to their starting values, we find that results are similar to those shown above. Consistent with some models of Lithgow-Bertelloni and Richards (1995), we find that the total mantle density and lithospheric contribution to the driving torques is always $\sim 70\%$ and $\sim 30\%$, respectively.

Effect of parameterized edge forces

We now evaluate the effects of edge forces on plate velocity inversions. First, we show how plate motion models that are based on mantle density only and η_D can be improved by inclusion of additional torques (Figure 4.21). We find that the ridge push (*rp*) leads to larger improvements in fit than the realistic lithospheric models ("lith_thick") that consider the sea-floor age. The good performance of *rp* is related to the ridge–trench geometry, as discussed in sec. 4.4.4.

Slab pull (*sp*/*spw*) leads to improvements for all models; they are nonetheless smaller than those resulting from the inclusion of *rum* or the upper mantle part of *lrr98d*. The viscous drag due to sinking slabs which acts on both plates at a convergent margin, therefore, appears to be more suited to driving the observed plate motions than a one-sided edge force which requires a stress guide and a strong slab. Except for the *P*-models, weighting the slab pull by age (*spw*) does not consistently lead to larger improvement in r_w than *sp* for different mantle models. All other edge forces lead to no significant increase in r_w if weights are restricted to $w_i \geq 0$.

Finally, we explore how globally parameterized edge forces change models that already contain lower mantle,

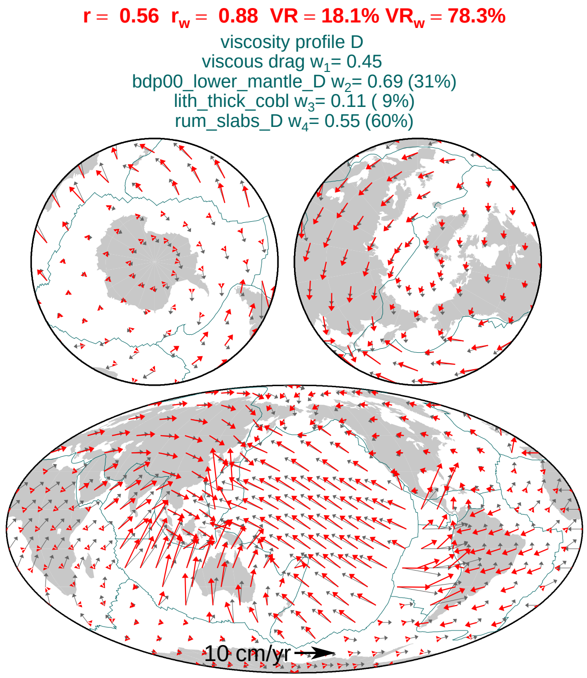

Figure 4.19: Predicted and observed plate motion based on the best fitting *P*-model *bdp00* (left) and *stb00d* slabs (right), η_D. (*cf.* Figure 4.18.)

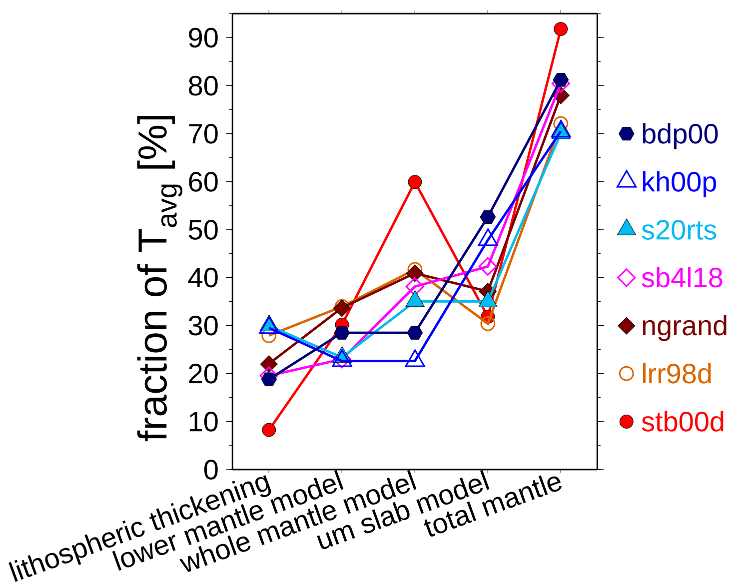

Figure 4.20: Fractional contribution of density models to the total driving torque, T_{avg}, for the optimized best-fit models with η_D as in Figure 4.17. "um slab model" indicates the contribution of additional *rum* upper mantle slabs, not included in "whole mantle model".

lithospheric, and *rum* density anomalies. We attempt to improve the model fit for η_D models while still enforcing $w_i \geq 0$ and maximizing r_w. The inclusion of one additional edge force (4.10 – 4.15) improved the models by at most $\Delta r_w = 0.02$ (*cr* for *s20rts*). However, introducing a colliding resistance typically led to an insignificant improvement of r_w, or no improvement at all for other viscosities. Other edge forces, such as *tft* and *tfn* on transform faults, were rejected by the inversion and weighted as zero.

If we allow for positive and negative weights, we find that models can not be significantly improved either, only the relative strengths of different torques are readjusted to achieve optimal fits. The largest improvement for η_D is $\Delta r_w = 0.03$ for an additional *tftw* that is weighted negatively, and therefore corresponds to nonphysical

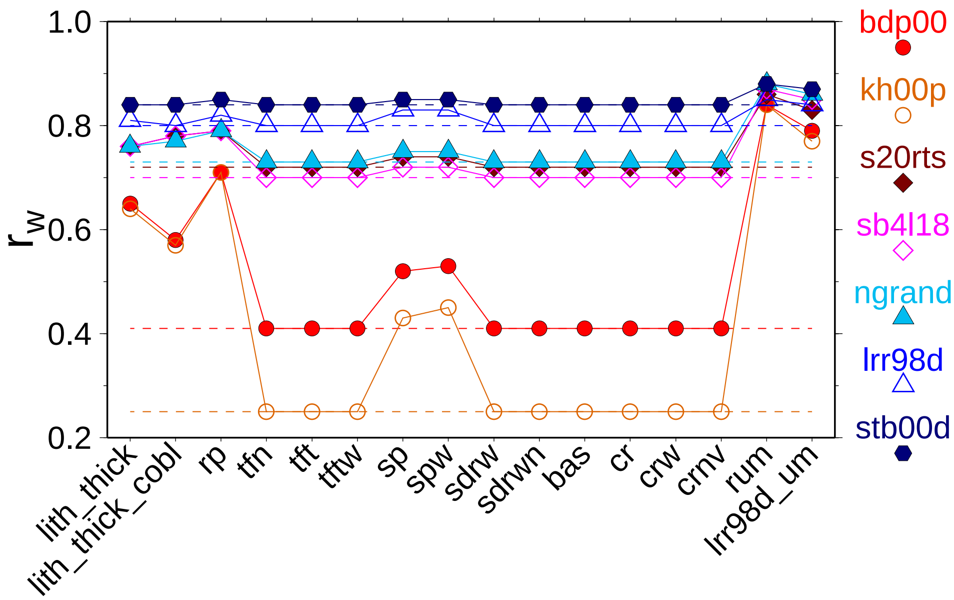

Figure 4.21: Effect of torque addition to mantle density only η_D models as in Figure 4.17. r_w is shown for mantle only (dashed base lines) and additional torques (symbols and solid lines). For edge force legend, see Table 4.2.

tangential transform fault driving forces. Results for the sign of other edge forces such as the collision resistance vary for different viscosity profiles, and between models, implying that we cannot resolve them reliably.

As expected from the correlation analysis of Figure 4.6, we find that a variety of forces can be combined to drive the plates. Since mantle, lithospheric, and upper mantle slab torques lead to models with good correlations of $r_w \sim 0.9$ already, we cannot justify any added complexity due to globally parameterized edge forces. This implies either that our global parameterization has to be improved, or that edge forces have to be specified according to more detailed regionalization for an enhanced prediction of plate motions. The treatment of forces, especially at convergent margins, might have to be improved to include the effect of lithospheric bending of the oceanic plate which could be important in determining the effectively transmitted forces between subducting and overriding plate (Conrad and Hager, 1999a, and chapter 1).

4.6 Conclusions

We have demonstrated that a number of combinations of driving forces can be invoked to explain observed plate motions. Lithospheric thickening (or ridge push) and slab pull forces are successful candidates since they are naturally aligned with the correct direction of motion, from ridges to trenches. In sec. 4.5.2 we have shown that fairly good predictions of plate velocities are indeed possible without invoking any driving agents other than cooling lithosphere and upper mantle slabs.

However, if we include lower mantle density variations as derived from tomography or subduction models, the fit to observed plate motions always improves. This finding is insensitive to the viscosity structure with depth as long as there is radial flow through 660-km (sec. 4.5.2). Individual density models lead to slightly different predictions, yet all achieve the same quality of fit with correlations of ~ 0.9 (sec. 4.5.2). *S*-wave tomography models lead to equally good results as do models with only sinking slabs or *P*-wave tomography. However, for the latter we had to replace the upper mantle density variations with a slab model, probably because the ray path coverage of *P*-models does not adequately image slabs.

Our conclusion that the slab signal, as imaged by tomography and predicted by geodynamic models, is the most important contribution of mantle-driven torques substantiates earlier studies. Estimates of the relative importance of mantle or lithosphere based density variations are somewhat different for our best fit-models but lithospheric thickening usually contributes $\sim 30\%$, and total mantle density anomalies contribute $\sim 70\%$ to the average plate-driving torque. Of the latter component, $\sim$40% is due to lower mantle heterogeneities. The lower mantle should therefore be explicitly taken into account when surface expressions of mantle convection are studied; it might be an oversimplification to neglect tractions caused by mantle flow in studies of intra-continental deformation.

We were only marginally successful in our attempt to improve plate motion models by including parameterized plate boundary forces. We showed that one reason for this is that most edge forces can be classified as globally driving or resisting plate motions in a well correlated manner for simple geometrical reasons (sec. 4.4.4). Consequently, without independent knowledge of their magnitude, not much new information is introduced when edge force derived torques are used, and the improvement in fit does not warrant the additional complexity.

Subduction zones in particular might require a more realistic treatment than was possible with our model. Our inversions did not, however, indicate that a colliding resistance was required, either on the subducting, or on both the subducting or overriding plate. A two-sided slab pull was found to be best suited to explain plate motions. These results imply that only a more detailed, regional specification of trench forces can be expected to improve plate motion models.

Chapter 5

Seismic anisotropy as an indicator for mantle flow

Chapters 3 and 4 laid the groundwork for a comprehensive exploration of the effects of global convective patterns on lithospheric deformation. We have already applied our models to the prediction of large-scale crustal stress (Becker and O'Connell, 2001a); here, we shall focus on deeper deformation as mapped out by seismic anisotropy.

5.1 Abstract

We present global models of strain accumulation in mantle flow to compare the predicted finite-strain ellipsoid orientations with observed seismic anisotropy. We focus on oceanic and young continental regions where we expect our models to agree best with azimuthal anisotropy from surface waves and shear-wave splitting. Finite-strain derived models lead to better model fits than the hypothesis of alignment of fast axes with absolute plate motions for surface-wave derived anisotropy. For the western US, we fit *SKS* shear-wave splitting observations using a coherent flow model and do not need to invoke a mantle that is decoupled from lithospheric motions to account for observations. Our study substantiates that seismic anisotropy can be used as an indicator for mantle flow and contributes to the establishment of a quantitative functional relationship between the two.

5.2 Introduction

Seismic wave propagation in the uppermost mantle is anisotropic, as has been demonstrated using a variety of methods and a number of different datasets (*e.g.* Hess, 1964; Forsyth, 1975; Anderson and Dziewonski, 1982; Silver and Chan, 1988; Montagner and Tanimoto, 1991; Ekström and Dziewonski, 1998; Smith and Ekström, 1999; Schulte-Pelkum *et al.*, 2001). Vertically polarized waves propagate more slowly than horizontally polarized waves in the upper $\sim$ 220 km of the mantle (*e.g.* Dziewonski and Anderson, 1981), implying widespread transverse isotropy with a vertical symmetry axis, also referred to as radial anisotropy. Surface-wave studies have established robust lateral variations in the pattern of radial anisotropy (*e.g.* Ekström and Dziewonski, 1998; Boschi and Ekström, 2002). Inverting for azimuthal anisotropy (where the fast axis of symmetry lies within the horizontal plane) is more difficult, partly because of severe trade-offs between model parameters (*e.g.* Tanimoto and Anderson, 1985; Laske and Masters, 1998). Ongoing efforts to map out azimuthal anisotropy in 3-D using surface waves (*e.g.* Montagner and Tanimoto, 1991) are reviewed by Montagner and Guillot (2000).

Surface-wave data are advantageous for their ability to place constraints on variations in anisotropy with depth, but their lateral resolution is limited. Shear-wave splitting measurements have the potential to image smaller-scale lateral variations, though they lack depth resolution. Shear-wave splitting is a phenomenon akin to optical birefringence (*e.g.* Silver, 1996). If a shear wave travels through an anisotropic medium, it will split into two wave trains with orthogonal polarizations and different propagation speeds. The azimuth of the fast polarization and the delay time between the two waves can be measured directly and interpreted in terms of current or past deformation

Research presented in this chapter was done in collaboration with James B. Kellogg (Harvard University).

in the lithosphere or convecting mantle underneath the recording station. Reviews of techniques, observations, and modeling have been given by Silver (1996) and Savage (1999). An initial comparison between observations and synthetic splitting based on surface-wave models was presented by Montagner *et al.* (2000). These authors found poor agreement between the two approaches. Possible reasons for this include the finding that azimuthally anisotropic surface-wave models are sensitive to the inversion procedure and data coverage (Laske and Masters, 1998), and that the modeling of shear-wave splitting measurements, usually performed for a single, transversely isotropic layer with a horizontal symmetry axis, needs to take variations of anisotropy with depth into account (Montagner *et al.*, 2000).

The existence of anisotropy in upper-mantle rocks can be associated with accumulated strain due to plate-tectonic motions (*e.g.* McKenzie, 1979), as reviewed by Montagner (1998). The use of seismic anisotropy as a constraint on mantle and lithospheric flow is therefore an important avenue to pursue since other constraints for deep mantle flow are scarce. There are currently few realistic and quantitative models that account for the 3-D geometry of mantle convection, and this chapter describes our attempts to fill that gap.

5.2.1 Causes of seismic anisotropy

Wave-propagation anisotropy in the deep lithosphere and upper mantle is most likely caused by the alignment of intrinsically anisotropic olivine crystals (lattice-preferred orientation, LPO) in mantle flow under dislocation creep (*e.g.* Nicolas and Christensen, 1987; Mainprice *et al.*, 2000). Seismic anisotropy can therefore be interpreted as a measure of flow velocity-gradients in the mantle and has thus received great attention as a possible indicator for mantle convection (*e.g.* McKenzie, 1979; Ribe, 1989; Chastel *et al.*, 1993; Russo and Silver, 1994; Tommasi, 1998; Buttles and Olson, 1998; Hall *et al.*, 2000; Blackman and Kendall, 2002). There is observational (Ben Ismail and Mainprice, 1998) and theoretical (Wenk *et al.*, 1991; Ribe, 1992) evidence that rock texture and the fast shear-wave polarization axis will line up with the orientation of maximum extensional strain. (We shall distinguish between *directions*, which refer to vectors with azimuths between 0° and 360°, and *orientations*, which refer to two-headed vectors with azimuths that are 180°-periodic. We will also use *texture* loosely for the alignment of mineral assemblages in mantle rocks such that there is a pronounced spatial clustering of particular crystallographic axes around a specific orientation, or in a well-defined plane.) More specifically, we expect that for a general strain state, the fast (a), intermediate (c), and slow (b) axes of olivine aggregates will align, to first order, with the longest, intermediate, and shortest axes of the finite strain ellipsoid (Ribe, 1992).

Figure 5.1 shows an example of observed and predicted orientations of crystallographic axes under uniaxial compression. The degree to which the fast axes cluster around the largest principal axis of the finite strain ellipsoid (FSE), or, alternatively, the orientation of the shear plane, will vary and may depend on the exact strain history, temperature, mineral assemblage of the rock, and possibly other factors as well (*e.g.* Savage, 1999; Tommasi *et al.*, 2000; Blackman *et al.*, 2002; Kaminski and Ribe, 2002). The simple correlation between FSE and texture might therefore not be universally valid. For large-strain experiments, the fast propagation orientations were found to rotate into the shear plane of the experiment (Zhang and Karato, 1995), an effect that was caused partly by dynamic recrystallization of grains and that is accounted for in some of the newer theoretical models for texture formation (*e.g.* Wenk and Tome, 1999; Kaminski and Ribe, 2001, 2002). Further complications for LPO alignment could be induced by the strain-weakening rheology of olivine (Bystricky *et al.*, 2000) or the presence of water (Jung and Karato, 2001). The orientation of melt-filled cracks (Kendall, 1994) might also be important for lithospheric anisotropy.

Instead of trying to account for all of these possible mechanisms, we approach the problem by using global flow models to predict the orientation of finite strain in the mantle. We then compare the anisotropy produced by these strains to the seismic data, using the theory of Ribe (1992). We focus our comparisons on oceanic plates and regional examples such as the Western US where the lithosphere is relatively young and should be less affected by inherited anisotropy in thick crust than old continental areas. We find a good correlation between predicted maximum extensional strain and the fast axes of anisotropy observations. This result lends credibility to the inferred relationship between strain and texture in the mantle. Furthermore, global circulation models can thus potentially be used as an independent argument for the validity and the appropriate parameter range of texture development models such as that of Kaminski and Ribe (2001).

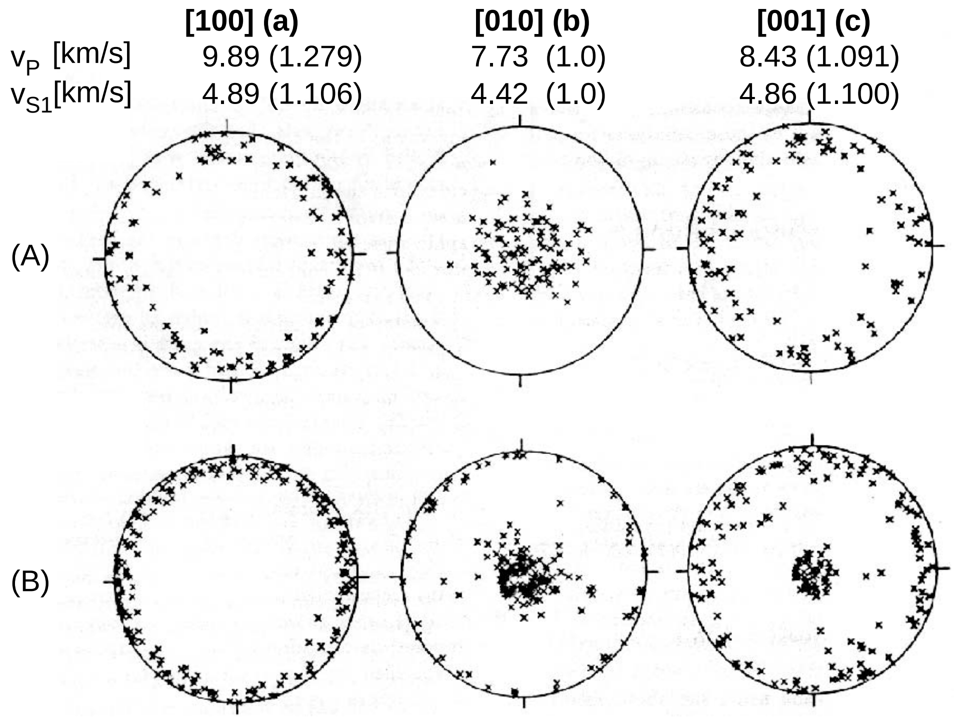

Figure 5.1: Pole figures (Lambert equal-area projection) for the distribution of crystallographic axes modified from Ribe and Yu (1991): (A) is from an uniaxial compression experiment on a dunite sample (Nicolas *et al.*, 1973), (B) from Ribe and Yu's (1991) numerical calculation for a similarly shortened olivine aggregate. Since the axis of maximum shortening is perpendicular to the plane, the slow wave propagation axis ([010] or b) orients itself mostly out of the plane, while the maximum extension axes ([100] or a) are found in a ring perpendicular to the shortening axes. Indicated wave speeds for *P* and *S* (*S*1) correspond to propagation along the crystallographic axes of an olivine single crystal and were calculated by Ribe (1992) based on measurements by Kumazawa and Anderson (1969). Numbers in parentheses are normalized to the wave speed for the slowest (b) axis in each row. The mismatch between experiment and model for the c-axes is reduced in an extension of Ribe's (1992) work by Kaminski and Ribe (2001) that includes the effect of dynamic recrystallization.

5.3 Observations of seismic anisotropy

We now discuss observations of radial and azimuthal anisotropy from surface waves and shear-wave splitting. These two datasets are complementary since they have different spatial sensitivities and coverage. Future work could also include other types of observations of anisotropy (*e.g.* Smith and Ekström, 1999; Schulte-Pelkum *et al.*, 2001) but here we will focus on Rayleigh wave phase-velocity inversions and *SKS* splitting data.

5.3.1 Surface waves

Radial anisotropy in the 1-D reference Earth model PREM (Dziewonski and Anderson, 1981) is limited to depths from 25 km to 220 km (Figure A.6) where horizontally polarized *S*-waves propagate significantly faster than vertically polarized *S*-waves. v_{SH} is $\sim 5\%$ larger than v_{SV} at its maximum, with the difference between v_{SH} and v_{SV} decreasing with depth. The existence of this trend was confirmed by Ekström and Dziewonski (1998), who mapped lateral variations in v_{SV} and v_{SH} and found that the PREM anisotropy is similar to the global average of their model.

Using the JWKB approximation (*e.g.* Dahlen and Tromp, 1998, p. 737ff), Boschi and Ekström (2002) constructed regional sensitivity kernels for their inversion for transversely isotropic anomalies and found that, depending on the crustal structure assumed in the starting model, local kernel amplitudes varied considerably from global, PREM-derived averages. Nevertheless, their model results confirmed most of the heterogeneity found by Ekström and Dziewonski (1998). The inversion by Boschi and Ekström (radially parameterized by splines) shows a smooth variation of global v_{SH} and v_{SV} averages with depth that roughly follow the PREM means (Figure A.6).

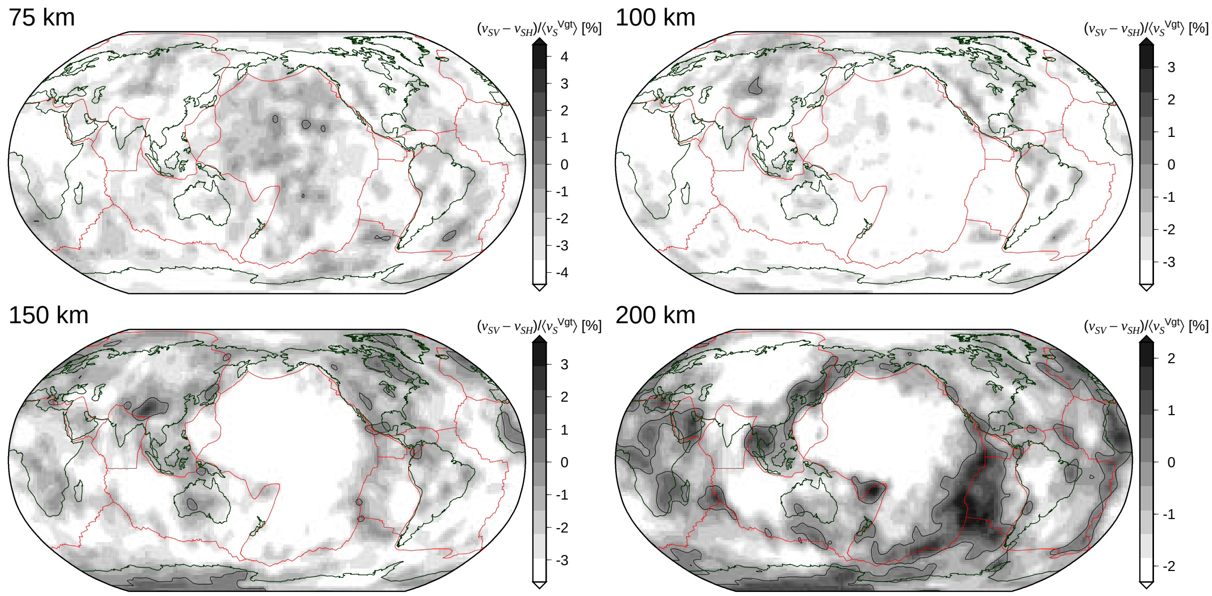

Figure 5.2: Lateral variations in radial anisotropy from Boschi and Ekström (2002). We show the difference $v_{SV} - v_{SH}$, normalized by the mean (Voigt) S-wave velocity, $\langle v_S^{\mathrm{Vgt}} \rangle$, at depths, z, of 75 km, 100 km, 150 km, and 200 km. The zero contour, where $v_{SV} = v_{SH}$, is marked by thick lines, delineating only small regions for $z \lesssim 150$ km, since v_{SH} is generally larger than v_{SV} at shallow z (Figure A.6). Plate boundaries here and in subsequent figures are from NUVEL1 (DeMets *et al.*, 1990). Colorscale is clipped at 50% of the maximum absolute anomaly at each depth.

Figure 5.2 shows the lateral variations in radial anisotropy for several depths at which we evaluated Boschi and Ekström's model. Unlike in most presentations of such models, we do not plot the difference between relative deviations of v_{SV} and v_{SH} from a 1-D reference model, but rather the absolute difference between v_{SV} and v_{SH}, normalized by the mean (Voigt) S-wave speed, $\langle v_S^{\mathrm{Vgt}} \rangle = \langle \sqrt{\left(v_{SH}^2 + 2v_{SV}^2\right)/3} \rangle$, at each depth (see Figure A.6). This quantity should be a more adequate measure of the total anisotropy. A relatively fast v_{SV} anomaly is seen in the central Pacific at shallow depth (75 km in Figure 5.2). The relatively slow v_{SV} anomaly at 150 km in the Pacific around Hawaii (detected by Ekström and Dziewonski, 1998) is also apparent, but is now recast as a fast anomaly in v_{SV} under the East Pacific Rise (EPR), especially notable at 200 km, where v_{SV} is actually larger than v_{SH}. Since the EPR is a region of rapid upwelling and seafloor spreading at the surface, it is tempting to interpret the observed anisotropy as due to mantle flow. Based on the global strain models we discuss below, we should, in the future, be able to develop a quantitative interpretation of radial anisotropy that goes beyond the general understanding of v_{SV}/v_{SH} anomalies as being related to convective boundary currents (*e.g.* Montagner, 1998). Such a study is, however, beyond the scope of this work.

Azimuthal anisotropy

Global models with 3-D variations of azimuthal anisotropy based on surface waves exist in the literature (*e.g.* Montagner and Tanimoto, 1991; Montagner and Guillot, 2000). Those models, however, were not available to us in electronic form at the time of writing. Since there are also a number of concerns about the resolving power of such models (*e.g.* Laske and Masters, 1998; Ekström, 2001), we focus on a few azimuthally-anisotropic phase-velocity maps provided by G. Ektröm (*cf.* Ekström, 2001). We review the depth sensitivity of surface waves to azimuthal anisotropy in sec. A.2.1. Phase velocity perturbations for weak anisotropy can be expressed as a series of isotropic, D^0, azimuthally anisotropic (π-periodic), $D^{2\phi}$, and $\pi/2$-periodic, $D^{4\phi}$, terms (Smith and Dahlen, 1973). Rayleigh waves are typically more sensitive to anisotropy variations with 2ϕ-dependence than Love waves (which is why we focus on Rayleigh waves), and kernels for 2ϕ-anisotropy have a depth dependence for Rayleigh waves that is similar to their sensitivity to variations in v_{SV} (Montagner and Nataf, 1986).

Figure 5.3 shows an example from the phase-velocity inversions of Ekström (2001) for Rayleigh waves with a period of 100 s. Ekström used a large dataset ($\sim 120{,}000$ measurements) and a surface-spline parameterization

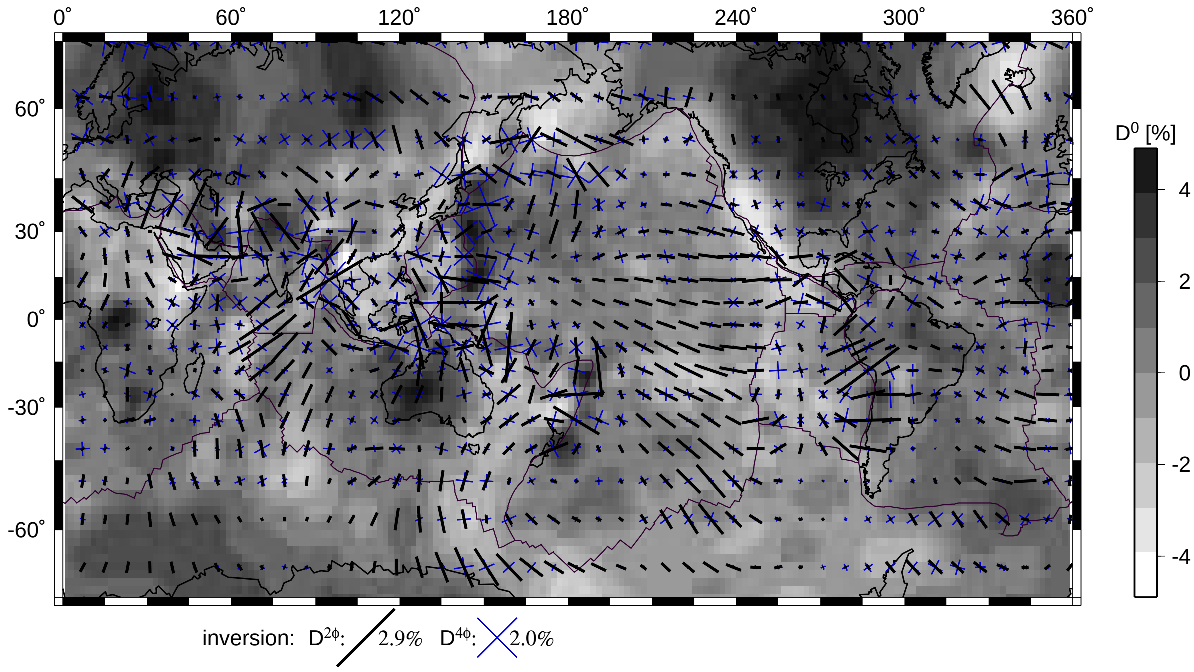

Figure 5.3: Isotropic and anisotropic variations of phase velocity for Rayleigh waves at 100 s period from Ekström (2001). We show isotropic variations in phase velocity as background shading (D^0 term in (A.4)), $D^{2\phi}$ fast orientations as sticks, and $D^{4\phi}$ terms as crosses. The RMS/maximum anomaly amplitudes are D^0: $\sim 1.3\%/4.9\%$; $D^{2\phi}$: $\sim 0.6\%/2.9\%$; and $D^{4\phi}$: $\sim 0.4\%/2.0\%$.

(1442 nodes, corresponding to $\sim 5^\circ$ spacing at the equator) to invert for lateral variations in the D terms of (A.4). To counter the trade-off between isotropic and anisotropic structure, Ekström (2001) damped 2ϕ and 4ϕ-terms 10 times more than the isotropic D^0 parameters. The isotropic and 2ϕ-anisotropic shallow structure imaged in Figure 5.3 (corresponding to a depth of $\sim$ 150 km, *cf.* Figure A.7b) appears to be dominated by plate-scale currents and by the well-known seafloor spreading-pattern close to the ridges (*e.g.* Forsyth, 1975; Montagner and Tanimoto, 1991). There are, however, deviations from this simple signal and the 4ϕ-contributions are smaller than those from 2ϕ, but not negligible. We will discuss these findings in more detail in our comparison with strain predictions in section 5.6.

5.3.2 Shear-wave splitting

The primary source of information about anisotropy in the upper mantle, other than surface waves, comes from observations of shear-wave splitting. In particular, measurements of *SKS* phases are widely used, since *SKS* has a near-vertical arrival angle and enters the mantle as a “clean” (unsplit) *S* wave after *P* to *S* conversion at the CMB; splitting is thus likely to be due to the waves’ passage through an anisotropic medium during the last several hundred km before reaching the surface (*e.g.* Silver, 1996; Savage, 1999). Figure 5.4 shows our compilation of shear-wave splitting measurements. (The most complete electronic data collection is that of Schutt and Kubo, 2001, which we have supplemented with results from several other studies.) Fast orientations are shown for both *SKS* and local *S* observations as described in the caption. There is a clear geographical data distribution bias toward the continents, where most permanent and roving seismic stations are found. Observations within oceanic plates are mostly confined to islands (*e.g.* Klosko *et al.*, 2001) with a few exceptions from OBS deployments (*e.g.* Wolfe and Solomon, 1998; Smith *et al.*, 2001).

Given the nearly vertical ray path incidence, *SKS* splitting data can be interpreted as a radial average of the seismic anisotropy underneath the recording station (*e.g.* Silver, 1996). *SKS* observations are thus somewhat easier to interpret than local *S* data, which are affected by anisotropy along the ray path and in the source region. To reduce the number of data and clarify the major trends, we experimented with various selection schemes. We show only one example (Figure 5.5a), a $3^\circ \times 3^\circ$ grid average of all teleseismic *SKS* data from Figure 5.4. The

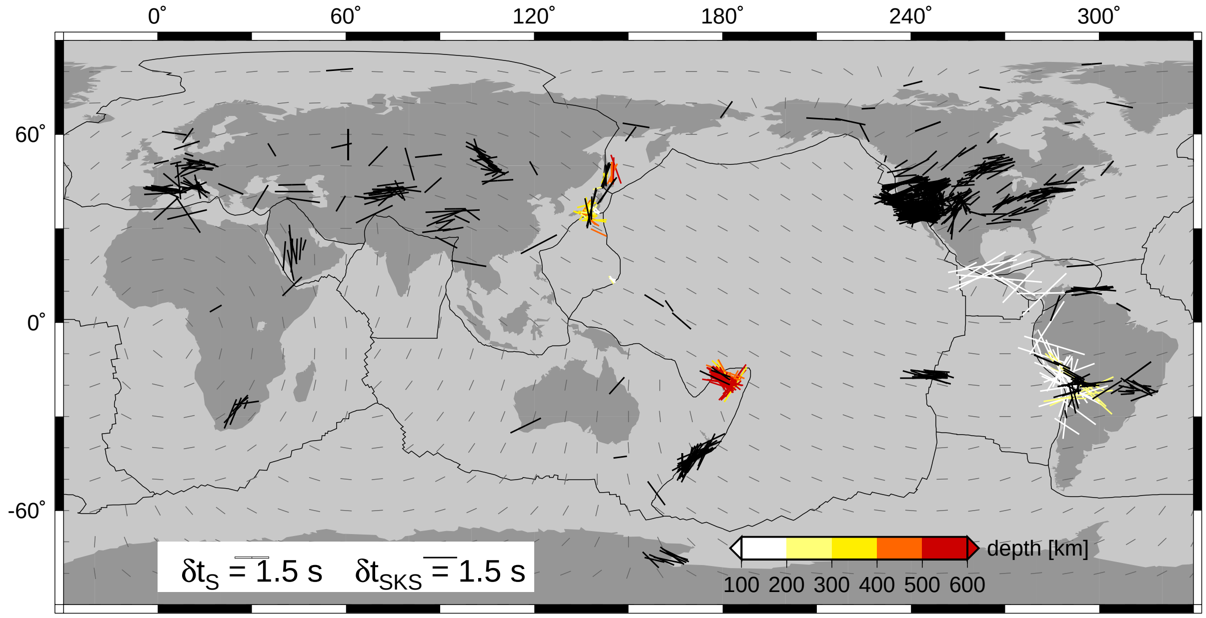

Figure 5.4: Compilation of shear-wave splitting observations. Fast propagation-plane azimuths are indicated by thick sticks; for time delay, δt, scale see the legend. Teleseismic *SKS* data (black) are from Silver (1996); Fischer and Wiens (1996); Fischer *et al.* (1998); Polet *et al.* (2000); Schutt and Kubo (2001); Klosko *et al.* (2001); and Polet and Kanamori (2002), and are plotted at the stations. Local *S*-phase anisotropy measurements are from Russo and Silver (1994); Fouch and Fischer (1996, 1998); Fischer *et al.* (1998); and Smith *et al.* (2001). Event depths for local *S* are indicated by shading of sticks which are plotted at the path midpoints for all *S* data but those of Russo and Silver (1994), which were corrected for receiver anisotropy and are therefore plotted at the earthquake hypocenters. Background thin sticks are absolute plate-motion orientations in the HS2 hotspot frame (Gripp and Gordon, 1990).

choice of an averaging procedure is not straightforward and somewhat arbitrary decisions about data selection have to be made. Data quality also varies between measurements and fluctuations in fast orientations at a single, or several close, stations may contain information about, *e.g.*, layered anisotropy (Silver and Savage, 1994) that is lost when measurements are simply summed up vectorially.

Figure 5.5a shows some well known patterns, such as ridge-perpendicular orientations of splitting and varying degrees of trench-parallel alignment of the fast axes (*e.g.* Savage, 1999). Within some continental areas (*e.g.* the eastern US), fast splitting orientations have an apparent correlation with absolute plate motion (APM) orientations in the HS2 hotspot reference frame. This may indicate shearing of the asthenosphere by motion of the lithosphere with respect to a deep, stagnant or decoupled mantle (*e.g.* Vinnik *et al.*, 1992). However, other hypotheses of anisotropy formation are plausible (Silver, 1996).

The global mean of the absolute misfit $\langle \Delta\alpha \rangle$ between the fast splitting axes and plate-velocity orientations is 31.2° for HS2-NUVEL1 (APM) and 37.5° for NNR NUVEL1, calculated using an area-weighted average of our $3^\circ \times 3^\circ$ splitting dataset from Figure 5.5a. If the two orientational fields had no correlation, we would expect a uniform distribution of absolute $\Delta\alpha$ deviations between 0° and 90°, implying a random misfit of $\langle \Delta\alpha \rangle_r = 45^\circ$. For N observations, the expected standard deviation of $\langle \Delta\alpha \rangle_r$ is $90^\circ/\sqrt{12N}$. For $N \sim 200$ as in our averaged *SKS* dataset, $\langle \Delta\alpha \rangle = 37.5^\circ$ for NNR is therefore significantly different from a random distribution of orientations at the 4σ-level. Including the net rotation of the lithosphere leads to better fits for fast axes than for NNR, mostly because of plate motions in South America, which have N-S velocity orientations in the NNR frame. We regard the misfit of splitting orientations with the current APM orientations as a hypothesis for the origin of anisotropy against which we will have to judge the performance of our more complex, strain-derived models.

To compare the regional *SKS* data with surface-wave derived anisotropy, we show synthetic fast orientations from Montagner *et al.* (2000) in Figure 5.5b that are based on the AUM model by Montagner and Tanimoto (1991). Along mid-ocean ridges, the anisotropic surface wave model predicts ridge-perpendicular orientations (in accordance with the sparse *SKS* data), as discussed previously. Within older oceanic plates and continents, the signal becomes more complex and, globally, alignment with *SKS* orientations is poor (Montagner *et al.*, 2000).

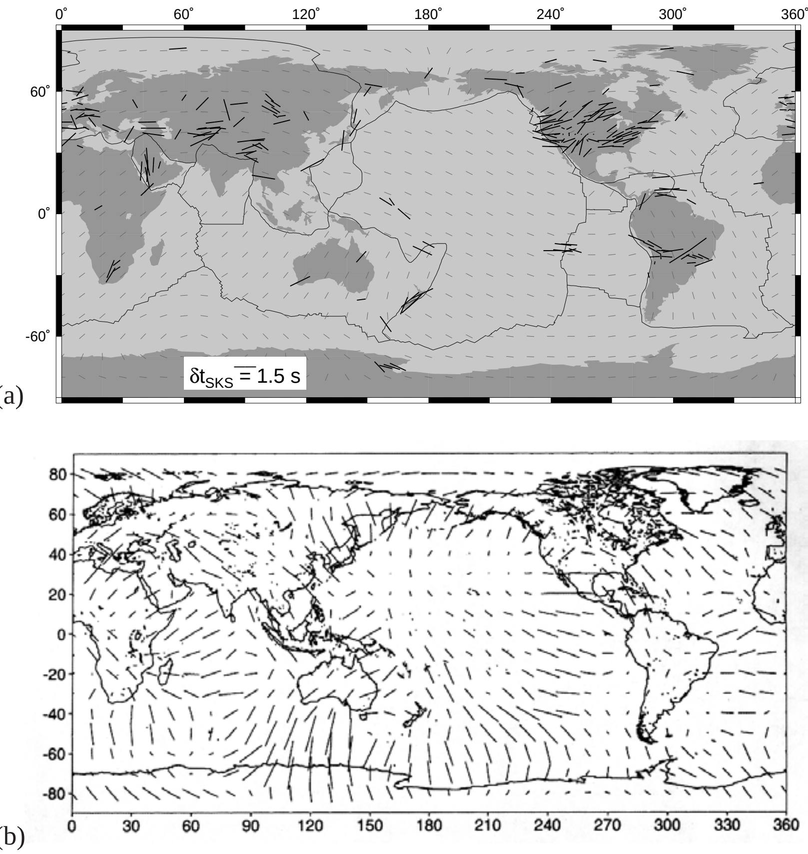

(a)

(b)

Figure 5.5: (a) $3^\circ \times 3^\circ$ block-averaged splitting orientations using teleseismic *SKS* from Figure 5.4. Background velocity orientations are NUVEL1 (DeMets *et al.*, 1990) in the no-net-rotation (NNR) frame.
(b) Synthetic fast azimuths for *SKS* splitting from plate 1 of Montagner *et al.* (2000) as derived by those authors from model AUM by Montagner and Tanimoto (1991) (compare also Figure 5.3).

Silver (1996) and Savage (1999) review possible contributions to sub-crustal anisotropy such as active tectonic deformation or frozen-in structure in the thick crust of old cratons. Seismic anisotropy in young continental regions may be due to recent tectonic deformation that is distributed with depth (*e.g.* Molnar *et al.*, 1999), leading to alignment of splitting orientations along shear zones, *i.e.* rotated from the compressional axes by $\sim 30^\circ$ (*e.g.* Holt, 2000). However, alignment with the major extensional orientation of surface strains as inferred from geodesy is also observed (Hatzfeld *et al.*, 2001) and, especially in back-arc areas, complex mantle flow may be important (*e.g.* Russo and Silver, 1994; Fischer *et al.*, 1998; Hall *et al.*, 2000). A comprehensive model of why young plate areas are strained in the way that splitting observations indicate is still missing.

5.4 Modeling strain and LPO anisotropy

We predict seismic anisotropy by calculating the finite strain that a rock would accumulate during its advection through mantle flow (*e.g.* McKenzie, 1979). Given a velocity field that is known as a function of time and space, the passive-tracer method lends itself to the problem of determining strain at any location $\mathbf{r}$. We can, first, follow material backward in time to some, initially unknown, location $\mathbf{x}$, and, second, advect forward again from $\mathbf{x}$ such that the material properties fulfill a cumulative criterion (discussed below) when arrived at $\mathbf{r}$. $\mathbf{r}$ might be the location of an *SKS* observation, where we are interested in the strain at different depths under the recording station, or $\mathbf{r}$ might be one of a large number of laterally distributed points from which we interpolate a global strain field.

5.4.1 The tracer method

We use a fourth-order Runge-Kutta scheme with adaptive stepsize control (*e.g.* Press *et al.*, 1993, p. 710) to numerically integrate the tracer paths through the flow field. We require all fractional errors to be smaller than 10^{-7} for all quantities solved for, including the finite strain matrix as outlined below. For this procedure, we need to

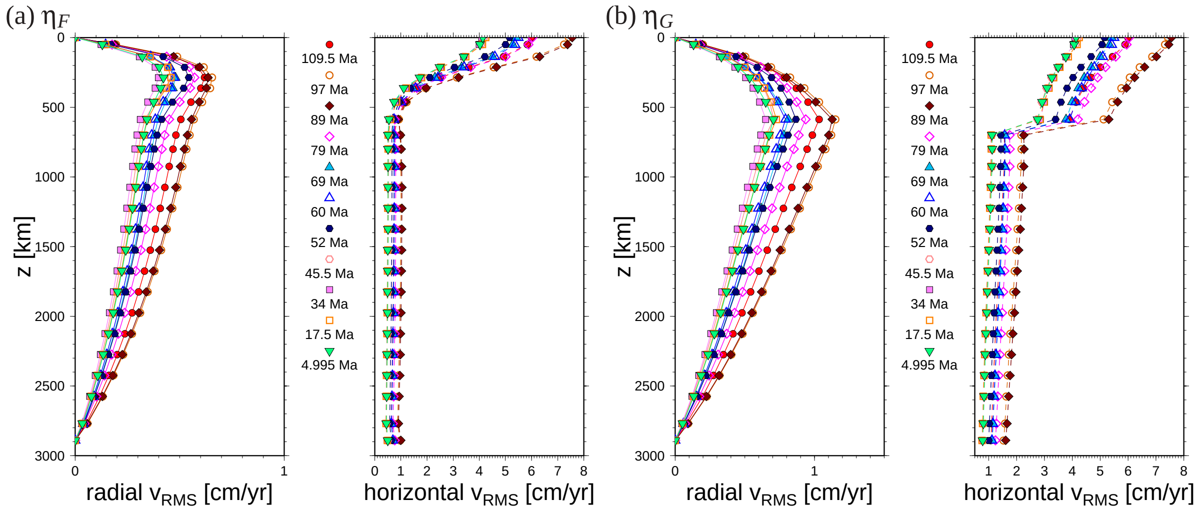

Figure 5.6: RMS of radial (left sub-plots) and horizontal $\left(\text{right sub-plots, } \sqrt{v_\theta^2 + v_\phi^2}\right)$ velocities induced by plate motions, plotted versus depth until 120 Ma given the plate-motion reconstructions of Figures A.4 and A.5, for viscosities η_F (a) and η_G (b) (*cf.* Figure 4.7). The RMS velocities at each radius r are evaluated on a $1° \times 1°$ grid to approximate the surface integral $\left(\int v(\theta,\phi)^2 d\Omega/(4\pi)\right)^{1/2}$.

determine the velocity at arbitrary locations within the mantle. Velocities and their first spatial derivatives are thus interpolated with a four-node shape-function method (corresponding to cubic basis functions, *e.g.* Fornberg, 1996, p. 168) from a grid expansion of the fields produced by global circulation models (sec. 2.3.1). Mantle velocities are expanded on $1° \times 1°$ grids with typical radial spacing of ~ 100 km; they are based on flow calculations with maximum spherical harmonic degree $\ell_{\max} = 63$ for plate motions and $\ell^{\rho}_{\max} = 31$ for density fields (tomographic models are typically limited to long wavelengths, *cf.* chapter 3). To suppress ringing introduced by truncation at finite harmonics, we use a $\cos^2$ taper for the plate motions.

The tracer procedure with adaptive stepsizes and polynomial interpolation can be expected to give accurate results (*cf.* van Keken and Zhong, 1999) and we have conducted several tests of our method. Using a typical plate-motion driven flow field, we were able to reverse a globally advected tracer set with evenly distributed starting locations at 50 km depth after 500 Myr so that the final locations differed from the initial ones by not more than ~ 1 m.

5.4.2 Reconstructing past mantle flow

We will show that strain accumulation at most depths is sufficiently fast that, under the assumption of ongoing reworking of texture, the last tens of Myr are likely to dominate present-day strain and anisotropy. However, we include results where our velocity fields are not steady-state but change with time according to plate-motion reconstructions and backward-advected density fields. Our method of calculating flow in the mantle involves specifying the surface velocities to account for the plate-motion related flow field. We use reconstructions from Gordon and Jurdy (1986) and Lithgow-Bertelloni *et al.* (1993). Figures A.4 and A.5 show the surface velocities and plate boundaries for these reconstructions; they have been applied within the indicated time-periods without interpolating between plate configurations during any given stage. To avoid discontinuities in the velocity field, the transition at the end of each tectonic period is smoothed over $\sim$1% of the respective stage length; velocities change to that of the next stage according to a $\cos^2$-tapered interpolation. The width of this smoothing interval was found to have little effect on the predicted long-term strain accumulation.

Figure 5.6 shows the RMS of the plate-motion induced flow as a function of depth for several time steps and best-fit viscosity profiles η_F and η_G from chapter 4 (*cf.* Figure 4.7). Circulation is focused in the upper mantle since both viscosity profiles exhibit an increase in the lower mantle. The shallow asthenospheric channel in η_F results in a pronounced maximum in radial flow at ~ 300 km depth, while the low viscosity "notch" at 660 km that characterizes η_G leads to an abrupt change between upper and lower mantle horizontal velocities. The rate of decrease of horizontal RMS velocities with depth in the upper mantle is smaller for η_G than for η_F because there is less drag exerted by the lower mantle. Since this implies slower shallow, plate-motion related straining for the η_G models, we will consider η_G as an endmember case alongside the more generic η_F (*cf.* discussion of mantle viscosity in chapter 4). However, the physical mechanisms that might lead to an η_G-type viscosity profile are only poorly understood (*e.g.* Panasyuk and Hager, 1998).

While we can infer the current density anomalies in the mantle from seismic tomography (sec. 4.4.1), estimates of the past distributions of buoyancy sources are more uncertain (*e.g.* Steinberger and O'Connell, 1997; Bunge and Grand, 2000). As Figure 5.6 indicates, plate-motion related flow can provide a good approximation for large-scale, near-surface straining patterns. Such flow will, however, not be representative of the overall straining and mixing properties of the mantle, and we expect vigorous thermal convection to exhibit stronger currents at depth (*e.g.* Ferrachat and Ricard, 1998; Kellogg and O'Connell, 1998; van Keken and Zhong, 1999). To address more realistic circulation patterns for past convection, we also advect density anomalies, $\delta\rho$, backward following Steinberger (1996). In an Eulerian frame, the time derivative of $\delta\rho$ is given by

$$\frac{d\delta\rho}{dt} = -\nabla\delta\rho \cdot \mathbf{v}, \tag{5.1}$$

where $\mathbf{v}$ and ∇ denote the velocity and gradient vectors, respectively. We neglect diffusion, heat production, and phase changes in the mantle and assume adiabatic conditions. These simplifications make the problem more tractable since diffusion is unstable under time-reversal. The density fields we predict using (5.1) will therefore become more uncertain as we move backward in time (diffusion lengths are of $\mathcal{O}(80\text{ km})$ for $\varkappa = 10^{-6}$ m^2/s and timescales of ~ 60 Myr). In addition, advection problems like (5.1) are also numerically unstable under certain conditions (see *e.g.* Press *et al.* (1993), p. 834ff, or Kaus and Podlachikov (2001) for a geological application).

We use Steinberger's (1996) method, in which $\nabla\delta\rho$ is approximated with central differences in the radial direction and spectrally in the horizontal directions. Once $d\delta\rho/dt$ is calculated by (5.1), $\delta\rho$ is integrated forward in time using a fourth-order Runge-Kutta scheme. We have found this approach to be somewhat unstable, even for moderate backward advection times of ~ 40 Ma. To damp short-wavelength structure that is artificially introduced into the $\delta\rho$ spectrum, especially at shallow depths, we therefore amend the method and taper $\delta\rho/dt$ using a $\cos^2$ filter for $\ell \geq 0.75\ell^{\rho}_{\max}$. With this modification, we obtain satisfactory results, as shown for an example calculation in Figure 5.7 for density anomalies that were backward-advected to 60 Ma. We compare the field method, discussed above, with a passive tracer approach (sec. 5.4.1) for which we distribute $\sim 15{,}000$ tracers at each of the 24 layers of the input model. Tracers carry the original density anomalies as attributes and are advected backward in time using the same velocities as for the field method. The depth slices for the final state (bottom row of Figure 5.7) are obtained by interpolating the unevenly distributed tracers that end up near the layers under consideration. The field and tracer methods agree overall in terms of the heterogeneity patterns (compare, *e.g.*, the structure within the Pacific plate at shallow depth). However, heterogeneity amplitudes are somewhat different and tracers are, as expected, better at preserving sharp contrasts, because the field method suffers from numerical diffusion.

The density distribution from the passive advection experiment can be compared with a field method calculation in which density itself partly drives the flow (Figure 5.8). Since density anomalies become more important with depth where the plate-related flow diminishes, passive-advection results (middle row in Figure 5.7) are similar to the actively advected structures at shallow depth (Figure 5.8) while they deviate more at greater depth. Figure 5.9 shows the RMS-velocity characteristics of the density-included models. As expected, radial RMS-velocity profiles for the density-included calculations are more similar to results for thermal convection (*e.g.* Puster and Jordan, 1997). Figure 5.10 shows a direct comparison with a convection model, in which we scale the present-day temperature field of Bunge and Grand's (2000) 3-D spherical model to density before recomputing the velocities for Newtonian viscosity. We see that both the shape and amplitude of the RMS profiles for this convection-model derived flow field are similar to the profiles we obtain for the η_F model, based on scaled tomography in Figure 5.9 (η_F is closer to Bunge and Grand's (2000) viscosity profile than η_G). Since Bunge and Grand's (2000) model is constructed such that the temperature heterogeneity matches that inferred from tomography, we should indeed expect that the profiles look similar. However, the similarity indicates that our scaled density anomalies are of the right order, as expected given our demonstration of dynamical self-consistency in the plate velocity inversions in chapter 4.

We shall not be concerned with any improvement of the backward advection scheme at this point. However, we

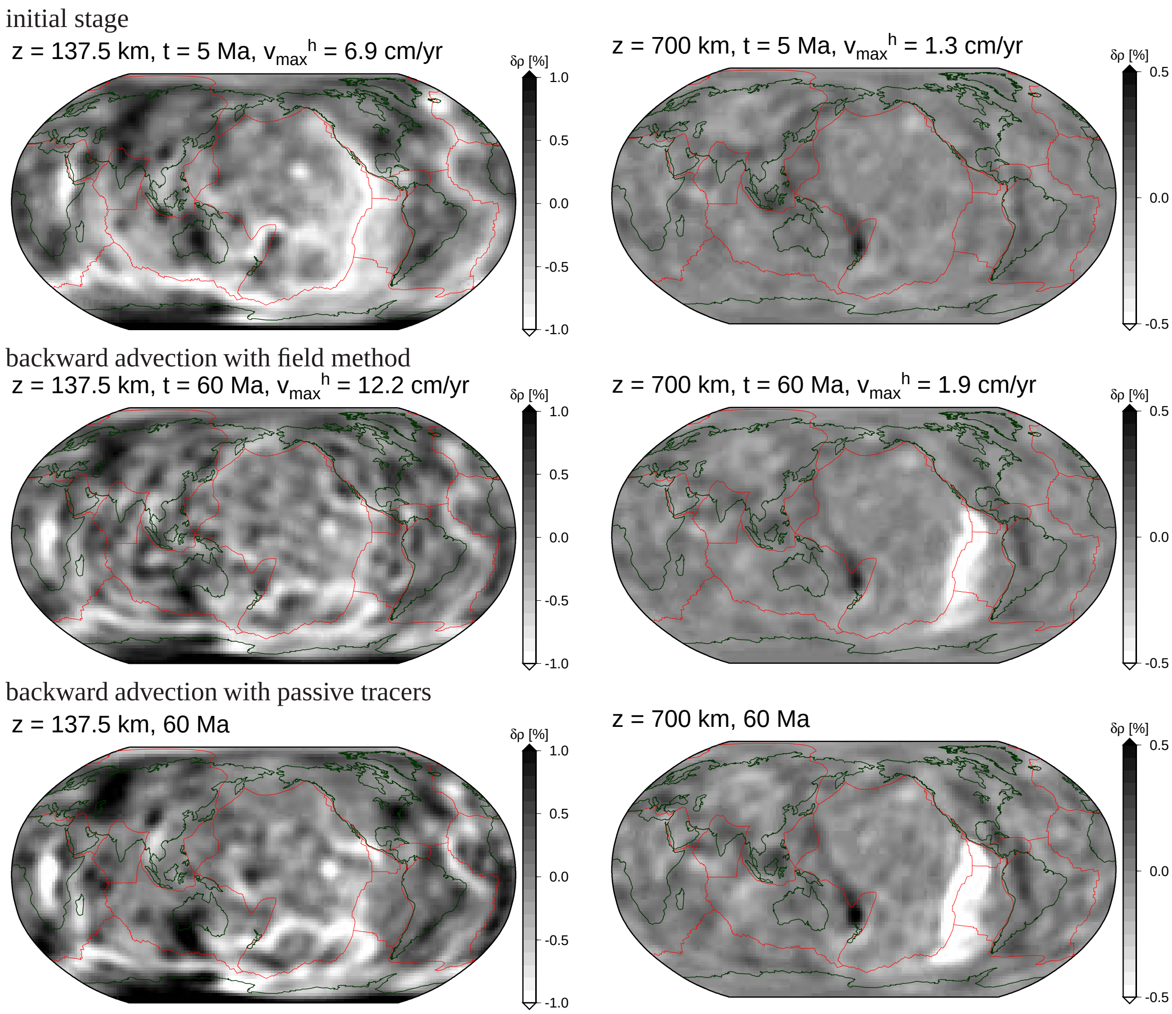

Figure 5.7: Comparison of density anomalies close to the present day (5 Ma, top plots) for depths of 137.5 km (left) and 700 km (right) with backward advected anomalies at the same depths at 60 Ma using the field method (middle plots) and a passive tracer approach (bottom plots). Density was converted from tomography model *ngrand* (sec. 3.3.2) by zeroing out all cratonic regions (based on 3SMAC by Nataf and Ricard, 1996) for depths shallower than 220 km and then reexpanding the gridded data up to $\ell_{\max} = 31$. $\delta\rho$ scaling is $R^S_\rho = 0.3$ (see sec. 4.4.1) for all z, but anomalies are carried passively by the plate-motion driven flow for testing purposes.

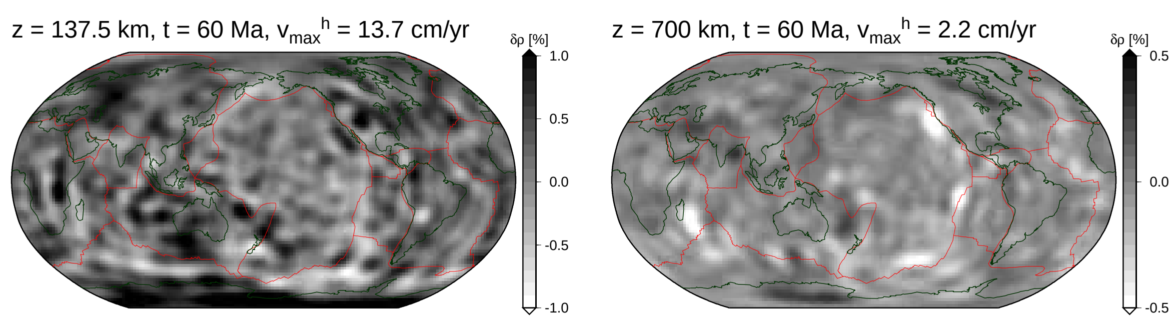

Figure 5.8: Actively backward-advected density anomalies at 60 Ma and 137.5 km (left) and 700 km depths (right) (as in Figure 5.7), calculated with the field method and including the driving effect of the density anomalies themselves ($R^S_\rho = 0.3$ for all z) as well as plate motion reconfigurations. Compare with Figure 5.7, middle row.

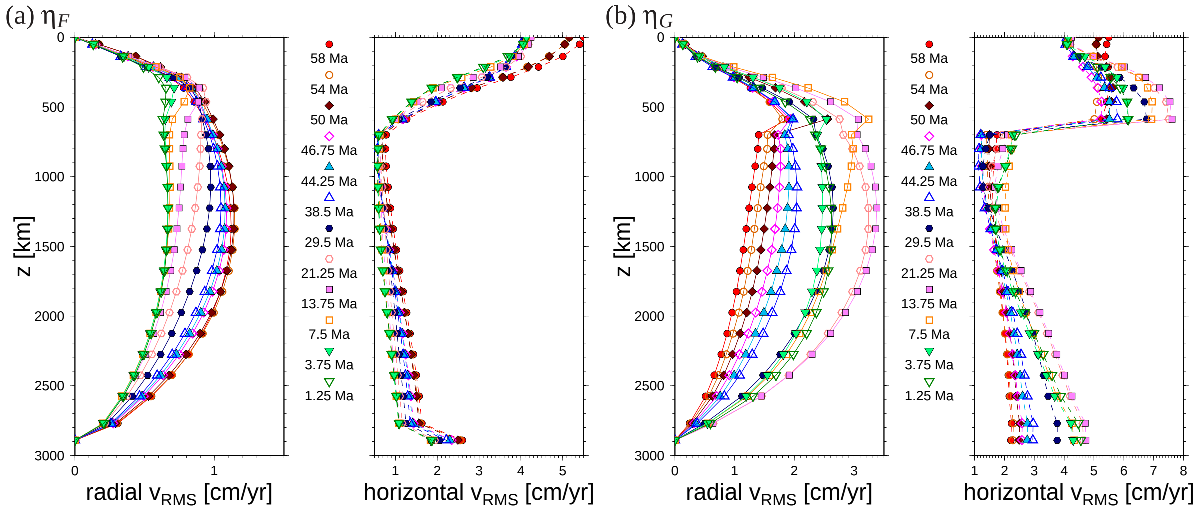

Figure 5.9: RMS of radial (left sub-plots) and horizontal (right sub-plots) velocities induced by plate motions and actively backward-advected density anomalies (derived from *ngrand* as described in the caption of Figure 5.7). We show RMS velocity variations versus depth until 60 Ma for η_F (a) and η_G (b).

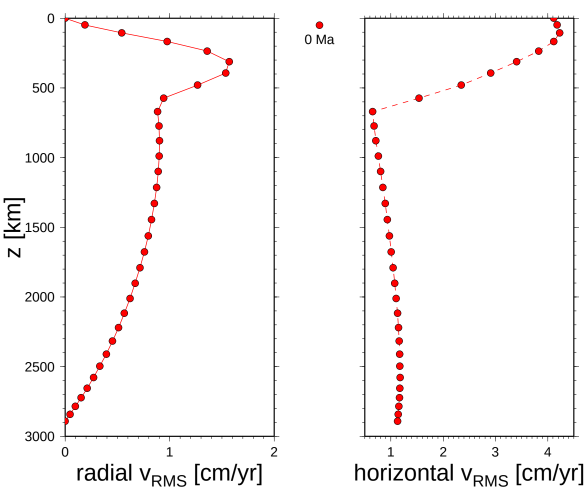

Figure 5.10: RMS flow profiles for a circulation calculation that uses the simplified viscosity profile of Bunge and Grand (2000) (viscosity of the lower mantle is larger than that of the upper mantle by a factor of 100). Density was converted from the final-stage temperature field of Bunge and Grand's calculation (P. Bunge, pers. comm.) for $\ell_{\max} = 63$, taking into account the depth-dependent thermal expansivity used by these authors. As in Bunge and Grand's (2000) model, our calculation includes the effect of plate motions.

note that active tracer methods (*e.g.* Schott *et al.*, 2000) would be better suited for problems in which the detailed distribution of density anomalies matters. The results from inversions that pursue a formal search for optimal mantle-flow histories such that the current density field emerges (Bunge *et al.*, 1998, 2001) should eventually be used for future strain modeling. However, since texture is unlikely to influence the pattern of convection significantly, the method we present next is completely general and can also be applied to a velocity field that has been generated with more sophisticated methods than we attempt to do here.

5.4.3 Finite strain

How can we measure the deformation of material around an imaginary particle that is advected in the mantle? The strain accumulation from an initial position $\mathbf{x}$ to a final position $\mathbf{r}$ can be estimated by tracking an initial infinitesimal displacement vector $d\mathbf{x}$ to its final state $d\mathbf{r}$ (*e.g.* Dahlen and Tromp, 1998, p. 26ff)

$$\mathbf{x} + d\mathbf{x} \longrightarrow \mathbf{r} + d\mathbf{r}. \tag{5.2}$$

We define the Eulerian deformation-rate tensor $\mathbf{G}$ based on the velocity $\mathbf{v}$ as

$$\mathbf{G} = (\nabla_{\mathbf{r}}\mathbf{v})^T \quad \text{such that} \quad d\mathbf{v} = \mathbf{G} \cdot d\mathbf{r}. \tag{5.3}$$

Here, $\nabla_{\mathbf{r}}$ is the gradient with respect to $\mathbf{r}$ and ^{T} indicates the transpose of a matrix. For finite strains, we are interested in the deformation tensor $\mathbf{F}$,

$$\mathbf{F} = (\nabla_{\mathbf{x}}\mathbf{r})^T, \tag{5.4}$$

where $\nabla_{\mathbf{x}}$ is the gradient with respect to the tracer $\mathbf{x}$, because $\mathbf{F}$ transforms $d\mathbf{x}$ into $d\mathbf{r}$ as

$$d\mathbf{r} = \mathbf{F} \cdot d\mathbf{x} \quad \text{or} \quad d\mathbf{x} = \mathbf{F}^{-1} \cdot d\mathbf{r}. \tag{5.5}$$

The latter form with the inverse of $\mathbf{F}$, $\mathbf{F}^{-1}$, allows us to solve for the deformation that corresponds to the reverse path from $\mathbf{r}$ to $\mathbf{x}$. $\mathbf{F}$ will be non-singular as long as the flow field is physical and does not contain any discontinuities. To obtain $\mathbf{F}$ numerically, we make use of the fact that $\mathbf{G}$ and $\mathbf{F}$ are related by

$$\frac{\partial}{\partial t}\mathbf{F} = \mathbf{G} \cdot \mathbf{F}, \tag{5.6}$$

where $\partial/\partial t$ denotes the time derivative. Our algorithm calculates $\mathbf{G}$ at each timestep to integrate (5.6) (starting from $\mathbf{F} \equiv \mathbf{I}$ at $\mathbf{x}$, where $\mathbf{I}$ denotes the identity matrix) with the same Runge-Kutta algorithm that is used to integrate the tracer position from $\mathbf{x}$ to $\mathbf{r}$. To ensure that volume is conserved, we set the trace of $\mathbf{G}$ to zero by subtracting any small non-zero divergence of $\mathbf{v}$ that might result from having to interpolate $\mathbf{v}$. Since $\mathbf{F}$ is non-singular, the deformation matrix can be polar-decomposed into an orthogonal rotation $\mathbf{Q}$ and a symmetric stretching matrix in the rotated reference frame, the left-stretch matrix $\mathbf{L}$, as

$$\mathbf{F} = \mathbf{L} \cdot \mathbf{Q} \quad \text{with} \quad \mathbf{L} = (\mathbf{F} \cdot \mathbf{F}^T)^{\frac{1}{2}}. \tag{5.7}$$

For the comparison with seismic anisotropy, we are only interested in $\mathbf{L}$ which transforms an unstrained sphere at $\mathbf{r}$ into an ellipsoid that characterizes the deformation that material accumulated on its path from $\mathbf{x}$ to $\mathbf{r}$. The eigenvalues of $\mathbf{L}$, $\lambda_1 > \lambda_2 > \lambda_3$, measure the length and the eigenvectors the orientation of the axes of that finite strain ellipsoid (FSE) at $\mathbf{r}$ after the material has undergone rotations. (The alternative polar-decomposition's right-stretch matrix $\mathbf{R}$, $\mathbf{F} = \mathbf{Q} \cdot \mathbf{R}$, corresponds to a strain-ellipsoid with principal axes that refer to the orientation and location before deformation; *e.g.* McKenzie and Jackson, 1983).

Our approach is similar to that of McKenzie (1979), as applied to subduction models by Hall *et al.* (2000). However, those workers solve (5.6) by central differences while we use Runge-Kutta integration. Moreover, Hall *et al.* calculate the FSE based on $\mathbf{B}^{-1}$ where

$$\mathbf{B}^{-1} = \left(\mathbf{F}^{-1}\right)^T \cdot \mathbf{F}^{-1}. \tag{5.8}$$

Hall *et al.* define a stretching ratio, s_i, from the undeformed to the deformed state in the direction of the i-th eigenvector of $\mathbf{B}^{-1}$ with eigenvalue γ_i as $s_i = 1/\sqrt{\gamma_i}$. Since $\mathbf{B}$ is equivalent to $\mathbf{L}^2$, and $\mathbf{B}$ as well as $\mathbf{L}$ are symmetric, both approaches yield the same results when we identify the λ_i with the s_i after sorting accordingly. Numerically, $\mathbf{L}^2$ is faster to calculate since it does not involve finding the inverse of $\mathbf{F}$.

We introduce "natural strains" as a convenient measure of stretching

$$\zeta = \ln\left(\frac{\lambda_1}{\lambda_2}\right) \quad \text{and} \quad \xi = \ln\left(\frac{\lambda_2}{\lambda_3}\right), \tag{5.9}$$

following Ribe (1992) who shows that the orientations of fast shear wave propagation rapidly align with maximum stretching eigenvectors in numerical deformation experiments, regardless of the initial conditions. After ζ and $\xi \gtrsim 0.3$, there are essentially no further fluctuations in fast orientations. Using a logarithmic measure of strain is also appropriate based on the modeling result of Ribe (1992) who found that the amplitude of seismic anisotropy grows rapidly with small linear strain and levels off at larger values, above $\lambda_1/\lambda_2 \sim 2$. When we average fast strain orientations with depth for the comparison with seismic anisotropy, we scale each observation with ζ to incorporate these findings. This is a simplification since some of Ribe's (1992) experiments indicate a more rapid saturation of anisotropy amplitude at large strains. However, differences between logarithmic and linear averaging of strain orientations are usually not large. We therefore defer the inclusion of a more detailed anisotropy amplitude scaling to future work when we can treat texture more realistically, *e.g.* using Kaminski and Ribe's (2001) approach.

All of our flow calculations are performed in the no-net-rotation reference frame since our model cannot generate any net rotation of the lithosphere as it has no lateral viscosity contrasts (see 4.3.1 and O'Connell *et al.*, 1991). A prescribed net rotation of the surface would not produce any strain but simply lead to a rotation of the whole mantle. Shear-wave splitting observations are, however, commonly compared with APM orientations in a hotspot reference frame (*e.g.* Vinnik *et al.*, 1992). As mentioned previously, the global misfit between velocities and splitting is indeed better if we allow for a net rotation in the plate motions. The simplest explanation for this agreement is that the orientation of velocity vectors in the APM frame at the surface corresponds to a simple shear layer in an asthenospheric channel between the plates and a stationary deep mantle. Such a view of mantle convection differs from our view of global circulation as closely coupled to the motion of the plates, arguments for which were reviewed in chapters 3 and 4. Since lateral viscosity variations exist in the mantle, a net rotation may be generated by convection. However, as shown by Steinberger and O'Connell (1998), the net rotation component in hotspot reference frames such as HS2 may be biased owing to the relative motion of hotspots. We will compare our NNR-frame derived strains with the quasi-null hypothesis of a correlation between splitting and plate-wide surface-velocity orientations below. In some cases, a better fit is obtained for strain-derived anisotropy, leading us to question the hypothesis of alignment with surface velocities, both for the APM and NNR reference frames. Since we cannot treat effects such as escape flow around continental keels properly with our method, questions about possible local alignment with flow relative to a deep mantle remain.

We formulate the following *ad hoc* rules to determine the finite strain from circulation models. Our first approach consists of following a tracer that starts at $\mathbf{r}$ backward in time for a constant interval τ to location $\mathbf{x}$ while keeping track of the deformation $\mathbf{F}'$ ($\tau \sim 5$ Myr). We then calculate the strain that would have accumulated if the tracer were to move from an unstrained state at $\mathbf{x}$ to $\mathbf{r}$, given by $(\mathbf{F}')^{-1}$. Such an approach would be appropriate if texture formation were only time-dependent; the $\tau \to 0$ result is related to the instantaneous strain rates. Our second, alternative, approach defines a threshold strain ζ_c above which any initial texture gets erased, as would be expected from the results of Ribe (1992) ($\zeta_c \sim 0.5$). In this case, we only have to advect backward until ζ or ξ, as based on $(\mathbf{F}')^{-1}$, reaches ζ_c; we iterate to match $\zeta(\mathbf{r})$ to ζ_c within 2%. The tracer trajectory will correspond to different time intervals depending on the initial position of the tracer, as will be addressed below. We stop backward advection for tracers once they are below 410 km, where we expect that the phase transition from olivine to the β-phase (*e.g.* Agee, 1998) will erase all previous texture. For most of the models, we will consider the flow field as steady-state but not advect back in time for more than 43 Ma, the age of the bend in the Hawaii-Emperor seamount chain that marks a major reorganization of plate motions (*e.g.* Gordon and Jurdy, 1986). We will show that changes in plate motions affect only the very shallowest strains for continuous strain accumulation.

Freezing of strain

As reviewed by Savage (1999), there is evidence that olivine crystals will not reorient themselves easily below a critical temperature of $\sim$900°C (Goetze and Kohlstedt, 1973). This implies that the shallowest anisotropy might be frozen in, representing previous tectonic strain accumulation which may have no correlation with the current pattern of convection (Silver, 1996). This is the reason we expect our models to have difficulty capturing the anisotropy in old continental regions. In the oceans, frozen-in fossil spreading directions have also been invoked to explain azimuthal anisotropy (*e.g.* Nishimura and Forsyth, 1989; Yu and Park, 1994).

In our models, strain accumulation is normally active at all times. However, the high viscosity of the lithosphere and the small lateral gradients in surface velocity limit the shallow strain-rates. If we had a good model of past seafloor ages to complement paleo plate-motion datasets, or a general thermal circulation model, it would be possible to infer a depth distribution of temperature and apply simple rules for the freezing of strain. While maps of past seafloor age have been published (Lithgow-Bertelloni and Richards, 1998), they are not easily accessible. Instead of assembling synthetic seafloor-age maps from the plate reconstructions, we use an empirical relationship between the horizontal divergence of near-surface velocities and seafloor age at the present day to infer past ages (Figure 5.11). While not very accurate, our approach should suffice to explore the effects of shallow, frozen-in strain and is easy to implement. In practice, we determine a critical depth, z_c, of the $T = 0.5T_m$ isotherm as described in the caption of Figure 5.11, limited to 70 km maximum depth. If tracers are closer to the surface

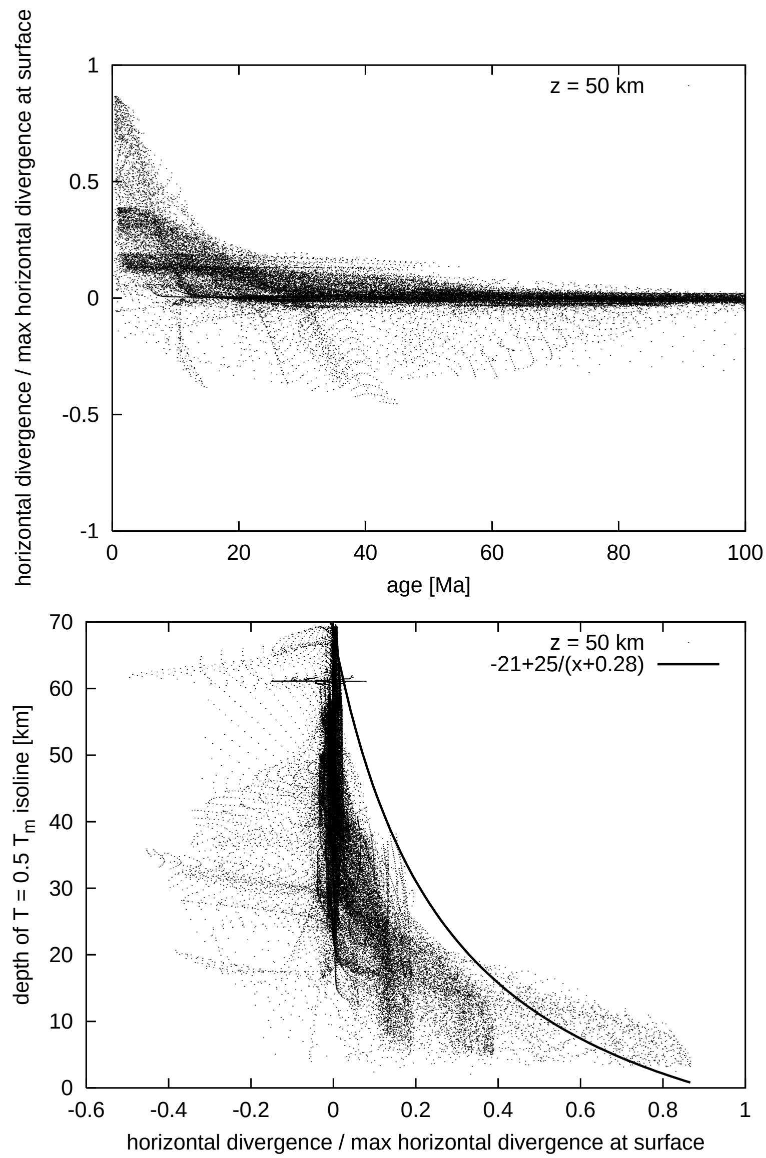

Figure 5.11: Top: Seafloor age from Müller *et al.* (1997) versus horizontal divergence, $\nabla_h \mathbf{v}$, of the velocity field of a $\ell_{\max} = 63$ plate-motion only calculation with η_F at 50 km depth (sampled at $1^\circ \times 1^\circ$ intervals for areas covered by Müller *et al.*'s (1997) data). The maximum horizontal divergence at the surface, $\nabla_h \mathbf{v}|^{\text{surf.}}_{\max}$, is used for normalizing $\nabla_h \mathbf{v}$. Bottom: normalized $\nabla_h \mathbf{v}$ versus inferred depth of the $T = 0.5 T_m$ isotherm from half-space cooling. Here, T_m denotes the temperature of the mantle below the lithosphere. The depth z_c of this isoline is given by $0.95\sqrt{\varkappa t}$ where $\varkappa = 10^{-6}$ m^2/s is thermal diffusivity, the prefactor is $\approx 2\times$ the inverse error function of 0.5, and t the age of the seafloor. We limit z_c to 70 km maximum depth and show an approximate upper bound that fits most of the data, $z_c[\text{km}] = -21 + 25/(\nabla_h \mathbf{v}/\nabla_h \mathbf{v}|^{\text{surf.}}_{\max} + 0.28)$.

than z_c, their symmetric strain-accumulation is halted and the previous strain ellipsoid is only allowed to rotate. Numerically, the freezing is modeled by replacing $\mathbf{G}$ in (5.6) with its anti-symmetric part $\mathbf{W}$ (the rotation-rate tensor, or vorticity) which we find by Cartesian decomposition

$$\mathbf{W} = \mathbf{G} - \mathbf{D} = \frac{1}{2}\left(\mathbf{G} - \mathbf{G}^T\right), \tag{5.10}$$

where the symmetric part, $\mathbf{D}$, is the strain-rate tensor.

5.4.4 Examples of finite strain accumulation

We examine strain accumulation by following individual tracers close to plate boundaries in order to develop an understanding of the global, convection-related strain field. Our examples are improvements over previous work (*e.g.* McKenzie, 1979; Ribe, 1989; Hall *et al.*, 2000) in that they are fully 3-D and are based on realistic estimates of present and past mantle circulation. Flow calculations were performed for a mantle model of the Hager and O'Connell (1981) type in which the creep rheology is Newtonian, as would be expected for the diffusion-creep regime of the high-temperature deep mantle (*e.g.* Ranalli, 1995). However, lattice-preferred orientation of olivine, and hence LPO-related anisotropy, forms only in the dislocation-creep regime, which is characterized by a stress

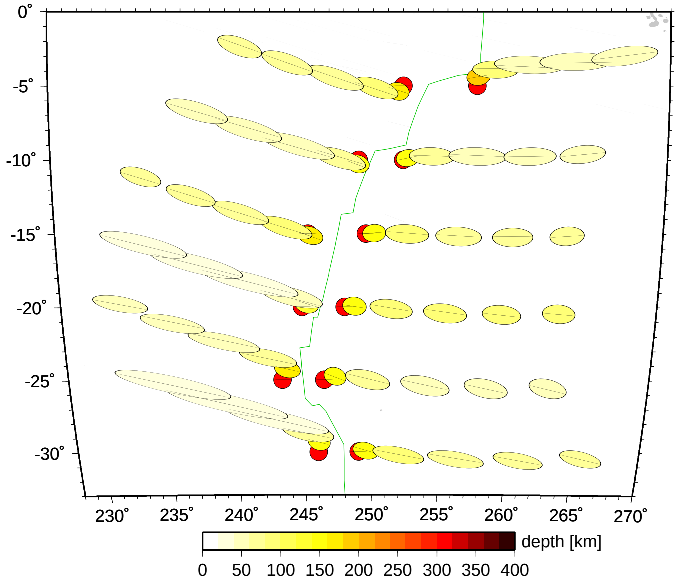

Figure 5.12: Horizontal projection of the largest principal axes of strain ellipsoids (sticks) and horizontal cut through FSEs (ellipses) centered at tracer positions in plate-motion driven flow around the East Pacific Rise (EPR, see sec. 5.4). Tracer positions are shown at 5 Myr intervals, starting at 300 km depth, with depth color-coded according to the scale given below the map.

weakening power-law. We expect that Newtonian mantle flow fields will be similar to those with power-law creep (*e.g.* Christensen, 1984) and therefore think that velocities in our models should resemble the actual large-scale circulation pattern in the mantle. A quantitative study of 3-D circulation with power-law rheology to validate this assumption remains to be undertaken. Given the variations in texture that were found in regional models that incorporated greater rheological complexity (Hall *et al.*, 2000), or a more sophisticated treatment of texture development (*e.g.* Blackman and Kendall, 2002), it seems reasonable not to attempt to combine all aspects of the problem at this point but to focus instead on treating flow with greater realism in global 3-D models.

For simplicity, the flow field used for our divergent margin example for the East Pacific Rise (Figure 5.12) includes only plate-motion related flow, calculated by prescribing NUVEL1 (DeMets *et al.*, 1990) NNR velocities at the surface. The largest stretching axes align roughly perpendicular to the ridge and mostly in the horizontal plane (horizontal projections of largest FSE axes align with the horizontal cut through the strain ellipsoid). The ridge-related strain pattern, with fast seismic anisotropy orientations parallel to spreading-directions, has been observed globally for surface waves (*e.g.* Forsyth (1975), Nishimura and Forsyth (1989), Montagner and Tanimoto (1991), Ekström (2001), and Figures 5.3 and 5.5c) and has been interpreted in terms of a general plate tectonic framework (*e.g.* Montagner, 1994). Local *SKS* measurements to complement observations around ridges are, so far, only available for the MELT experiment (see Wolfe and Solomon (1998) and Figure 5.4); we discuss our fit to Wolfe and Solomon's (1998) data in sec. 5.7.1.

The strain evolution at convergent margins (Figure 5.13) can be divided into two stages: first, we see compression in the plane of the slab as material is forced into the mantle, as shown in Figure 5.13a (without slab pull) and the initial phases of Figure 5.13b. In this stage, the largest stretching axes are nearly radial, and the horizontal part of the FSE shows trench-parallel elongation. In the second stage, for greater depths and when slab pull is included (*stb00d* density, see sec. 3.3.4, in Figure 5.13b), deep stretching becomes more important and leads to deformations such that the largest stretching axes rotate perpendicular to the trench and become more horizontal. In the regions where the largest eigenvector points in a nearly radial direction, the elongated horizontal part of the FSE approximately follows the trench geometry and shows varying degrees of trench-parallel alignment. In regions where measurements for *SKS* waves, traveling nearly radially, yield zero or small anisotropy but where more horizontally propagating local *S* phases show splitting (Fouch and Fischer, 1998), the (smaller) horizontal deformation component may be important. This is particularly the case if crystallographic fast axes are distributed in a ring rather than tightly clustered around the largest FSE eigendirection (*cf.* Figure 5.1), in which case the resolved anisotropy may be trench parallel. However, Hall *et al.* (2000) show that synthetic splitting in 3-D flow derived from ray-tracing is mostly trench-perpendicular in the back-arc region if fast wave propagation is assumed to be always oriented with the largest eigenvector of the FSE. Therefore, slab rollback or escape flow around a slab that impedes large scale currents in the mantle is usually invoked as an explanation for trench-parallel splitting measurements (*e.g.* Russo and Silver, 1994; Buttles and Olson, 1998; Hall *et al.*, 2000; Smith *et al.*, 2001). We

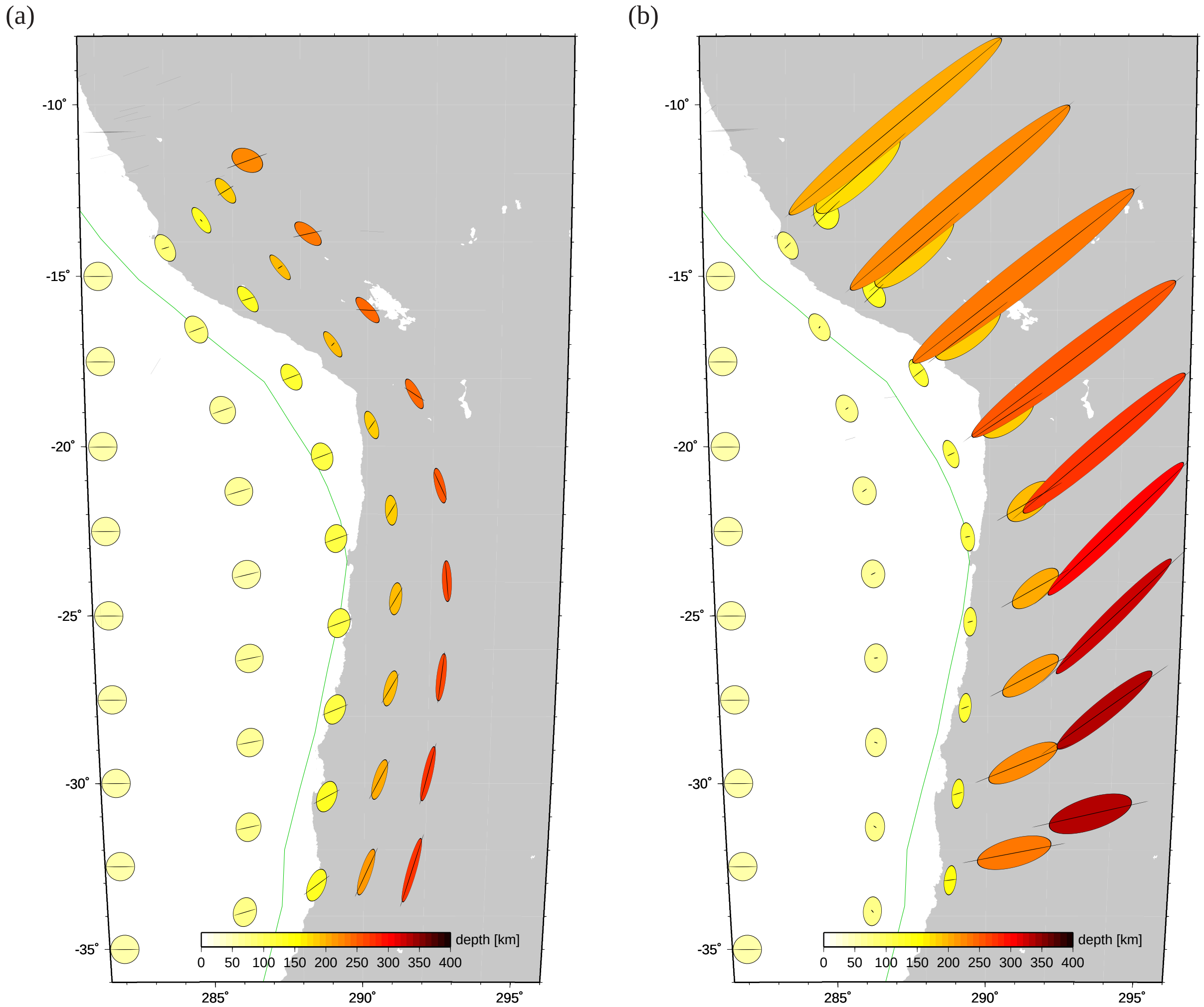

Figure 5.13: Horizontal slices through FSEs and projections of the largest stretching axes (sticks) for tracers in (a) plate-motion-only and (b) *stb00d* density-included flow at 5 Myr intervals for part of the South American subduction zone. Ellipses are drawn at tracer positions as in Figure 5.12, moving from west to east and starting at 50 km depth in the Nazca plate. Note the variations in predicted slab dip along strike as indicated by the final depth of the tracer locations (*cf.* sec. 2.3.2).

will analyze our predictions for circum-Pacific subduction zones further in sec. 5.7.2.

First, we put regional flow into a global framework by discussing individual tracers that accumulate $\zeta_c = 1$ strain before arriving in the lithosphere (Figure 5.14). We now use evolving paleo plate-motions since 60 Ma, for simplicity without any density-driven flow. The convective reorganization at 43 Ma is clearly seen in the Pacific tracer paths in Figure 5.14a. From comparing the lengths of the individual trajectories in Figure 5.14a and Figure 5.14c (final locations of tracers are identical for Figure 5.14a – c; tracers are plotted in 5 Myr intervals along their paths) we can estimate the rate of strain accumulation that material undergoes along the tracer paths. At 50 km depth (Figure 5.14a), strain rates are small, especially under the continents, and some tracers do not reach $\zeta_c = 1$, even after 60 Ma. However, strains of $\zeta \sim 1$ are reached within a few tens of Myr at 100 km depth. Figure 5.14b is identical to Figure 5.14a except that we allow "freezing" of shallow strain according to sec. 5.4.3. As a consequence, little strain accumulates globally at 50 km since all deformation is focused around the ridges and tracers do not travel far enough in 60 Ma for large areas to be affected. Local orientations for frozen-in strain differ somewhat from those for constant reworking (Figure 5.14a).

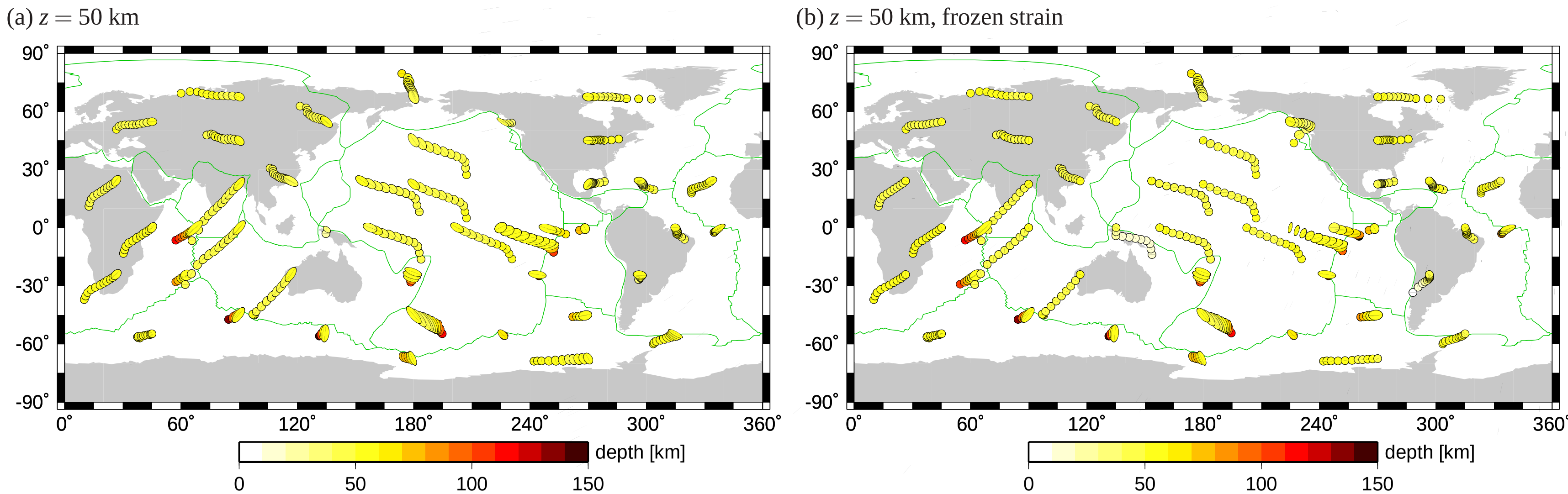

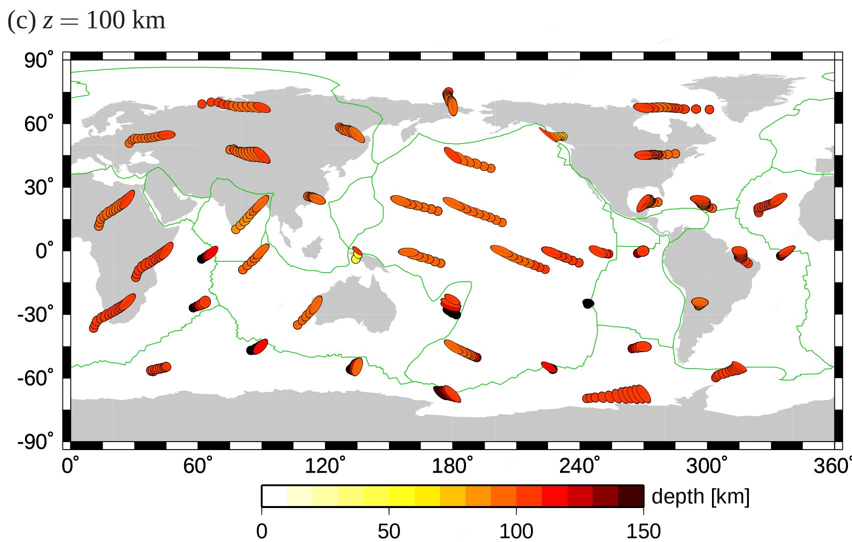

Figure 5.14: Trajectories for $\zeta_c = 1$ strain accumulation in plate-motion related flow for η_F; tracers have final (strained) depths of $z = 50$ km (a and b) and 100 km (c). The final lateral positions are identical for (a) through (c) while the initial (unstrained) positions depend on the rate of strain accumulation. We show horizontal projections of the largest principal axes (sticks) and horizontal cuts through the FSE at 5 Myr intervals (ellipses) as in Figure 5.13; ellipses are shaded according to the tracer depth as specified in the colorbars. Plate motion evolves back to 60 Ma as in Figure A.4. (b) differs from (a) in that the strain remains frozen in for tracers that are shallower than a critical z_c (sec. 5.4.3).

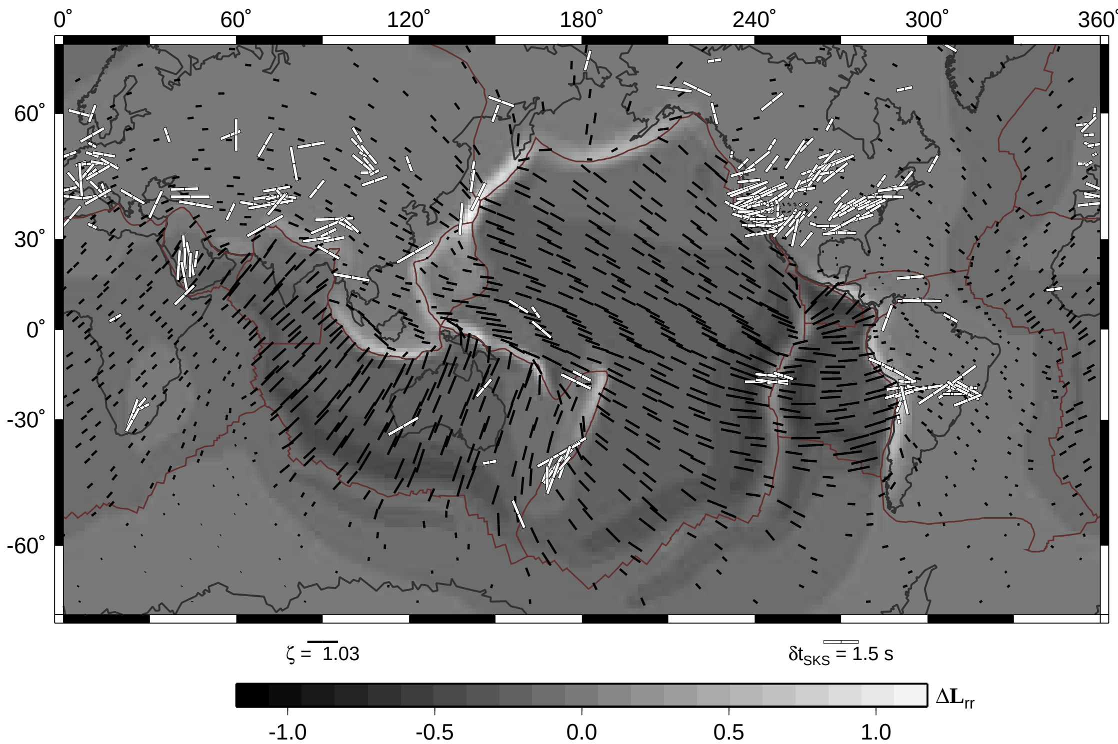

Figure 5.15: Depth-averaged (upper mantle, 50 km $\leq z \leq$ 400 km) finite strain for $\tau = 10$ Myr strain accumulation and plate-motion related flow only, viscosity profile η_F. Thin black sticks are plotted at every $\sim$5th tracer location and indicate the orientation of the horizontal projection of the largest axis of the FSE, scaled with the logarithmic strain ζ (see legend below map). Background shading denotes $\Delta F_{rr} = F_{rr} - 1$, and thick gray sticks show fast orientations and amplitude of our $3^\circ \times 3^\circ$ averaged shear-wave splitting (*SKS* only) dataset (*cf.* Figure 5.5a).

5.5 Global finite-strain maps

5.5.1 Plate-scale circulation

Figure 5.15 shows the global, $\tau = 10$ Myr time interval, depth-averaged strain field for a circulation calculation that incorporates only plate-driven flow using η_F. For simplicity, plate motion is assumed to be steady-state. We focus on the horizontal projection of the largest stretching direction of **L**, showing the orientation of maximum FSE extension as sticks whose lengths scale with ζ. The background shading in Figure 5.15 shows $\Delta L_{rr} = L_{rr} - 1$ as an indication of stretching in the radial, r, direction. Strain was calculated for $\sim 10,000$ approximately evenly distributed tracers ($\approx 2^\circ$ spacing at equator) for each layer, which were placed from 50 km through 400 km depth at 50 km intervals to sample the upper mantle above the 410-km phase transition. The horizontal projections of the largest principal axes of the strain ellipsoid are depth averaged after weighting them with the ζ-scaled strain at each location (*cf.* sec. 5.4.3), while the radial, ΔL_{rr}, part is obtained from a simple depth average. The strain orientations will be interpreted as a measure of the depth-averaged anisotropy, and as the cause of the shear-wave splitting that is observed. A more elaborate approach that includes raytracing (*e.g.* Hall *et al.*, 2000) might be needed for work that goes beyond exploring regional-scale patterns since variations in anisotropy with depth might affect the measured splitting in a non-linear fashion (Saltzer *et al.*, 2000).

The finite-strain field of Figure 5.15 is similar to instantaneous strain-rates in terms of the orientations of largest extension, which are dominated by the shearing of the upper mantle due to plate motions. However, orientations are not identical to those expected to be produced directly from the surface velocities (*e.g.* Figure 5.5a) because of return flow effects. The depth-averaged strain for $\tau = 10$ Myr is furthermore dominated by radial extension (positive ΔF_{rr}, *i.e.* horizontal compression) at both ridges and trenches, unlike for instantaneous strain (or small τ) where ridges are under average radial compression. This effect is due to the large radial stretching

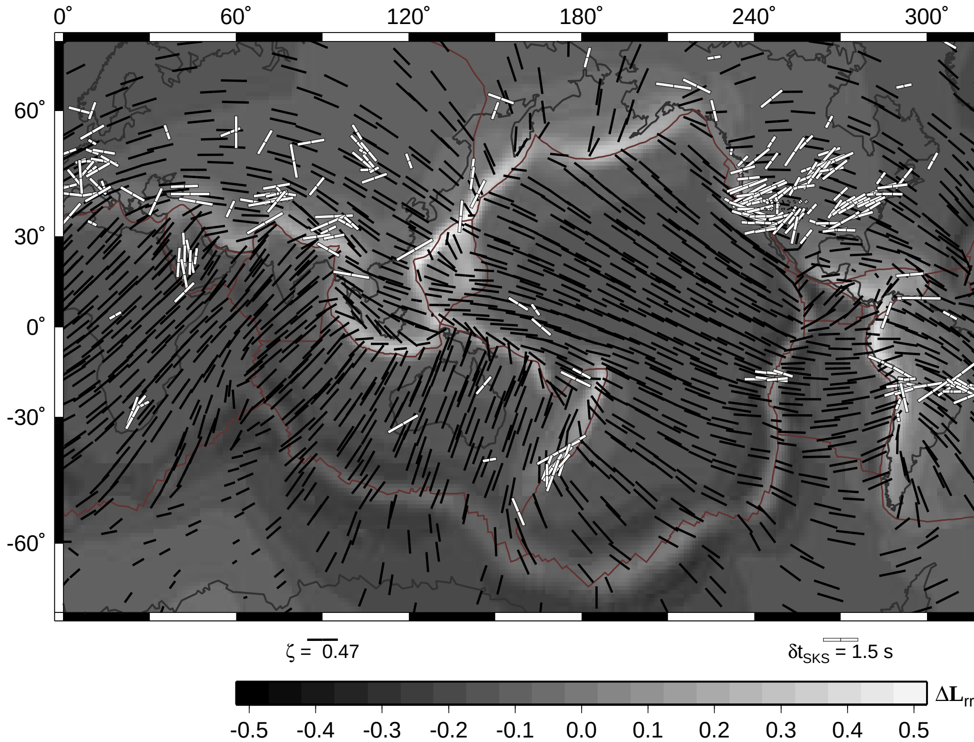

Figure 5.16: Depth averaged finite strain for constant $\zeta_c = 0.5$ strain accumulation and plate-motion related flow only, viscosity profile η_F. We use steady-state flow and stop advection at 43 Ma (*cf.* Figure 5.15, but note that strain scale is changed).

of material that rises underneath the ridges before being pulled apart sideways and radially compressed at the surface. This observation may explain the fast v_{SV} anomaly in surface wave models for the EPR (sec. 5.3.1). In general, strain accumulation for constant time models is strongest underneath the fast-moving oceanic plates.

Figure 5.16 shows results for constant finite strain, $\zeta_c = 0.5$, assuming that this is a relevant reworking strain after which all previous texture is erased (Ribe, 1992). As a consequence, most horizontal strains are of comparable strength, with some exceptions, such as the Antarctic plate around 30° W/60° S. There, shearing is sufficiently slow that it would take more than our cutoff value of 43 Ma to accumulate the ζ_c strain. Figures 5.17 and 5.18 explore such variations in the rate of strain accumulation, showing histograms of tracer advection distance and time required to achieve ζ_c (“age”, Figure 5.17) and maps of tracer age (Figure 5.18) for 50 km and 250 km depth for the $\zeta_c = 0.5$ model of Figures 5.16. In accord with the examples from Figure 5.14, we find that most shallow strain markers (within the high-viscosity lithospheric layer) have our age-limit of $t_c = 43$ Ma, implying that strain accumulation is limited within the “plates” that move coherently without large interior velocity gradients (Figures 5.17a and 5.18a). For deeper layers (Figures 5.17b and 5.18b), where shearing is stronger, strain is accumulated more rapidly such that $\zeta = 0.5$ is reached by most tracers before 20 Myr and at smaller horizontal advection distances than at shallow depth. Figure 5.18b demonstrates that certain regions underneath continents have particularly slow strain accumulation from plate-scale flow; most of these features occur where minima in the amplitudes of surface velocities are found.

All of the observations for strain due to plate motions are robust in the sense that the large-scale patterns have only moderate dependence on the details of the viscosity structure as long as a canonical profile with high-viscosity lithosphere, lower-viscosity upper mantle (100 km $< z <$ 660 km), and higher-viscosity lower mantle (*e.g.* η_D or η_F in sec. 4.5) is used. However, considering only plate motions means that flow is concentrated in shallow layers, especially when there is a strong increase in viscosity with depth. If we include a low-viscosity channel at 660 km by using η_G (*cf.* Figure 4.7), the velocity gradient in the upper mantle is smaller than for η_F since most of the shear is focused in the low viscosity channel (sec. 5.4.2). For our constant-strain models, this implies that larger areas will fail to reach ζ_c strains of 0.5 before the cut-off time when η_G is used instead of η_F.

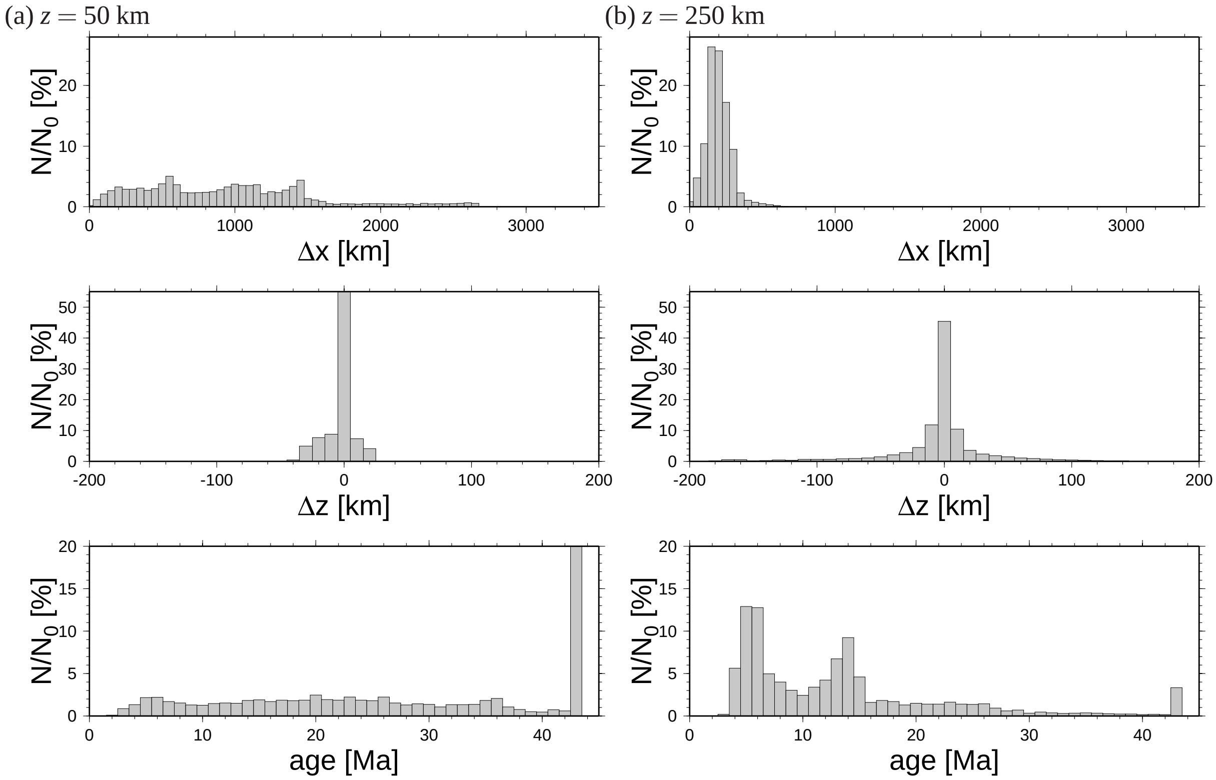

Figure 5.17: Histograms of tracer "ages" (*i.e.* duration of ζ_c-strain accumulation) and approximate path lengths for $\zeta_c = 0.5$ (see Figure 5.16) for plate motions only and η_F. We show horizontal (Δx) and vertical (Δz) distance traveled between initial and final position, and age for tracers at final depths of 50 km (a) and 250 km (b). N/N_0 denotes relative frequency, and tracer locations are chosen such that they evenly sample the surface areas of the respective layers. (Velocities are assumed to be steady-state and the cut-off age is 43 Ma.)

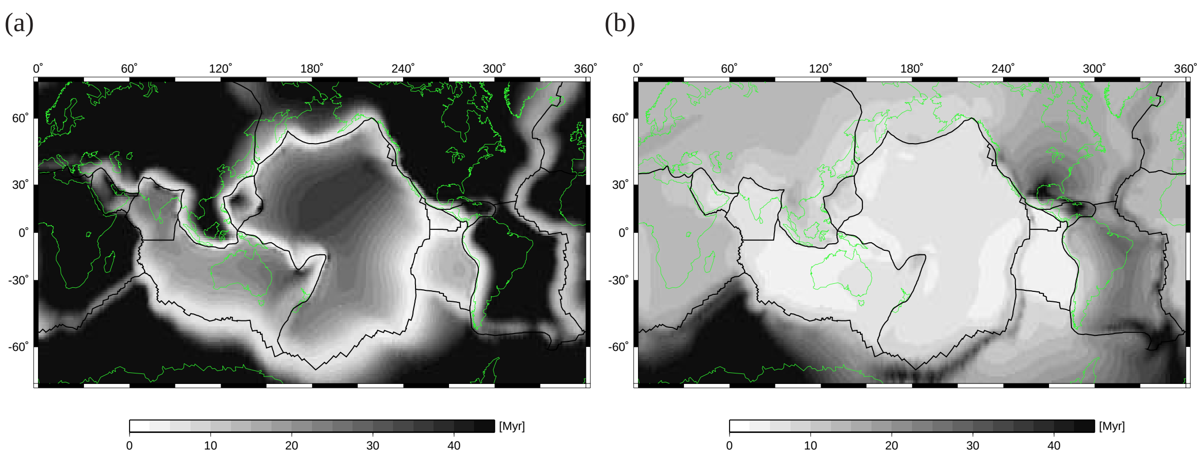

Figure 5.18: Age of tracers at 50 km (a) and 250 km (b) depth for constant strain accumulation ($\zeta_c = 0.5$) and plate-motion related flow only (*cf.* Figures 5.16 and 5.17), with viscosity η_F.

Largest stretching orientations for the plate-motions only η_G model are also somewhat different from those for η_F, and correlate better with *SKS* splitting, mostly because strain underneath the Americas follows the observed orientations more closely than strain for η_F.

5.5.2 Mantle density driven flow

Figure 5.19 shows $\zeta_c = 0.5$ depth-averaged strain for flow that includes the effect of plate-related motion plus internal densities as derived from tomography model *smean* from sec. 3.3.3. R_ρ^S (sec. 4.3.4) is assumed to be zero for depths shallower than 220 km and 0.2 elsewhere, as in sec. 4.4.1. With the caveat that we are interpreting the instantaneous flow that should be characteristic of mantle convection at the present day as steady state for several tens of Myr, we find that the inclusion of mantle density leads to a concentration of radial flow and deformation underneath South America and parts of East Asia. These features are related to past subduction where the circum-Pacific downwellings exert strong forces on the overlying plates (*cf.* Steinberger *et al.*, 2001; Becker and O'Connell, 2001a). For η_F, smaller-scale structure due to density anomalies is most clearly visible within continental plates, which were characterized by large-scale trends for plate motions alone. Other patterns include a west-east extensional orientation in East Africa, related to an upwelling that correlates with the rift-zone tectonics. The predicted strain for η_G (Figure 5.19b) is, expectedly, more complex. Since the low viscosity notch of η_G partly decouples the upper and lower mantle in terms of shearing, upwellings such as the one in the southwestern Pacific (the superswell region) are able to cause a relatively stronger anisotropy signal than for the η_F model. Figure 5.20 shows how the tracer strain accumulation is affected by the additional density-related flow. We show results for tracer ages and path lengths for 250 km depth only (*cf.* Figures 5.17b and 5.18b) because shallow strains are similar to those from plate motions only. Tracers are shifted toward smaller strain ages on average and distributions are smoother for flows that include buoyancy.

In contrast to the plate-motion only models, finite strain from density-driven flow is quite sensitive to the input models and viscosity structures in terms of the local orientations of the largest stretching axes (*e.g.* Figure 5.19). This is to be expected, given that tracer advection will amplify small differences between tomographic models. Figure 5.19 is therefore only an illustration of the large-scale features predicted by the lowest-common-denominator tomography model *smean*; individual high resolution models (*e.g. ngrand*) lead to more complex strain predictions. One measure of radial variations of strain in the upper mantle is presented in Figure 5.21; we show the cumulative, absolute difference in orientations of the horizontal projection of largest principal FSE axes (regardless of ζ-amplitude) from 50 km to 400 km depth, $\Phi = (\Sigma\Delta\alpha)/\Delta z$. Figure 5.21 compares plate-motion only and *smean* density-included flow for $\zeta_c = 0.5$. The largest cumulative rotations of strain are found in regions of strong radial flow and stretching in the mantle, at ridges and trenches. Absolute angles of rotation of strain with depth reach $\sim 300^\circ$ in places; such rotations might have a significant effect on shear-wave splitting (Saltzer *et al.*, 2000). However, a direct comparison is complicated since Saltzer *et al.* used a continuous rotation of fast orientations and we are dealing with clockwise and counterclockwise rotations (which both are counted positive for Φ). Figure 5.21b shows Φ for flow that includes *smean* density; as in the global maps for strain, we observe that additional structure is found within the continents and the large oceanic plates. Refinement of such analyses of rotations of anisotropy with depth together with ray-tracing should help clarify splitting observations.

If we visually compare the horizontal projections of the largest principal axes of the FSE from the global, depth-averaged strain predictions with the observed and synthetic splitting orientations from Figure 5.5, we see that agreement between strain and splitting is good in most oceanic and young continental regions, *e.g.* the western US. In older continental regions (*e.g.* the eastern US and eastern South America) agreement is poor. We also observe large misfits between extensional strain and splitting in New Zealand and NE Tibet, both regions where shearing has been supposed to dominate tectonic deformation. Figure 5.22 quantifies the global misfit of several models with a $1^\circ \times 1^\circ$ average of *SKS* splitting orientations similar to Figure 5.5a. We show strain-derived models (see caption for acronyms, flow was calculated with scaling factors as in sec. 4.4.1) and those that are based on the corresponding velocity orientations (also depth-averaged) to test the hypothesis that splitting is aligned with with APM ("v.nr") or NNR ("v") flow orientations. Viscosity profiles were selected based on our inversions in chapter 4 and mantle models are representative of tomography (*smean*) and geodynamic (*stb00d*) approaches; *rum* contains upper mantle slabs in regions with seismicity only.

The radially averaged $\langle\Delta\alpha\rangle$ values of Figure 5.22 can be compared with the surface APM orientation derived misfits of $\langle\Delta\alpha\rangle = 31.2^\circ$ (sec. 5.3). Most APM misfits are better than those for NNR velocities. Figure 5.22 also shows that some strain-derived models have comparably low misfits, but none of the strain-derived orientations fit the *SKS* data better than alignment with velocities. Some of the tomography-included models lead to smaller misfits for larger ζ_c or τ strains while the opposite is true for plate-motion only models. It is difficult to interpret these findings given the uneven distribution of the *SKS* data that samples mostly continents where we expect that our method will lead to the least reliable estimates of anisotropy. It is therefore possibly premature to draw any

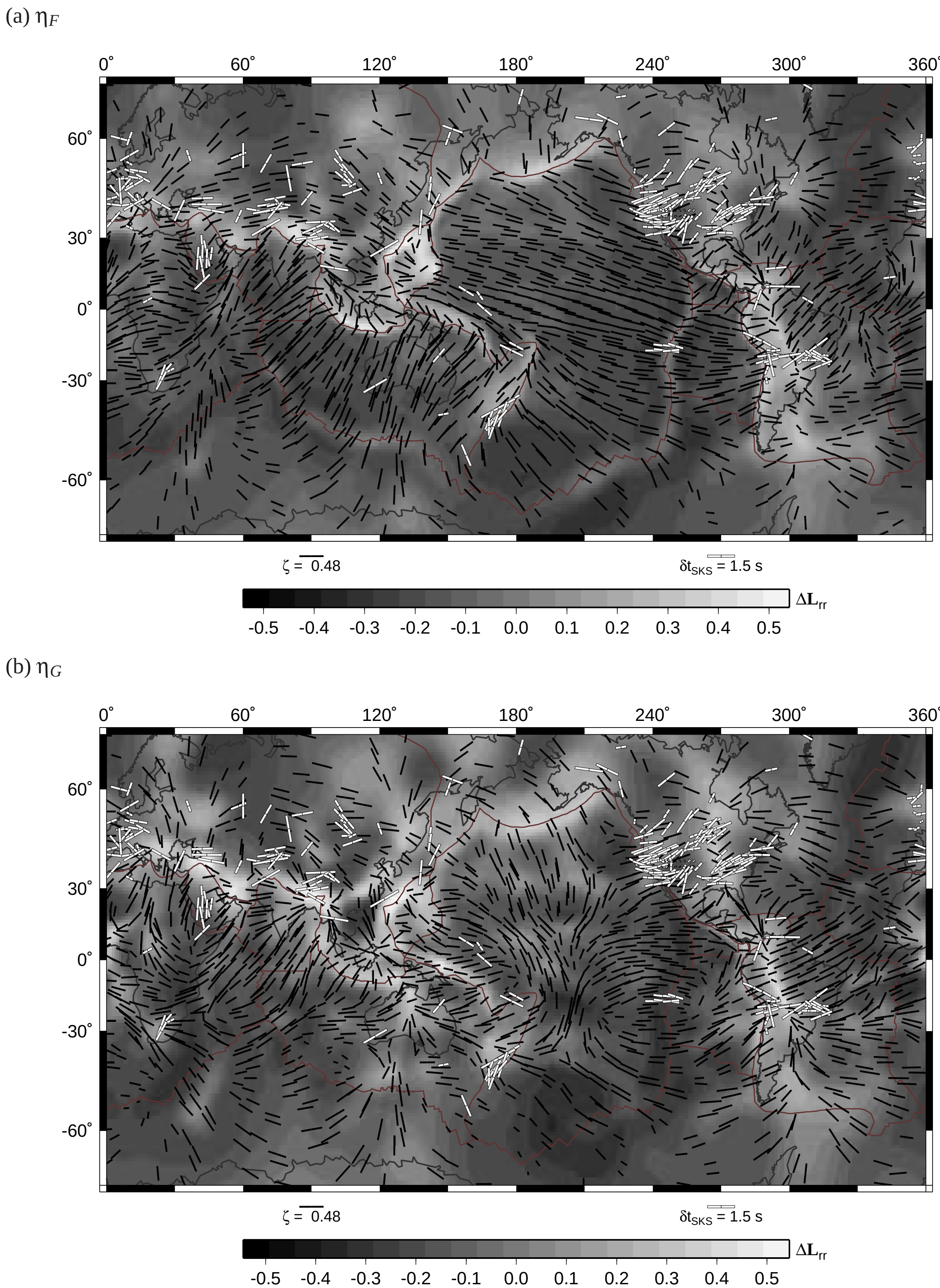

Figure 5.19: Depth-averaged finite-strain for $\zeta_c = 0.5$ strain accumulation in plate-motion and *smean*-driven flow for viscosity profiles η_F (a, *cf*. Figure 5.16) and η_G (b).

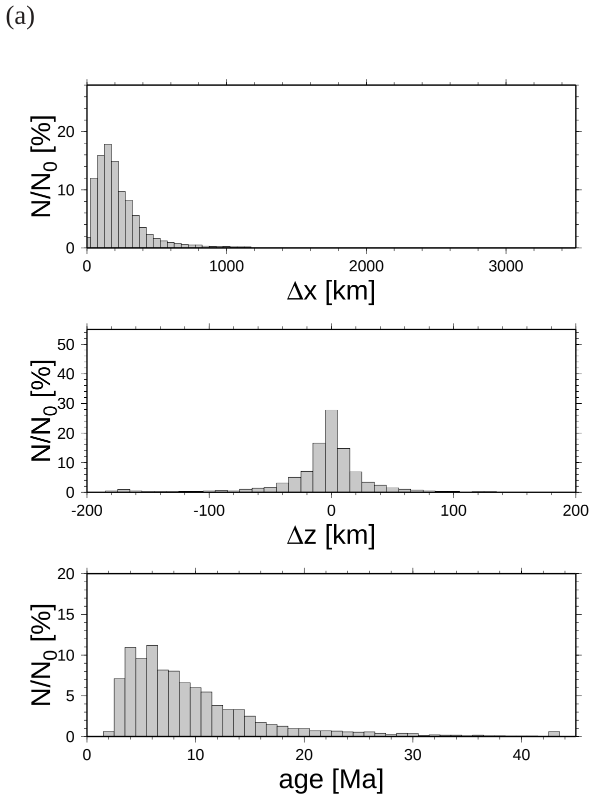

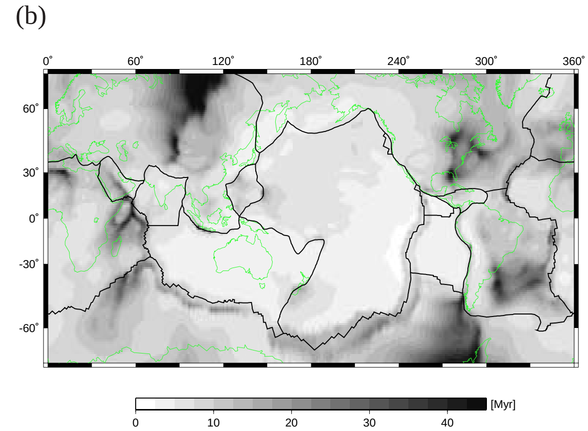

Figure 5.20: Tracer trajectory endpoint and age histograms (a, *cf.* Figure 5.17b) as well as age map (b, *cf.* Figure 5.18b) for tracers at 250 km from a $\zeta_c = 0.5$ model with plate-motions plus *smean*, η_F.

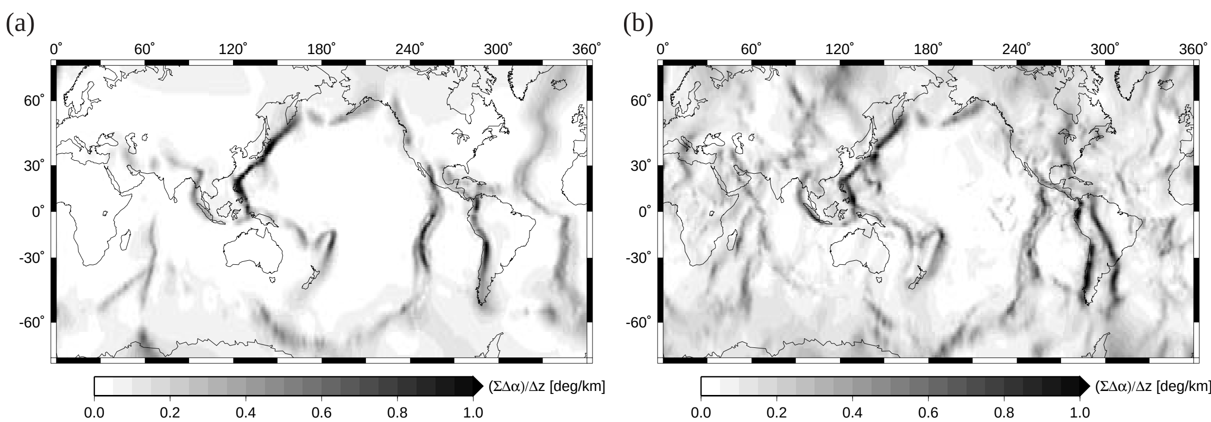

Figure 5.21: Cumulative absolute rotation of the horizontal projection of largest FSE axis, Φ, for $\zeta_c = 0.5$ plate-motion only model (a, *cf.* Figure 5.16) and plate motions and *smean* (b, *cf.* Figure 5.19a), both with η_F. Φ was calculated by summing up absolute orientation differences (no ζ-weighting, $0^\circ \leq \Delta\alpha \leq 90^\circ$) for tracers between subsequent layers with mid-layer depths between 50 km and 400 km ($\Delta z = 400$ km; 50 km thick layers from 25 km – 425 km). $\Sigma\Delta\alpha/\Delta z = 0.5\,^\circ$/km therefore corresponds to 200° cumulative differences in fast axes orientations.

conclusions from a global misfit estimate such as Figure 5.22. However, flow-field derived strain does not lead to better results than alignment with flow itself in terms of mean orientational misfit with *SKS*.

5.5.3 Changes in plate motions

The global models described in the previous section were all based on steady-state flow with a cut-off age, t_c, of 43 Ma. We conducted additional experiments where we allowed for evolving plate boundaries and backward-

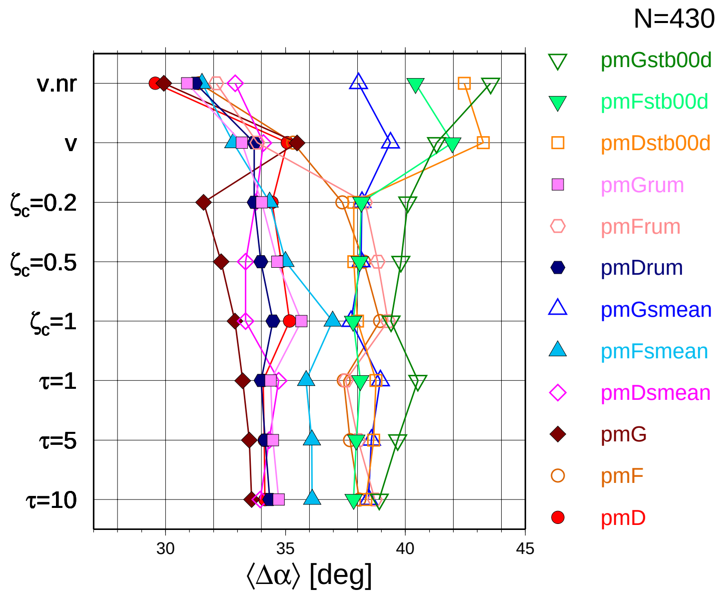

Figure 5.22: Global mean orientational misfit $\langle \Delta\alpha \rangle$ between $1^\circ \times 1^\circ$ averaged *SKS* splitting data and depth-averaged "anisotropy" as derived from the horizontal projection of the largest FSE axes (ζ-weighting) or from velocity field orientations. *y*-axes: "v" and "v.nr" are for NNR and APM (HS2-NUVEL1) reference-frame velocities, respectively; τ and ζ_c refer to fixed time (in Myr) and fixed strain, respectively. "pmX" indicates plate-motion only models with viscosity η_X, appended model names like *rum* imply that density driven flow was included. $\Delta\alpha$ was calculated at the center of grid boxes with entries in our splitting data, $\langle \Delta\alpha \rangle$ is the area weighted mean, and *N* the number of observations. For simplicity, we do not weight by the anisotropy amplitudes.

advected density anomalies as described in sec. 5.4.2. Given our findings for the depth dependence of strain-rates from above, results for $z \gtrsim 150$ km were, as expected, similar to the steady-state models; depth averages with uniform weight for each layer as in Figures 5.16 and 5.19 are, thus, not strongly modified. Figure 5.23 explores some of the variations in predicted strains for shallow depth, at $z = 50$ km. We show results from $\zeta_c = 1$ calculations to allow for long tracer paths before the cut-off strain is reached, choosing z and t_c such that the differences between strain as produced from steady-state and evolving circulation are largest. Plate boundaries that change with time and advected density anomalies will introduce more complexity at small scales. We find that the large-scale effects of evolving plate boundaries are modest, however, even when we go back beyond the bend in the Hawaii-Emperor seamount chain at 43 Ma to $t_c \sim 60$ Ma (Figure 5.23c). The most prominent feature for $t_c \sim 60$ Ma for plate motions is a break in the Pacific pattern such that fast orientations are locally oriented perpendicularly to the present-day spreading orientations around 225 °W/15°S. Only for very long times, *e.g.* $t_c = 120$ Ma, do we find significantly different plate-scale patterns, such as in the Western Pacific (Figure 5.24a). If we include buoyancy (*smean* with no $z < 220$ km contributions) we find that the shallow strain pattern underneath regions that moved coherently for plate-motions only is weakened or disrupted (Figure 5.23b). This effect is particularly strong for non steady-state flow (Figure 5.23d) since the smaller-scale density-related currents change over time. If we include non-tectosphere density from *smean* for $z < 220$ km, details in the fast orientations change slightly and more pronounced straining occurs underneath Eastern Africa.

Since evolving plate boundaries mainly affect shallow structure, we can expect that *SKS*-based shear-wave splitting observations will be only slightly modified by the uncertainties in such reconstructions and the overall effect of non steady-state flow. For short-period surface waves with strong sensitivity to shallow structure, such as 50-s Rayleigh waves (sec. A.2.1) the effect may be larger. We therefore analyze whether strain predictions that include evolving plate boundaries lead to a better fit to the surface-wave data than steady-state models.

5.5.4 Frozen strain

Like evolving plates, frozen strain orientations should only affect the shallow regions of the mantle and lithosphere for long advection times. Figure 5.24 compares two models based on plate-motion related flow for $t_c = 120$ Ma and $\zeta_c = 1$ at 50 km depth with and without frozen-in shallow strains below z_c (sec. 5.4.3). Most regions that are covered by continents at the present day show almost no strain accumulation at 50 km in the frozen-strain model since those regions are, by definition, so "cold" that z_c is at the depth limit of 70 km at all times. In the oceans, the ridge pattern of Figures 5.24a and b are similar up to a seafloor age of ~ 30 Ma, after which z_c is deeper than most tracers. The large-scale effects of frozen strain in the oceanic plates are most clearly seen in the Pacific, where most of the Central Pacific pattern in Figure 5.24a is rotated counterclockwise toward the south in Figure 5.24b.

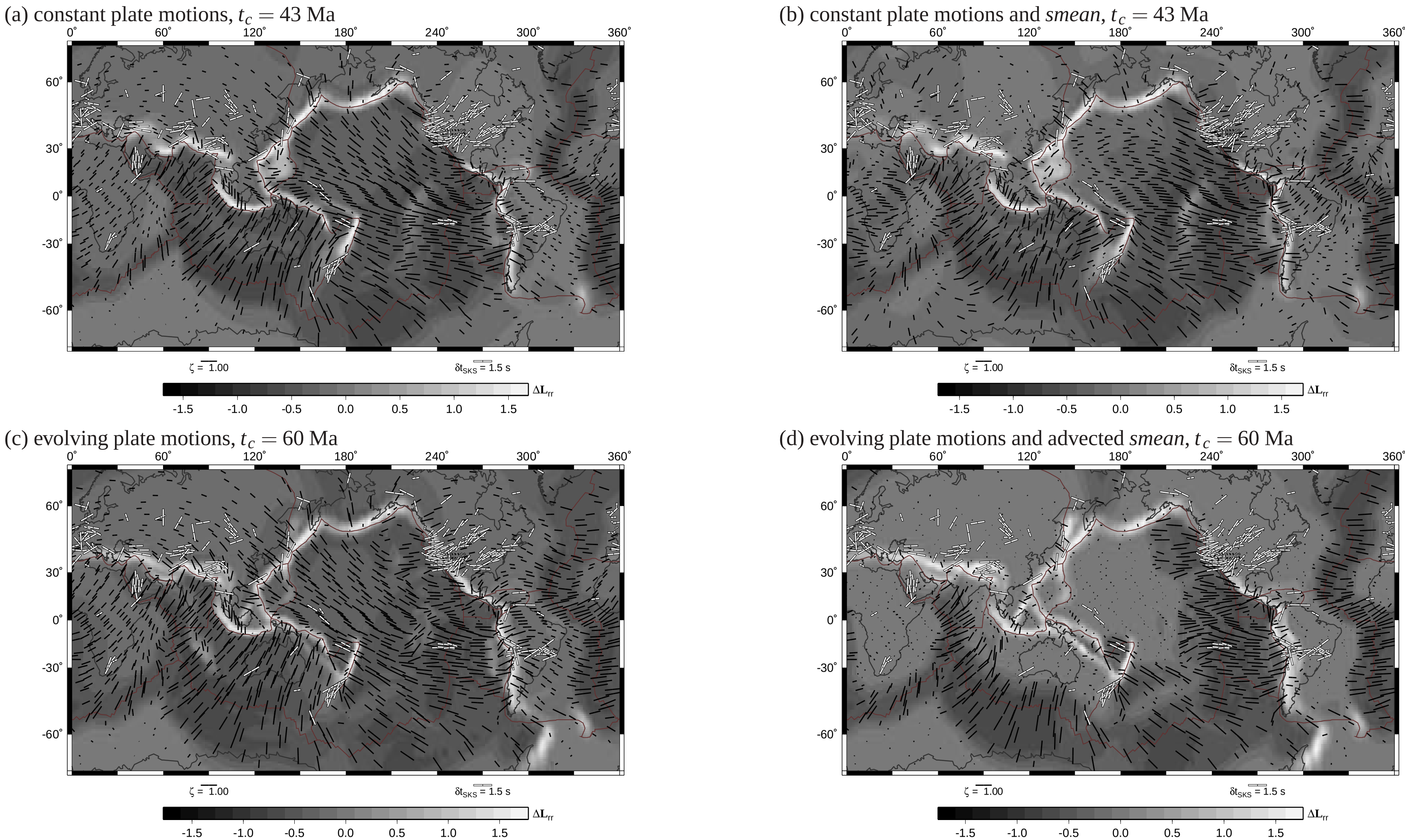

Figure 5.23: Largest FSE axes for $\zeta_c = 1$ at 50 km depth, viscosity η_F. (a) and (b) are from steady-state flow, allowing for tracer backtracking until the cut-off time $t_c = 43$ Ma (*cf.* Figure 5.19), (c) and (d) are for evolving plates and $t_c = 60$ Ma (for $t_c = 120$ Ma, see Figure 5.24a). (b) is from a steady-state model that includes the effect of density anomalies (*smean*, with $R^S_\rho = 0.2$ for $z \geq 220$ km, *cf.* Figure 5.19a); (d) includes evolving plates and backward-advected *smean* densities. For (d), strain accumulation is slow and spatially incoherent underneath continents and old oceanic regions.

(a)

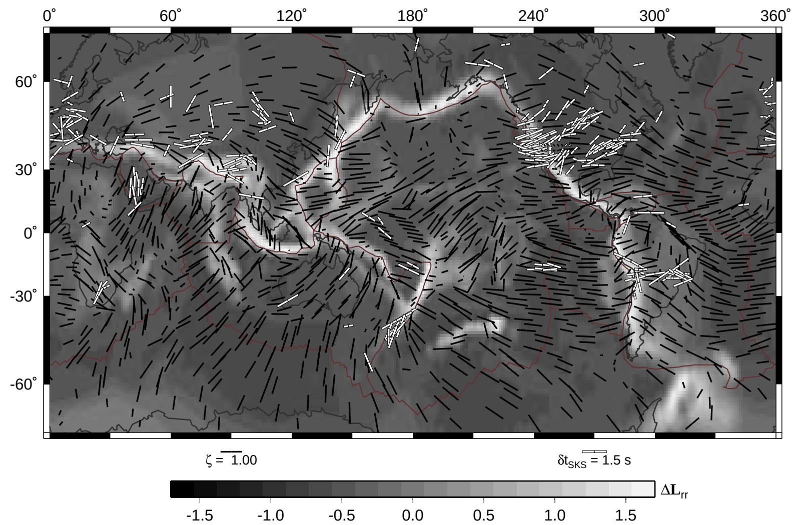

(b)

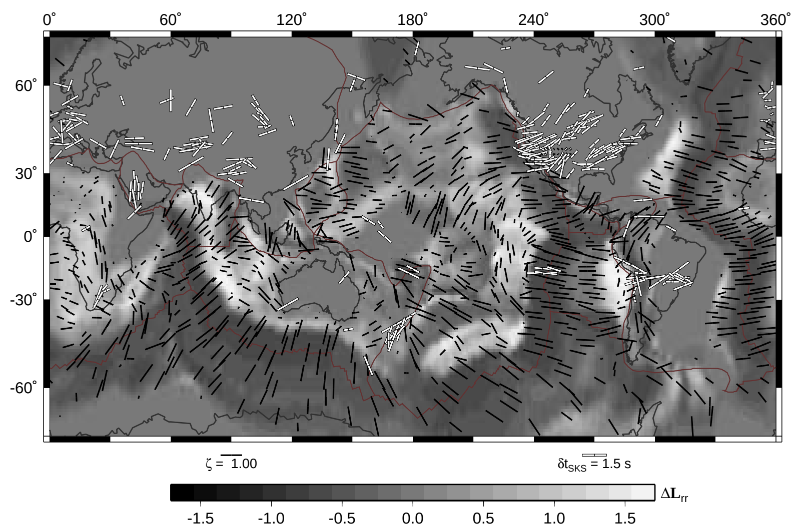

Figure 5.24: Horizontal projection of largest FSE stretching orientation for plate-motion only calculation with η_F for $\zeta_c = 1$ at 50 km depth, cut-off time for the plate motion history is $t_c = 120$ Ma. (a): normal calculation, to be compared with Figure 5.23a and b, (b): shallow strain above z_c is "frozen in" according to sec. 5.4.3.

5.6 Global comparison with surface waves

We now present an initial comparison of our results for global strain with azimuthal anisotropy maps from Rayleigh waves.

5.6.1 Resolution of Rayleigh wave 2ϕ-anisotropy inversions

As discussed in secs. 5.3.1 and A.2.1, inversions of phase velocities for azimuthal anisotropy are complicated by trade-offs between isotropic and anisotropic parameters (*e.g.* Laske and Masters, 1998). Furthermore, the uneven spatial and azimuthal coverage of raypaths might map itself into apparent anisotropic structure (*e.g.* Tanimoto and Anderson, 1985). To address these issues, we show a recovery test for Rayleigh waves at $T = 50$ s period by G. Ekström (pers. comm.) in Figure 5.25. The same inversion procedure that led to the phase-velocity maps

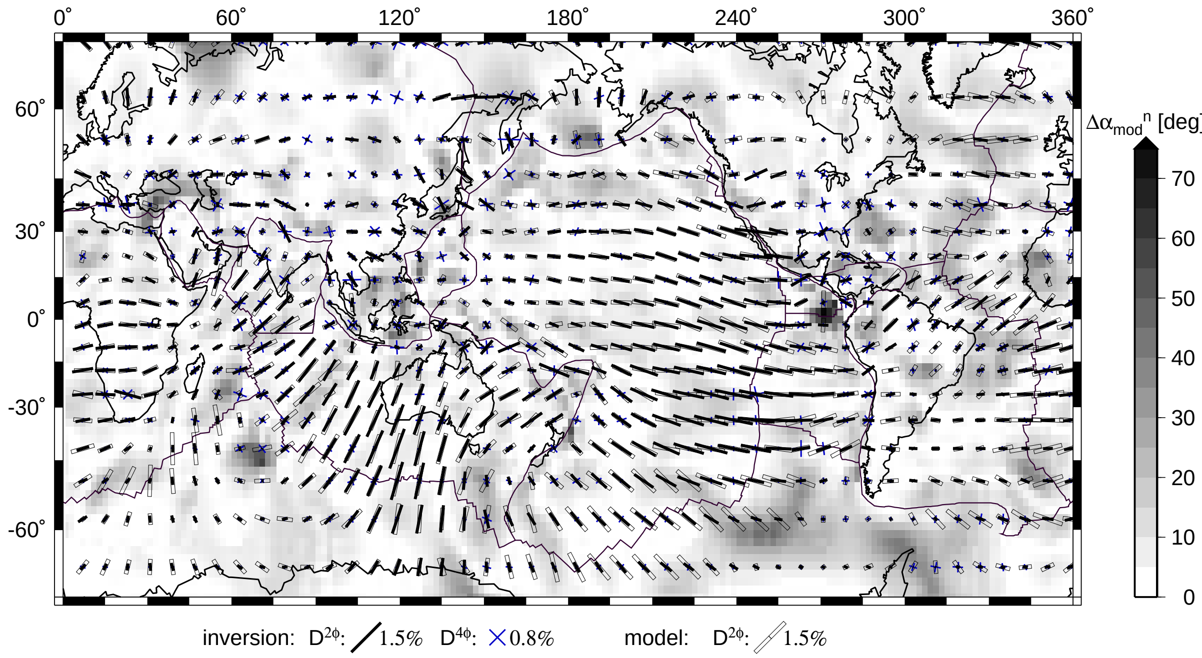

Figure 5.25: Input (open bars) and recovered (black sticks) azimuthal anisotropy for Rayleigh waves with period 50 s using the dataset and inversion procedure of Ekström (2001). The inverted structure has some artificial 4ϕ-power (thin crosses), zero in the input model which is based on $\zeta_c = 0.5$, plate motions, and *smean* (*cf.* Figure 5.19a). All anisotropy shown on the same, linear scale; maximum amplitudes are indicated below the map. Background shading is $\widehat{\Delta\alpha}$, the orientational deviation $\Delta\alpha$ scaled by the local $D^{2\phi}$ amplitude of the input model, normalized such that the maximum of $\widehat{\Delta\alpha}$ and $\Delta\alpha$ are identical.

shown in Figure 5.3 and below ($D^{2\phi}$ and $D^{4\phi}$ damped 10 times stronger than D^0) was used to test our ability to recover a synthetic input model using the available data coverage. To make structure in the input model as realistic as possible, 2ϕ-anisotropy was inferred from a steady-state circulation model with η_F which we consider to be representative of our results for global strain. The flow model includes the buoyancy effect of *smean* and strains were calculated for $\zeta_c = 0.5$ (*cf.* Figure 5.19a). As for the global maps in sec. 5.5, the horizontal projections of the largest FSE axes were scaled with ζ to account roughly for the strength of inferred seismic anisotropy; we additionally weighted each layer according to the 50-s Rayleigh wave sensitivity-kernel of Figure A.7a. Maximum predicted strains were scaled to a 1.5% 2ϕ-anisotropy amplitude (resulting in 0.6% RMS variation) and the isotropic and $D^{4\phi}$ variations were set to zero. Then, random noise without spatial coherence was added to mimic the observational uncertainties and to test the robustness of the method. The resulting variance reduction of the inversion was only 14% for D^0, implying that little of the spurious signal was fit.

Figure 5.25 shows that the orientations of azimuthal anisotropy of the input model are generally well recovered. Exceptions are found in the Middle East, in the Aleutians, the Cocos-Nazca plate area, and along the northern mid-Atlantic ridge system. To quantify these azimuthal deviations, we calculate the local misfit $\Delta\alpha$ ($0^\circ \leq \Delta\alpha \leq 90^\circ$), shown in a histogram in Figure 5.26a. We also compute $\widehat{\Delta\alpha}$ by multiplying $\Delta\alpha$ with the input model amplitudes to give less weight to small-signal regions; $\widehat{\Delta\alpha}$ is shown as background shading in Figure 5.25 and normalized such that weighted and original maximum deviations are identical. We will experiment with the function

$$1 - \widehat{\Delta\alpha}/\widehat{\Delta\alpha}_{\max}, \tag{5.11}$$

where $\widehat{\Delta\alpha}_{\max}$ is the maximum scaled deviation, as a measure of the reliability of surface-wave inversions in recovering 2ϕ orientations in our comparison of model predictions and real phase-velocity inversions in the next section.

The amplitude recovery of the test inversion is not as good as the azimuthal fit; it is poor for the south-west Indian Ocean, the northern Atlantic, the Scotia plate region, and the north-west Pacific. Globally, the average of the $\log_{10}$ of the recovered 2ϕ signal over the input 2ϕ amplitude is -0.062, corresponding to a mean amplitude

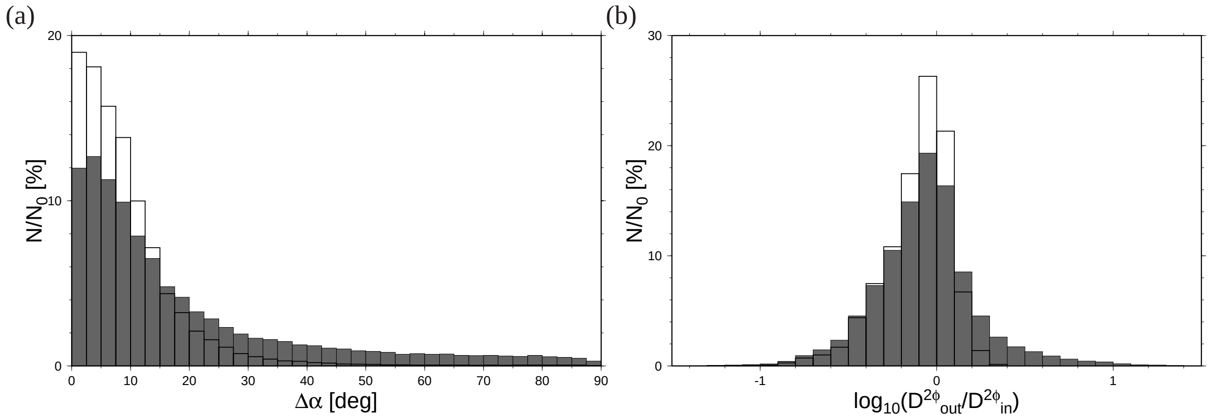

Figure 5.26: Orientational misfit histogram $\Delta\alpha$ (a, gray bars) for equal-area spatial sampling of the recovery test of Figure 5.25, N/N_0 denotes relative frequency. Open bars show misfit observations restricted to areas with input model 2ϕ-amplitudes $\geq 25\%$ of the maximum input. (b) Histogram of amplitude recovery as expressed by the decadic logarithm of inversion $D^{2\phi}$ over input $D^{2\phi}$-amplitudes (gray bars, open bars restricted to strong-amplitude input as in (a)).

recovery of 86.7% (Figure 5.26b). Regions in which anisotropy strength is overpredicted are found at some trenches (*e.g.* Central Chile), where the inversion gives a trench-perpendicular signal while the input model has small amplitude with FSE primarily radial. The area-weighted mean orientational misfit, $\langle\Delta\alpha\rangle$, is 18.8°, which is reduced to 13.4° if we weight the misfit by the input-model 2ϕ amplitudes. Restricting ourselves further to oceanic lithosphere (as given by 3SMAC; Nataf and Ricard, 1996), $\langle\Delta\alpha\rangle|_{\mathrm{oc.}} = 11.8°$. If we weight the global misfit by input and output model amplitudes (assuming small output amplitudes indicate poor resolution), $\langle\Delta\alpha\rangle = 9.9°$. These values can be used to guide us in judging misfits between observations and model predictions.

To evaluate the (possibly different) trade-offs that occur in the presence of coherent isotropic structure, we have analyzed a second resolution test by G. Ekström in which the random noise in the input D^0 signal was replaced by slowness anomalies derived from the crustal model CRUST5.1 (Mooney *et al.*, 1998). The recovered anisotropic signal is similar to that of the first experiment, with mean azimuthal misfit $\langle\Delta\alpha\rangle = 13.7°$ (weighted by input $D^{2\phi}$) and mean $\log_{10}$-amplitude recovery of 87.1%. If the 4ϕ-terms are suppressed by damping them much more strongly than $D^{2\phi}$, the result is, again, similar to that shown in Figure 5.25 but the azimuthal misfit and amplitude recovery are slightly improved to $\langle\Delta\alpha\rangle = 12.5°$ (weighted by input $D^{2\phi}$) and 90.3%, respectively. Assuming that the $T = 50$ s results are representative of deeper-sensing waves as well, the resolution tests are very encouraging since they imply that surface-wave based inversions for azimuthal anisotropy are robust when performed carefully. The number of parameters of an inversion for $D^{2\phi}$ is larger than that of an isotropic inversion; the corresponding increase in degrees of freedom cannot be justified based on the improvement in variance reduction alone (Laske and Masters, 1998; Ekström, 2001). However, the pattern that such an anisotropic inversion predicts is likely to be a real feature of the Earth and not an artifact. If our synthetic input model is a valid first-order representation of real large-scale anisotropic structure in nature, the resolution analysis can guide us in the interpretation of model misfit when compared to the inversion results.

5.6.2 Global azimuthal-anisotropy model fit

Figures 5.27 and A.8 compare maps for Rayleigh wave 2ϕ anisotropy from Ekström's (2001) inversion with predictions from our preferred strain model, obtained by depth averaging (using the appropriate kernels from sec. A.2.1) of the ζ-scaled horizontal projection of the largest axes of the FSE. The calculation uses $\zeta_c = 0.5$-strain and includes the effects of plate motions, *smean* buoyancy (including non-tectosphere structure for $z < 220$ km), and changes in plate-configurations for $t_c = 60$ Ma. We find that much of the measured signal in the oceans can be explained by LPO orientations and finite strain as predicted from our global circulation model. We show a histogram of the angular misfit, $\Delta\alpha$, for $T = 50$ s in Figure 5.28; the largest misfits are typically found in regions of small $D^{2\phi}$-amplitudes or in the continents, where anisotropy may be related to past deformation episodes.

The laterally averaged misfits are compared for several different models in Figure 5.29, Figures A.9, and A.10 for $T = 50$ s, $T = 100$ s, and $T = 150$ s, respectively. We tried weighting the misfit in a number of ways but think

(a) $T = 50$ s

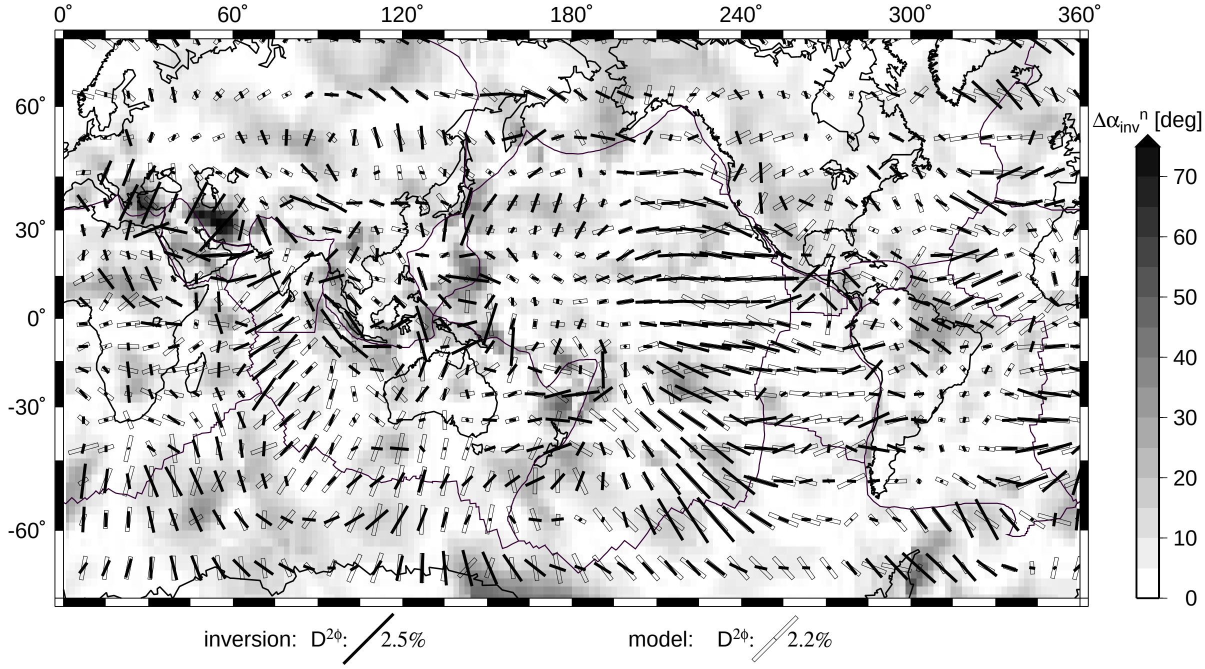

(b) $T = 150$ s

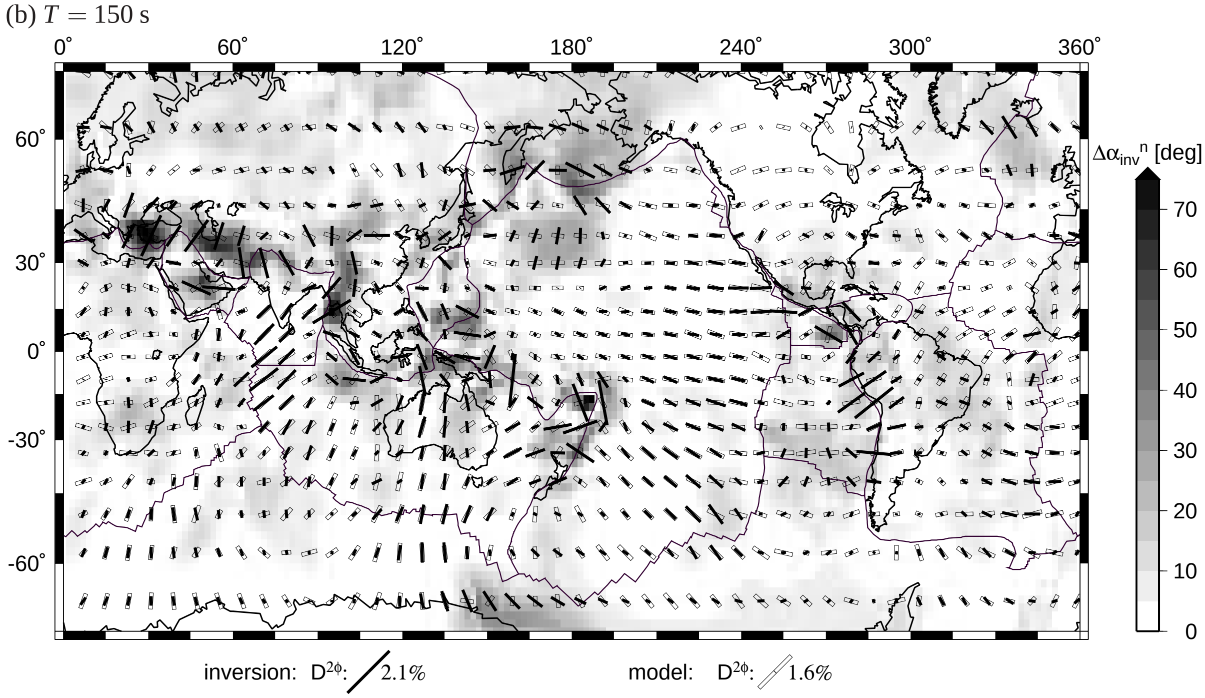

Figure 5.27: Comparison of Rayleigh wave 2ϕ-azimuthal anisotropy from Ekström (2001) for $T = 50$ s (a) and $T = 150$ s (b), shown as black sticks (maximum $D^{2\phi}$ values shown to scale below map) and model anisotropy for $\zeta_c = 0.5$, evolving plates ($t_c = 60$ Ma), η_F, and *smean* advected density (non-tectosphere buoyancy only for $z < 220$ km), shown as open bars. We omit $D^{4\phi}$ from the inversions and scale the predicted anisotropy such that the RMS $D^{2\phi}$ are identical to those from the inversions. Background shading indicates azimuthal misfit scaled by the inverted $D^{2\phi}$ amplitude such that maximum $\Delta\alpha$ remains constant. (For $T = 100$ s, see Figure A.8.)

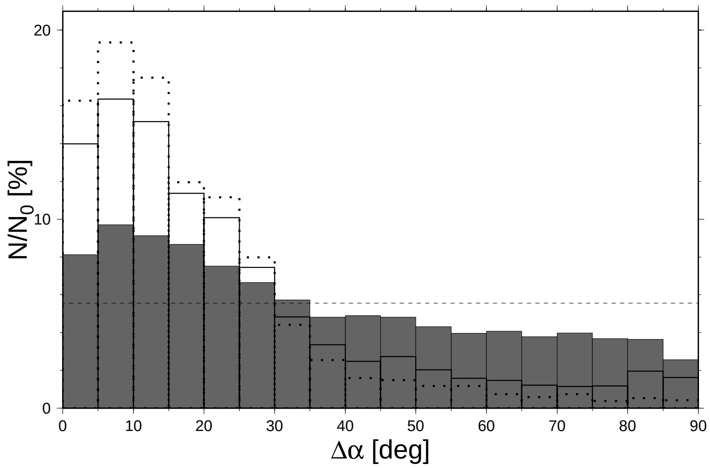

Figure 5.28: Histogram of orientational misfit, $\Delta\alpha$, between $T = 50$ s Rayleigh wave 2ϕ anisotropy and model prediction for $\zeta_c = 0.5$ strain, η_F, evolving plates ($t_c = 60$ Ma), and *smean* advected density as in Figure 5.27a. Solid bars: all data; open bars: data restricted to regions where $D^{2\phi}$ of the inversion is ≥ 0.25 times its maximum; and open bars with dotted lines: further restricted to oceanic lithosphere. Dashed horizontal line indicates the expected random distribution of $\Delta\alpha$.

that, in general, accounting for both the inversion's and the model's $D^{2\phi}$-amplitudes is most appropriate in order to avoid having poorly sampled regions bias $\langle\Delta\alpha\rangle$. For consistency, we have also weighted the surface-velocity derived misfits by the model (*i.e.* plate-velocity) amplitudes. However, such velocity-weighted misfits are biased toward the oceanic plates, which move faster than continental ones, relative to $\zeta_c = 0.5$-strain models, which show a more uniform anisotropy-amplitude globally (*e.g.* Figure 5.19).

We find that most circulation-based strain models outperform the hypotheses of alignment with NNR or APM plate motions. This distinction in model quality supports our modeling approach; it is not as clear for shear-wave splitting, as discussed in sec. 5.5.2 and below. The average fit to Ekström's (2001) anisotropy maps is better for shorter ($T = 50$ s in Figure 5.29) than for longer periods ($T = 150$ s in Figure A.10). This could be due to differences in resolution of the surface waves, or the dominance of the plate-related strains at shallow depths, presumably the best-constrained large-scale features. We also observe a wider range in $\langle\Delta\alpha\rangle$ for different types of models at $T = 50$ s than at $T = 150$ s. This is expected, given that strains accumulate more rapidly at depth, so that it is, for instance, less important whether flow is treated as steady-state or with evolving plate boundaries. For η_F, models that include buoyancy-driven flow lead to $\langle\Delta\alpha\rangle$ improvements of $\sim 6^\circ$ compared to those with plate motions only. Comparing different density models, *smean* typically leads to better results than higher resolution tomography (*ngrand*) or models that are based on slabs only (*stb00d* or *lrr98d*). Including shallow density variations underneath younger plate regions (non-tectosphere models, "nt"), slightly improves the model fit.

Globally weighted results typically show the same dependence on model type as those that include only the oceanic lithosphere, $\langle\Delta\alpha\rangle|_{\text{oc.}}$; the latter are, however, generally smaller than the global estimates by $\sim 4^\circ$. The best models yield $\langle\Delta\alpha\rangle|_{\text{oc.}} \approx 24^\circ$ for $T = 50$ s and $\langle\Delta\alpha\rangle|_{\text{oc.}} \approx 28^\circ$ for $T = 100$ s and $T = 150$ s, to be compared with 45° for random alignment and $\sim 35^\circ$ for alignment with plate velocities. Taking the surface resolution function (5.11) into account improves the misfit, but not significantly. Regional variations in misfit might therefore be due to poor surface-wave resolution but, globally, $\Delta\alpha$ is independent of the surface-wave resolution pattern.

There are a number of second-order observations that have guided us in the choice of the preferred model shown in Figure 5.27. τ-limited (time limited) strain-accumulation models lead to results that are similar to those of ζ-models (strain limited) without weighting. Results from τ calculations with $D^{2\phi}$ model-amplitude weighted $\langle\Delta\alpha\rangle$ are always, as expected, better than ζ-models because of the additional bias that is introduced toward the oceans (where all models are more similar to the inversions). We therefore limit consideration to ζ_c-models, for which we find that density-included flow calculations lead to better results for η_F than for η_G ($\sim 2^\circ$ difference in average $\langle\Delta\alpha\rangle$). For shallow ($T = 50$ s) structure where strain accumulation is representative of a longer timespan, $\langle\Delta\alpha\rangle$ values are slightly improved when we include "freezing" of strains for $z < z_c$ (sec. 5.4.3) but this is, again, partly due to the resulting bias toward the oceans. We cannot find any significant global improvement compared to continuous strain-accumulation models. Comparing models with steady-state velocities or evolving plates in Figure 5.29 we do, however, see a small ($\sim 2^\circ$) decrease in global misfit when the last 60 Ma of plate reconfiguration and density advection are taken into account.

In summary, we find that the strain produced by global mantle circulation is a valid explanation for the az-

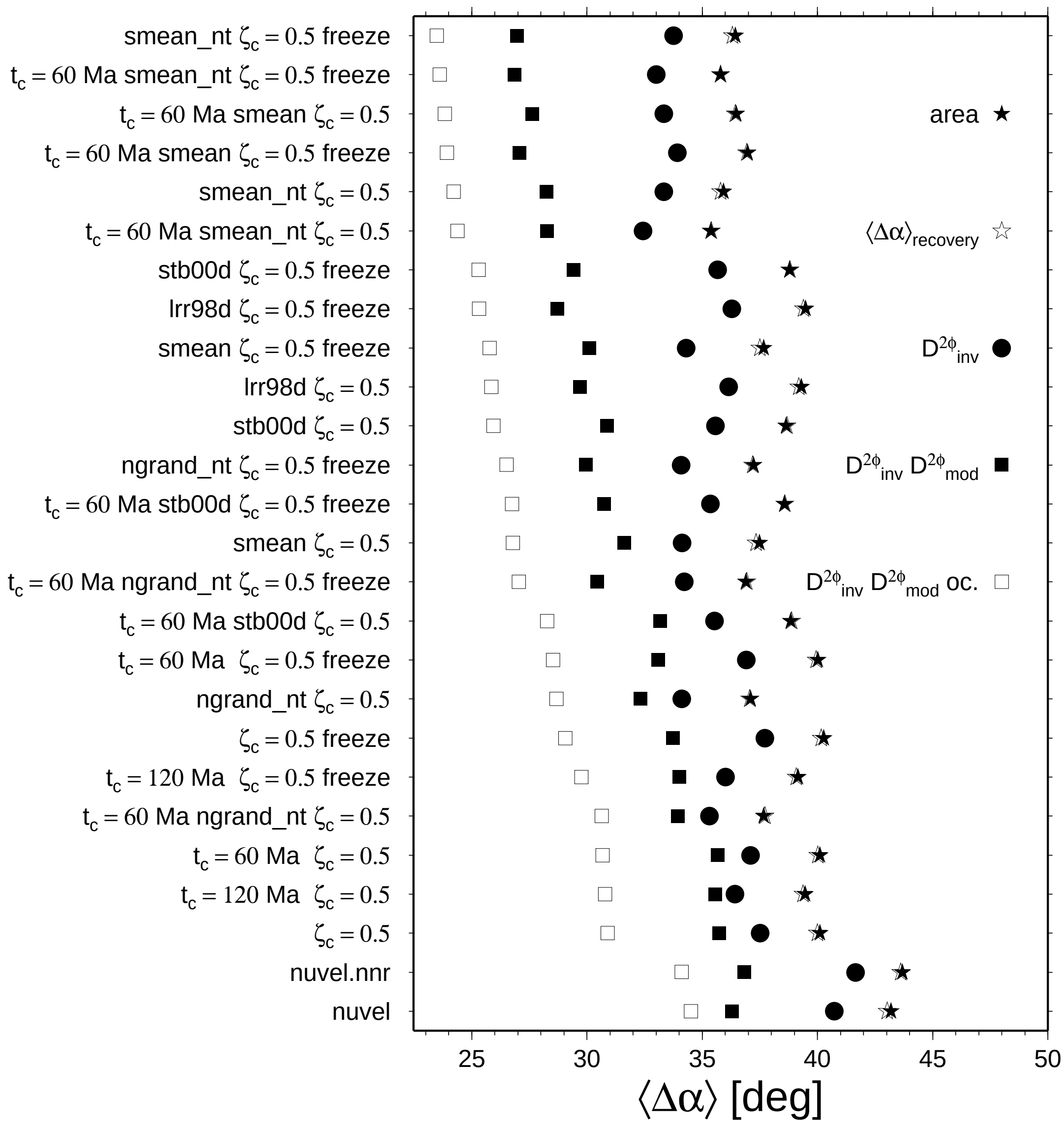

Figure 5.29: Mean orientational misfit between 2φ anisotropy of $T = 50$ s Rayleigh waves (*cf.* Figures 5.27a and 5.28), a selection of circulation-derived $\zeta_c = 0.5$-models, and surface plate-velocity orientations. y-axis indicates different models, viscosity profile is always η_F. Types of density models: *stb00d*, *lrr98d*, *ngrand*, and *smean* as in chapter 3; if "nt" is appended, non-tectosphere (from 3SMAC Nataf and Ricard, 1996) shallow structure is used, else $R^S_p = 0$ for $z < 220$ km. If no time interval is specified, velocities are steady-state with a cut-off in backward advection time, t_c, of 43 Ma; $t_c = 60$ Ma or $t_c = 120$ Ma implies backward advection using evolving plate-boundaries and possibly density sources until t_c. "nuvel" and "nuvel.nnr" refer to the azimuthal misfit as calculated from surface plate-velocity orientations for HS2 (APM) or NNR reference frames, respectively. The misfits, $\langle\Delta\alpha\rangle$, are obtained by area-weighted lateral averaging (filled stars). We additionally weight models by the surface-wave recovery function (5.11) (open stars), the inversion's $D^{2\phi}$-amplitude (filled circles), the inversion's and the model's $D^{2\phi}$-amplitudes (filled boxes), and the latter quantity restricted to oceanic plates (open boxes). (For APM and NNR velocities, weighting by the model amplitudes implies a strong bias toward the oceanic plates relative to $\zeta_c = 0.5$-models.) If we randomize the 2φ orientations of our models, we find a standard deviation of $\approx 0.4°$ indicating that $\langle\Delta\alpha\rangle \lesssim 43°$ is significantly different from the random mean of 45° at the 5σ-level.

imuthal anisotropy mapped by surface waves, and that such circulation-produced strain explains the pattern of azimuthal anisotropy better than does the pattern of absolute plate motions. Further exploration of regional and global model performance can guide us in our understanding of anisotropy in the upper mantle. Short-period surface-waves with good shallow sensitivity might be able to provide us with constraints on the strain history for times longer than a few tens of Myr.

5.7 Regional comparison with shear-wave splitting

To complement our findings on global variations in anisotropy, we now discuss several plate-boundary settings where we compare shear-wave splitting data with the predicted strain fields. Since we found that plate reorganization is likely to affect only the shallowest strains, and *SKS* data are assumed to average over the upper ~ 400 km, all flow models are based on steady-state velocities and a backward advection cut-off time of $t_c = 43$ Ma.

5.7.1 East Pacific Rise

Wolfe and Solomon (1998) obtained *SKS* splitting data from the MELT experiment across the East Pacific Rise (EPR). The fast wave-propagation axes they find are oriented roughly perpendicular to the ridge, both directly off and on the ridge axis (Figure 5.30). This finding renders the distribution of melt pockets an unlikely explanation for anisotropy since tensile cracks, and hence fast propagation orientations, should align parallel to the ridge axis (Kendall, 1994). Geodynamic models that include convective flow and texture development (*e.g.* Blackman *et al.*, 1996) also fail to explain completely the data of Wolfe and Solomon (1998); flow close to the ridge axis will be mostly radial so that no strong azimuthal anisotropy is predicted by the models. Our circulation models (sec. 5.5) also predict that ridge-perpendicular strain will occur mostly in off-axis regions. Close to the ridge, perpendicular stretching is found only for small finite strains and shallow depths ($\lesssim 150$ km). The most appropriate models are thus those for $\zeta_c = 0.2$ and plate-motion only or *smean* density for $z > 220$ km (Figure 5.30). These two cases correspond to completely passive and semi-active spreading, respectively. Since our tomography-derived density models usually exclude the upper 220 km, we likely underestimate the actual upwelling underneath the ridge. If we include the non-tectosphere density from *smean* for shallow regions, results are, however, very similar.

The fit to the off-axis *SKS* splits is good and the plate motions imprint an asymmetry on the spreading pattern that is also seen in the data (Figure 5.30a and c). At shallower depths, the passive-spreading model (Figure 5.30a) shows roughly ridge-parallel orientations of largest stretching within the region of large radial extension ($\Delta F_{rr} > 0$). However, the buoyancy anomaly imaged by *smean* reduces the strength of this feature such that on-axis regions show ridge-perpendicular orientations for $z \lesssim 150$ km. The depth-averaged fit of Figure 5.30d is as a result superior to that of Figure 5.30c; it is less affected by the ridge-parallel alignment at larger depths. We show the orientational misfit for depth-averaged FSE orientations in Figure 5.31. There is no strong preference for any model type. However, smaller ζ_c strains generally lead to better predictions and *smean*-included strain models outperform those for plate-motions only, motivating our choice of models for Figure 5.30. Best $\langle \Delta\alpha \rangle$ values are $\sim 5^\circ$, similar to the typical uncertainties in *SKS* measurements. As for the global fit to *SKS* data (Figure 5.22), strain-derived models are not superior to alignment with surface velocities ("v.nr" in Figure 5.31). While the small number of data points make a quantitative interpretation of misfits questionable, we prefer the small ζ models as they lead to ridge-perpendicular fast axes close to the ridge; it is plausible that the ridge environment leads to short strain memories.

5.7.2 Subduction zones

The cause of anisotropy in back-arc settings, and the varying orientations and strengths of splitting observations in these regions, is a matter of ongoing debate (*e.g.* Fischer *et al.*, 1998; Hall *et al.*, 2000; Smith *et al.*, 2001). Previous modeling work has emphasized the consequences of slab rollback (*e.g.* Buttles and Olson, 1998; Hall *et al.*, 2000) and trench-parallel flow (*e.g.* Russo and Silver, 1994). There is, however, no study that includes the effect of 3-D circulation with realistic plate geometries. We intend to fill that gap and explore how our predictions of finite strain correlate with regional anisotropy measurements. We focus on comparing observed and predicted orientations of splitting and strain directly and do not attempt to correlate the strength of the anisotropy as measured by the delay times with the magnitude of strain. For this, a more sophisticated treatment like that of Hall *et al.* (2000)

(a) plate-motions only, $z = 150$ km

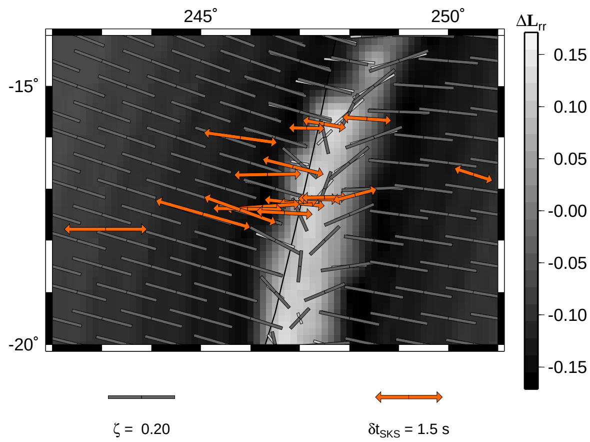

(b) plate-motions and *smean*, $z = 150$ km

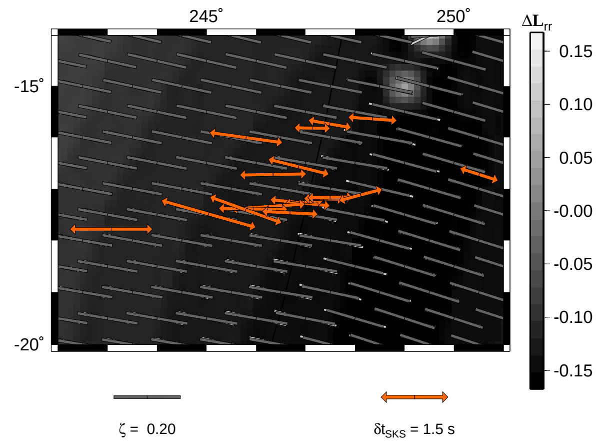

(c) plate-motions only, depth average

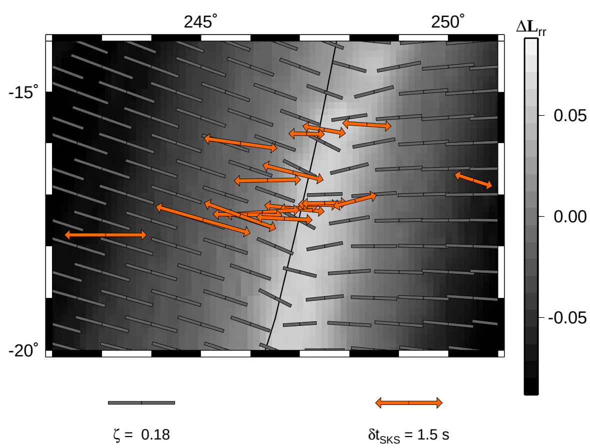

(d) plate-motions and *smean*, depth average

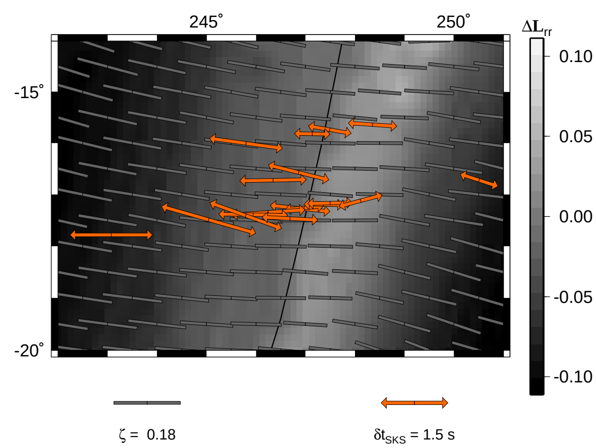

Figure 5.30: Comparison of Wolfe and Solomon's (1998) *SKS* data and horizontal projections of largest FSE axes for $\zeta_c = 0.2$ calculations for the EPR, (a) and (c) are for plate-motion related flow only (η_F). Fast axes are shown for a layer at 150 km depth (a) and the depth-averaged strain (c). (b) and (d) models include density scaled from *smean* for $z > 220$ km, at $z = 150$ km (c) and depth-averaged (d).

would be more appropriate. These authors inferred elastic moduli from strain, traced rays, calculated synthetic seismograms, and then measured the synthetic splitting times. We show that the observed strain fields are very complex and vary on small scales both laterally and with depth. A ray-tracing approach, beyond the scope of this work, might therefore eventually be needed to explore the correlation of our results with *SKS* data quantitatively.

Western Pacific

Figures 5.32 through 5.34 show depth-averaged finite strains for $\zeta_c = 0.5$ focusing on three areas in the Western Pacific around subduction zones with relatively good data coverage: the Lau basin with the Tonga slab, around Japan with the Kurile, Japan, and Izu-Bonin Wadati-Benioff zones, and the area around the Philippine sea plate with the Mariana and Ryukyus trenches. Figure 5.32 shows our depth-averaged strain predictions for Tonga, the subject of a study by Smith *et al.* (2001). We show both *SKS* data and local *S* wave derived splitting which

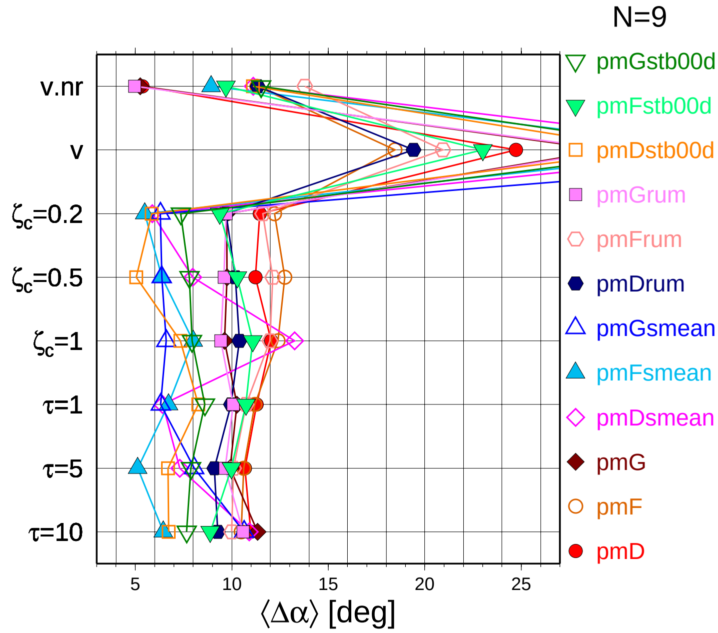

Figure 5.31: Average orientational misfit between the EPR splitting data of Wolfe and Solomon (1998), averaged on a $1^{\circ} \times 1^{\circ}$ grid, and our depth-averaged model predictions for horizontal projections of the largest FSE eigendirection. Abbreviations and *y*-axis labels as in Figure 5.22.

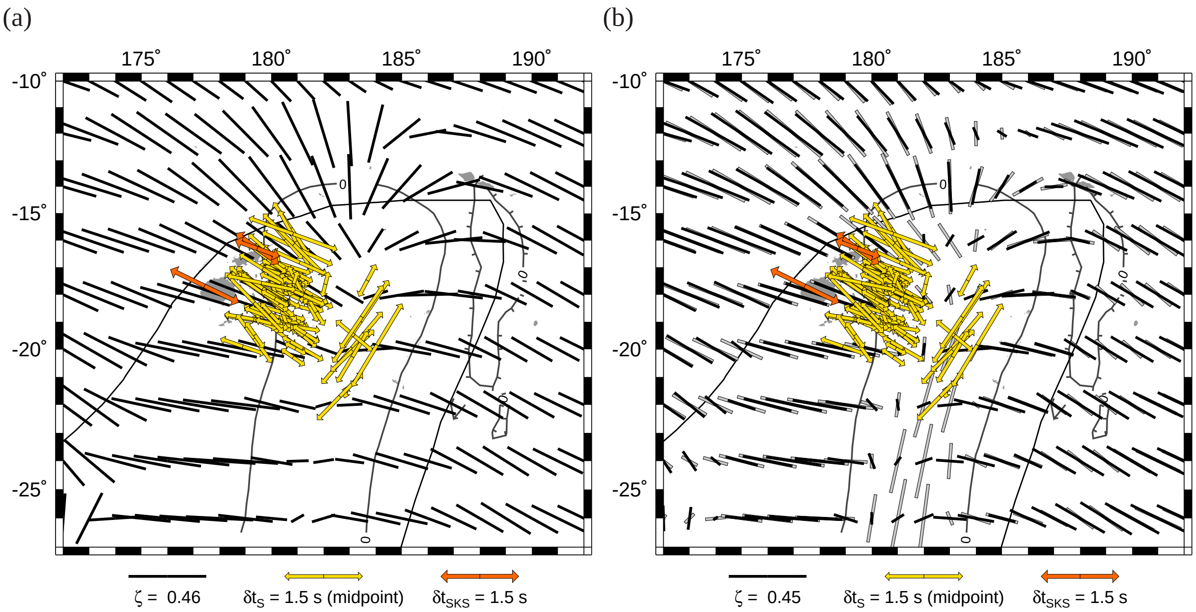

Figure 5.32: Lau basin and Tonga trench (see Figure 5.4 for overview): $\zeta_c = 0.5$ strain model for η_F, plate motions and *rum* slab densities using ζ-weighted horizontal projections of the largest FSE axes (a) and horizontal projection of FSE axes (black sticks) plus largest stretching of the horizontal component of the FSE (light gray sticks) based on linearly depth-averaged **L** (b). Splitting observations are from Fischer *et al.* (1998) and Smith *et al.* (2001), note different symbols for *SKS* and local *S* observations. The latter are shown at the raypath midpoints. Thin and thick lines trace NUVEL1 plate boundaries and $\Delta F_{rr} = 0$ contours, respectively. Tickmarks along closed contours point in the downward direction.

is, unlike *SKS* data, not affected by anisotropy below the earthquake source depth. The comparison of depth-averaged strains with splitting in Figure 5.32a shows that the two western *SKS* orientations are consistent with our flow-derived strain (*cf.* Figure 5.16), both for plate-motions only (not shown) and when we include the slab pull according to *rum*. The eastern, *S*-based observations (whose locations are somewhat arbitrary, here plotted at the path midpoint) are not well fit since we predict mostly trench-perpendicular fast orientations. If we examine depth-averaged strain and obtain horizontal FSE major-axis projections as well as largest stretching in the horizontal FSE planes instead (Figure 5.32b), we see that the largest axes of the FSE are oriented mostly vertical in the center of

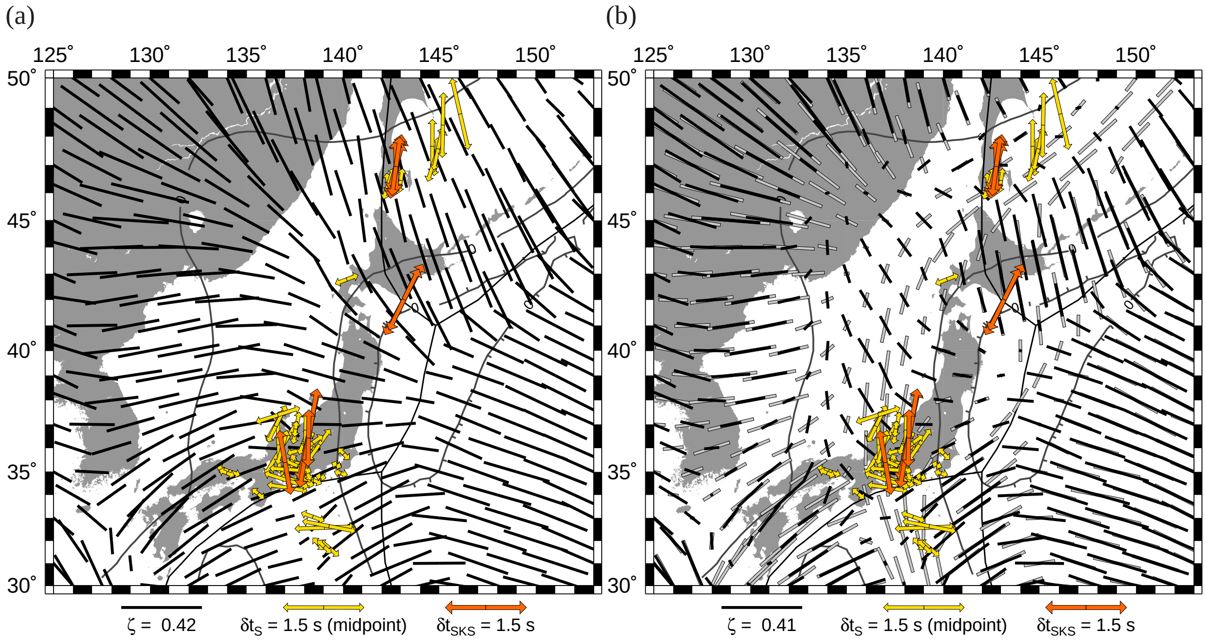

Figure 5.33: Japan trenches: $\zeta_c = 0.5$ finite strain model for plate motion and *rum*. Depth-averaged horizontal projection of largest FSE axes (a) and horizontal projections of largest FSE axes (black sticks) and horizontally largest stretching (gray sticks) based on depth-averaged **L** (b). For explanation, see Figure 5.32.

the Lau basin because of the slab related downwelling. The component of trench-parallel flow that is observed at sub-lithospheric depths leads to an additional shearing which aligns the horizontally largest stretching parallel to the trench, as observed for the *S* splitting data in Figure 5.32. We therefore have some indication that the data of Smith *et al.* (2001) can be fit using a global flow model. However, we need to invoke a second order effect, that of the horizontal plane straining.

Turning to the Japan trenches (Figures 5.33a and b), we observe that both splitting data and strain predictions are more complex than for the Lau basin (Fischer *et al.*, 1998). The source–receiver paths are also longer than for Tonga; the decision of where to plot *S*-based splits is thus more important to the interpretation. The region has two triple junctions producing flow and strains that vary rapidly with depth, with or without density-driven flow. Model fit to the *SKS* orientations from Honshu, Hokkaido, and Sakhalin is poor. As for the Lau basin, the slab-related flow leads to trench-parallel orientations in the horizontal stretching component (Figure 5.33b) while the projections of largest FSE axes into the horizontal plane are mostly trench perpendicular (Figure 5.33a) and fan out toward the West following the geometry of the Wadati-Benioff zone in Japan.

The Philippine sea plate (Figures 5.34a and b) is sampled by only one *SKS* split and one null measurement at Guam (Fouch and Fischer, 1998). There are, however, local event observations, most importantly the *S* splits from Guam, which all have consistent azimuths of $\sim 315^\circ$ (Fouch and Fischer, 1998); delay times are small, as seen in the data at $\sim 12^\circ$N/145°W. For the Philippine plate, both the horizontal projections of FSE axes (Figure 5.34a) and the horizontal components of the FSE (light gray sticks in Figure 5.34b) show some degree of trench-parallel orientation. The finding of Fouch and Fischer (1998) that Guam had no vertical-incidence *SKS* splitting but did have NW-trending local *S*-phase splits might be related to the complicated strain field at this plate boundary.

We predict considerable complexity in strain orientations in convergent zones along the Western Pacific. Regional variations in fast orientations are much more rapid than would be expected given the surface velocities with which *SKS* data are commonly compared. However, we cannot fit all of the data in a simple, consistent fashion. Given the rapid radial and lateral variations in largest stretching orientations, we do not attempt a quantitative comparison of our predictions.

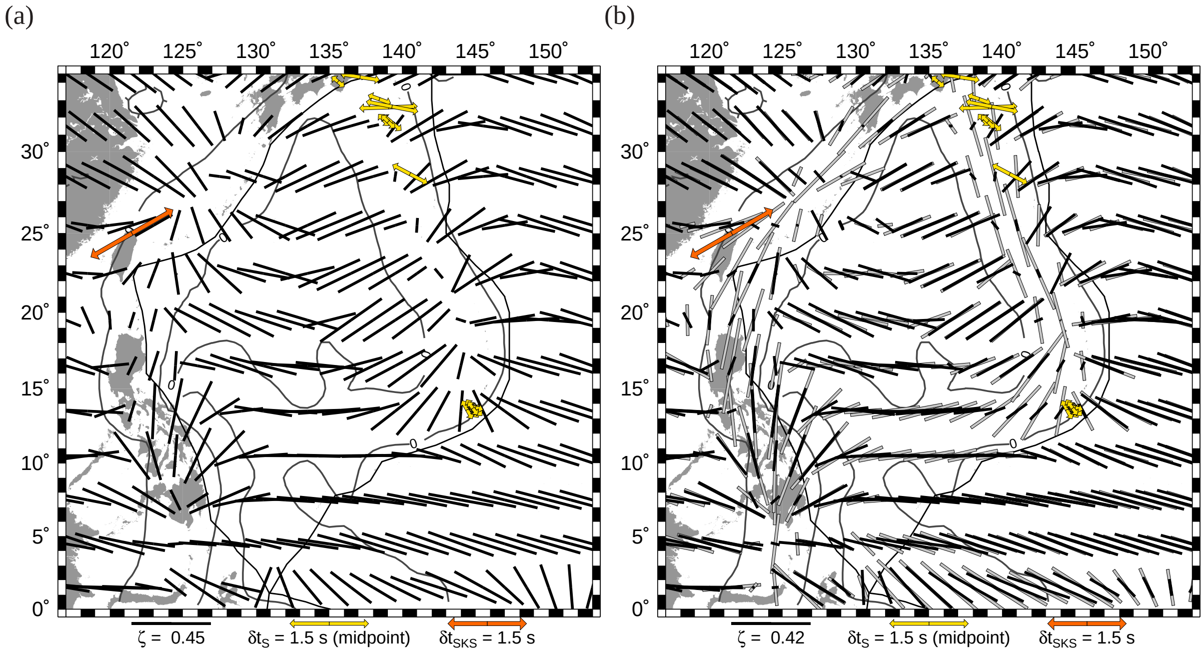

Figure 5.34: Philippine sea plate: $\zeta_c = 0.5$ finite strain model for plate motion and *rum*. Depth-averaged horizontal FSE stretching directions (a) horizontal projections of largest FSE axes (black sticks) and horizontally largest stretching (gray sticks) based on depth-averaged **L** (b). For explanation, see Figure 5.32.

Eastern Pacific

The only convergent margin on the eastern Pacific rim that is well sampled by *SKS* observations is the Central Andes trench. Backprojected measurements (where the station anisotropy, *e.g.* in North America, is subtracted from the measured anisotropy to derive the source structure in the South American slab) were used by Russo and Silver (1994) to argue for trench-parallel flow. Their data show remarkable complexity in orientations and included only three direct *SKS* measurements. More recently, Polet *et al.* (2000) presented new *SKS* measurements from regional seismic experiments. These authors found two contrasting trends of fast orientations: one parallel to the trench and a second with trench-perpendicular orientations at $\sim$20 ° S.

Figure 5.35 shows predictions of $\zeta_c = 0.5$ finite strain and all available splitting data (*SKS* and backprojected *S*). For shallow depths (Figure 5.35a), the trench-parallel alignment of the horizontal strain components is strong and some of the largest FSE axes also align parallel to the trench when projected into the horizontal plane. The fast propagation plane that shear-wave splitting measurements sample is, however, more readily interpreted as corresponding to the radially averaged horizontal projections of the FSE orientations. These are mostly trench perpendicular (Figure 5.35b), and *SKS* splits are not well fit in general.

We conclude that we cannot distinguish between different possible explanations for the observed splitting. Most *SKS* data are interpreted by assuming that the anisotropy is constant throughout the upper mantle and has a hexagonal symmetry axis in the horizontal plane. We confirm Hall *et al.*'s (2000) result that this assumption is probably too simplistic for plate boundaries where 3-D flow leads to FSE orientations that vary considerably on small length scales. While there appears to exist a straightforward association between depth-averaged strain and the *SKS* data at ridges, trenches are more complex, and a ray-tracing approach should be used in the future to evaluate how the 3-D strain field is "seen" by the shear-wave splitting measurement procedure. If this undertaking leads to poor predictions of the data, then other effects such as that of lateral viscosity variations, which we have neglected, might have to be included.

5.7.3 The Western US: evidence for deep mantle return flow?

Sub-lithospheric flow is also important for the seismic anisotropy in our last regional example, the Western US. The plate boundary zone between the San Andreas fault and the Basin and Range is heavily instrumented, both

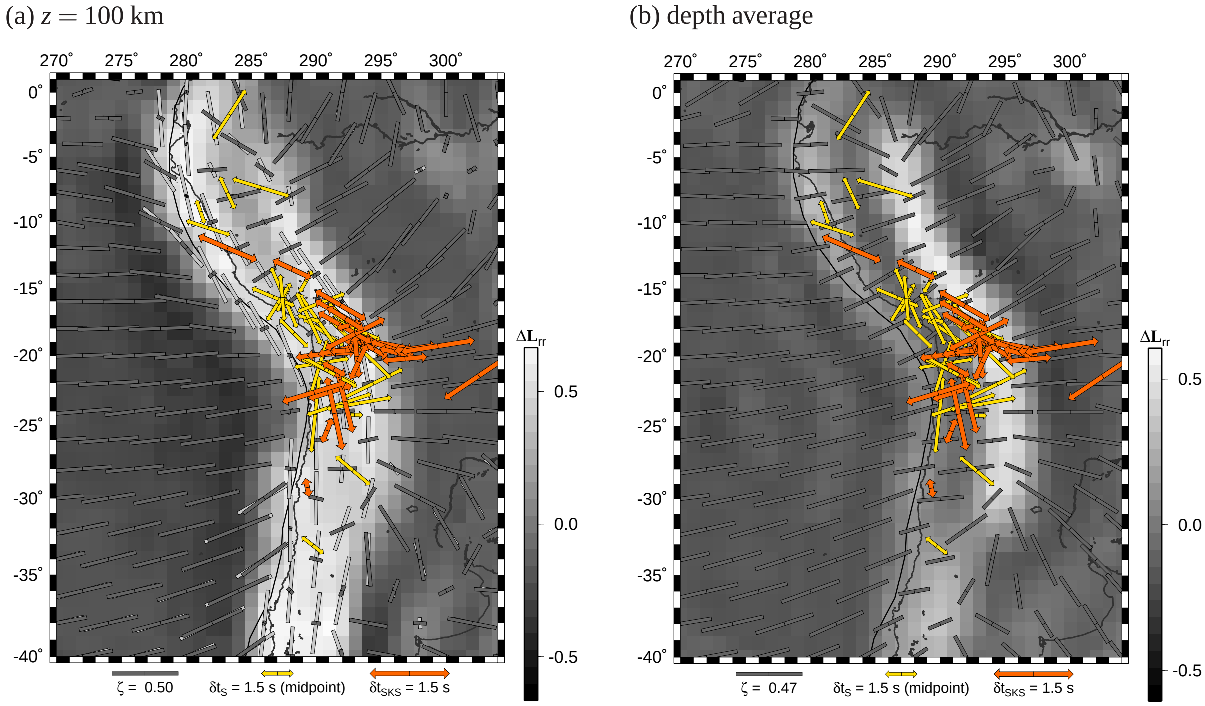

Figure 5.35: Comparison of $\zeta_c = 0.5$ strain predictions for South America with splitting data. The three northern *SKS* orientations are based on Russo and Silver's (1994) splits, while most *SKS* observations in the Arica bend and further south are from Polet *et al.* (2000). *S*-phase derived data are from Russo and Silver's (1994) backprojection method and are therefore shown at the hypocenters. (Note that *S*-data δt-scale is 40% of *SKS* in this plot.) Flow models are based on plate motions, η_F, and *rum* slabs. We show horizontal projection of largest FSE axis (black) and largest stretching orientation of the horizontal component of the FSE (gray) for $z = 100$ km (a) and the ζ-weighted depth average of horizontal principal axes projections (b).

with seismometers and GPS stations. Since it is also a region where the lithosphere is likely to be thin (*e.g.* van der Lee and Nolet, 1997), it allows a good test of models of lithospheric flow and mantle convection. For this reason, Silver and Holt (2002) inverted *SKS* splitting measurements and showed that anisotropy tends to align with the APM motions in the region (APM directions are similar to NNR for the Western US). However, Silver and Holt reject the APM hypothesis since the transition between North American and Pacific plate motion is less abrupt in the splitting data than a rigid plate model would suggest. Instead of the APM hypothesis, Silver and Holt (2002) prefer a model in which the mantle moves coherently (without any information about the plate boundary) to the West with respect to stable North America, in a direction roughly opposite to the surface motion. Assuming this coherent, deep mantle flow takes place, these authors derive its rotation pole by adding information about intraplate velocity gradients from geodesy.

Figure 5.36 shows our 0.5°-averaged splitting data compilation for which we have used only data within the slow $d\ln v_S$ areas at 150 km depth from van der Lee and Nolet's (1997) tomography model to be consistent with Silver and Holt (2002). Our data differs slightly from those authors', probably because of different ways of tracking the zero contour. We see that the surface velocities in a hotspot frame (black sticks) show some correspondence to the observed fast splitting orientations. However, as noted by Silver and Holt (2002) (their Figure 3), there are some deviations between the rigid plate motions and the splitting data, especially noticeable in the SE of the study region. Velocity orientations from our η_F flow calculation (gray sticks in Figure 5.36) show a smooth transition at the plate boundary and are closer to the anisotropy data. This plate-boundary deformation is both a result of the decreasing gradients of the velocity field with depth and our spectral method. Since we are using a $\cos^2$-tapered expansion of plate motions and perform calculations up to $\ell_{\max} = 63$, sharp contrasts in velocities at the plate boundary are smoothed out. The width of this deformation zone is $\sim$300 km (also see Figure 5.41), in agreement with geodetic observations in the Western US (*cf.* Flesch *et al.*, 2000). This further supports the applicability of our simplified method of treating mantle flow.

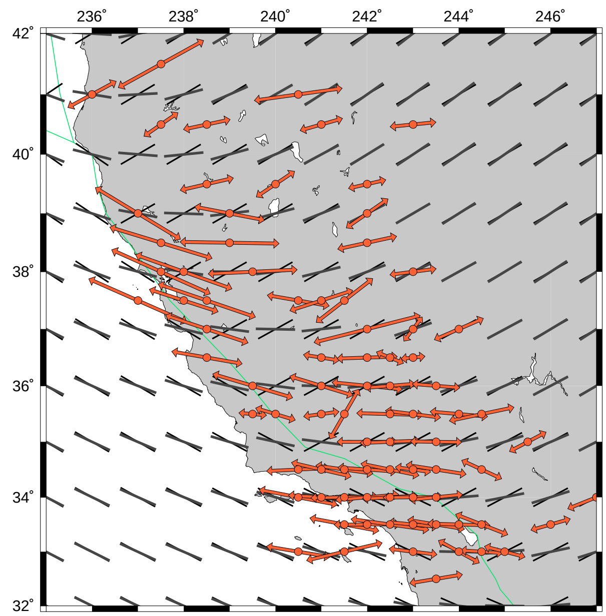

Figure 5.36: 0.5° averaged *SKS* splitting data based on Schutt and Kubo (2001) and Polet and Kanamori (2002) but restricted to slow regions from van der Lee and Nolet (1997) at 150 km depth for the Western US (double-headed vectors). Background: velocity orientations for rigid-plate surface motions from NUVEL1 (black sticks) and for a plate-motion driven circulation calculation at 138 km depth using η_F and $\ell_{\max} = 63$ (gray sticks), both are shown in the HS2 hotspot reference-frame.

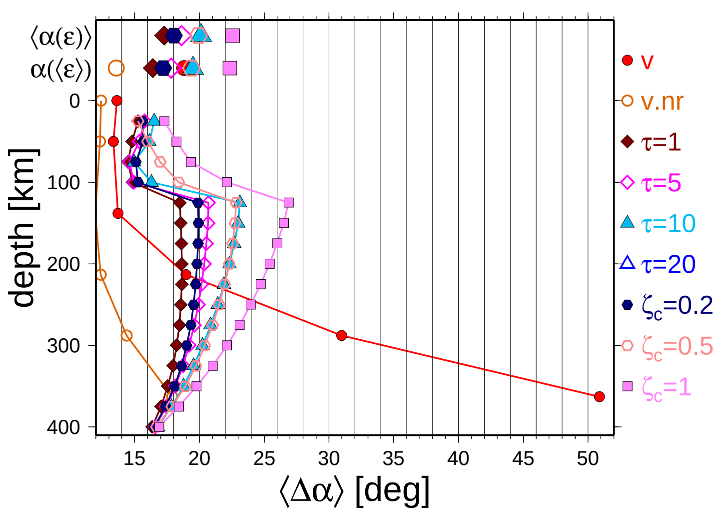

Figure 5.37: Depth-averaged and mean orientational misfit at each depth for plate-motion only model with η_F. While previous misfit plots (*e.g.* Figure 5.22) focus on the ζ-weighted depth average of the horizontal projection of the major FSE axis, $\langle\alpha(\varepsilon)\rangle$, shown at negative depths, we also show the orientational misfit at each depth, and the misfit we obtained from the horizontal projection of the major FSE axis based on depth-averaged **L**-strain, $\alpha(\langle\varepsilon\rangle)$.

Figure 5.37 gives a quantitative estimate of misfits between our velocity and strain predictions and *SKS* splitting for plate-motion driven flow and η_F. We see that flow orientations lead to lower misfits than any of our strain-based models (but see below). From the surface down, the fit improves until $\sim$150 km, after which it deteriorates, both for APM and NNR models, mostly because flow underneath the plate boundary region and the Pacific plate is oriented more west-east than it is at the surface. The $\langle\Delta\alpha\rangle$ misfit for the rigid-plate surface velocities from HS2-NUVEL1 (shown with black sticks in Figure 5.36) is 21.4°, worse than all velocity-based orientations from our circulation calculation. Our model, with splitting caused by mantle circulation, leads to results that are comparable in model fit to Silver and Holt's (2002) preferred model. One of those authors' conclusions is that there is an asthenospheric decoupling zone under North America that allows eastward flow at depth. While we proceed to explore a scenario in which we indeed find such flow, our previous results indicate that such complexity might not be needed to explain the data. A circulation model with smooth velocity transitions between plates leads to good misfits both for NR flow orientations ($\langle\Delta\alpha\rangle = 12.5°$) and for alignment with $\zeta_c = 0.2$ Myr strain ($\langle\Delta\alpha\rangle = 13.5°$).

Can we improve the fit to the splitting data by including density anomalies in the mantle? Figure 5.38 shows mean misfits for the study region using a suite of models, some of which include density anomalies. For most

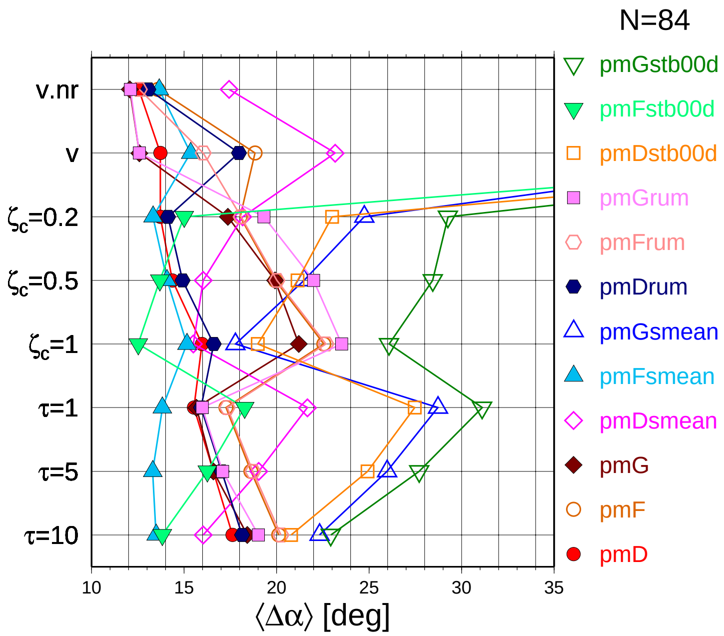

Figure 5.38: Mean orientational misfit $\langle\Delta\alpha\rangle$ between splitting and depth-averaged horizontal projections of largest FSE axes or velocity orientations for the Western US. Results for *pmF* are hidden by those for *pmFrum* since there is little difference between the two flow fields in the study region. $\langle\Delta\alpha\rangle$ for the *stb00d* models is off scale for v and v.nr at $\sim 60°$. For model abbreviations, see Figure 5.22.

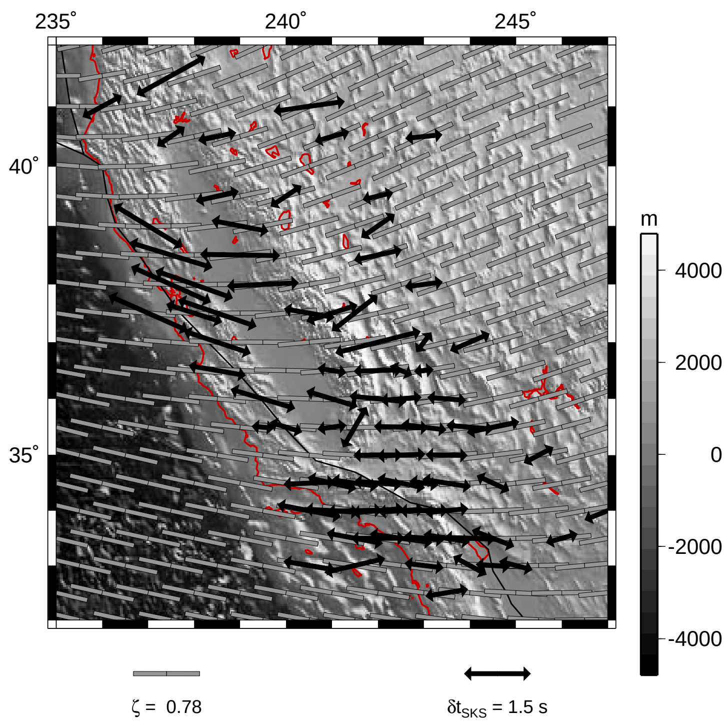

Figure 5.39: Comparison of depth-averaged $\zeta_c = 1$ largest FSE axes predictions for η_F including the effect of plate motions and *stb00d* slabs with the *SKS* data-selection that was shown in Figure 5.36. Background shading is topography from EDC (1996).

models, azimuth predictions have low orientational misfits both for the assumption of alignment with flow and alignment with strain. Larger ζ and τ values are generally preferred, although exceptions exist. The best depth-averaged misfit for FSE axes is found for the $\zeta_c = 1$ model using η_F and *stb00d* (Figure 5.39), whose velocity orientations, in contrast, lead to extremely poor fits. This is caused by a rotation due to a deep velocity component that is roughly northeasterly trending, caused by the Farallon slab anomaly as included in *stb00d*. If we use another mantle model such as *smean*, the deep counter-flow is significantly reduced, implying that the exact location and strength of density anomalies is important. The deep flow underneath the Western US for *stb00d* (Figure 5.40) is similar to that suggested by Silver and Holt (2002), although their best-fit, decoupled-mantle velocity trends more easterly throughout the study region.

The mean angular misfits vary strongly with depth for the subduction model and alignment of deep flow with

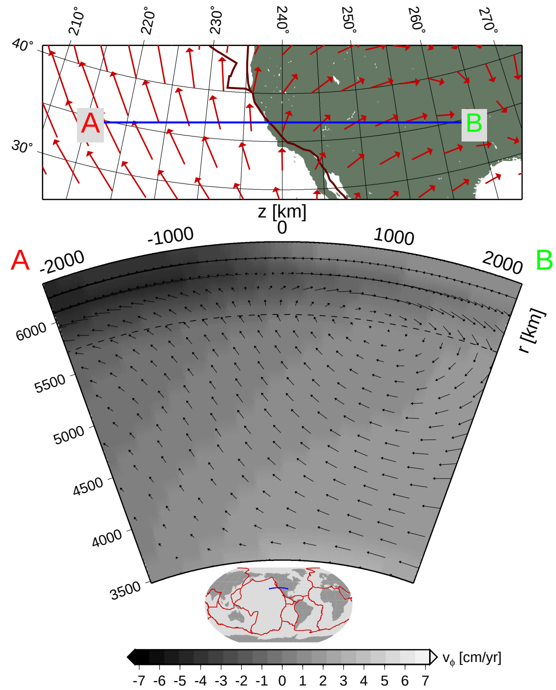

Figure 5.40: Flow profile underneath the Western US as predicted from plate motions and subduction model *stb00d*. Plot is similar to Figures 2.13 and 2.14 in that the profile along which velocities are depicted is presented in the overview map above the main plot. However, the map shows horizontal velocities at 350 km depth (HS2 hotspot frame), which are roughly opposite in direction to the surface motion of western North America.

splitting is very poor. This is illustrated in Figure 5.41 which shows how strain accumulates for plate motions alone and when *std00d* slab densities are included. The simplest pattern is that of plate-motion related flow for $\tau = 5$ Myr (Figure 5.41a). As in our global models, strain-rates are higher underneath the oceanic plate; deformation underneath North America is mostly due to the smooth transition between the two surface velocity fields. For both plates, we observe a simple-shear straining that tapers off with depth since there are no internal density sources in the flow field. Assuming constant strain, the $\zeta_c = 0.5$ model (Figure 5.41b) shows that, within the cut-off time of 43 Ma, such strains can be reached only at sub-lithospheric depths for North America since the upper ~ 100 km deform coherently. The situation changes if we include density anomalies due to past subduction. Shallow (~ 100 km) and deep (~ 350 km) regions for the $\tau = 5$ Myr model (Figure 5.41c) show strain orientations that are similar to those expected from plate-motion related flow (Figure 5.41a). However, the slab sinker to the east induces a NE-trending flow component that leads to strong shearing at ~ 225 km depth and that dominates the average strain azimuths at the surface. For constant strain (Figure 5.41d), the dominance of this NE shearing is reduced and surface-near strain orientations are relatively more important, leading to the observed good fit between fast shear-wave propagation orientations and strain. This complicated story shows that models that either implicitly or explicitly assume that shearing occurs within a single layer between moving lithosphere and stationary mantle may be too simplistic. Observations of surface velocities would not have led us to predict variations of strain orientations with depth.

Misfits for our strain-based model (η_F, plate motions, and *stb00d*) and Silver and Holt's (2002) best-fit model, which assumes straining in an asthenospheric channel over decoupled mantle flow, are shown in Figure 5.42; this is the most quantitative comparison we can make with Silver and Holt's (2002) model. Although there are small differences in the data selection, we conclude that model quality is similar for the two approaches. We can therefore reconcile the results of Silver and Holt (2002) with our modeling. Silver and Holt assume that there is complete decoupling between surface velocities and mantle flow at depth. As Figure 5.40 shows, some of our mantle circulation models indeed predict a corresponding rapid change in the horizontal direction of flow with depth. This is due to past subduction, as suggested by Silver and Holt (2002) based on Steinberger's (2000) results. We find a small but robust improvement in fit when we include *stb00d* as compared to plate-motion only models.

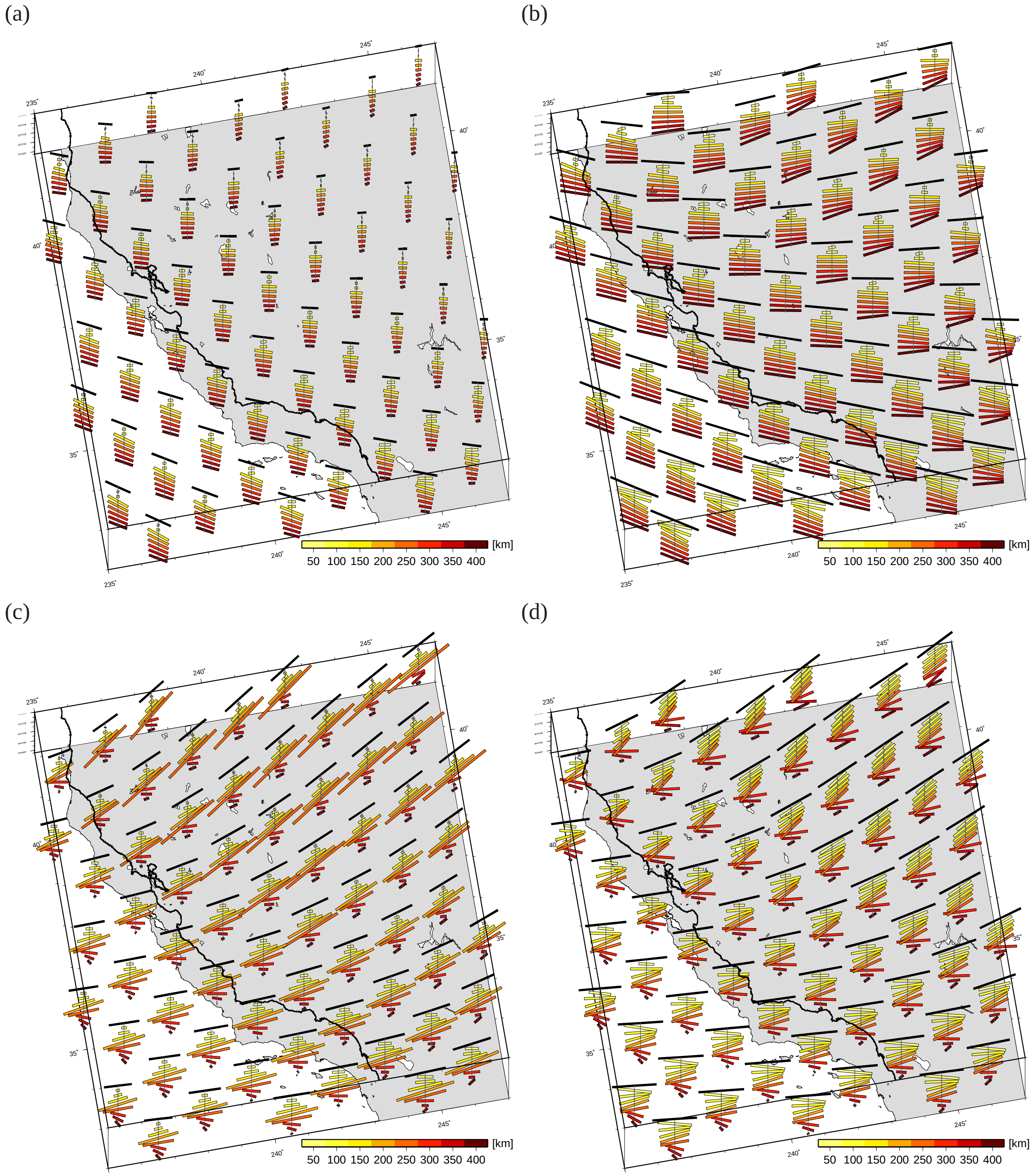

Figure 5.41: Orientations of the horizontal projection of the largest stretching axis scaled with ζ at different depths underneath the Western US, plate-motion related flow (η_F) for $\tau = 5$ Myr (a) and $\zeta_c = 0.5$ (b), and for circulation with slab-pull (*stb00d*) for $\tau = 5$ Myr (a) and $\zeta_c = 0.5$ (d). Stick colors scale with the depth as given in the colorbar, black sticks at the surface indicate the ζ-averaged largest FSE orientations.

5.8 Summary

Some observations of seismic anisotropy can be explained by global circulation models, under the assumption that fast orientations are aligned with the largest axis of the finite strain ellipsoid, as suggested by the theory of Ribe (1992). For azimuthal anisotropy derived from surface-wave phase velocities, mantle-flow derived models

(a) (b)

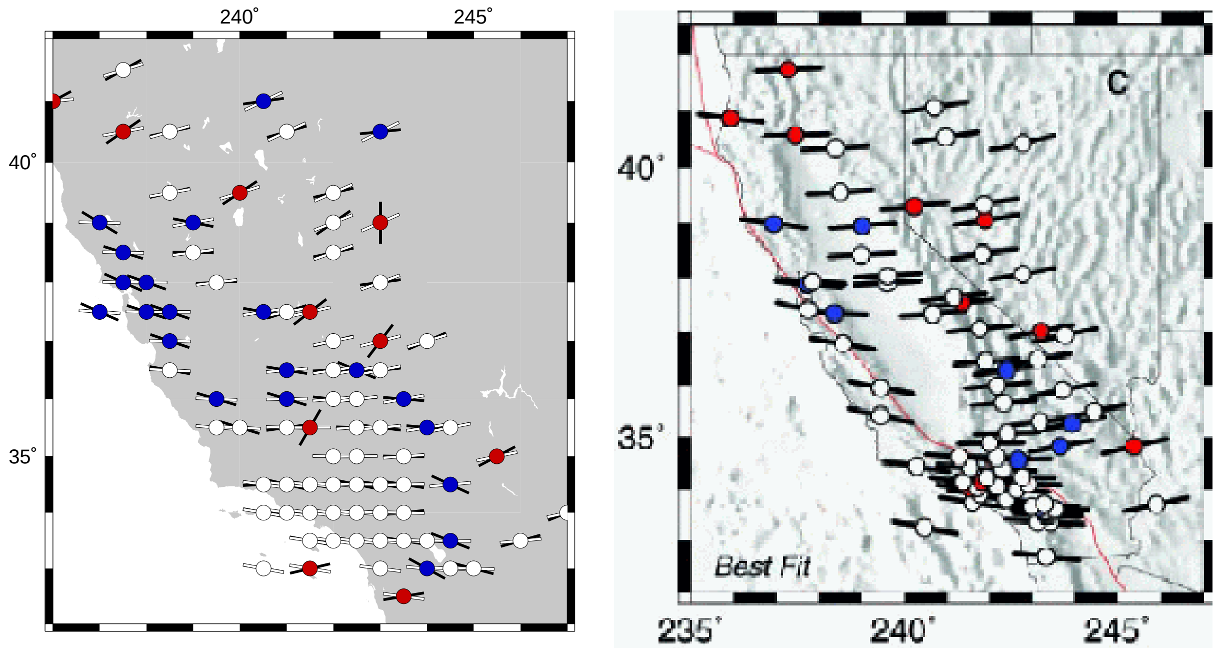

Figure 5.42: (a) Misfit between predicted and measured anisotropy for our model using plate-motion and *stb00d*-driven flow and $\zeta_c = 1$ strain, as in Figure 5.39. Black sticks indicate data as in Figure 5.36 and white denotes model predictions. Circles are shaded dark (light) gray if the model deviates by more than 14° counterclockwise (clockwise) from the data. (b) Best-fit from Silver and Holt's (2002) Figure 3C. Here, only the model fit is shown with sticks but color coding of circles is same as for (a). Note that data selection varies slightly between (a) and (b).

lead to smaller misfits than models based on alignment with surface velocities. Beneath the East Pacific Rise and the Western US, tectonic settings in which our simplified treatment of mantle convection is likely to be most appropriate, *SKS* shear-wave splitting can be modeled with low residual misfit. In the Western US, our models provide a natural explanation for the deep eastward flow inferred by Silver and Holt (2002). In subduction zones, where the strain field is complex, estimated orientations of fast wave propagation vary rapidly. Where the largest axis of the FSE is radial, the horizontal components of the FSE may be of importance; close to the trench, these components are aligned mostly arc-parallel. Given the complex strain-fields, it seems prudent at this point to refrain from further interpretation of our model results in terms of shear-wave splitting until we can convert strain into elastic moduli and carry out synthetic splitting measurements. Coupling of the strain history to texture development algorithms (*e.g.* Kaminski and Ribe, 2001) should be attempted thereafter.

Outlook

We derived a global circulation model based on our understanding of mantle convection in the Earth. The present-day and reconstructed velocities predicted by this model were successfully applied to the study of anisotropy in the upper mantle. We feel that we have now stretched the simplified Hager and O'Connell (1981) approach to the study of mantle convection about as far as one should. We were able to show that many observations can be explained using flow derived from such simple models. However, a more realistic treatment of mantle rheology should next be explored; this will be especially important in subduction zones. A finite-element calculation would allow us to address the role of temperature- and stress-dependent rheology and how it might affect seismic anisotropy. A model that includes lateral variations in viscosity would also be a useful tool for substantiating our findings from the first two chapters regarding effective slab strength, trench roll-back, and circulation effects on slab morphology. Regardless of the exact method of calculating flow, the analysis of mantle models in chapter 3 will be of great use. The same is true for our method of quantitatively comparing seismic anisotropy with mantle flow. The application of these techniques to a more sophisticated flow model is, like an improved treatment of texture development, a natural extension of our work. We have already begun to utilize another global data set, that of crustal stress measurements, as an additional constraint on mantle flow and lithospheric deformation. We find that mantle-derived stresses lead to a good fit in terms of principal orientations but that other contributions to tectonic stress may be of equal importance (Becker and O'Connell, 2001a). The inclusion of GPS data, which can provide a direct measure of strain-rates within plates, should lead to improvements in this regard. Combining all of these datasets in a future model will allow us to further our understanding of mantle-plate interactions significantly.

Bibliography

Abbate, E. (1984). Pre-orogenic tectonics and metamorphism in western Tethys Ophiolites. *Ofioliti*, *9*, 245–278.

Agee, C. B. (1998). Phase transformations and seismic structure in the upper mantle and transition zone. In: *Ultrahigh-Pressure Mineralogy. Physics and Chemistry of the Earth's Deep Interior*, ed. R. J. Hemley, vol. 37 of *Reviews in Mineralogy*, pp. 165–203. Mineralogical Society of America, Washington DC.

Anderson, D. L. (1987). A seismic equation of state. II. Shear properties and thermodynamics of the lower mantle. *Phys. Earth Planet. Inter.*, *45*, 307–323.

Anderson, D. L. and A. M. Dziewonski (1982). Upper mantle anisotropy: evidence from free oscillations. *Geophys. J. R. Astr. Soc.*, *69*, 383–404.

Andrews, D. J. and N. H. Sleep (1974). Numerical modeling of tectonic flow behind Island Arc. *Geophys. J. R. Astr. Soc.*, *38*, 237–251.

Antolik, M., G. Ekström, A. M. Dziewonski, Y. J. Gu, J.-f. Pan, and L. Boschi (2001). A new joint *P* and *S* velocity model of the mantle parameterized in cubic B-splines. In: *22nd Annual DoD/DOE Seismic Research Symposium: Planning for Verification of and Compliance with the Comprehensive Nuclear-Test-Ban Treaty (CTBT): Proceedings*, vol. II.

Artyushkov, E. V. (1973). Stresses in the lithosphere caused by crustal thickness inhomogeneities. *J. Geophys. Res.*, *78*, 7675–7708.

Backus, G., J. Park, and D. Garbasz (1981). On the relative importance of the driving forces of plate motion. *Geophys. J. R. Astr. Soc.*, *67*, 415–435.

Bai, W., C. Vigny, Y. Ricard, and C. Froidevaux (1992). On the origin of deviatoric stresses in the lithosphere. *J. Geophys. Res.*, *97*, 11,729–11,737.

Barchi, M., G. Minelli, and G. Pialli (1998). The CROP03 profile: a synthesis of result on deep structures of the Northern Apennines. *Mem. Soc. Geol. It.*, *52*, 383–400.

Bartole, R. (1995). The North Tyrrhenian-Northern Apennines post-collisional system: constraint for a geodynamic model. *Terra Nova*, *7*, 7–30.

Beccaluva, L., P. Brotzu, G. Macciotta, L. Morbidelli, G. Serri, and G. Traversa (1989). Cainozoic tectono-magmatic evolution and inferred mantle sources in the Sardo-Tyrrhenian area. In: *The Lithosphere in Italy. Advances in Science Research*, eds. A. Boriani, M. Bonafede, G. B. Piccardo, and G. B. Vai, pp. 15–40. Accademia Nazionale dei Lincei, Rome.

Becker, T. W. and L. Boschi (2002). A comparison of tomographic and geodynamic mantle models. *Geochemistry, Geophysics, Geosystems*, *3* (2001GC000168).

Becker, T. W., C. Faccenna, and R. J. O'Connell (1998). Mantle winds and back-arc spreading: the influence of background flow on subdution in the upper mantle (abstract). *EOS Trans. AGU*, *79*, F849.

Becker, T. W., C. Faccenna, R. J. O'Connell, and D. Giardini (1999a). The development of slabs in the upper mantle: insight from numerical and laboratory experiments. *J. Geophys. Res.*, *104*, 15,207–15,225.

Becker, T. W., J. B. Kellogg, and R. J. O'Connell (1999b). Thermal constraints on the survival of primitive blobs in the lower mantle. *Earth Planet. Sci. Lett.*, *171*, 351.

Becker, T. W. and R. J. O'Connell (2001a). Lithospheric stresses caused by mantle convection: The role of plate rheology (abstract). *EOS Trans. AGU*, *82* (47), T12C–0921.

Becker, T. W. and R. J. O'Connell (2001b). Predicting plate velocities with geodynamic models. *Geochemistry, Geophysics, Geosystems*, *2* (2001GC000171).

Ben Ismail, W. and D. Mainprice (1998). An olivine fabric database; an overview of upper mantle fabrics and seismic anisotropy. *Tectonophysics*, *296*, 145–157.

Bergeron, S. Y., D. A. Yuen, and A. P. Vincent (2000). Capabilities of 3-D wavelet transforms to detect plume-like structures from seismic tomography. *Geophys. Res. Lett.*, *27*, 3433–3436.

Bevis, M. (1986). The curvature of Wadati-Benioff zones and the torsional rigidity of subducting plates. *Nature*, *323*, 52–53.

Bevis, M. (1988). Seismic slip and down dip strain rate in Wadati-Benioff zones. *Science*, *240*, 1317–1319.

Bevis, M., F. W. Taylor, B. E. Schutz, J. Recy, B. L. Isacks, S. Helu, R. Singh, E. Kendrick, J. Stowell, B. Taylor, and S. Calmant (1995). Geodetic observations of very rapid convergence and back-arc extension at the Tonga arc. *Nature*, *374*, 249–251.

Blackman, D. K. and J.-M. Kendall (2002). Seismic anisotropy of the upper mantle: 2. Predictions for current plate boundary flow models. *Geochemistry, Geophysics, Geosystems*, *submitted*.

Blackman, D. K., J.-M. Kendall, P. R. Dawson, and R. H. Wenk (1996). Teleseismic imaging of subaxial flow at mid-ocean ridges: traveltime effects of anisotropic mineral texture in the mantle. *Geophys. J. Int.*, *127*, 415–426.

Blackman, D. K., H.-R. Wenk, and J.-M. Kendall (2002). Seismic anisotropy of the upper mantle: 1. Factors that affect mineral texture and effective elastic properties. *Geochemistry, Geophysics, Geosystems*, *submitted*.

Boccaletti, M., P. Elter, and G. Guazzone (1971). Polaritá strutturali delle alpi e dell' appennino settentrionale in rapporto all'inversione di una zona di subduzione nord-tirrenica. *Mem. Soc. Geol. It.*, *10*, 371–378.

Bodri, L. and B. Bodri (1978). Numerical investigation of tectonic flow in island-arc areas. *Tectonophysics*, *50*, 163–175.

Bokelmann, G. and E. Humphreys (2000). Plate-mantle interaction and forces that move plates. *EOS Trans. AGU*, *81* (48). Special session at AGU Fall Meeting.

Borsi, S. and R. Dubois (1968). Donnes geochronologiques sue l'histoire hercynienne et alpine de la Calabre centrale. *C. R. Acad. Sci. Paris*, *266*, 72–75.

Bortolotti, V., G. Principi, and B. Treves (1990). Mesozoic evolution of western Tethys and the Europe/Iberia/Adria plate junction. *Mem. Soc. Geol. It.*, *45*, 393–407.

Boschi, L. and A. M. Dziewonski (1999). 'High' and 'low' resolution images of the Earth's mantle – Implications of different approaches to tomographic modeling. *J. Geophys. Res.*, *104*, 25,567–25,594.

Boschi, L. and G. Ekström (2002). New images of the Earth's upper mantle from measurements of surface-wave phase velocity anomalies. *J. Geophys. Res.*, *in press*.

Bosworth, W., R. Guirath, and L. G. Kessler II (1999). Late Cretaceous (ca. 84 Ma) compressive deformation of the stable platform of northeast Africa (Egypt): far-field stress effects of the "Santonian event" and origin of the Syrian arc deformation belt. *Geology*, *27*, 633–636.

Brace, W. F. and D. L. Kohlstedt (1980). Limits on lithospheric stress imposed by laboratory experiments. *J. Geophys. Res.*, *85*, 6248–6252.

Brunet, C., P. Monié, L. Jolivet, and J. P. Cadet (2000). Migration of compression and extension in the Tyrrhenian Sea, insights from 40Ar/39Ar ages on micas along a transect from Corsica to Tuscany. *Tectonophysics*, *321*, 127–155.

Bunge, H.-P. and S. P. Grand (2000). Mesozoic plate-motion history below the northeast Pacific Ocean from seismic images of the subducted Farallon slab. *Nature*, *405*, 337–340.

Bunge, H.-P., C. Hagelberg, and B. Travis (2001). Mantle circulation models with variational data assimilation: Inferring past mantle flow and structure from plate motion histories and seismic tomography (abstract). *EOS Trans. AGU*, *82* (47), NG51C–07.

Bunge, H.-P., M. A. Richards, C. Lithgow-Bertelloni, J. R. Baumgardner, S. P. Grand, and B. A. Romanowicz (1998). Time scales and heterogeneous structure in geodynamic earth models. *Science*, *280*, 91–95.

Burrus, J. (1984). Contribution to a geodynamic synthesis of the Provençal basin (north-western Mediterranean). *Mar. Geol.*, *55*, 247–269.

Buttles, J. and P. Olson (1998). A laboratory model of subduction zone anisotropy. *Earth Planet. Sci. Lett.*, *164*, 245–262.

Bystricky, M., K. Kunze, L. Burlini, and J.-P. Burg (2000). High shear strain of olivine aggregrates: rheological and seismic consequences. *Science*, *290*, 1564–1567.

Čadek, O. and L. Fleitout (2000). Effect of lateral viscosity variations in the top 300 km of the mantle on the geoid, dynamic topography and lithospheric stresses. In: *European Geophysical Society, 25th general assembly*, vol. 2 of *Geophys. Res. Abstr.*. European Geophysical Society.

Carlson, R. L. and H. P. Johnson (1994). On modeling the thermal evolution of the oceanic upper-mantle – an assessment of the cooling plate model. *J. Geophys. Res.*, *99*, 3201–3214.

Carmignani, L. and R. Kligfield (1990). Crustal extension in the Northern Apennines: the transition from compression to extension in the Alpi Apuane core complex. *Tectonics*, *9*, 1275–1305.

Castle, J. C. and R. D. van der Hilst (2000). Searching for seismic observations of deep mantle structure (abstract). *EOS Trans. AGU*, *81*, F832.

Chamot-Rooke, N., J.-M. Gaulier, and F. Jestin (1999). Constraints on Moho depth and crustal thickness in the Liguro-Provençal Basin from a 3D gravity inversion; geodynamic implications. In: *The Mediterranean basins: Tertiary extension within the Alpine Orogen*, eds. B. Durand, A. Mascle, L. Jolivet, F. Horvàth, and M. Séranne, vol. 156 of *Geol. Soc. Lond. Spec. Pubs*, pp. 37–61. Geological Society of London, London.

Channell, J. E. T. (1986). Paleomagnetism and continental collision in the Alpine belt and the formation of late-tectonic extensional basins. In: *Collision Tectonics*, eds. M. P. Coward and A. C. Reis, vol. 19 of *Geol. Soc. Lond. Spec. Pubs.*, pp. 261–284. Geological Society of London, London.

Chapple, W. M. and T. E. Tullis (1977). Evaluation of the forces that drive the plates. *J. Geophys. Res.*, *82*, 1967–1984.

Chase, C. G. (1978). Extension behind island arcs and motion relative to hot spots. *J. Geophys. Res.*, *83*, 5385–5387.

Chase, C. G. (1979). Subduction, the geoid, and lower mantle convection. *Nature*, *282*, 464–468.

Chastel, Y. B., P. R. Dawson, H.-R. Wenk, and K. Bennett (1993). Anisotropic convection with implications for the upper mantle. *J. Geophys. Res.*, *98*, 17,757–17,771.

Cherchi, A. and L. Montandert (1982). Oligo-Miocene rift of Sardinia and the early history of the Western Mediterranean basin. *Nature*, *298*, 736–739.

Christensen, U. R. (1984). Convection with pressure- and temperature-dependent non-newtonian rheology. *Geophys. J. R. Astr. Soc.*, *77*, 343–384.

Christensen, U. R. (1996). The influence of trench migration on slab penetration into the lower mantle. *Earth Planet. Sci. Lett.*, *140*, 27–39.

Christensen, U. R. (1997). Influence of chemical buoyancy on the dynamics of slabs in the transition zone. *J. Geophys. Res.*, *102*, 22,435–22,443.

Christensen, U. R. and D. A. Yuen (1984). The interaction of a subducting lithospheric slab with a chemical or phase boundary. *J. Geophys. Res.*, *89*, 4389–4402.

Čížková, H., O. Čadek, and A. Slancová (1998). Regional correlation analysis between seismic heterogeneity in the lower mantle and subduction in the last 180 Myr: implications for mantle dynamics and rheology. *Pure Appl. Geophys.*, *151*, 527–537.

Cloos, M. N. (1993). Lithospheric buoyancy and collisional orogenesis: subduction of oceanic plateaus, continental margins, island arcs, spreading ridges and seamounts. *Geol. Soc. Am. Bull.*, *105*, 715–737.

Coblentz, D. D., R. M. Richardson, and M. Sandiford (1994). On the gravitational potential of the Earth's lithosphere. *Tectonics*, *13*, 929–945.

Cohen, C. R. (1982). Model for a passive to active continental margin transition: implications for hydrocarbon exploration. *Am. Ass. Petrol. Geol. Bull.*, *66*, 708–818.

Conrad, C. P. and B. H. Hager (1997). The role of plate bending and fault strength at subduction zones on plate dynamics (abstract). *EOS Trans. AGU*, *78*, F4.

Conrad, C. P. and B. H. Hager (1999a). The effects of plate bending and fault strength at subduction zones on plate dynamics. *J. Geophys. Res.*, *104*, 17,551–17,571.

Conrad, C. P. and B. H. Hager (1999b). The thermal evolution of an earth with strong subduction zones. *Geophys. Res. Lett.*, *26*, 3041–3044.

Conrad, C. P. and P. Molnar (1997). The growth of Rayleigh-Taylor-type instabilities in the lithosphere for various rheological and density structures. *Geophys. J. Int.*, *129*, 95–112.

Cox, A. M., G. Debiche, and D. C. Engebretson (1989). Terrane trajectories and plate interaction along continental margins in the north Pacific basin. In: *The evolution of the Pacific Ocean margins*, ed. Z. Ben-Avraham, pp. 20–35. Oxford University Press, Oxford.

Cross, T. A. and R. C. Pilger (1982). Controls of subduction geometry, location of magmatic arcs, tectonics of arc and back-arc regions. *Geol. Soc. Am. Bull.*, *93*, 545–562.

Dahlen, F. A. and J. Tromp (1998). *Theoretical Global Seismology*. Princeton University Press, Princeton, New Jersey.

D'Argenio, B. and A. Mindszenty (1991). Karst Bauxite at regional unconformity and the geotectonic correlation in the Cretaceous of the Mediterranean. *Bull. Soc. Geol. It.*, *110*, 85–92.

Davies, G. F. (1988). Role of the lithosphere in mantle convection. *J. Geophys. Res.*, *93*, 10,451–10,466.

Davies, G. F. and M. A. Richards (1992). Mantle convection. *J. Geology*, *100*, 151–206.

Davy, P. and P. R. Cobbold (1991). Experiments on shortening of a 4-layer model of the continental lithosphere. *Tectonophysics*, *188*, 1–25.

DeMets, C., R. G. Gordon, D. F. Argus, and S. Stein (1990). Current plate motions. *Geophys. J. Int.*, *101*, 425–478.

Deparis, V., H. Legros, and Y. Ricard (1995). Mass anomalies due to subducted slabs and simulations of plate motion since 200 My. *Earth Planet. Sci. Lett.*, *89*, 271–280.

Dercourt, J., L. E. Ricou, and B. Vrielinck (1993). *Atlas Tethys, paleoenvironmental maps*. Gauthier-Villars, Paris.

Dercourt, J., L. P. Zonenshain, L. E. Ricou, V. C. Karmin, X. Le Pichon, A. L. Knipper, C. Grandjacquet, I. M. Sburtshickov, J. Geyssant, C. Lepvrier, D. A. Pechersky, J. Boulin, J. C. Sibuet, L. A. Savostin, O. Sorokhtin, M. Westphal, M. L. Bazhenov, J. P. Laver, and B. Biju-Duval (1986). Geological evolution of the Tethys belt from the Atlantic to the Pamir since the Lias. *Tectonophysics*, *123*, 241–315.

Dewey, J. F. (1980). Episodicity, sequence and style at convergent plate boundaries. In: *The Continental crust and its mineral deposits*, vol. 20 of *GAC Special Paper*, pp. 553–573. Geological Association of Canada.

Dewey, J. F., M. L. Helman, E. Turco, D. H. W. Hutton, and S. D. Knot (1989). Kinematics of the western Mediterranean. In: *Conference on Alpine tectonics*, eds. M. P. Coward, D. Dietrich, and R. G. Park, vol. 45 of *Geol. Soc. Lond. Spec. Pubs.*, pp. 265–283. Geological Society of London, London.

Doglioni, C. (1990). The global tectonic pattern. *J. Geodynamics*, *12*, 21–38.

Doglioni, C., E. Gueguen, F. Sàbat, and M. Fernandez (1997). The western Mediterranean extensional basins and the Alpine orogen. *Terra Nova*, *9*, 109–112.

Dziewonski, A. M. (1984). Mapping the lower mantle: determination of lateral heterogeneity in P velocity up to degree and order 6. *J. Geophys. Res.*, *89*, 5929–5952.

Dziewonski, A. M. (2000). Global seismic tomography: past, present and future. In: *Problems in Geophysics for the New Millenium*, eds. E. Boschi, G. Ekström, and A. Morelli, pp. 289–349. Istituto Nazionale di Geofisica e Vulcanologia, Editrice Compositori, Bologna, Italy.

Dziewonski, A. M. and D. L. Anderson (1981). Preliminary reference Earth model. *Phys. Earth Planet. Inter.*, *25*, 297–356.

Dziewonski, A. M., T.-A. Chou, and J. H. Woodhouse (1981). Determination of earthquake source parameters from waveform data for studies of global and regional seismicity. *J. Geophys. Res.*, *86*, 2825–2852.

Dziewonski, A. M., B. H. Hager, and R. J. O'Connell (1977). Large scale heterogeneity in the lower mantle. *J. Geophys. Res.*, *82*, 239–255.

EDC (1996). *Global 30 Arc Second Elevation Data Set*. EROS Data Center, Sioux Falls, South Dakota.

Ekström, G. (2000). Global studies of earthquakes. In: *Problems in Geophysics for the New Millenium*, eds. E. Boschi, G. Ekström, and A. Morelli, pp. 111–123. Istituto Nazionale di Geofisica e Vulcanologia, Editrice Compositori, Bologna, Italy.

Ekström, G. (2001). Mapping azimuthal anisotropy of intermediate-period surface waves (abstract). *EOS Trans. AGU*, *82* (47), S51E–06.

Ekström, G. and A. M. Dziewonski (1998). The unique anisotropy of the Pacific upper mantle. *Nature*, *394*, 168–172.

Elsasser, W. M. (1969). Convection and stress propagation in the upper mantle. In: *The Application of Modern Physics to the Earth and Planetary Interiors*, ed. S. K. Runcorn, pp. 223–249. Wiley, New York.

Engdahl, E. R., R. D. van der Hilst, and R. Buland (1998). Global teleseismic earthquake relocation with improved travel times and procedures for depth determination. *Bull. Seism. Soc. Am.*, *88*, 722–743.

Faccenna, C., T. W. Becker, F. P. Lucente, L. Jolivet, and F. Rossetti (2001a). History of subduction and back-arc extension in the central Mediterranean. *Geophys. J. Int.*, *145*, 809–820.

Faccenna, C., P. Davy, J.-P. Brun, R. Funiciello, D. Giardini, M. Mattei, and T. Nalpas (1996). The dynamics of back-arc extension: an experimental approach to the opening of the Tyrrhenian Sea. *Geophys. J. Int.*, *126*, 781–795.

Faccenna, C., F. Funiciello, D. Giardini, and P. Lucente (2000). Why did Sardinia stop rotating? *Geophys. Res. Abstr.*, *2*, 16.

Faccenna, C., F. Funiciello, D. Giardini, and P. Lucente (2001b). Episodic back-arc extension during restricted mantle convection in the Central Mediterranean. *Earth Planet. Sci. Lett.*, *187*, 105–116.

Faccenna, C., D. Giardini, P. Davy, and A. Argentieri (1999). Initiation of subduction at Atlantic type margins: Insights from laboratory experiments. *J. Geophys. Res.*, *104*, 2749–2766.

Faccenna, C., M. Mattei, R. Funiciello, and L. Jolivet (1997). Styles of back-arc extension in the Central Mediterranean. *Terra Nova*, *9*, 126–130.

Ferrachat, S. and Y. Ricard (1998). Regular vs. chaotic mantle mixing. *Earth Planet. Sci. Lett.*, *155*, 75–86.

Finetti, I. and A. del Ben (1986). Geophysical study of the Tyrrhenian opening. *Boll. Geofis. Teorica Ed Applicata*, *28*, 75–155.

Fischer, K. M., M. J. Fouch, D. A. Wiens, and M. S. Boettcher (1998). Anisotropy and flow in Pacific subduction zone back-arcs. *Pure Appl. Geophys.*, *151*, 463–475.

Fischer, K. M. and D. A. Wiens (1996). The depth distribution of mantle anisotropy beneath the Tonga subduction zone. *Earth Planet. Sci. Lett.*, *142*, 253–260.

Fleitout, L. and C. Froidevaux (1982). Tectonics and topography for a lithosphere containing density heterogeneities. *Tectonics*, *1*, 21–56.

Fleitout, L. and C. Froidevaux (1983). Tectonic stresses in the lithosphere. *Tectonics*, *2*, 315–324.

Flesch, L. M., W. E. Holt, A. J. Haines, and S.-T. Bingmin (2000). Dynamics of the Pacific-North American plate boundary in the western United States. *Science*, *287*, 834–836.

Fornberg, B. (1996). *A practical guide to pseudospectral methods*. Cambridge University Press, Cambridge UK.

Forsyth, D. and S. Uyeda (1975). On the relative importance of the driving forces of plate motion. *Geophys. J. R. Astr. Soc.*, *43*, 163–200.

Forsyth, D. W. (1975). The early structural evolution and anisotropy of the oceanic upper mantle. *Geophys. J. R. Astr. Soc.*, *43*, 103–162.

Forte, A. M., A. M. Dziewonski, and R. J. O'Connell (1995). Continent–ocean chemical heterogeneity in the mantle based on seismic tomography. *Science*, *268*, 386–388.

Forte, A. M. and J. X. Mitrovica (2001). Deep-mantle high-viscosity flow and thermochemical structure inferred from seismic and geodynamic data. *Nature*, *410*, 1049–1056.

Forte, A. M. and W. R. Peltier (1987). Plate tectonics and aspherical earth structure: the importance of poloidal-toroidal coupling. *J. Geophys. Res.*, *92*, 3645–3679.

Forte, A. M., W. R. Peltier, and A. M. Dziewonski (1991). Inferences of mantle viscosity from tectonic plate velocities. *Geophys. Res. Lett.*, *18*, 1747–1750.

Fouch, M. J. and K. M. Fischer (1996). Mantle anisotropy beneath Northwest Pacific subduction zones. *J. Geophys. Res.*, *101*, 15,987–16,002.

Fouch, M. J. and K. M. Fischer (1998). Shear wave anisotropy in the Mariana subduction zone. *Geophys. Res. Lett.*, *25*, 1221–1224.

Frepoli, A., G. Selvaggi, C. Chiarabba, and A. Amato (1996). State of stress of the Southern Tyrrhenian subduction zone from fault-plane solutions. *Geophys. J. Int.*, *126*, 555–578.

Funiciello, F., C. Faccenna, D. Giardini, and K. Regenauer-Lieb (2002). Dynamics of retreating slabs (part 2): insights from 3D laboratory experiments. *J. Geophys. Res.*, *submitted*.

Furlong, K. P., D. S. Chapman, and P. W. Alfeld (1982). Thermal modeling of the geometry of subduction with implications for the tectonics of the overriding plate. *J. Geophys. Res.*, *87*, 1786–1802.

Gable, C. W. (1989). *Numerical Models of Plate Tectonics and Mantle Convection in Three Dimensions*. Ph.D. thesis, Harvard University, Cambridge MA.

Gable, C. W., R. J. O'Connell, and B. J. Travis (1991). Convection in three dimensions with surface plates: generation of toroidal flow. *J. Geophys. Res.*, *96*, 8391–8405.

Gaherty, J. B. and B. H. Hager (1994). Compositional vs. thermal buoyancy and the evolution of subducted lithosphere. *Geophys. Res. Lett.*, *21*, 141–144.

Garfunkel, Z., C. A. Anderson, and G. Schubert (1986). Mantle circulation and the lateral migration of subducted slabs. *J. Geophys. Res.*, *91*, 7205–7223.

Giardini, D. and M. Velonà (1988). La sismicita profonda del Mar Tirreno. Deep seismicity of the Tyrrhenian Sea. *Mem. Soc. Geol. It.*, *41*, 1079–1087.

Giardini, D. and J. H. Woodhouse (1984). Deep seismicity and modes of deformation in Tonga subduction zone. *Nature*, *307*, 505–509.

Giardini, D. and J. H. Woodhouse (1986). Horizontal shear flow in the mantle beneath the Tonga arc. *Nature*, *319*, 551–555.

Giunchi, C., R. Sabadini, E. Boschi, and P. Gasperini (1996). Dynamic models of subduction: geophysical and geological evidence in the Tyrrhenian sea. *Geophys. J. Int.*, *126*, 555–578.

Goetze, C. and D. L. Kohlstedt (1973). Laboratory study of dislocation climb and diffusion in olivine. *J. Geophys. Res.*, *78*, 5961–5971.

Gordon, R. G., A. Cox, and C. E. Harter (1978). Absolute motion of an individual plate estimated from its ridge and trench boundaries. *Nature*, *274*, 752–755.

Gordon, R. G. and D. M. Jurdy (1986). Cenozoic global plate motions. *J. Geophys. Res.*, *91*, 12,389–12,406.

Gorini, C., A. Mauffret, P. Guennoc, and A. Le Marrec (1994). Structure of the gulf of Lions (Northwestern Mediterranean Sea): a review. In: *Hydrocarbon and Petroleum Geology of France*, ed. A. Mascle, vol. 4 of *Europ. Assoc. Petrol. Geol.*, pp. 223–243. Springer, New York.

Gouillou-Frottier, L., J. Buttles, and P. Olson (1995). Laboratory experiments on the structure of subducted lithosphere. *Earth Planet. Sci. Lett.*, *133*, 19–34.

Grand, S. P. (1994). Mantle shear structure beneath the Americas and surrounding oceans. *J. Geophys. Res.*, *99*, 11,591–11,621.

Grand, S. P., R. D. van der Hilst, and S. Widiyantoro (1997). Global seismic tomography; a snapshot of convection in the Earth. *GSA Today*, *7*, 1–7.

Griffiths, R. W., R. I. Hackney, and R. D. van der Hilst (1995). A laboratory investigation of effects of trench migration on the descent of subducted slabs. *Earth Planet. Sci. Lett.*, *133*, 1–17.

Gripp, A. E. and R. G. Gordon (1990). Current plate velocities relative to the hotspots incorporating the NUVEL-1 global plate motion model. *Geophys. Res. Lett.*, *17*, 1109–1112.

Gu, Y. J., A. M. Dziewonski, W.-j. Su, and G. Ekström (2001). Models of the mantle shear velocity and discontinuities in the pattern of lateral heterogeneities. *J. Geophys. Res.*, *106*, 11,169–11,199.

Gudmundsson, O. and M. Sambridge (1998). A regionalized upper mantle (RUM) seismic model. *J. Geophys. Res.*, *103*, 7121–7136.

Gueguen, E., C. Doglioni, and M. Fernandez (1998). On the post-25 Ma geodynamic evolution of the western Mediterranean. *Tectonophysics*, *298*, 259–269.

Guieu, G. and J. Roussel (1990). Arguments for the pre-rift uplift and rift propagation in the Ligurian-Provençal basin (northwestern Mediterranean) in the light of Pyrenean Provençal orogeny. *Tectonics*, *9*, 1113–1142.

Gurnis, M. (1992). Rapid continental subsidence following the initiation and evolution of subduction. *Science*, *255*, 1556–1558.

Gurnis, M. and B. H. Hager (1988). Controls of the structure of subducted slabs. *Nature*, *335*, 317–321.

Guynn, J. H. and C. R. Lithgow-Bertelloni (2001). Modeling mantle contributions to the global lithospheric stress field (abstract). *EOS Trans. AGU*, *82* (47), T12C–0922.

Hager, B. H. (1978). Oceanic plate motions driven by lithospheric thickening and subducted slabs. *Nature*, *276*, 156–159.

Hager, B. H. (1984). Subducted slabs and the geoid: constraints on mantle rheology and flow. *J. Geophys. Res.*, *89*, 6003–6015.

Hager, B. H. and R. W. Clayton (1989). Constraints on the structure of mantle convection using seismic observations, flow models, and the geoid. In: *Mantle convection; plate tectonics and global dynamics*, ed. W. R. Peltier, vol. 4 of *The Fluid Mechanics of Astrophysics and Geophysics*, pp. 657–763. Gordon and Breach Science Publishers, New York, NY.

Hager, B. H., R. W. Clayton, M. A. Richards, R. P. Comer, and A. M. Dziewonski (1985). Lower mantle heterogeneity, dynamic topography and the geoid. *Nature*, *313*, 541–545.

Hager, B. H. and R. J. O'Connell (1978). Subduction zone dip angles and flow derived by plate motion. *Tectonophysics*, *50*, 111–133.

Hager, B. H. and R. J. O'Connell (1979). Kinematic models of large-scale flow in the Earth's mantle. *J. Geophys. Res.*, *84*, 1031–1048.

Hager, B. H. and R. J. O'Connell (1981). A simple global model of plate dynamics and mantle convection. *J. Geophys. Res.*, *86*, 4843–4867.

Hager, B. H., R. J. O'Connell, and A. Raefsky (1983). Subduction, back-arc spreading and global mantle flow. *Tectonophysics*, *99*, 165–189.

Hales, A. L. (1969). Gravitational sliding and continental drift. *Earth Planet. Sci. Lett.*, *6*, 31–34.

Hall, C. E., K. M. Fischer, and E. M. Parmentier (2000). The influence of plate motions on three-dimensional back arc mantle flow and shear wave splitting. *J. Geophys. Res.*, *105*, 28,009–28,033.

Harper, J. F. (1975). On the driving forces of plate tectonics. *Geophys. J. R. Astr. Soc.*, *40*, 465–474.

Hassani, R., D. Jongmans, and J. Chéry (1997). Study of plate deformation and stress in subduction processes using two-dimensional numerical models. *J. Geophys. Res.*, *102*, 17,951–17,965.

Hatzfeld, D., E. Karagianni, I. Kassaras, A. Kiratzi, E. Louvari, H. Lyon-Caen, K. Makropoulos, P. Papadimitriou, G. Bock, and K. Priestley (2001). Shear wave anisotropy in the upper mantle beneath the Aegean related to internal deformation. *J. Geophys. Res.*, *106*, 30,737.

Hess, H. H. (1964). Seismic anisotropy of the uppermost mantle under oceans. *Nature*, *203*, 629–631.

Holt, W. E. (2000). Correlated crust and mantle strain fields in Tibet. *Geology*, *28*, 67–70.

Houseman, G. A. and D. Gubbins (1997). Deformation of subducted oceanic lithosphere. *Geophys. J. Int.*, *131*, 535–551.

Hsui, A. T. (1988). Application of fluid mechanic principles to the study of trench back-arc systems. *Pure Appl. Geophys.*, *128*, 661–681.

Inoue, H. Y., Y. Fukao, K. Tanabe, and Y. Ogata (1990). Whole mantle P wave travel time tomography. *Phys. Earth Planet. Inter.*, *59*, 294–328.

Isacks, B. and M. Barazangi (1977). Geometry of Benioff zones: lateral segmentations and downward bending of subducted lithosphere. In: *Island arcs, Deep Sea Trenches, and Back-Arc Basins*, eds. M. Talwani and W. C. Pitman III, vol. 1 of *Maurice Ewing*, pp. 99–114. AGU, Washington DC.

Isacks, B. and P. Molnar (1971). Distribution of stresses in the descending lithosphere from a global survey of focal-mechanism solutions of mantle earthquakes. *Rev. Geophys. Space Phys.*, *9*, 103–175.

Isacks, B. L., J. Oliver, and L. R. Sykes (1968). Seismology and the new global tectonics. *J. Geophys. Res.*, *73*, 5855–5899.

Ishii, M. and J. Tromp (2001). Even-degree lateral variations in the earth's mantle constrained by free oscillations and the free-air gravity anomaly. *Geophys. J. Int.*, *145*, 77–96.

Jacob, K. H., K. Nakamura, and J. N. Davies (1976). Trench-volcano gap along the Alaska-Aleutian trench: facts and speculations on the role of terrigenous sediments for subduction. In: *Island arcs, deep sea trenches and back-arc basins*, eds. M. Talwani and W. C. Pitman III, pp. 243–259. American Geophysical Union, Washington DC.

Jacoby, W. R. and H. Schmeling (1981). Convection experiments and driving mechanism. *Geol. Rundschau*, *24*, 217–284.

Jarrard, R. D. (1986). Relations among subduction parameters. *Rev. Geophys.*, *24*, 217–284.

Jarvis, G. T. and W. R. Peltier (1989). Convection models and geophysical observations. In: *Mantle convection; plate tectonics and global dynamics*, ed. W. R. Peltier, vol. 4 of *The Fluid Mechanics of Astrophysics and Geophysics*, pp. 479–593. Gordon and Breach Science Publishers, New York, NY.

Ji, S., X. Zhao, and D. Francis (1994). Calibration of shear-wave splitting in the subcontinental upper mantle beneath active orogenic belts using ultramafic xenoliths from the Canadian Cordillera and Alaska. *Tectonophysics*, *239*, 1–27.

Jolivet, L. and C. Faccenna (2000). Mediterranean extension and the Africa-Eurasia collision. *Tectonics*, *6*, 1095–1107.

Jolivet, L., C. Faccenna, N. d'Agostino, M. Fournier, and D. Worrall (1999). The kinematics of back-arc basins, examples from the Tyrrhenian, Aegean and Japan Seas. In: *The Mediterranean Basins: Tertiary extension within the Alpine orogen*, eds. C. Mac Niocaill and P. D. Ryan, vol. 164 of *Geol. Soc. London Spec. Publ.*, pp. 21–53. Geological Society of London, London.

Jolivet, L., C. Faccenna, B. Goffè, M. Mattei, F. Rossetti, C. Brunet, F. Storti, R. Funiciello, J. P. Cadet, N. d'Agostino, and T. Parra (1998). Midcrustal shear zones in postorogenic extension: Example from the northern Tyrrhenian sea. *J. Geophys. Res.*, *103*, 12,123–12,161.

Jordan, T. H. (1978). Composition and development of the continental tectosphere. *Nature*, *274*, 544–548.

Jung, H. and S.-i. Karato (2001). Water-induced fabric transitions in olivine. *Science*, *293*, 1460–1463.

Kameyama, M., D. A. Yuen, and H. Hiromi (1997). The interaction of viscous heating with grain-size dependent rheology in the formation of localized slip zones. *Geophys. Res. Lett.*, *24*, 2523–2526.

Kaminski, E. and N. M. Ribe (2001). A kinematic model for for recrystallization and texture development in olivine polycrystals. *Earth Planet. Sci. Lett.*, *189*, 253–267.

Kaminski, E. and N. M. Ribe (2002). Time scales for the evolution of seismic anisotropy in mantle flow. *Geochemistry, Geophysics, Geosystems*, *in press*.

Kárason, H. and R. D. van der Hilst (2000). Constraints on mantle convection from seismic tomography. In: *The History and Dynamics of Global Plate Motion*, eds. M. R. Richard, R. G. Gordon, and R. D. van der Hilst, vol.

121 of *Geophysical Monograph*, pp. 277–288. American Geophysical Union, Washington DC.

Kárason, H. and R. D. van der Hilst (2001). Tomographic imaging of the lowermost mantle with differential times of refracted and diffracted core phases (PKP, Pdiff). *J. Geophys. Res.*, *106*, 6569–6588.

Karato, S.-i. (1993). Importance of anelasticity in the interpretation of seismic tomography. *Geophys. Res. Lett.*, *20*, 1623–1626.

Karato, S.-i. and B. B. Karki (2001). Origin of lateral variation of seismic wave velocities and density in the deep mantle. *J. Geophys. Res.*, *106*, 21,771–21,783.

Karato, S.-i., M. R. Riedel, and D. A. Yuen (2001). Rheological structure and deformation of subducted slabs in the mantle transition zone: implications for mantle circulation and deep earthquakes. *Phys. Earth Planet. Inter.*, *127*, 83–108.

Karpychev, M. and L. Fleitout (1996). Simple considerations on forces driving plate motion and on the plate-tectonic contribution to the long-wavelength geoid. *Geophys. J. Int.*, *127*, 268–282.

Karpychev, M. and L. Fleitout (2000). Long-wavelength geoid: the effect of continental roots and lithosphere thickness variations. *Geophys. J. Int.*, *143*, 945–963.

Kastens, K. A. and J. Mascle (1990). The geological evolution of the Tyrrhenian sea: an introduction to the scientific results of ODP Leg 107. In: *Proc. ODP, Scientific Results*, eds. K. A. Kastens and J. Mascle, vol. 107, pp. 3–26. ODP Program.

Kaus, B. and Y. Y. Podlachikov (2001). Forward and reverse modeling of the three-dimensional Rayleigh-Taylor instability. *Geophys. Res. Lett.*, *28*, 1095–1098.

Keith, S. B. (1978). Paleosubduction geometries inferred from Cretaceous and Tertiary magmatic patterns in southwestern North America. *Geology*, *6*, 516–521.

Kellogg, J. B. and R. J. O'Connell (1998). Toroidal motion and mixing in three dimensions (abstract). *EOS Trans. AGU*, *79*, S334.

Kellogg, L. H., B. H. Hager, and R. D. van der Hilst (1999). Compositional stratification in the deep mantle. *Science*, *283*, 1881–1884.

Kendall, J.-M. (1994). Teleseismic arrivals at a mid-ocean ridge: effects of mantle melt and anisotropy. *Geophys. Res. Lett.*, *21*, 301–304.

Kennett, B. L. N., E. R. Engdahl, and R. Buland (1995). Constraints on seismic velocities in the earth from travel times. *Geophys. J. Int.*, *122*, 108–124.

Kennett, B. L. N., S. Widiyantoro, and R. D. van der Hilst (1998). Joint seismic tomography for bulk sound and shear wave speed in the Earth's mantle. *J. Geophys. Res.*, *103*, 12,469–12,493.

Kincaid, C. and P. Olson (1987). An experimental study of subduction and slab migration. *J. Geophys. Res.*, *92*, 13,832–13,840.

King, S. D. (2001). Subduction: Observations and geodynamic models. *Phys. Earth Planet. Inter.*, *127*, 9–24.

King, S. D., C. W. Gable, and S. A. Weinstein (1992). Models of convection-driven tectonic plates: a comparison of methods and results. *Geophys. J. Int.*, *109*, 481–487.

King, S. D. and B. H. Hager (1990). The relationship between plate velocity and trench viscosity in newtonian and power-law subduction calculations. *Geophys. Res. Lett.*, *17*, 2409–2412.

King, S. D. and B. H. Hager (1994). Subducted slabs and the geoid 1. Numerical experiments with temperature-dependent viscosity. *J. Geophys. Res.*, *99*, 19,843–19,852.

King, S. D. and J. Ita (1995). Effect of slab rheology on mass transport across a phase transition boundary. *J. Geophys. Res.*, *100*, 20,211–2022.

King, S. D., D. A. Raefsky, and B. H. Hager (1990). ConMan: vectorizing a finite element code for incompressible two-dimensional convection in the Earth's mantle. *Phys. Earth Planet. Inter.*, *59*, 195–207.

Klosko, E. R., R. M. Russo, E. A. Okal, and W. P. Richardson (2001). Evidence for a rheologically strong chemical mantle root beneath the Ontong-Java Plateau. *Earth Planet. Sci. Lett.*, *186*, 347–361.

Knott, S. D. (1987). The Liguride Complex of southern Italy – A Cretaceous to Paleogene accretionary wedge. *Tectonophysics*, *142*, 217–226.

Kostrov, B. V. (1974). Seismic moment and energy of earthquakes and seismic flow of rock. *Izv., Acad. Sci., USSR, Phys. Solid Earth (Engl. Translation)*, *1*, 23–40.

Kumazawa, M. and O. L. Anderson (1969). Elastic moduli, pressure derivatives, and temperature derivatives of single-crystal olivine and single-crystal forsterite. *J. Geophys. Res.*, *74*, 5961–5972.

Lahondère, D. and C. Guerrot (1997). Datation Sm-Nd du métamorphisme éclogitique en Corse Alpine: un argument pour l'existence au Crétacé supériuer d'une zone de subduction active localisée sous le bloc Corse-

Sarde. *Geol. France*, *3*, 3–11.

Lallemand, S. (1995). High rates of arc consumption by subduction processes: some consequences. *Geology*, *23*, 551–554.

Laske, G. and G. Masters (1998). Surface-wave polarization data and global anisotropic structure. *Geophys. J. Int.*, *132*, 508–520.

Lenardic, A. and W. M. Kaula (1993). A numerical treatment of geodynamic viscous flow problems involving the advection of material interfaces. *J. Geophys. Res.*, *98*, 8243–8260.

Lister, C. R. B. (1975). Gravitational drive on oceanic plates caused by thermal contraction. *Nature*, *257*, 663–665.

Lithgow-Bertelloni, C. and M. A. Richards (1995). Cenozoic plate driving forces. *Geophys. Res. Lett.*, *22*, 1317–1320.

Lithgow-Bertelloni, C. and M. A. Richards (1998). The dynamics of Cenozoic and Mesozoic plate motions. *Rev. of Geophys.*, *36*, 27–78.

Lithgow-Bertelloni, C., M. A. Richards, Y. Ricard, R. J. O'Connell, and D. C. Engebretson (1993). Toroidal-poloidal partitioning of plate motions since 120 Ma. *Geophys. Res. Lett.*, *20*, 375–378.

Lithgow-Bertelloni, C. and P. G. Silver (1998). Dynamic topography, plate driving forces and the African super-swell. *Nature*, *395*, 269–272.

Lliboutry, L. A. (1969). Sea floor spreading, continental drift and lithosphere sinking with an asthenosphere at melting point. *J. Geophys. Res.*, *74*, 6525–6540.

Lonergan, L. and N. White (1997). Origin of the Betic-Rif mountain belt. *Tectonics*, *16*, 504–522.

Love, A. E. H. (1927). *A Treatise on the Mathematical Theory of Elasticity*. Cambridge University Press, Cambridge. Reprinted in 1944 by Dover Publications, New York.

Lucente, F. P., C. Ciarabba, G. B. Cimini, and D. Giardini (1999). Tomographic constraints on the geodynamic evolution of the Italian region. *J. Geophys. Res.*, *104*, 20,307–20,327.

Luyendyk, B. P. (1970). Dip of downgoing lithospheric plates beneath island arcs. *Geol. Soc. Am. Bull.*, *81*, 3411–3416.

Mainprice, D., G. Barruol, and W. Ben Ismail (2000). The seimic anisotropy of the Earth's mantle: From single crystal to polycrystal. In: *Earth's deep interior. Mineral physics and tomography from the atomic to the global scale*, eds. S.-i. Karato, A. M. Forte, R. C. Liebermann, G. Masters, and L. Stixrude, vol. 117 of *Geophysical Monograph*, pp. 237–264. American Geophysical Union, Washington DC.

Malinverno, A. and W. Ryan (1986). Extension in the Tyrrhenian sea and shortening in the Apennines as result of arc migration driven by sinking of the lithosphere. *Tectonics*, *5*, 227–245.

Marroni, M., S. Monechi, N. Perilli, G. Principi, and B. Treves (1992). Late Cretaceous flysch deposits of the Northern Apennines Italy: age of inception of orogenesis-controlled sedimentation. *Cretaceous Res.*, *13*, 487–504.

Martinod, J. and P. Davy (1992). Periodic instabilities during compression or extension of the lithosphere. 1. Deformation modes from an analytical perturbation method. *J. Geophys. Res.*, *97*, 1999–2014.

Martinod, J. and P. Davy (1994). Periodic instabilities during compression or extension of the lithosphere. 2. Analogue experiments. *J. Geophys. Res.*, *99*, 12,057–12,069.

Masters, G., H. Bolton, and G. Laske (1999). Joint seismic tomography for P and S velocities: How pervasive are chemical anomalies in the mantle? (abstract). *EOS Trans. AGU*, *80*, S14.

Masters, G., T. H. Jordan, P. G. Silver, and F. Gilbert (1982). Aspherical Earth structure from fundamental spheroidal-mode data. *Nature*, *298*, 609–613.

Masters, G., G. Laske, H. Bolton, and A. M. Dziewonski (2000). The relative behavior of shear velocity, bulk sound speed, and compressional velocity in the mantle: implications for chemical and thermal structure. In: *Earth's deep interior. Mineral physics and tomography from the atomic to the global scale*, eds. S.-i. Karato, A. M. Forte, R. C. Liebermann, G. Masters, and L. Stixrude, vol. 117 of *Geophysical Monograph*, pp. 63–87. American Geophysical Union, Washington DC.

Mauffret, A. and I. Contrucci (1999). Crustal structure of the North Tyrrhenian Sea: First result of the multi-channel seismic LISA cruise. In: *The Mediterranean basins: Tertiary extension within the Alpine Orogen*, eds. B. Durand, A. Mascle, L. Jolivet, F. Horvàth, and M. Séranne, vol. 156 of *Geol. Soc. Lond. Spec. Pubs*, pp. 169–193. Geological Society of London, London.

Mauffret, A., G. Pascal, A. Maillard, and C. Gorini (1995). Tectonics and deep structure of the north-western Mediterranean basin. *Mar. Preto. Geol.*, *12*, 645–666.

McKenzie, D. and J. Jackson (1983). The relationship between strain rates, crustal thickening, paleomagnetism,

finite strain and fault movements within a deforming zone. *Earth Planet. Sci. Lett.*, *65*, 182–202.
McKenzie, D. P. (1967). Some remarks on heat flow and gravity anomalies. *J. Geophys. Res.*, *72*, 6261–6273.
McKenzie, D. P. (1968). Speculations on the consequences and causes of plate motions. *Geophys. J. R. Astr. Soc.*, *18*, 1–32.
McKenzie, D. P. (1977). The initiation of trenches: a finite amplitude instability. In: *Island Arcs, Deep Sea Trenches and Back-Arc basins*, eds. M. Talwani and W. C. Pitman III, vol. 1 of *Maurice Ewing*, pp. 57–61. AGU, Washington DC.
McKenzie, D. P. (1979). Finite deformation during fluid flow. *Geophys. J. R. Astr. Soc.*, *58*, 689–715.
Mégnin, C. and B. Romanowicz (1999). The effects of the theoretical formalism and data selection on mantle models derived from waveform tomography. *Geophys. J. Int.*, *138*, 366–380.
Mégnin, C. and B. Romanowicz (2000). The shear velocity structure of the mantle from the inversion of body, surface, and higher modes waveforms. *Geophys. J. Int.*, *143*, 709–728.
Mitrovica, J. X., C. Beaumont, and G. T. Jarvis (1989). Tilting of continental interiors by the dynamical effects of subduction. *Tectonics*, *8*, 1079–1094.
Mitrovica, J. X. and A. M. Forte (1997). Radial profile of mantle viscosity: results from the joint inversion of convection and postglacial rebound observables. *J. Geophys. Res.*, *102*, 2751–2769.
Mitrovica, J. X. and G. T. Jarvis (1985). Surface deflections due to transient subduction in a convecting mantle. *Tectonophysics*, *120*, 211–237.
Molnar, P., H. J. Anderson, E. Audoine, D. Eberhart-Phillips, K. R. Gledhill, E. R. Klosko, T. V. McEvilly, D. Okaya, M. K. Savage, T. Stern, and F. T. Wu (1999). Continuous deformation versus faulting through the continental lithosphere of New Zealand. *Science*, *286*, 516–519.
Molnar, P. and T. Atwater (1978). Interarc spreading and cordillera tectonics as alternates related to the age of subducted oceanic lithosphere. *Earth Planet. Sci. Lett.*, *41*, 330–340.
Monaco, C. and L. Tortorici (1995). Tectonic role of ophiolite-bearing terranes in the development of the Southern Apennines orogenic belt. *Terra Nova*, *7*, 153–160.
Monié, P., L. Jolivet, C. Brunet, R. L. Torres-Roldan, R. Caby, B. Goffé, and R. Dubois (1996). Cooling paths of metamorphic rocks in the western Mediterranean region and tectonic implications. In: *The Mediterranean basins: Tertiary extension within the alpine orogen. An international workshop. Abstracts*. Université Cergy-Pentoise, Cergy-Pentoise.
Montagner, J.-P. (1994). What can seismology tell us about mantle convection? *Rev. Geophys,*, *32*, 115–137.
Montagner, J.-P. (1998). Where can seismic anisotropy be detected in the Earth's mantle? in boundary layers. *Pure Appl. Geophys.*, *151*, 223–256.
Montagner, J.-P., D.-A. Griot-Pommera, and J. Laveé (2000). How to relate body wave and surface wave anisotropy? *J. Geophys. Res.*, *105*, 19,015–19,027.
Montagner, J.-P. and L. Guillot (2000). Seismic anisotropy in the Earth's mantle. In: *Problems in Geophysics for the New Millenium*, eds. E. Boschi, G. Ekström, and A. Morelli, pp. 217–253. Istituto Nazionale di Geofisica e Vulcanologia, Editrice Compositori, Bologna, Italy.
Montagner, J.-P. and H.-C. Nataf (1986). A simple method for inverting the azimuthal anisotropy of surface waves. *J. Geophys. Res.*, *91*, 511–520.
Montagner, J.-P. and T. Tanimoto (1991). Global upper mantle tomography of seismic velocities and anisotropies. *J. Geophys. Res.*, *96*, 20,337–20,351.
Mooney, W. D., G. Laske, and G. Masters (1998). CRUST 5.1: a global crustal model at 5 degrees $\times$ 5 degrees. *J. Geophys. Res.*, *103*, 727–747.
Moreau, M. G., J. Y. Berthou, and J.-A. Malod (1997). New paleomagnetic Mesozoic data from the Algarve (Portugal): fast rotation of Iberia between the Hauterivian and the Aptian. *Earth Planet. Sci. Lett.*, *146*, 686–701.
Moresi, L. and M. Gurnis (1996). Constraints on the lateral strength of slabs from three-dimensional dynamic flow models. *Earth Planet. Sci. Lett.*, *138*, 15–28.
Moresi, L. and V. Solomatov (1998). Mantle convection with a brittle lithosphere: thoughts on the global tectonic styles of the Earth and Venus. *Geophys. J. Int.*, *133*, 669–682.
Moretta, A. M. and R. Sabadini (1995). The styles of Tyrrhenian subduction. *Geophys. Res. Lett.*, *22*, 747–750.
Müller, D., W. R. Roest, J.-Y. Royer, L. M. Gahagan, and J. G. Sclater (1997). Digital isochrons of the world's ocean floor. *J. Geophys. Res.*, *102*, 3211–3214.
Nataf, H.-C. and Y. Ricard (1996). 3SMAC: an *a priori* tomographic model of the upper mantle based on geo-

physical modeling. *Phys. Earth Planet. Inter.*, *95*, 101–122.
Nelder, J. A. and R. Mead (1965). A simplex method for function minimization. *Computer Journal*, *7*, 308–313.
Nicolas, A., F. Boudier, and A. M. Bouillier (1973). Mechanisms of flow in naturally and experimentally deformed peridotites. *Am. J. Seis.*, *273*, 853–876.
Nicolas, A. and N. I. Christensen (1987). Formation of anisotropy in upper mantle peridotites; a review. In: *Composition, structure and dynamics of the lithosphere-asthenosphere system*, eds. K. Fuchs and C. Froidevaux, vol. 16 of *Geodynamics*, pp. 111–123. American Geophysical Union, Washington DC.
Nishimura, C. E. and D. W. Forsyth (1989). The anisotropic structure of the upper mantle in the Pacific. *Geophys. J.*, *96*, 203–229.
NOAA (1988). *Data Announcement 88-MGG-02, Digital relief of the Surface of the Earth*. National Geophysical Data Center, Boulder, Colorado.
O'Connell, R. J., C. W. Gable, and B. H. Hager (1991). Toroidal-poloidal partitioning of lithospheric plate motions. In: *Glacial Isostasy, Sea-Level and Mantle Rheology*, ed. R. Sabadini, pp. 535–551. Kluwer Academic Publishers, Amsterdam.
Oganov, A. R., J. P. Brodholt, and G. D. Price (2001). The elastic constants of $MgSiO_3$ perovskite at pressures and temperatures of the Earth's mantle. *Nature*, *411*, 934–937.
Olbertz, D., M. J. R. Wortel, and U. Hansen (1997). Trench migration and subduction zone geometry. *Geophys. Res. Lett.*, *24*, 221–224.
Olivet, J.-L. (1996). La cinematique de la plaues Iberique. *Bull. Centres Recherches Expl.-Prod. Elf Aquitane*, *20*, 131–195.
Oxburgh, E. R. and D. L. Turcotte (1976). The physico-chemical behaviour of the descending lithosphere. *Tectonophysics*, *32*, 107–128.
Pacheco, J. F., L. R. Sykes, and C. H. Scholz (1993). Nature of seismic coupling along simple plate boundaries of the subduction type. *J. Geophys. Res.*, *98*, 14,133–14,159.
Panasyuk, S. V. and B. H. Hager (1998). A model of transformational superplasticity of the upper mantle. *Geophys. J. Int.*, *133*, 741–755.
Panasyuk, S. V. and B. H. Hager (2000). Inversion for mantle viscosity profiles constrained by dynamic topography and the geoid, and their estimated errors. *Geophys. J. Int.*, *143*, 821–836.
Panasyuk, S. V., B. H. Hager, and A. M. Forte (1996). Understanding the effects of mantle compressibility on geoid kernels. *Geophys. J. Int.*, *124*, 121–133.
Pari, G. and W. R. Peltier (2000). Subcontinental mantle dynamics: a further analysis based on the joint constraints of dynamic surface topography and free-air gravity. *J. Geophys. Res.*, *105*, 5635.
Parker, R. L. (1994). *Geophysical Inverse Theory*. Princeton University Press, Princeton, New Jersey.
Parsons, B. and J. G. Sclater (1977). An analysis of the variation of ocean floor bathymetry and heat flow with age. *J. Geophys. Res.*, *82*, 803–827.
Patacca, E., R. Sartori, and P. Scadone (1990). Tyrrhenian Basin and Apenninic arcs; kinematic relations since late Tortonian times. *Memorie della Societa Geologica Italiana*, *45*, 425–451.
Peacock, S. (1996). Thermal and petrological structure of subduction zones. In: *Subduction: Top to Bottom*, eds. G. E. Beobout, D. Scholl, S. Kirby, and J. Platt, vol. 96 of *Geophysical Monograph*, pp. 119–135. American Geophysical Union.
Peselnick, L. and A. Nicolas (1978). Seismic anisotropy in an ophiolite peridotite. Application to oceanic upper mantle. *Geophys. Res. Lett.*, *83*, 1227–1235.
Piromallo, C. and A. Morelli (1997). Imaging the Mediterranean upper mantle by P-wave travel time tomography. *Annali di Geofisica*, *4*, 963–979.
Polet, J. and H. Kanamori (2002). Anisotropy beneath California: shear wave splitting measurements using a dense broadband array. *Geophys. J. Int.*, *149*, 31–327.
Polet, J., P. G. Silver, S. Beck, T. Wallace, G. Zandt, S. Ruppert, R. Kind, and A. Rudloff (2000). Shear wave anisotropy beneath the andes from the BANJO, SEDA, and PISCO experiments. *J. Geophys. Res.*, *105*, 6287–6304.
Press, W. H., S. A. Teukolsky, W. T. Vetterling, and B. P. Flannery (1993). *Numerical Recipes in C: The Art of Scientific Computing*. Cambridge University Press, Cambridge, 2nd edn.
Principi, G. and B. Treves (1984). Il sistema corso-appennino come prisma d'accrezione. Riflessi sul problema generale del limite Alpi-Appennino. *Mem. Soc. Geol. It.*, *28*, 529–576.
Puster, P. and T. H. Jordan (1997). How stratified is mantle convection? *J. Geophys. Res.*, *102*, 7625–7646.

Pysklywec, R. N. and J. X. Mitrovica (1997). Mantle avalanches and the dynamic topography of continents. *Earth Planet. Sci. Lett.*, *148*, 447–455.

Ranalli, G. (1995). *Rheology of the Earth*. Chapman & Hall, London, 2nd edn.

Ranalli, G. and D. C. Murphy (1986). Rheological stratification of the lithosphere. *Tectonophysics*, *132*, 291–295.

Ray, T. R. and D. L. Anderson (1994). Spherical disharmonics in the Earth sciences and the spatial solution: Ridges, hotspots, slabs, geochemistry and tomography correlations. *J. Geophys. Res.*, *99*, 9605–9614.

Regenauer-Lieb, K., D. A. Yuen, and J. Branlund (2001). The initiation of subduction; criticality by addition of water? *Science*, *294*, 578–580.

Ribe, N. M. (1989). Seismic anisotropy and mantle flow. *J. Geophys. Res.*, *94*, 4213–4223.

Ribe, N. M. (1992). On the relation between seismic anisotropy and finite strain. *J. Geophys. Res.*, *97*, 8737–8747.

Ribe, N. M. and Y. Yu (1991). A theory for plastic deformation and textural evolution of olivine polycrystals. *J. Geophys. Res.*, *96*, 8325–8335.

Ricard, Y., C. Doglioni, and R. Sabadini (1991). Differential rotation between lithosphere and mantle: A consequence of lateral mantle viscosity variations. *J. Geophys. Res.*, *96*, 8407–8415.

Ricard, Y., M. A. Richards, C. Lithgow-Bertelloni, and Y. Le Stunff (1993). A geodynamic model of mantle density heterogeneity. *J. Geophys. Res.*, *98*, 21,895–21,909.

Ricard, Y. and C. Vigny (1989). Mantle dynamics with induced plate tectonics. *J. Geophys. Res.*, *94*, 17,543–17,559.

Richards, M. A. and B. H. Hager (1989). Effects of lateral viscosity variations on long-wavelength geoid anomalies and topography. *J. Geophys. Res.*, *94*, 10,299–10,313.

Richards, M. A., B. H. Hager, and N. H. Sleep (1988). Dynamically supported geoid highs over hotspots: Observation and theory. *J. Geophys. Res.*, *93*, 7690–7708.

Richardson, R. M. (1992). Ridge forces, absolute plate motions, and the intraplate stress field. *J. Geophys. Res.*, *97*, 11,739–11,748.

Richardson, R. M., S. C. Solomon, and N. H. Sleep (1979). Tectonic stresses in plates. *Rev. Geophys. Space Phys.*, *17*, 981–1019.

Richter, F. M. (1973). Dynamical models for sea floor spreading. *Rev. Geophys. Space Phys.*, *11*, 223–287.

Riedel, M. R. and S.-i. Karato (1997). Grain-size evolution in subducted oceanic lithosphere associated with the olivine-spinel transformation and its effects on rheology. *Earth Planet. Sci. Lett.*, *148*, 27–43.

Ritsema, J. and H. J. van Heijst (2000). Seismic imaging of structural heterogeneity in Earth's mantle: Evidence for large-scale mantle flow. *Sci. Progr.*, *83*, 243–259.

Ritsema, J., H. J. van Heijst, and J. H. Woodhouse (1999). Complex shear wave velocity structure imaged beneath Africa and Iceland. *Science*, *286*, 1925–1928.

Ritzwoller, M. H. and E. M. Lavely (1995). Three dimensional models of the Earth's mantle. *Rev. Geophys. Space Phys.*, *33*, 1–66.

Robertson, G. S. and J. H. Woodhouse (1996). Ratio of relative S to P velocity heterogeneity in the lower mantle. *J. Geophys. Res.*, *101*, 20,041–20,052.

Rodkin, M. V. and A. G. Rodnikov (1996). Origin and structure of back-arc basins: new data and model discussion. *Phys. Earth Planet. Inter.*, *93*, 123–131.

Romanowicz, B. and R. Snieder (1988). A new formalism for the effect of lateral heterogeneity on normal modes and surface waves. II. General anisotropic perturbation. *Geophys. J.*, *93*, 91–99.

Rossetti, R., C. Faccenna, B. Goffé, P. Monié, A. Argentieri, R. Funiciello, and M. Mattei (2001). Alpine structural and metamorphic evolution of the Sila Piccola Massif: Insights for the tectonic evolution of the Calabrian Arc. *Tectonics*, *20*, 112–133.

Royden, L. H. (1993). Evolution of retreating subduction boundaries formed during continental collision. *Tectonics*, *12*, 629–638.

Russo, R. M. and P. G. Silver (1994). Trench-parallel flow beneath the Nazca plate from seismic anisotropy. *Science*, *263*, 1105–1111.

Russo, R. M. and P. G. Silver (1996). Cordillera formation, mantle dynamics, and the Wilson cycle. *Geology*, *24*, 511–514.

Sacks, I. S. (1983). The subduction of young lithosphere. *J. Geophys. Res.*, *88*, 3355–3366.

Saltzer, R. L., J. B. Gaherty, and T. H. Jordan (2000). How are vertical shear wave splitting measurements affected by variations in the orientation of azimuthal anisotropy with depth? *Geophys. J. Int.*, *141*, 374–390.

Saltzer, R. L., R. D. van der Hilst, and H. Kárason (2001). Comparing P and S wave heterogeneity in the mantle.

Geophys. Res. Lett., *28*, 1335–1338.

Sartori, R. (1990). The main results of ODP Leg 107 in the frame of Neogene to recent geology of peri-tyrrhenian areas. In: *Proc. ODP, Scientific Results*, eds. K. A. Kastens and J. Mascle, vol. 107, pp. 715–730. ODP Program.

Savage, M. K. (1999). Seismic anisotropy and mantle deformation: What have we learned from shear wave splitting? *Rev. Geophys.*, *37*, 65–106.

Schmid, S. M., O. A. Pfiffner, N. Froitzheim, G. Schönborn, and E. Kissling (1996). Geophysical-geological transect and tectonic evolution of the Swiss-Italian Alps. *Tectonics*, *15*, 1036–1064.

Schöffel, H.-J. and S. Das (1998). Fine details of the Wadati-Benioff zone under Indonesia and its geodynamic implications (abstract). *EOS Trans. AGU*, *79*, F634.

Schöffel, H.-J. and S. Das (1999). Fine details of the Wadati-Benioff zone under Indonesia and its geodynamic implications. *J. Geophys. Res.*, *104*, 13,101–13,114.

Scholz, C. H. and J. Campos (1995). On the mechanism of seismic decoupling and back arc spreading at subduction zones. *J. Geophys. Res.*, *100*, 22,103–22,115.

Schott, B., D. A. Yuen, and H. Schmeling (2000). The significance of shear heating in continental delamination. *Phys. Earth Planet. Inter.*, *118*, 273–290.

Schulte-Pelkum, V., G. Masters, and P. M. Shearer (2001). Upper mantle anistropy from long-period *P* polarization. *J. Geophys. Res.*, *106*, 21,917–21,934.

Schutt, D. and A. Kubo (2001). *Anisotropy Resource Page*. Carnegie Institution of Washington, http://www.ciw.edu/schutt/anisotropy/aniso_source.html.

Selvaggi, G. and A. Amato (1992). Subcrustal earthquakes in the northern Appennines (Italy): evidence for a still active subduction? *Geophys. Res. Lett.*, *19*, 2127–2130.

Seranne, M. (1999). The Gulf of Lyon continental margin (NW Mediterranean) revisited by IBS: an overview. In: *The Mediterranean basins: Tertiary extension within the Alpine Orogen*, eds. B. Durand, L. Mascle, A. Jolivet, F. Horvàth, and M. Séranne, vol. 156 of *Geol. Soc. Lond. Spec. Pubs*, pp. 21–53. Geological Society of London, London.

Serri, D., F. Innocenti, and P. Manetti (1993). Geochemical and petrological evidence of the subduction of deliminated Adriatic continental lithosphere in the genesis of the Neogene-Quaternary magmatism of central Italy. *Tectonophysics*, *223*, 117–147.

Shemenda, A. I. (1993). Subduction of the lithosphere and back arc dynamics: insights from physical modeling. *J. Geophys. Res.*, *98*, 16,167–16,185.

Shenk, V. (1980). U-Pb and Rb-Sr radiometric dates and their correlation with metamorphic events in the granulite facies basement of the Serre, southern Calabria (Italy). *Contrib. Min. Petrol.*, *73*, 23–38.

Silver, P. G. (1996). Seismic anisotropy beneath the continents: probing the depths of geology. *Ann. Rev. Earth Planet. Sci.*, *24*, 385–432.

Silver, P. G. and H. H. Chan (1988). Implications for continental structure and evolution from seismic anisotropy. *Nature*, *335*, 34–39.

Silver, P. G. and W. E. Holt (2002). The mantle flow field beneath Western North America. *Science*, *295*, 1054–1057.

Silver, P. G., R. M. Russo, and C. Lithgow-Bertelloni (1998). Coupling of South American and African plate motion and plate deformation. *Science*, *279*, 60–63.

Silver, P. G. and M. K. Savage (1994). The interpretation of shear wave splitting parameters in the presence of two anisotropic layers. *Geophys. J. Int.*, *119*, 949–963.

Smith, G. P. and G. Ekström (1999). A global study of P_n anisotropy beneath continents. *J. Geophys. Res.*, *104*, 963–980.

Smith, G. P., D. A. Wiens, K. M. Fischer, L. M. Dorman, S. C. Webb, and J. A. Hildebrand (2001). A complex pattern of mantle flow in the Lau backarc. *Science*, *292*, 713–716.

Smith, M. L. and F. A. Dahlen (1973). The azimuthal dependence of Love and Rayleigh wave propagation in a slightly anisotropic medium. *J. Geophys. Res.*, *78*, 3321–3333.

Solomon, S. C. and N. H. Sleep (1974). Some simple physical models for absolute plate motions. *J. Geophys. Res.*, *79*, 2557–2567.

Solomon, S. C., N. H. Sleep, and R. M. Richardson (1975). On the forces driving plate tectonics: inferences from absolute plate velocities and intraplate stress. *Geophys. J. R. Astr. Soc.*, *42*, 769–801.

Spadini, G., S. Cloething, and G. Bertotti (1995). Thermo-mechanical modeling of the Tyrrhenian sea: lithospheric necking and kinematics of rifting. *Tectonics*, *14*, 629–644.

Spakman, W., S. van der Lee, and R. D. van der Hilst (1993). Travel-time tomography of the European-Mediterranean mantle down to 1400 km. *Phys. Earth Planet. Inter.*, *79*, 3–74.

Spence, W. (1987). Slab pull and the seismotectonics of subducting lithosphere. *Rev. of Geophys.*, *25*, 55–69.

Stacey, F. D. (1992). *Physics of the Earth*. Brookfield Press, Kenmore, Australia, 3rd edn.

Steinberger, B. (1996). *Motion of hotspots and changes of the Earth's rotation axis caused by a convecting mantle*. Ph.D. thesis, Harvard University, Cambridge MA.

Steinberger, B. (2000a). Plumes in a convecting mantle: Models and observations for individual hotspots. *J. Geophys. Res.*, *105*, 11,127–11,152.

Steinberger, B. (2000b). Slabs in the lower mantle – results of dynamic modelling compared with tomographic images and the geoid. *Phys. Earth Planet. Inter.*, *118*, 241–257.

Steinberger, B. and R. J. O'Connell (1997). Changes of the earth's rotation axis owing to advection of mantle density heterogeneities. *Nature*, *387*, 169–173.

Steinberger, B. and R. J. O'Connell (1998). Advection of plumes in mantle flow: implications for hotspot motion, mantle viscosity, and plume distribution. *Geophys. J. Int.*, *132*, 412–434.

Steinberger, B., H. Schmeling, and G. Marquart (2001). Large-scale lithospheric stress field and topography induced by global mantle circulation. *Earth Planet. Sci. Lett.*, *186*, 75–91.

Stern, T. A. and W. E. Holt (1994). Platform subsidence behind an active subduction zone. *Nature*, *368*, 233–236.

Stevenson, D. J. and J. S. Turner (1972). Angle of subduction. *Nature*, *270*, 334–336.

Su, W.-j. and A. M. Dziewonski (1991). Predominance of long-wavelength heterogeneity in the mantle. *Nature*, *352*, 121–126.

Su, W.-j. and A. M. Dziewonski (1992). On the scale of mantle heterogeneity. *Phys. Earth Planet. Inter.*, *74*, 29–45.

Su, W.-j. and A. M. Dziewonski (1997). Simultaneous inversion for 3-D variations in shear and bulk velocity in the mantle. *Phys. Earth Planet. Inter.*, *100*, 135–156.

Suhadolc, P. and G. F. Panza (1989). Physical properties of the lithosphere-asthenosphere system in Europe from geophysical data. In: *The Lithosphere in Italy. Advances in Science Research*, eds. A. Boriani, M. Bonafede, G. B. Piccardo, and G. B. Vai, pp. 15–40. Accademia Nazionale dei Lincei, Rome.

Tackley, P. J. (1996). Effects of strongly variable viscosity on three-dimensional compressible convection in planetary mantles. *J. Geophys. Res.*, *101*, 3311–3332.

Tackley, P. J. (2000). Mantle convection and plate tectonics: Toward an integrated physical and chemical theory. *Science*, *288*, 2002–2007.

Tackley, P. J. (2001a). Self-consistent generation of tectonic plates in time-dependent, three-dimensional mantle convection simulations 1. Pseudoplastic yielding. *Geochemistry, Geophysics, Geosystems*, *1* (2000GC000036).

Tackley, P. J. (2001b). Self-consistent generation of tectonic plates in time-dependent, three-dimensional mantle convection simulations 2. Strain weakening and asthenosphere. *Geochemistry, Geophysics, Geosystems*, *1* (2000GC000043).

Tanimoto, T. and D. L. Anderson (1985). Lateral heterogeneity and azimuthal anisotropy of the upper mantle: Love and Rayleigh waves 100–250 s. *J. Geophys. Res.*, *90*, 1842–1858.

Tao, W. C. (1991). *Ablative subduction and the dynamics of weak slabs*. Ph.D. thesis, Harvard University, Cambridge, MA.

Tao, W. C. and R. J. O'Connell (1992a). Ablative subduction: A two-sided alternative to the conventional subduction model. *J. Geophys. Res.*, *97*, 8877–8904.

Tao, W. C. and R. J. O'Connell (1992b). Back-arc spreading and slab-plate interactions: a feedback mechanism for episodic back-arc spreading (abstract). *EOS Trans. AGU*, *73*, 281.

Tao, W. C. and R. J. O'Connell (1993). Deformation of a weak subducted slab and variation of seismicity with depth. *Nature*, *361*, 626–628.

Taylor, B. and G. D. Karner (1983). On the evolution of marginal basins. *Rev. Geophys. Space Phys.*, *21*, 1727–1741.

Tetzlaff, M. and H. Schmeling (2000). The influence of olivine metastability on deep subduction of oceanic lithosphere. *Phys. Earth Planet. Inter.*, *120*, 29–38.

Thoraval, C. and M. A. Richards (1997). The geoid constraint in global geodynamics: viscosity structure, mantle heterogeneity models and boundary conditions. *Geophys. J. Int.*, *131*, 1–8.

Toksöz, M. N. and A. T. Hsui (1978). Numerical studies of back-arc convection and the formation of marginal basins. *Tectonophysics*, *50*, 177–196.

Tommasi, A. (1998). Forward modeling of the development of seismic anisotropy in the upper mantle. *Earth Planet. Sci. Lett.*, *160*, 1–13.

Tommasi, A., D. Mainprice, G. Canova, and Y. Chastel (2000). Viscoplastic self-consistent and equilibrium-based modelling of olivine lattice preferred orientation. 1. Implications for the upper mantle seismic anisotropy. *J. Geophys. Res.*, *105*, 7893–7908.

Toth, J. and M. Gurnis (1998). Dynamics of subduction initiation at pre-existing fault zones. *J. Geophys. Res.*, *103*, 18,053–18,067.

Tovish, A. and G. Schubert (1978). Island arc curvature, velocity of continents and angle of subduction. *Geophys. Res. Lett.*, *5*, 329–332.

Turcotte, D. L. and E. R. Oxburgh (1967). Finite amplitude convective cells and continental drift. *J. Fluid Mech.*, *28*, 29–42.

Turcotte, D. L. and G. Schubert (1973). Frictional heating of the descending lithosphere. *J. Geophys. Res.*, *78*, 5876–5886.

Turcotte, D. L. and G. Schubert (1982). *Geodynamics. Applications of Continuum Physics to Geological Problems*. John Wiley, New York.

Uyeda, S. and H. J. Kanamori (1979). Back-arc opening and the mode of subduction. *J. Geophys. Res.*, *84*, 1049–1061.

van den Berg, A. P. and D. A. Yuen (1997). The role of shear heating in lubricating mantle flow. *Earth Planet. Sci. Lett.*, *151*, 33–42.

van der Hilst, R. D. (1995). Complex morphology of subducted lithosphere in the mantle beneath the Tonga trench. *Nature*, *374*, 154–157.

van der Hilst, R. D., E. R. Engdahl, R. Spakman, and T. Nolet (1991). Tomographic imaging of subducted lithosphere below northwest Pacific island arcs. *Nature*, *353*, 47–53.

van der Hilst, R. D. and H. Kárason (1999). Compositional heterogeneity in the bottom 1000 kilometers of Earth's mantle: toward a hybrid convection model. *Science*, *283*, 1885–1887.

van der Hilst, R. D., S. Widiyantoro, and E. R. Engdahl (1997). Evidence of deep mantle circulation from global tomography. *Nature*, *386*, 578–584.

van der Lee, S. and G. Nolet (1997). Upper mantle S velocity structure of North America. *J. Geophys. Res.*, *102*, 22,815–22,838.

van der Voo, R. (1993). *Paleomagnetism of the Atlantic Thethys and Iapetus Oceans*. Cambridge University Press, Cambridge.

van Hunen, J., A. P. van den Berg, and N. J. Vlaar (2000). A thermomechanical model of horizontal subduction below an overriding plate. *Earth Planet. Sci. Lett.*, *182*, 157–169.

van Keken, P. and S. Zhong (1999). Mixing in a 3D spherical model of present-day mantle convection. *Earth Planet. Sci. Lett.*, *171*, 533–547.

Vassiliou, M. S. and B. H. Hager (1988). Subduction zone earthquakes and stress in slabs. *Pure Appl. Geophys.*, *128*, 547–624.

Vinnik, L. P., L. I. Makeyeva, A. Milev, and Y. Usenko (1992). Global patterns of azimuthal anisotropy and deformation in the continental mantle. *Geophys. J. Int.*, *111*, 433–447.

Ward, S. N. (1994). Constraints on the seismotectonics of the central Mediterranean from Very Long Baseline Interferometry. *Geophys. J. Int.*, *117*, 441–452.

Weijermars, R. (1992). Flow behavior and physical chemistry of bouncing putty and related polymers in view of tectonic laboratory applications. *Tectonophysics*, *124*, 325–358.

Wenk, H.-R. and C. N. Tome (1999). Modeling dynamic recrystallization of olivine aggregates deformed in simple shear. *J. Geophys. Res.*, *104*, 25,513–25,527.

Wenk, R., K. Bennett, G. R. Canova, and A. Molinari (1991). Modelling plastic deformation of peridotite with the self-consistent theory. *J. Geophys. Res.*, *96*, 8337–8349.

Wessel, P. and W. H. F. Smith (1991). Free software helps map and display data. *EOS Trans. AGU*, *72*, 445–446.

Whittaker, A., M. H. P. Bott, and G. D. Waghorn (1992). Stress and plate boundary forces associated with subduction plate margins. *J. Geophys. Res.*, *97*, 11,933–11,944.

Widiyantoro, S. and R. D. van der Hilst (1996). Structure and evolution of lithospheric slab beneath the Sunda arc, Indonesia. *Science*, *271*, 1566–1569.

Widiyantoro, S. and R. D. van der Hilst (1997). Mantle structure beneath Indonesia inferred from high-resolution tomographic imaging. *Geophys. J. Int.*, *130*, 167–182.

Wolfe, C. J. and S. C. Solomon (1998). Shear-wave splitting and implications for mantle flow beneath the MELT region of the East Pacific rise. *Science*, *280*, 1230–1232.

Woodhouse, J. H. and A. M. Dziewonski (1984). Mapping the upper mantle: three dimensional modeling of Earth structure by inversion of seismic waveforms. *J. Geophys. Res.*, *89*, 5953–5986.

Wortel, M. J. R. and W. Spakman (2000). Subduction and slab detachment in the Mediterranean-Carpathian region. *Science*, *209*, 1910–1917.

Wortel, R. (1982). Seismicity and rheology of subducted slabs. *Nature*, *296*, 553–556.

Yoshioka, S., R. Daessler, and D. A. Yuen (1997). Stress fields associated with metastable phase transitions in descending slabs and deep-focus earthquakes. *Phys. Earth Planet. Inter.*, *104*, 345–361.

Yu, Y. and J. Park (1994). Hunting for azimuthal anisotropy beneath the Pacific Ocean region. *J. Geophys. Res.*, *99*, 15,399–15,421.

Zhang, S. and U. Christensen (1993). Some effects of lateral viscosity variations on geoid and surface velocities induced by density anomalies in the mantle. *Geophys. J. Int.*, *114*, 531–547.

Zhang, S. and S.-I. Karato (1995). Lattice preferred orientation of olivine aggregates deformed in simple shear. *Nature*, *375*, 774–777.

Zhong, S. and G. F. Davies (1999). Effects of plate and slab viscosities on geoid. *Earth Planet. Sci. Lett.*, *170*, 487–496.

Zhong, S. and M. Gurnis (1992). Viscous flow model of a subduction zone with a faulted lithosphere: long and short wavelength topography, gravity. *Geophys. Res. Lett.*, *18*, 1891–1894.

Zhong, S. and M. Gurnis (1994). Controls on trench topography from dynamic models of subducted slabs. *J. Geophys. Res.*, *99*, 15,683–15,695.

Zhong, S. and M. Gurnis (1995). Mantle convection with plates and mobile, faulted plate margins. *Science*, *267*, 838–842.

Zhong, S., M. T. Zuber, L. Moresi, and M. Gurnis (2000). Role of temperature-dependent viscosity and surface plates in spherical shell models of mantle convection. *J. Geophys. Res.*, *105*, 11,063–11,082.

Zhou, H.-W. (1990). Observations on earthquake stress axes and seismic morphology of deep slabs. *Geophys. J. Int.*, *103*, 377–401.

Appendix

A.1 Additional material for chapter 4

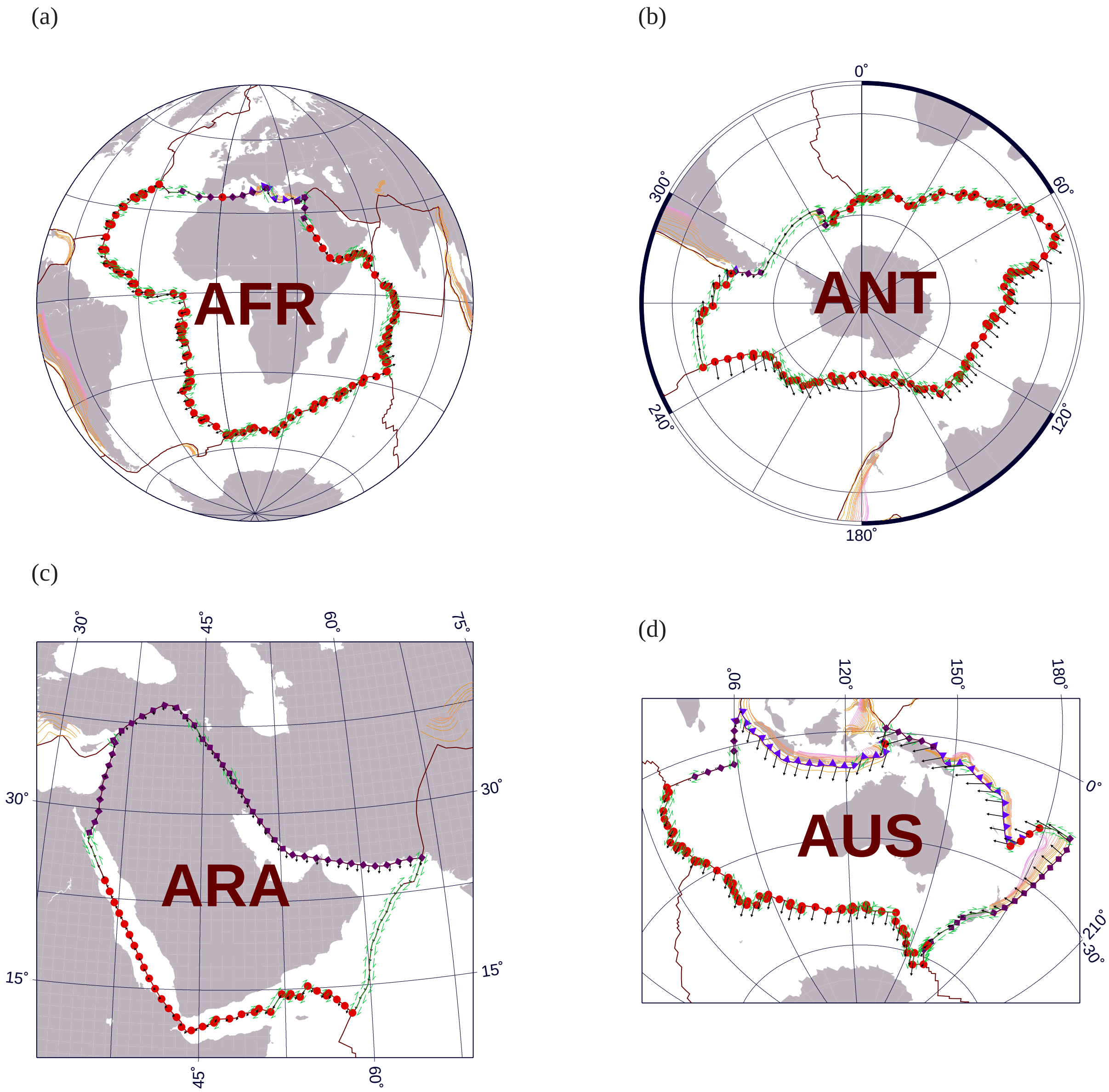

Figure A.1: Plates and boundaries from NUVEL-1 as used in the velocity inversion and integration of edge forces of chapter 4, part 1. (AFR: Africa (a); ANT: Antarctica (b); ARA: Arabia (c); AUS: Australia (d); CAR: Caribbean; COC: Cocos; EUR: Eurasia; IND: India; NAM: North America; NAZ: Nazca; PAC: Pacific; PHI: Philippine Sea plate; and SAM: South America.) Margin types: circles: ridge; slip-arrows: transform boundary; one-sided triangle: convergent margin with seismic slab; and centered triangle: convergent margin without deep seismicity. Thick vectors and contour lines (50 km depth intervals) indicate relative motion of neighboring plates and Wadati-Benioff zone geometry from RUM (Gudmundsson and Sambridge, 1998), respectively.

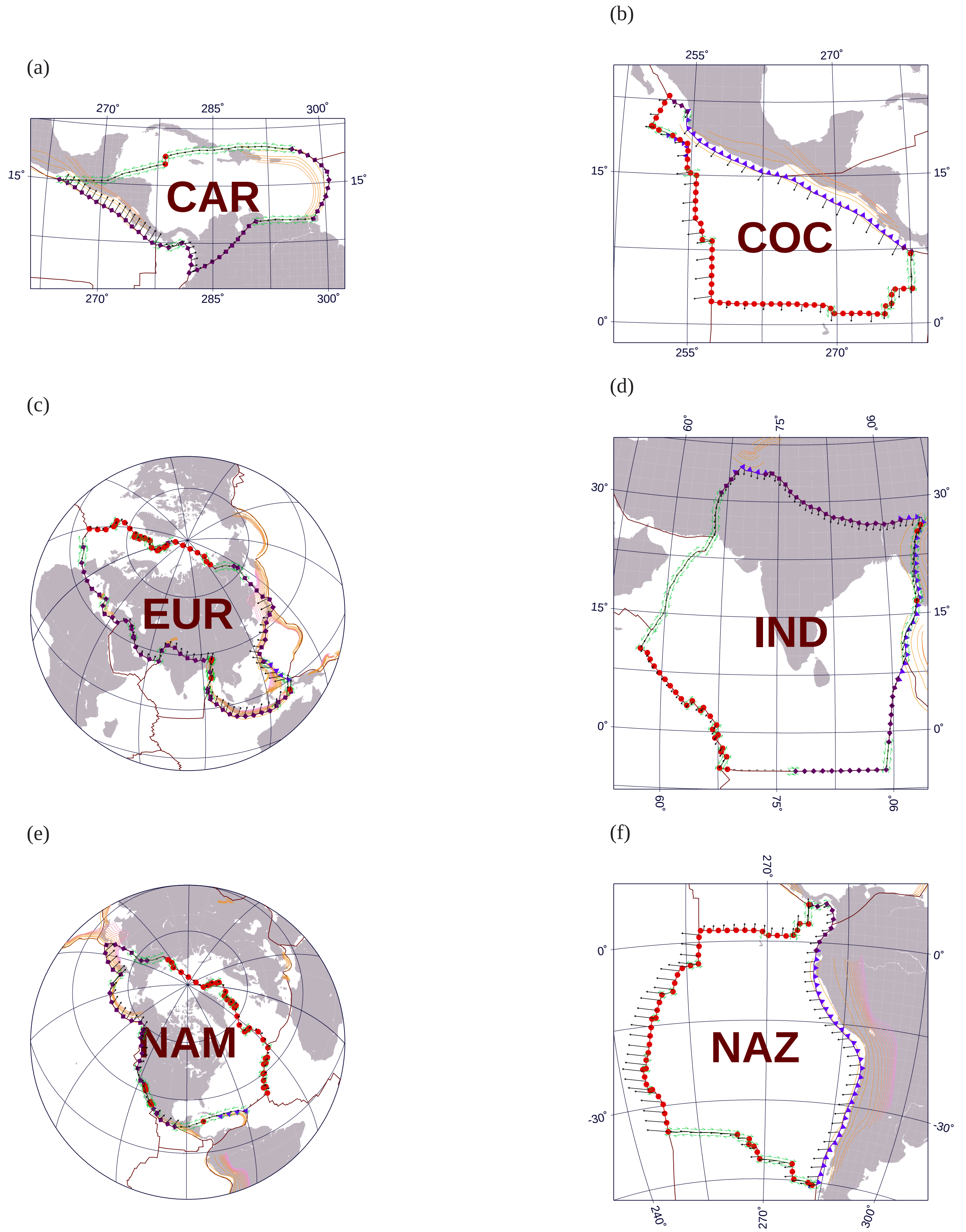

Figure A.2: Plate boundaries as used in the velocity inversion and the integration of plate-boundary forces of chapter 4, part 2: CAR (a), COC (b), EUR (c), IND (d), NAM (e), and NAZ (f). For explanation see Figure A.1.

(a)

(b)

(c)

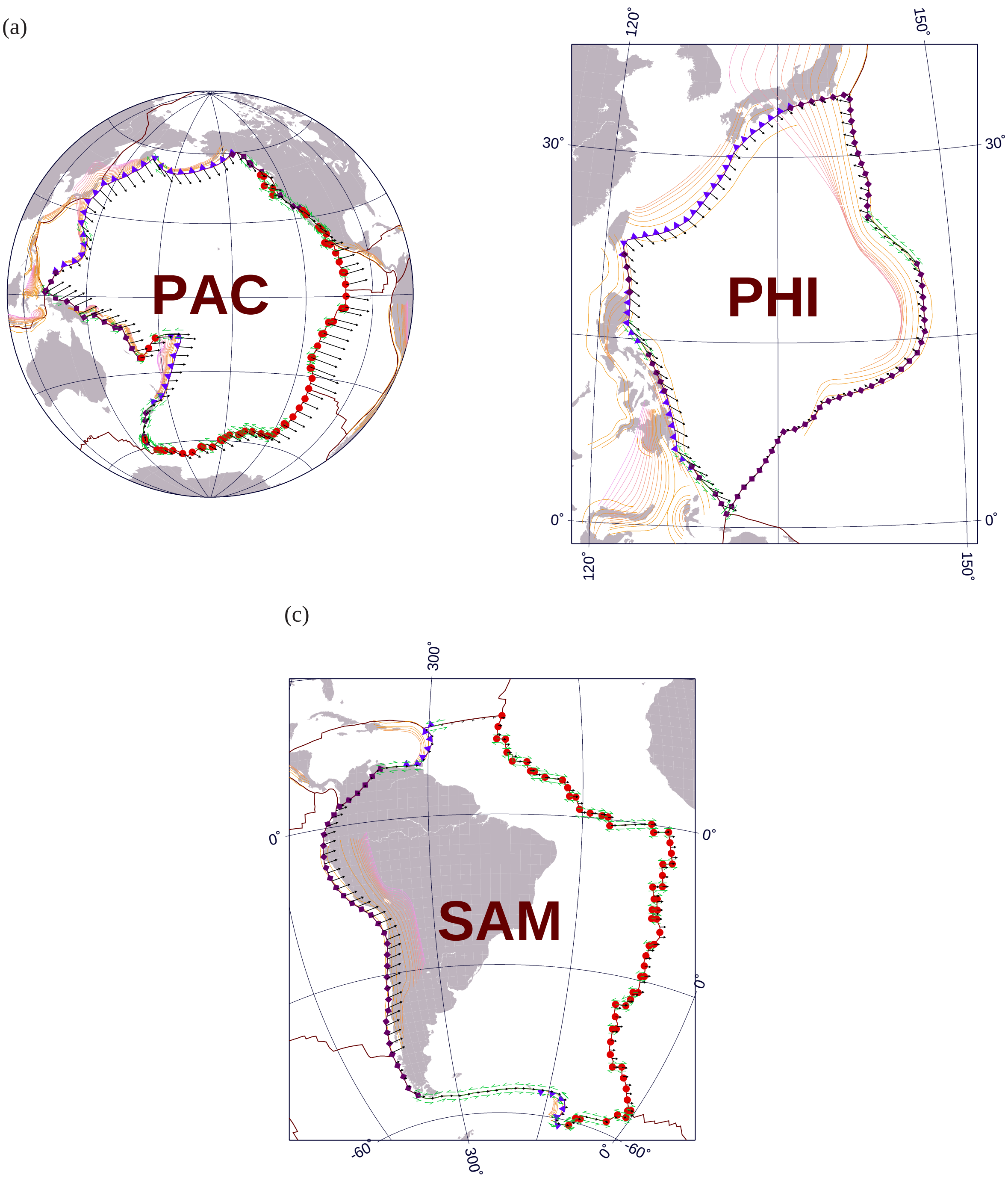

Figure A.3: Plate boundaries as used in the velocity inversion and the integration of plate boundary forces, part 3: PAC (a), PHI (b), and SAM (c). For explanation see Figure A.1.

Table A.1: Best two models for mantle density plus lithospheric thickening driving torques of sec. 4.5.2. Scaling factors are normalized such that the lithospheric contribution is assumed to be known ($w_{\mathrm{lith}} \equiv 1$), and for *lrr98d* and *stb00d* $R_\rho^{\mathrm{tomo}} \neq 1$ indicates scaling of the density field.

viscosity	*density model*	*type*	r_w	VR_w	η_0 [10^{21} Pas]	R_ρ^{tomo}
		scaling factors fixed				
C	stb00d	whole	0.83	54.7%	1	1
	sb4l18	whole	0.75	42.1%	1	0.2
D	lrr98d	whole	0.84	70.2%	1	1
	s20rts	whole	0.83	68.5%	1	0.2
E	stb00d	whole	0.83	54.4%	1	1
	sb4l18	whole	0.75	42.3%	1	0.2
F	stb00d	whole	0.83	68.5%	1	1
	sb4l18	whole	0.77	56.8%	1	0.2
G	ngrand	whole	0.84	−79.0%	1	0.2
	bdp00	whole	0.60	−94.1%	1	0.4
H	ngrand	whole	0.81	65.4%	1	0.2
	lrr98d	whole	0.86	62.1%	1	1
		scaling factors optimized				
C	stb00d	whole	0.83	69.7%	0.32	0.53
	lrr98d	whole	0.83	68.1%	0.21	0.55
D	stb00d	whole	0.85	73.0%	1.55	1.05
	lrr98d	whole	0.84	71.0%	1.05	1.28
E	stb00d	whole	0.83	69.2%	0.32	0.52
	lrr98d	whole	0.82	67.8%	0.22	0.57
F	stb00d	whole	0.83	69.2%	0.68	0.71
	lrr98d	whole	0.82	67.2%	0.44	0.73
G	lrr98d	whole	0.89	79.5%	1.41	0.34
	s20rts	whole	0.88	76.8%	0.94	0.03
H	lrr98d	whole	0.88	76.8%	0.58	0.32
	stb00d	whole	0.87	75.8%	0.77	0.27

Table A.2: Best two models for mantle density, lithospheric thickening torques from ocean age progression, and *rum* upper mantle slabs of sec. 4.5.2. Scaling factors are normalized such that lithospheric sources are assumed to be known ($w_{\mathrm{lith}} \equiv 1$). $R_\rho^{\mathrm{tomo}} \neq 1$ or $R_\rho^{\mathrm{rum}} \neq 1$ implies scaling of the density field for *lrr98d*, *stb00d*, or *rum*. (Not all optimized weights correspond to realistic solutions.)

viscosity	*density model*	*type*	r_w	VR_w	η_0 [10^{21} Pas]	R_ρ^{tomo}	R_ρ^{rum}
			scaling factors fixed				
C	stb00d	whole	0.87	68.9%	1	1	1
	sb4l18	whole	0.84	60.4%	1	0.2	1
D	bdp00	lower	0.86	73.5%	1	0.4	1
	ngrand	whole	0.88	71.6%	1	0.2	1
E	stb00d	whole	0.87	68.2%	1	1	1
	sb4l18	whole	0.84	59.9%	1	0.2	1
F	sb4l18	whole	0.85	72.0%	1	0.2	1
	stb00d	whole	0.86	72.0%	1	1	1
G	bdp00	whole	0.83	−508.7%	1	0.4	1
	kh00p	whole	0.78	−528.2%	1	0.4	1
H	bdp00	lower	0.88	74.4%	1	0.4	1
	kh00p	lower	0.83	57.4%	1	0.4	1
			scaling factors optimized				
C	bdp00	lower	0.87	76.4%	0.99	1.42	3.90
	stb00d	whole	0.87	76.2%	0.62	0.69	1.24
D	sb4l18	whole	0.89	79.1%	1.78	0.14	1.41
	ngrand	whole	0.89	79.1%	2.40	0.51	1.93
E	bdp00	lower	0.87	75.9%	0.98	1.40	4.00
	ngrand	whole	0.87	75.9%	0.42	0.19	1.11
F	bdp00	lower	0.87	75.9%	2.19	1.98	5.03
	sb4l18	whole	0.87	75.6%	0.74	0.09	1.09
G	stb00d	whole	0.90	81.7%	2.95	0.32	0.53
	bdp00	lower	0.90	81.1%	3.22	0.41	1.24
H	stb00d	whole	0.90	80.2%	1.41	0.39	0.54
	ngrand	whole	0.88	77.7%	0.95	0.10	0.50

A.2 Additional material for chapter 5

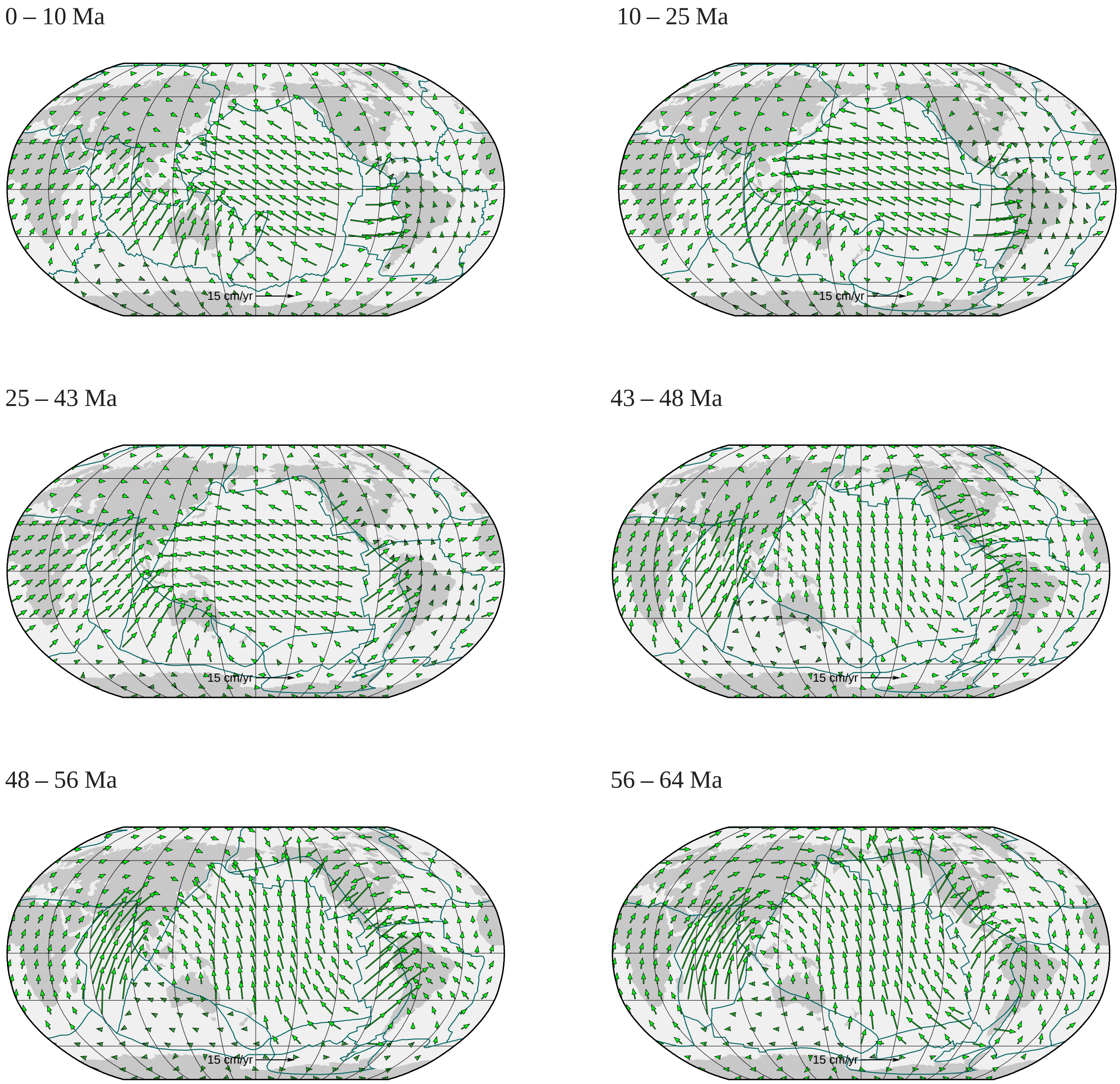

Figure A.4: Plate-tectonic stages from Gordon and Jurdy (1986) for 0 through 64 Ma. Plate velocities were expanded up to $\ell_{max} = 63$ using programs provided by R. J. O'Connell (pers. comm.), no-net-rotation reference frame. Shaded coastlines are from the present-day and shown stationary for reference only.

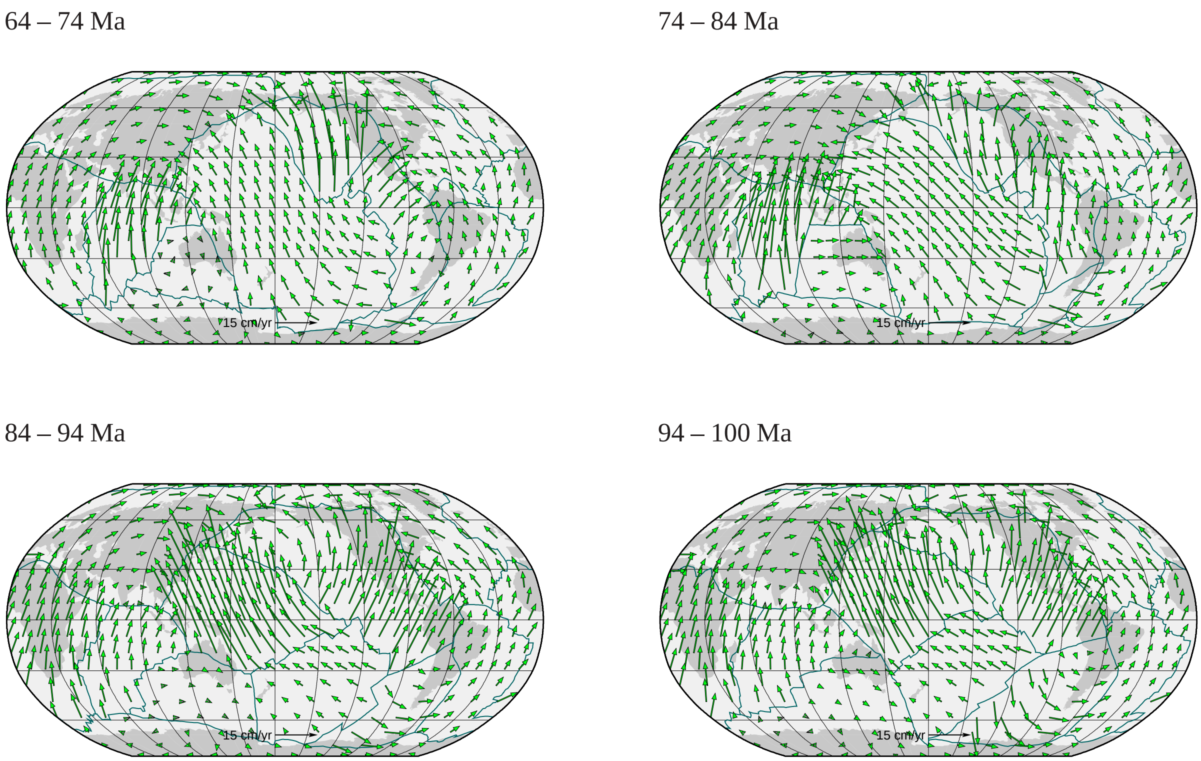

Figure A.5: Plate tectonic stages from Lithgow-Bertelloni *et al.* (1993) for 64 through 100 Ma, no-net-rotation reference frame as in Figure A.4.

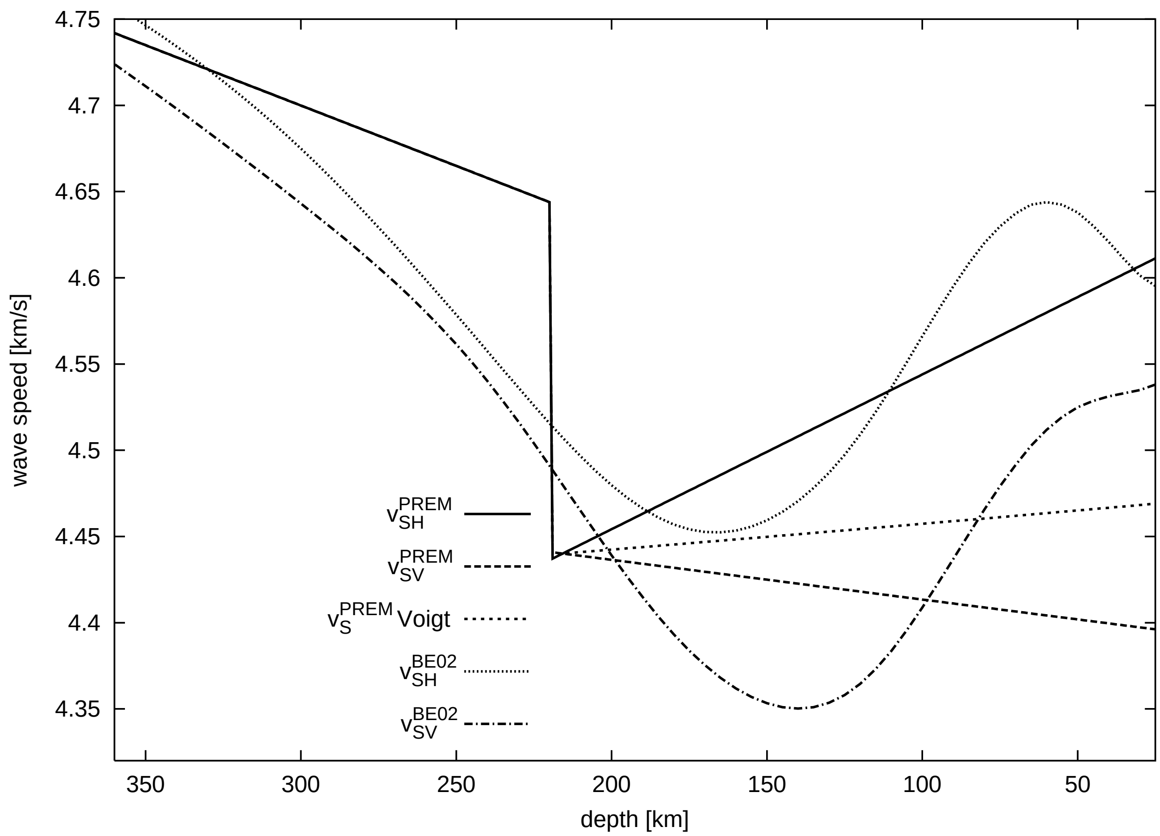

Figure A.6: Shear-wave velocities in the upper mantle from the 1-D reference model PREM (Dziewonski and Anderson, 1981) and lateral average from Boschi and Ekström's (2002) 3-D inversion (BE02). Wave speeds are shown for horizontally polarized S waves (v_{SH}), vertically polarized S waves (v_{SV}), and the "Voigt" averaged S velocity, v_S^{Vgt}. v_S^{Vgt} can be derived from the Voigt-averaged (homogeneous strain) elastic shear modulus, μ^{Vgt}, of a transversely isotropic medium, which is given by $\mu^{\mathrm{Vgt}} = (A+C-2F+5N+6L)/15$ in the notation of Love (1927) (*e.g.* Dziewonski and Anderson, 1981, see also sec. A.2.1). Assuming that $A \approx C$ ($v_{PV} \approx v_{PH}$) and $\eta = F/(A-2L) \approx 1$, the equivalent velocity for μ^{Vgt} is $v_S^{\mathrm{Vgt}} = \sqrt{\left(v_{SH}^2 + 2v_{SV}^2\right)/3}$ (*e.g.* Ekström and Dziewonski, 1998).

A.2.1 Depth sensitivity of surface waves to azimuthal anisotropy

In chapter 5, we compare surface-wave observations of anisotropy with flow-model derived strains. We will therefore briefly review how the appropriate sensitivity kernels for Rayleigh waves can be constructed.

Rayleigh and Love waves are equivalent to spheroidal (${}_n\mathrm{S}_\ell$) and toroidal (${}_n\mathrm{T}_\ell$) normal modes, respectively, for $n \ll \ell/4$ (*e.g.* Dahlen and Tromp, 1998, p. 405ff). The wavenumber k of a surface wave with angular frequency ω and phase velocity c ($c = \omega/k$) relates to the degree ℓ as $Rk = \ell + 1/2$, where R is the radius of the Earth. The eigenfunctions of high-ℓ normal modes can thus be used to construct Fréchet derivatives (or *sensitivity kernels*), K_m, that characterize the effect of small perturbations in a parameter m at a certain depth r on changing ω:

$$k_m(\omega, r) = mK_m = m\frac{\partial\omega}{\partial m}. \tag{A.1}$$

Here, m can be an elastic modulus or density ρ (*e.g.* Dahlen and Tromp, 1998, p. 335). For a transversely isotropic Earth model such as PREM, the elasticity tensor C_{ij} ($1 \le i, j \le 6$, notation as in Montagner and Nataf, 1986) is reduced from its most general form with 21 independent components to five constants, which are commonly named A, C, F, L, and N in the notation of Love (1927). Transversely isotropic wave propagation implies a reduction of elastic anisotropy to hexagonal symmetry. If the symmetry axis is further assumed to be in the radial direction (radial anisotropy), these Love parameters relate to the vertically and horizontally propagating P waves as $v_{PV} = \sqrt{C/\rho}$ and $v_{PH} = \sqrt{A/\rho}$, respectively, and to S waves as $v_{SV} = \sqrt{L/\rho}$ and $v_{SH} = \sqrt{N/\rho}$ (*e.g.* Dahlen and Tromp, 1998, p. 321). The fifth parameter F does not have an obvious physical interpretation but $\eta = F/(A-2L)$ is generally close to unity. For isotropic wave propagation (deeper than 220 km in PREM, *cf.* Figure A.6), $C = A = F$ are equal to the incompressibility, $L = N$ are equal to the shear modulus, and $\eta = 1$. We write the perturbations in the eigenfrequency ω of a normal mode in a transversely isotropic medium as

$$d\omega \approx \int_0^R \left(\frac{dC}{C}k_C + \frac{dA}{A}k_A + \frac{dL}{L}k_L + \frac{dN}{N}k_N + \frac{dF}{F}k_F + \frac{d\rho}{\rho}k_\rho \right) \tag{A.2}$$

while the equivalent variations in phase velocity can be obtained with the relation

$$dc = \frac{c^2}{v_g\omega}d\omega. \tag{A.3}$$

Here, v_g is the group velocity of the surface wave ($v_g = d\omega/dk$).

For wave propagation in an elastic medium that has the most general form of anisotropy, with 21 independent coefficients, Smith and Dahlen (1973) showed that the azimuthal (ϕ) dependence of Love and Rayleigh wave speed anomalies can be expanded as

$$\delta c = \frac{dc}{c} \approx D^0 + D_C^{2\phi}\cos(2\phi) + D_S^{2\phi}\sin(2\phi) + D_C^{4\phi}\cos(4\phi) + D_S^{4\phi}\sin(4\phi) \tag{A.4}$$

for small amounts of anisotropy. Montagner and Nataf (1986) demonstrated that the sensitivity kernels for the D-terms can be retrieved from the kernels already constructed for transversely isotropic models. Montagner and Nataf also found that the 4ϕ terms should generally be small for predominantly horizontal alignment of fast propagation axes based on measurements of C_{ij} from the field. Rayleigh waves are more sensitive to the 2ϕ component than Love waves, and only the 2ϕ term has a simple interpretation in terms of fast propagation axes in a strained medium with lattice-preferred orientation. Phase-velocity inversions do not require a 4ϕ contribution, and the 4ϕ signal is typically smaller than the 2ϕ signal if both are damped with the same strength (sec. 5.3.1).

We shall therefore focus on $D^{2\phi}$ for Rayleigh waves. Montagner and Nataf (1986) find that sensitivity kernels for the $\cos(2\phi)$ and $\sin(2\phi)$ ($D_{C,S}^{2\phi}$) terms can be written as

$$k^{\mathrm{Rayleigh}}_{\cos(2\phi),\sin(2\phi)} = \frac{B_{C,S}}{A}k_A + \frac{H_{C,S}}{F}k_F + \frac{G_{C,S}}{L}k_L. \tag{A.5}$$

The six fractions with $B_{C,S}$, $H_{C,S}$, and $G_{C,S}$ are simple functions of C_{ij} (Montagner and Nataf, 1986, eq. 5) and determine the relative weights of the $k_{A,F,L}$ kernels. While Montagner and Nataf's (1986) analysis of the effect of anisotropy was restricted to a flat Earth, Romanowicz and Snieder (1988) were able to recover Montagner

type	$\frac{B_{C,S}}{A}$	$\frac{H_{C,S}}{F}$	$\frac{G_{C,S}}{L}$
Peselnick and Nicolas (1978)			
cos	0.034	0.003	0.028
sin	-0.002	0.006	-0.008
$\sqrt{\cos^2+\sin^2}_{\text{norm}}$	1.0	0.176	0.853
Nunuvak (Ji *et al.*, 1994)			
cos	0.075	0.014	0.054
sin	-0.009	-0.004	-0.009
$\sqrt{\cos^2+\sin^2}_{\text{norm}}$	1.0	0.197	0.724

Table A.3: Ratios of elastic coefficients for 2ϕ contributions as in (A.5) for two different rock samples from the indicated sources. cos and sin denote the C,S constants. Since the partitioning of these ratios depends on the horizontal coordinate frame, we also give the amplitude $\sqrt{\cos^2+\sin^2}_{\text{norm}}$, normalized by the maximum ratio in each row.

and Nataf's approximation asymptotically for large ℓ in a more complete treatment. Following Montagner and Tanimoto (1991), we can therefore obtain the depth sensitivity of Rayleigh waves to azimuthal anisotropy with (A.5) if we use elastic moduli for some representative anisotropic material whose fast propagation axis is assumed to be in the horizontal plane. Table A.3 lists the relevant parameters for an oceanic sample from Peselnick and Nicolas (1978) (as used by Montagner and Nataf, 1986) and for Nunuvak from Ji *et al.*'s (1994) data (as used by Savage, 1999).

We note that the $B_{C,S}$ and $G_{C,S}$ ratios are consistently larger than the $H_{C,S}$ ratio. Since the k_L kernel is additionally somewhat larger than k_A and k_F, the $G_{C,S}/Lk_L$ term is mostly responsible for the depth sensitivity of Rayleigh waves to the 2ϕ anisotropy, shown in Figure A.7 for surface waves with periods of $T = 50$ s, $T = 100$ s, and $T = 150$ s. Phase-velocity sensitivity kernels were estimated based on normal-mode eigenfunctions computed for radially anisotropic PREM with the `MINEOS` program by G. Masters (*cf.* Dahlen and Tromp, 1998, p. 335). As discussed by Montagner and Nataf (1986), the k_L kernel dominates most of the deep sensitivity while the k_A contribution leads to a second sensitivity peak at shallow depth. For the elastic parameters under consideration, the sensitivity of Rayleigh waves to azimuthal anisotropy has a depth dependence that is very similar to their $k_{V_{SV}}$ kernels. The approximate rule that the depth, z_s, to which Rayleigh waves sense structure is given by half their wavelength (*e.g.* Dahlen and Tromp, 1998, p. 449) can be rewritten in terms of ℓ as $z_s = \pi R/(\ell+1/2)$, which gives ~ 110 km, ~ 215 km, and ~ 320 km for periods of 50 s, 100 s, and 150 s, in agreement with Figure A.7. We will use the 2ϕ kernels to average the horizontal projections of the inferred fast-propagation axes from strain at each depth when we compare our modeling results with surface-wave based anisotropy in section 5.6.

(a) $T = 50$ s

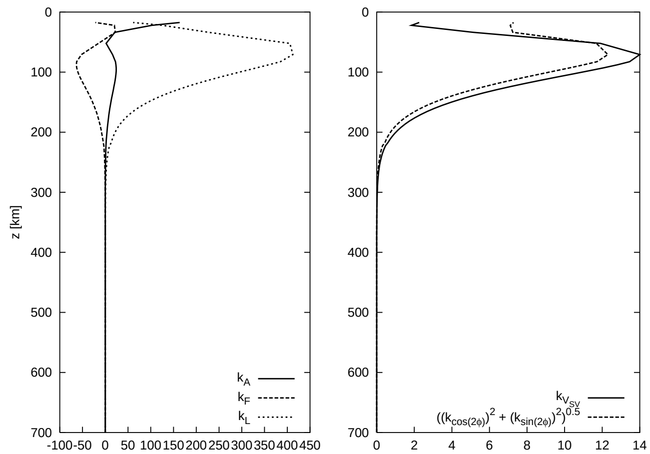

(b) $T = 100$ s

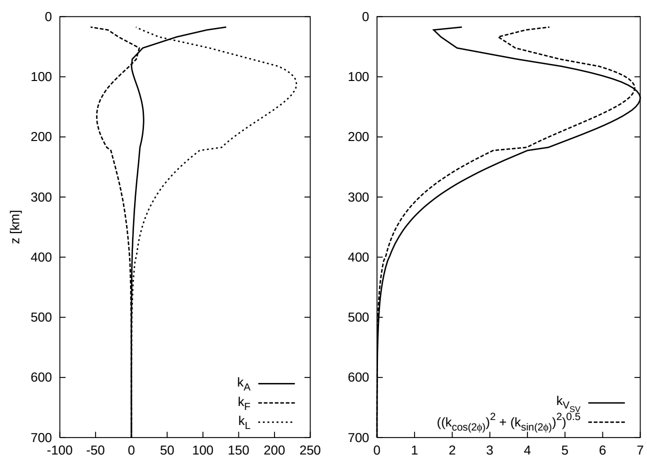

(c) $T = 150$ s

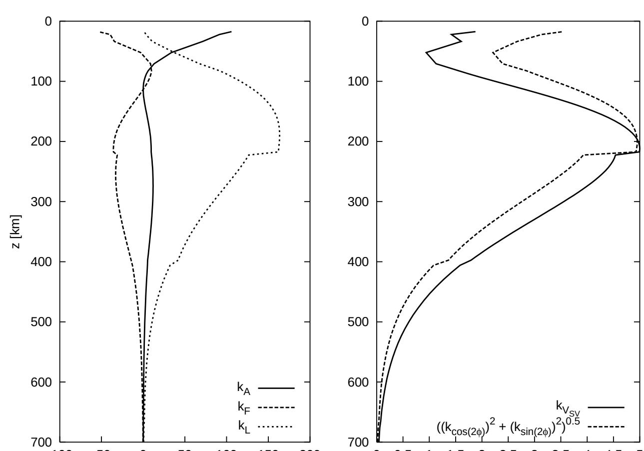

Figure A.7: Sensitivity kernels for Rayleigh waves with periods, T, of 50 s (a, $\ell = 202$), 100 s (b, $\ell = 97$), and 150 s (c, $\ell = 62$) for anisotropic PREM. Left plots show k_A, k_F, and k_L on the same scale with arbitrary units against depth z; right plots compare the kernel for the amplitude of all 2ϕ terms (calculated from (A.5) and the data of Peselnick and Nicolas (1978) in Table A.3) with the kernel for vertically polarized S waves, $k_{V_{SV}}$. The latter two kernels are scaled such that peak amplitudes are comparable.

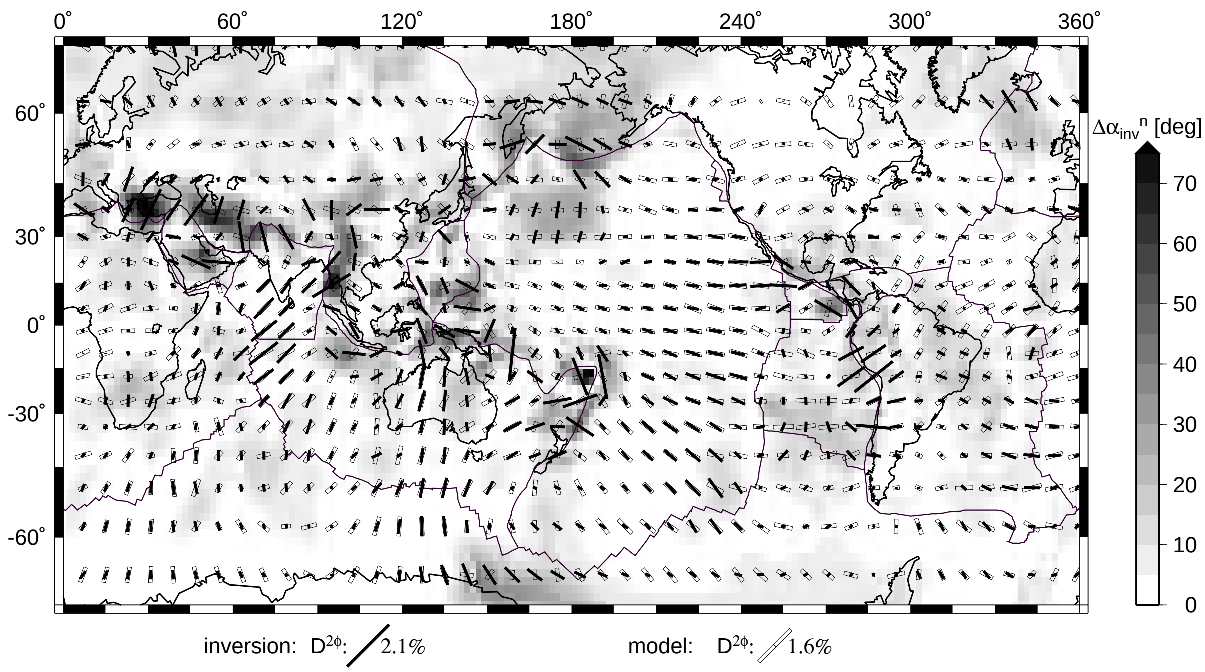

Figure A.8: Comparison of phase-velocity derived 2ϕ anisotropy from Ekström (2001) for $T = 100$ s and predicted $\zeta_c = 0.5$ anisotropy for evolving plates ($t_c = 60$ Ma), η_F, and *smean* advected density (non-tectosphere buoyancy for $z < 220$ km included). See Figure 5.27 for explanation.

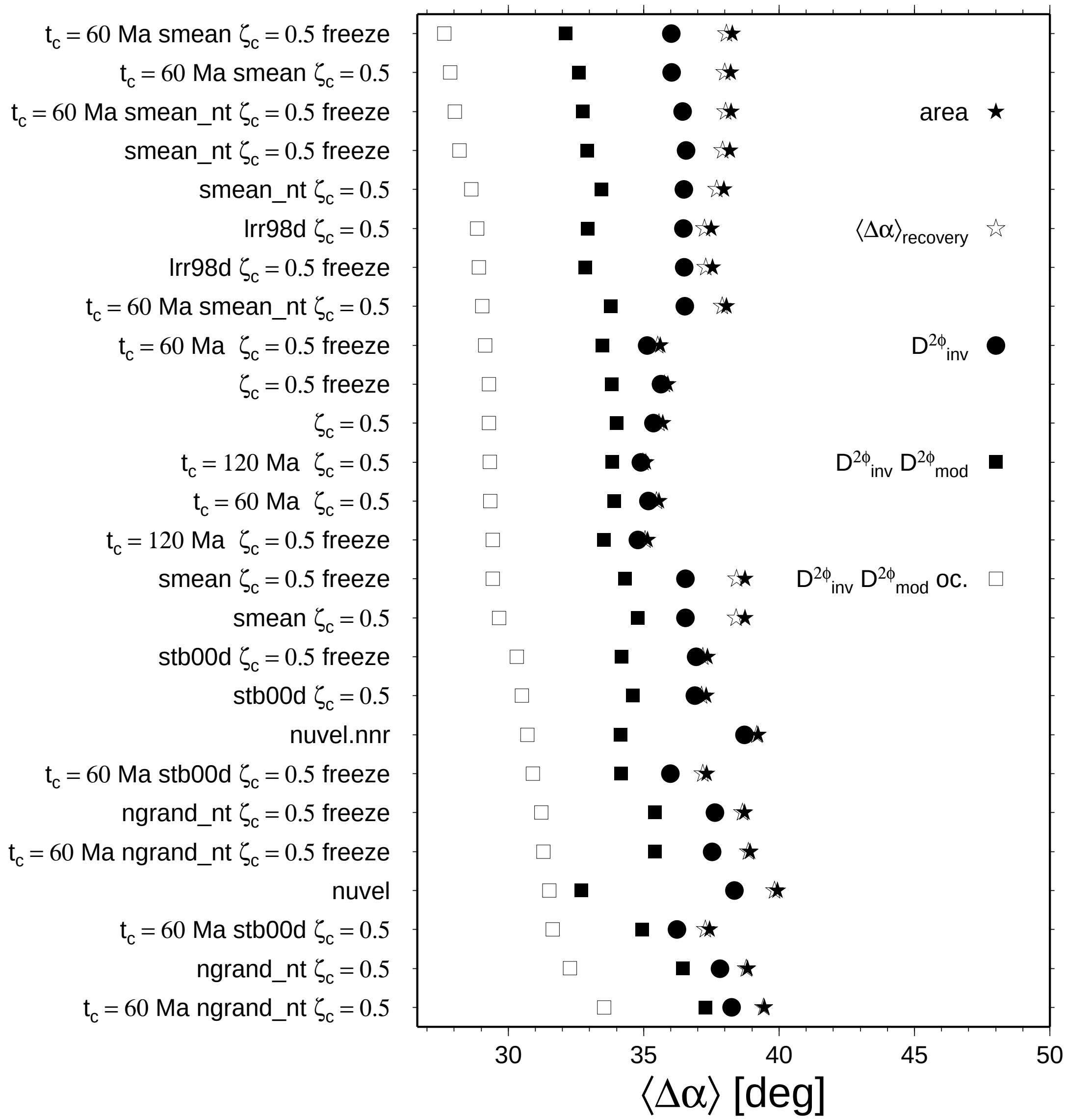

Figure A.9: Mean orientational misfit between 2ϕ anisotropy of $T = 100$ s Rayleigh wave inversions (Ekström, 2001) and circulation model predictions. See Figure 5.29 for legend.

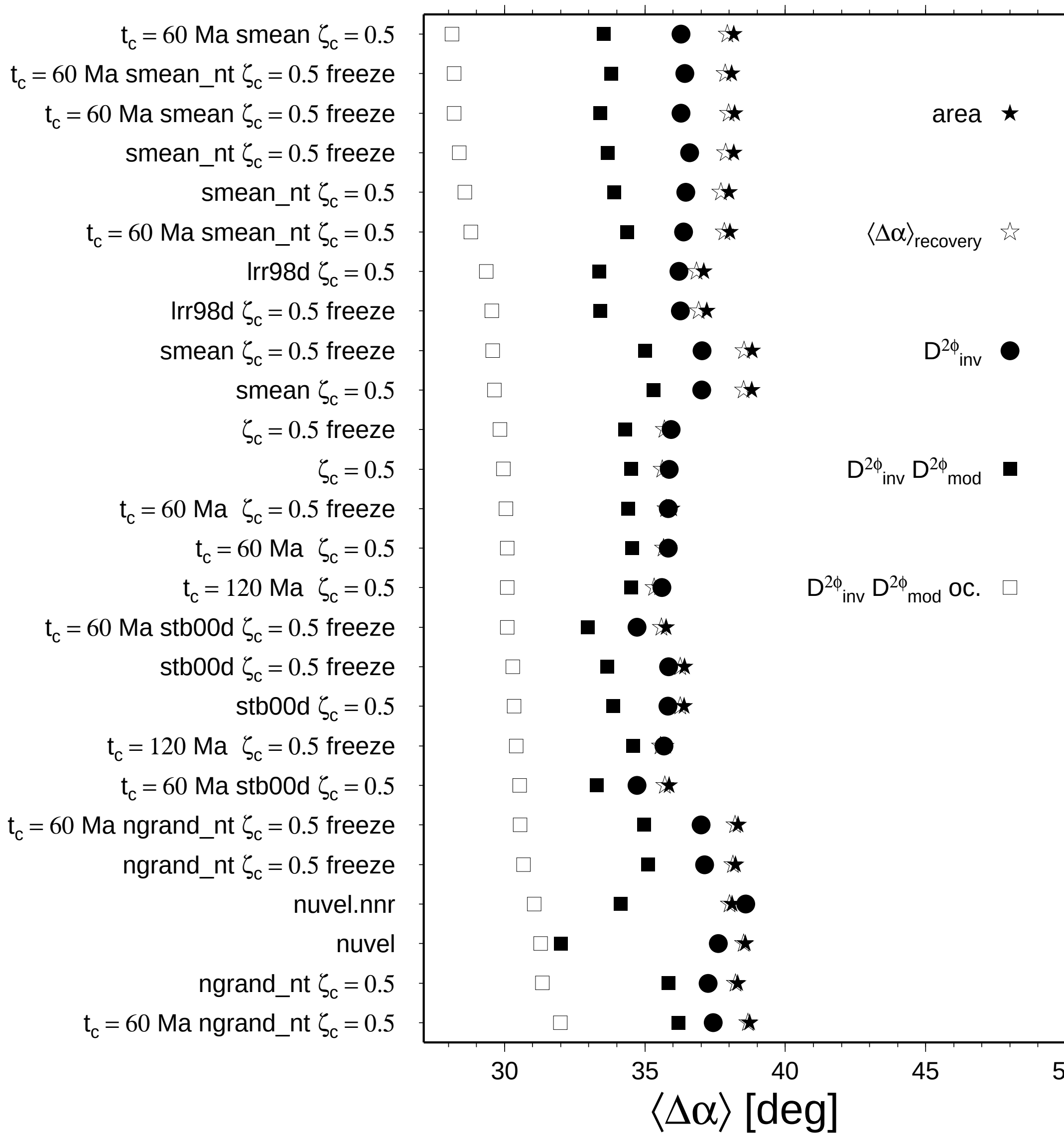

Figure A.10: Mean orientational misfit between 2ϕ anisotropy of $T = 150$ s Rayleigh wave inversions (Ekström, 2001) and circulation model predictions. See Figure 5.29 for legend.